

University of Nottingham
UK | CHINA | MALAYSIA

EPSRC
Engineering and Physical Sciences Research Council



Exploring the Electronic and Photocatalytic Properties of Organic-Inorganic Hybrid Polyoxometalates

Alexander John Kibler

14260935

School of Chemistry

A thesis submitted to the University of Nottingham for the degree of Doctor of Philosophy

Acknowledgements

Whilst a PhD is often considered to be a self-lead, independent research venture, it would be naïve to think that such a mammoth undertaking could ever be accomplished without the help and support of friends, colleagues and loved ones.

I would firstly like to thank Dr. Graham Newton for all the support and guidance offered over the entire PhD program. He has been an exemplary mentor that has kept me motivated and driven these past four years. Thank you for always giving excellent advice on both scientific and non-scientific matters, for your openness and for your infectious passion for research.

I would also like to thank Dr. Jamie Cameron for his willingness to talk through any problem and try and fix any situation, and for indulging my tirades of questions especially during write-up times. On the same chord I would like to thank Newton Group alumni Dr. Katharina Kastner for all her guidance and patience when starting in the lab and Dr. Maria Martin-Gandul for her experimental and mental input into the POM-IL project, as well as being a powerhouse of energy that kept the lab in shape during her time here. Furthermore, I would like to extend my thanks to Dr. Jesum Alves Fernandes for our usually amusing adventures into the world of photochemistry, for teaching me all the basics and for all his help with solid state analyses.

I would like to express gratitude towards collaborators on the BTD project; Prof. Jairton Dupont and Virginia De Souza for all their help in initially seeding the ideas and providing samples from the get-go. Equally I would like to thank, our collaborators Dr. David Robinson and Mr. Max Winslow for their excellent DFT calculations and continued collaboration on the project. I would like to thank Dr. Darren Walsh for his guidance on the electrochemistry of the POM-ILs.

I would like to thank our past and present X-ray crystallographers Dr. William Lewis and Dr. Stephen Argent, the latter of which has been immensely helpful in teasing the data out from my crystal structures and for showing enthusiasm for otherwise daunting POM-based crystallographic nightmares. Additionally, I would like to thank Mr. Ben Pointer Gledhill for producing excellent mass spectra of my compounds and Tong Liu for all of the elemental analysis work.

I would next like to thank my fellow PhD students, particularly Sharad Amin for indulging my wanton demands for TEM time and Neelam Mughal the same with cyclic voltammetry experiments. Both

deserve thanks for being hugely supportive especially during crunch times of my PhD both academically and personally. I would also like to thank Catherine Peake for always being available to reason out my electrochemical quandaries no matter how complex. I would like to generally thank the whole of the Newton group for being such a pleasure to work with. Also, thanks to the contributions of Masters students Agata Rogalska and Ezra Lyons.

I would like to thank the EPSRC for funding and the CDT in Sustainable Chemistry for giving me the opportunity to undertake this research, I would like to thank the director Prof. Peter Licence for his candid advice throughout the CDT journey.

I would lastly like to thank my partner Bradley who has been a rock to me over this PhD adventure, for his ability to give unrestrained advice and guidance at times when its most needed and for his selfless support during my most selfish moments.

Abbreviations List

ATR-IR	Attenuated total reflectance infra-red
BMIM	1-butyl-3-methylimidazolium
Bpy	2,2-bipyridine
BTD	2,1,3-benzothiadiazole
CHN	Carbon, Hydrogen, Nitrogen – elemental analysis
CT	Charge transfer
CV	Cyclic voltammetry
DCM	Dichloromethane
DFT	Density functional theory
DMF	N,N-dimethylformamide
DMSO	Dimethylsulfoxide
DSC	Differential scanning salorimetry
EMIM	1-ethyl-3-methylimidazolium
ESIPT	Excited-state intramolecular proton transfer
ESI-MS	Electrospray ionisation mass spectrometry
FET	Field effect transistor
FID	Flame ionisation detector
HAT	Hydrogen atom transfer
HOMO	Highest occupied molecular orbital
IL	Ionic liquid
IVCT	Intervalence charge transfer
LB	Langmuir-Blodgett
LMCT	Ligand to metal charge transfer
LUMO	Lowest unoccupied molecular orbital
MeCN	Acetonitrile
MOF	Metal organic framework
NMR	Nuclear magnetic resonance
NOE	Nuclear overhauser effect
OLED	Organic Light Emitting Diode
POM	Polyoxometalate
POM-IL	Polyoxometalate-ionic liquid
PXRD	Powder X-ray Diffraction
SCE	Standard calomel electrode
SET	Single electron transfer

TBA	Tetra-n-butylammonium
TBADT	Tetran-butylammonium decatungstate
TEA	Tetra-n-ethylammonium
TGA	Thermogravimetric analysis
THTP	Trihexyl(tetradecyl)phosphonium
TOF	Turnover frequency
TON	Turnover number
TTF	Tetrathiafulvalene
UV	Ultraviolet
UV-vis	Ultraviolet visible

Colour Scheme

All figures that have not been reproduced from literature and that pertain to specific structures adhere to the following colour scheme:

Tungsten: Light blue

Phosphorus: Pink

Molybdenum: Plum

Vanadium: Blue-grey

Silicon: Orange

Arsenic: Teal

Sulfur: Yellow

Carbon: Dark grey

Hydrogen: Light grey

Oxygen: Red

Nitrogen: Blue

NB. General structures will be given in Light blue (addenda atoms) and pink (heteroatoms)

Publications

The following articles bave been published as a result of the work undertaken during the course of this PhD program:

Redox-active organic–inorganic hybrid polyoxometalate micelles, K. Kastner, A. J. Kibler, E. Karjalainen, J. A. Fernandes, V. Sans and G. N. Newton, J. Mater. Chem. A, 2017, 5, 11577, DOI: 10.1039/C7TA00408G

Tuning the electronic structure of organic-inorganic hybrid polyoxometalates: The crucial role of the covalent linkage, A. J. Kibler, G. N. Newton, Polyhedron, 2018, 154, 1, DOI: 10.1016/j.poly.2018.06.027.

Physical and Electrochemical Modulation of Polyoxometalate Ionic Liquids via Organic Functionalization, A. J. Kibler, C. Martin, A. Rogalska, J. Dupont, D. A. Walsh, G. N. Newton, Eur. J. Inorg. Chem., 2019, 3-4, 456, DOI: 10.1002/ejic.201800578

Contents

1. Introduction **1**
1.1 Polyoxometalates 1
1.2 Structure, bonding and formation 1
1.3 Archetypal polyoxometalate structures 5
1.3.1 Lindqvist anion 5
1.3.1 Keggin anion 6
1.3.1 Wells-Dawson anion 8
1.3.1 Lacunary anions 9
1.3.1 Miscellaneous anions 11
1.4 Electronic nature of POMs 12
1.5 Photocatalytic properties of POMs 15
1.6 Polyoxometalate hybridisation 17
1.6.1 Class 1 hybrids for photocatalytic applications 21
1.6.2 Class 2 hybrids for photocatalytic applications 31
1.7 References 46
2. Combining POMs with cationic dyes for photocatalytic small molecule activation **50**
2.1 Introduction 50
2.2 Aims 58
2.3 Results and discussion 59
2.3.1 Synthetic development 59
2.3.2 Structural characterisation 61
2.3.3 Thermophysical characterisation 67
2.3.4 Electronic characterisation 70
2.3.5 Solid-state Electronic characterisation 75
2.3.6 Photocatalytic studies 86
2.4 Conclusion 90
2.5 Experimental 92
2.6 References 96
3. Electronic structure and photocatalytic abilities of organoarsenic hybrid POMs **101**
3.1 Introduction 101
3.2 Aims 105
3.3 Results and Discussion 106
3.3.1 Synthetic development 106
3.3.2 Structural characterisation 109
3.3.3 Electronic characterisation 119

3.3.4 Photoreduction studies 130
3.4 Conclusion 137
3.5 Experimental 139
3.6 References 144
4. Physical and electrochemical tuning of POM-ILs via organic functionalisation 145
4.1 Introduction 145
4.2 Aims 150
4.3 Results and discussion 151
4.3.1 Synthetic development 151
4.3.2 Structural characterisation 153
4.3.3 Thermophysical characterisation 156
4.3.4 Electronic characterisation 164
4.4 Conclusion 170
4.5 Experimental 172
4.6 References 176
5. Conclusions and Outlook 178
6. Methods, Materials and Instrumentation 180
7. Appendix 183
7.1 Crystal data and structure refinement for BTDImH[W_{18}] 183
7.2 Crystal data and structure refinement for [$AsPhW_{17}$] 185

Abstract

This thesis encompasses the synthesis and characterisation of electro- and photoactive organic-inorganic hybrid polyoxometalates (POMs). Specifically, the use of aromatic organic groups, either as countercations (Class I), as covalently grafted moieties (Class II) or combination thereof, have been explored with regards to their abilities to fine-tune the inherent properties of the POM cluster. The ability to tune the properties of redox and photo-active polyoxometalates represents an important step in the formation of “designer” materials, where the physical and electronic properties of the system can be tailored towards bespoke applications.

In Chapter 2, the combination of redox rich Wells-Dawson phosphotungstates with fluorescent dye-type π-extended benzathiadiazole (BTD) cations yield a family of Class I hybrids with different modes of quaternization (proton, methyl, acetic acid). Crystallographic studies on the protonated derivative showed that the planar BTDImH structure is perturbed by hydrogen bonding to the POM and the solvent. Measurements of the electronic properties of the materials in the solution and solid state revealed stark differences, suggesting that the properties of the material are a product of interactions between the two components in the solid state. It also demonstrated that the different quaternisation strategies resulted in different electrochemical behaviour due to the different protic environments provided. Finally, preliminary studies on the hybrid featuring BTDImH cations revealed that the compound is capable of acting as a carbon dioxide photoreduction catalyst, whereas the respective components showed no activity, testament to the synergic effects gained when the photoactive components are combined.

Chapter 3 explores a new strategy for the covalent functionalisation of the Wells-Dawson phosphotungstate anion through the use of arylarsonic acids (Class II hybrids). Three different arylarsonic acids were explored bearing electron withdrawing (NO_2), electron donating (NH_2) and “neutral” (H) substituents in the para- position. Akin to their phenylphosphorus analogues, the arylarsonic hybrids were reduced at more positive potentials than the parent anion, and the redox potentials were tuneable based on the electronic nature of the rings. The perceived trends in the lowering of the LUMO energies was corroborated with DFT. The phenylarsonic hybrid was compared to phenylphosphonic and phenylsiloxane hybrids for the photoreduction of DMF with both UV-vis and

visible light. The phenylarsonic hybrid was photosensitised towards visible light, and whilst the phenylphosphonic hybrid was more easily reduced, the phenylarsonic was more easily reoxidised with molecular oxygen.

In Chapter 4, a combined approach is adopted in the synthesis of covalently functionalised polyoxometalate ionic liquids (POM-ILs) based on the Keggin anion. This work used the bulky trihexyltetradecylphosphonium cation (THTP) to generate ionic liquids from two covalently functionalised Keggins featuring phenylphosphonic and phenylsiloxane groups (Class I/II hybrids). Thermophysical techniques determined that the POM-ILs exhibited higher stability than their classical salt precursors and had a wider liquid range than the plenary POM-IL analogue, despite their physical similarities, the POM-ILs gave contrasting electrochemical properties due to the different nature of the linker atoms used to graft the phenyl ring to the POM. Remarkably, the phenylphosphonic derivative which is highly unstable as a classical salt showed drastic improvement in both its thermal and electrochemical stability due to the shrink-wrapping effect of the bulky cations.

1. Introduction

1.1 Polyoxometalates

Polyoxometalates (POMs) are an intriguing class of discrete anionic metal oxide clusters, composed of transition metals in their highest oxidation state ligated by bridging and terminal oxo ligands. Characterised by impressive structural diversity coupled with rich redox properties, photoactivity and high thermal and chemical stability, these species have shown promise in a myriad of applications including conventional, electro- and photocatalysis,[1, 2] functional materials,[3] optoelectronics,[4] battery technologies,[5] magnetism,[6] medicine,[7] and sensing.[8]

Whilst the structural diversity of these species attracts the attention of chemists that specialise in structural design, the exponentially increasing interest in POMs lie with their fascinating electronic character. Their unique position between the molecular and macroscopic regimes, in combination with their equally valid application in solution and solid-state technologies, gives rise to a family of compounds whose electronic properties straddle the line between molecular orbitals and band structure characteristics. Furthermore, various avenues exist to fine-tune their electronic nature through the modification of the POMs immediate surroundings or direct manipulation of the structure itself, the "designer" aspect of these systems through simple post-synthetic modification ensures that both POM and non-POM chemists alike continue to be ensorcelled by this ever-expanding and evolving field.

1.2 Structure, bonding and formation

Whilst the understanding of the principles of POM formation and bonding can seem quite daunting given the extensive library of polyoxometalate structures of different shapes, sizes and composition, their structures can, for the most part, be described by a set of simple rules and concepts. Firstly, we consider the smallest unit of the polyoxometalate, the $[MO_x]$ polyhedron (where x = 4-7, typically 6), which is composed of a central metal atom, referred to as the addenda atom, coordinated to between 4 and 7 oxo-ligands which are formally O^{2-} anions (Figure 1a). The individual addenda atoms must possess certain properties to be able to polycondense to form discrete clusters, namely; 1) the ability to change coordination number from 4 to 6 upon polymerisation in solution, 2) possess high positive charges and are among the smaller atoms that can form octahedral packing arrangements with oxygen, 3) the ability to form double bonds with unshared (terminal) oxygen atoms through pπ-dπ orbital interactions.[9] Thus,

obeying these rules, the addenda atoms that typically constitute polyoxometalates are the early transition metals of groups V and VI (V, Nb, Ta, Mo, W) in their highest oxidation states (usually d^0 or d^1 configuration).

The oxo-ligands that comprise the vertices of the polyhedron are the structurally versatile components of the POM that both allow their polycondensation by acting as bridging atoms between metals and limit their extension into infinite metal oxide structures via stable terminal multiple bonds. The bridging oxo-ligands can link anywhere between two and six addenda atoms and is represented by the notation μ_n, where n is the number of bridged metals. The key to the stability of many POM clusters lies with the terminal oxo-groups, in the common octahedral configuration, the terminal oxo ligands exhibit a strong thermodynamic *trans*-effect by weakening the bond to the bridging oxygen atom located at the opposite vertex of the octahedron which share its orbital. Structurally, this results in a displacement of the metal centre towards the terminal oxo-ligand, outwardly from the core of the structure, resulting in a displacement from idealised octahedral geometry (Figure 1b). The electronic effect of this is the high polarisation of the terminal oxo-groups towards the addenda atom (relative to the bridging oxo-ligands), this in turn markedly decreases the basicity of the oxide surface which, which inhibits protonation and hence reduces the propensity towards further condensation reactions, which are typically acid mediated. The *trans*-effect is therefore the reason that discrete POM clusters can be isolated at all and do not simply form the more commonly encountered polymeric metal oxides.

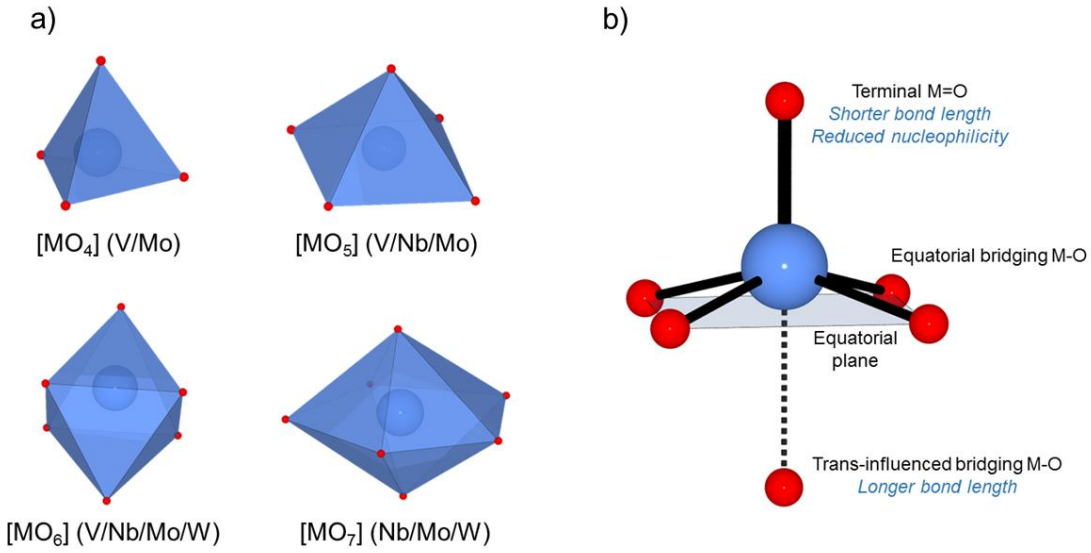


Figure 1. a) Polyhedral units that are commonly encountered as building blocks in POM structures. b) Visual representation of the trans-effect upon the coordination environment of the metal in polyoxometalates.

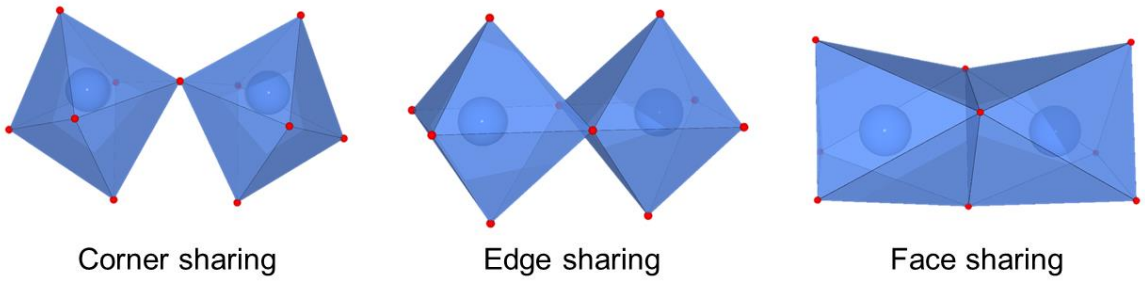


Figure 2. Connectivity modes between polyhedral units upon oligomerisation based on the sharing of one (corner), two (edge) or three (face) oxygen atoms between two metal centres.

There is also a great variety in which the polyhedral units can polymerise, as each unit can be connected through corner sharing, edge sharing and face sharing, which corresponds to the sharing of one, two or three oxo-ligands between two octahedral units (Figure 2). A single polyoxometalate anion is often constructed from a combination of these modes, whereby their architecture is limited only by the restraint that each single polyhedron must contain either one or two terminal oxo-ligands, known as the Lipscomb principle.[10] This principle is applicable to almost all POM structures, with rare examples of structures that violate the rule compensated by protonation of the oxo ligands or drastic displacement of the addenda atoms from their predicted geometry.[11] In addition to the structural ramifications of this rule, the number of terminal oxo atoms that each metal centre possesses directly affects the electronic properties of the polyoxometalate, which will be discussed later (Section 1.4).

A final structural element that is common to the majority of POM structures is the presence of heteroatoms. Heteroatoms are non-addenda atoms that typically reside within the core of the POM structure and are integral for its formation, as such they have also gained the moniker of “templating” atoms. The atom that resides in this position can be metallic or non-metallic in nature but must be able to bond to at least three oxygen atoms. This usually limits the selection of heteroatom to p-block and d-block elements in high oxidation states that can form 4-coordinate and 6-coordinate oxyanions. The structures that contain heteroatoms are called heteropolyoxometalates, whereas those that do not are called isopolyoxometalates (Figure 3), in lieu of a templating atom, the cores of isopolyoxometalates often contain a μ_6 oxo-ligand. Despite the imposed structural rigidity of the addenda atoms, for a single heteropolyoxometalate structure with the same addenda atoms, many different heteroatoms of varying sizes may be employed. This is another result of the trans-effect, as the inwardly facing oxo-ligands of the addenda atoms (opposite to the terminal oxo ligand), which bridges the heteroatom, is weakened and therefore subject to less harsh geometric constraints.

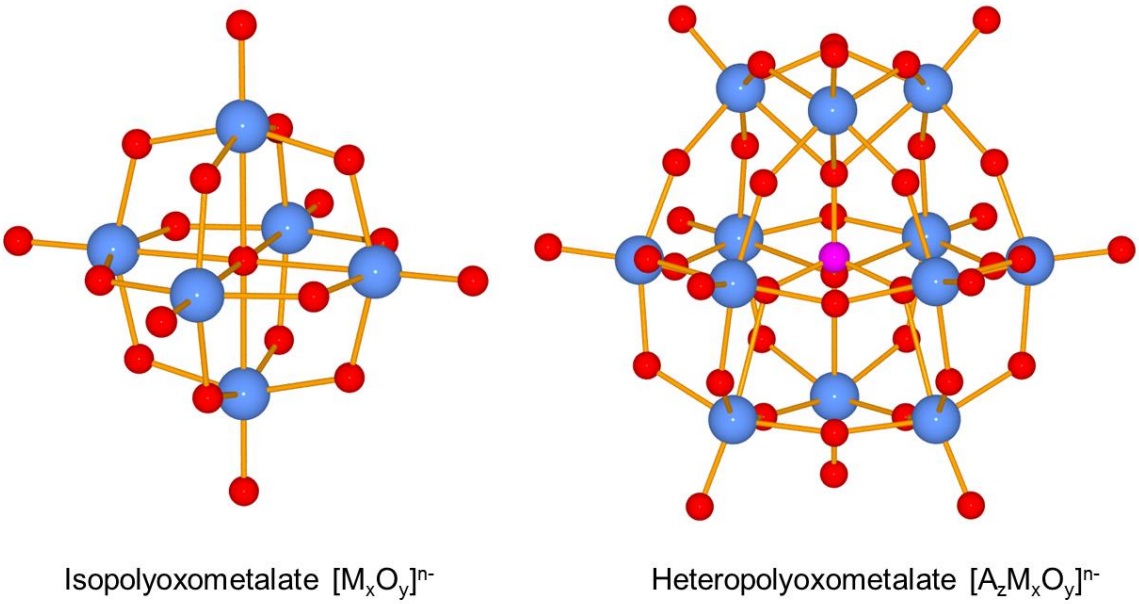
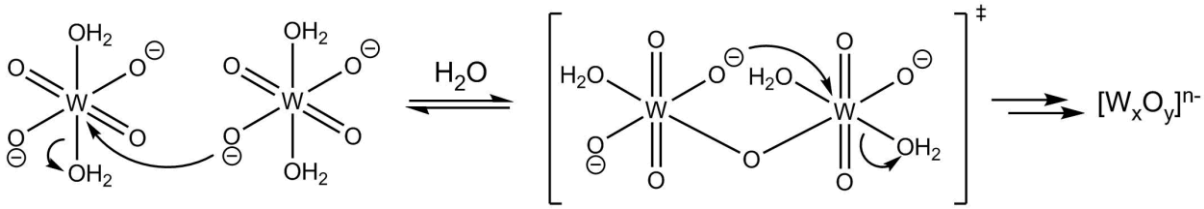


Figure 3. Comparison between isoplyoxometalates $[M_xO_y]^{n-}$ and heteropolyoxometalates $[A_zM_xO_y]^{n-}$ whereby the latter usually features a non-addenda non-oxygen core as a stabilising template.

Polyoxometalates are typically formed through pH mediated self-assembly of metal oxoanions (introduced via a water soluble oxometalate salt such as Na_2WO_4, Na_2MoO_4 or $NaHVO_3$) in aqueous solution. For the synthesis of heteropolyoxometalates, a source of heteroatom (usually mineral acids or alkali metal derivatives) is also added either before or during the reaction. As alluded to previously, single oxometalate units upon protonation can undergo polycondensation (also known as olation) reactions to form discrete anionic clusters. Lowering of the pH induces an expansion of the metal coordination sphere from tetrahedral to octahedral, leading to a polarisation of the M=O bonds and subsequent protonation generating labile water ligands. Condensation reactions between these hydrated complexes readily occurs due to the increased Lewis acidity of the metal and the lability of the water ligands, forming bridged metal complexes. The unstable intermediates can fuse further via the same mechanism until kinetically stable species are formed (Scheme 1).[12] This process is highly sensitive to several experimental factors including the pH, temperature, solvent, cation and ratio of addenda atom to heteroatom. Typically, once the desired POM has been formed in solution, it is then precipitated by the addition of a suitable countercation, however given the complexity of the self-assembly processes, the compound may need to be purified several times to isolate the desired structure in its pure form. Whilst the synthesis of several well-established structures are easy to reproduce due to their inherent stability and simplicity, the intentional formation of new structures from

small building blocks is very challenging, with the self-assembly and speciation of polyoxometalates in solution still a poorly understood aspect of polyoxometalate chemistry.[13]



Scheme 1. Condensation reaction between MO_6 octahedra forming polynuclear M_xO_y units. Adapted from [12] with permission from Springer Pulishing.

1.3 Archetypal polyoxometalate structures

Despite the conceptually limitless morphologies that octahedral and tetrahedral units can form through the sharing of oxide ligands, several common structures have been recognised as general building blocks, both isolable as their discrete anions and used as the basis of construction of larger clusters.[14]

1.3.1. Lindqvist anion

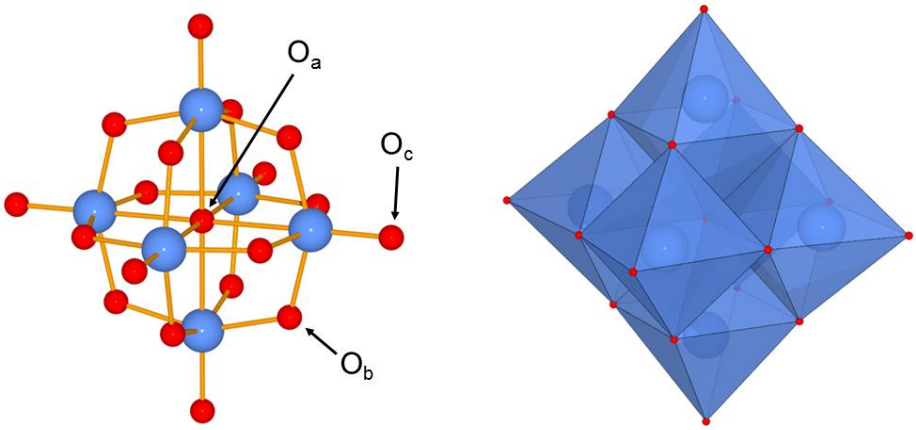


Figure 4. Ball and stick (left) and polyhedral (right) representation of the Lindqvist polyoxometalate (M_6O_{19}) showing the unique oxygen atom environments within the cluster.

The Lindqvist structure is regarded as one of the simplest isopolyoxometalates and was first solved in 1953 with the characterisation of sodium hexaniobate $Na_7[HNb_6O_{19}]$.[15] The structure (Figure 4) is composed of 6 octahedral MO_6 units that share edges to form a superoctahedron (O_h symmetry) with a common vertex in the central oxygen atom. There is one metal environment and three oxygen atom environments; the central μ_6-oxo ligand (O_a), the 12 bridging μ_2-oxo ligands (O_b), and the 6 terminal oxo ligands (O_c); giving the general formula $[M_6O_{19}]^{x-}$.[16] The presence of the unusual μ_6-oxo ligand within the cage can be explained by the extremely strong interaction between the highly charged metal and the terminal oxo ligands (“yl” oxygens) which remove electron density trans to the multiple bond. This

results in the central atom of the cage resembling a non-bonding O^{2-}, and the metal environment closer resembling pentahedrons than octahedrons.[17] Lindqvist structures are well reported for niobium, molybdenum, tungsten and tantalum, however for 1st row transition metals of group V and VI (vanadium and chromium), neither form stable isohexametalates (note that they do form similar polyoxoalkoxometalates) due to the large ligand repulsion and small (d-p)π interactions coupled with second order Jahn-Teller instability.[18]

1.3.2. Keggin anion

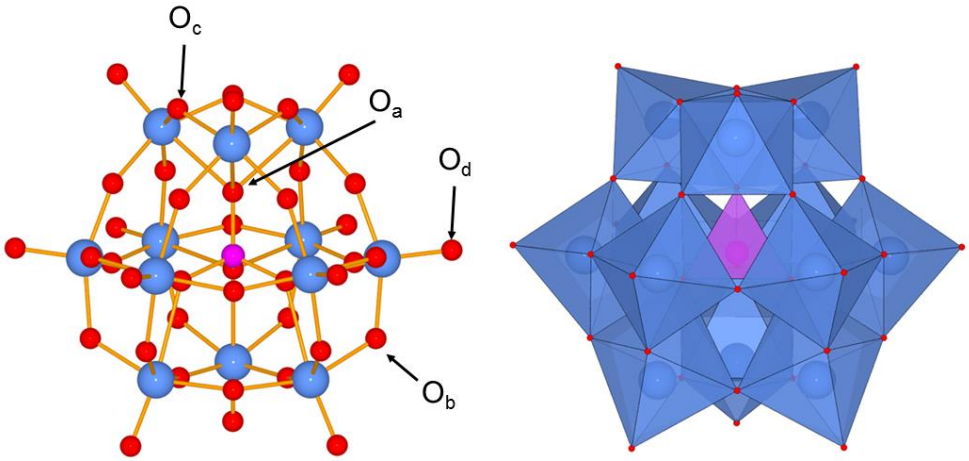


Figure 5. Ball and stick (left) and polyhedral (right) representation of the Keggin polyoxometalate ($XM_{12}O_{40}$) showing the unique oxygen atom environments within the cluster.

The Keggin structure was the first polyoxometalate structure to be crystallographically elucidated with the characterisation of 12-phosphotungstic acid in 1933 and represents the simplest of the heteropolyoxometalates.[19] They adopt the general formula $[XM_{12}O_{40}]^{n-}$ where X represents the heteroatom that can be either a metal or a non-metal.[20] Whilst the Keggin motif is extremely common for both tungsten and molybdenum derivatives,[21] those of niobium are much rarer and exhibit unusual features such as extremely high charge, reverse in pH stability and can only by accessed hydrothermally.[22] Tantalate, vanadate and chromate Keggin structures in their unadulterated forms have yet to be isolated.

The structure (Figure 6) has overall tetrahedral symmetry and is based around an XO_4 tetrahedron which shares it oxygen atoms with four groups of M_3O_{13} clusters. These subunits are linked through corner-sharing and are comprised of three edge sharing MO_6 octahedra.[23] Within this structure there are four different oxygen environments; there are 4 O_a atoms that bridge M atoms to the heteroatom X.

A total of 24 O_b and O_c atoms bridge the metal octahedra to one another by either corner or by edge respectively and 12 O_d terminal atoms for each M octahedron.[24]

Unlike the Lindqvist structure, Keggin anions have a degree of rotational isomerism. This arises from the fact that the four M_3O_{13} clusters can exist in one of two possible orientations. Starting from the α-isomer (T_d symmetry), successively rotating each of the M_3O_{13} units through 60° gives the other four possible isomers (β C_{3v}, γ C_{2v}, δ C_{3v}, ε T_d), represented in Figure 6.[25] The most stable, symmetrical and prolific throughout the literature is the α-isomer, the β-isomer is also stable though less common with fewer structures being fully characterised by X-ray diffraction.[26] The propensity of Keggin-type POMs to self-assemble as the β isomer is governed by an equilibrium that is dependent on factors such as the heteroatom and the solvent environment.[27] Conversely, relatively few examples exist of the γ,[28] δ,[29] [26][26]and ε isomers,[30] as these often require specialist synthetic procedures for their isolation.

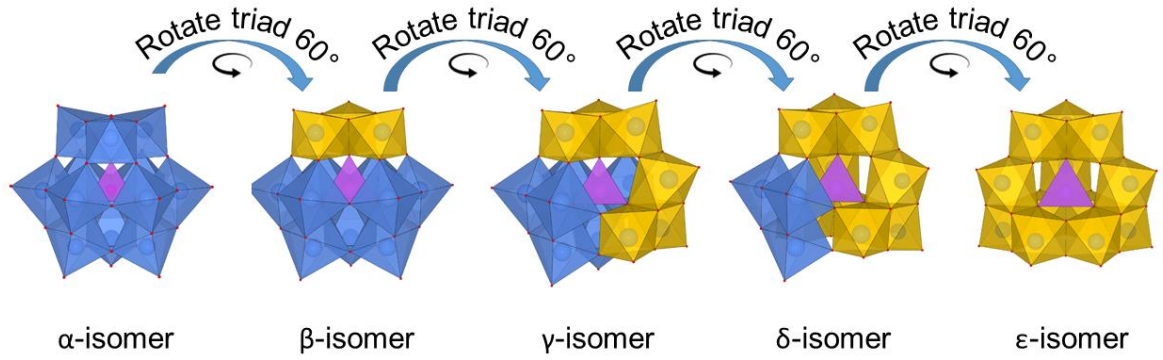


Figure 6. Five isomers of the Keggin anion, accessed by successive rotations of the four M3 triads through 60°C.

1.3.3. Wells-Dawson anion

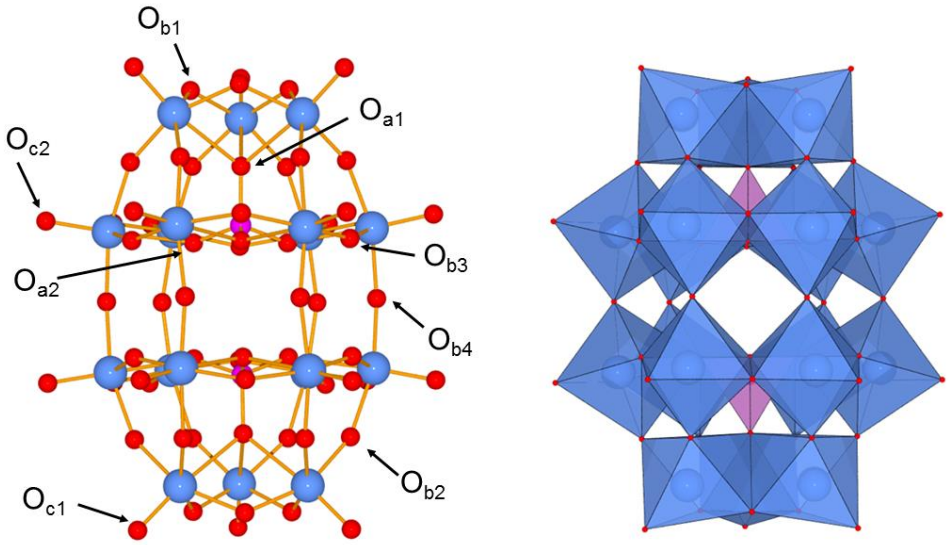


Figure 7. Ball and stick (left) and polyhedral (right) representation of the Wells-Dawson polyoxometalate ($X2M_{18}O_{62}$) showing the unique oxygen atom environments within the cluster.

The Wells-Dawson structure was first identified in 1953 with the characterisation of potassium 9(18)-tungstophosphate.[31] The heteropolyoxometalate structure is viewed as the linkage between two A-type trilacunary Keggin clusters $[XM_9O_{34}]^{n-}$ via corner sharing, giving a structure that can be described as two belts of six MO_6 units capped by two M_3O_{13} groups (Figure 7) with the general formula $[X_2M_{18}O_{62}]^{n-}$.[32] For this structure, only the molybdate and tungstate analogues are known. As with the Keggin ion, X usually represents a tetrahedral XO_4 unit, however there are cases where pyramidal centres are known such as arsonite, AsO_3, and pyrophosphate, P_2O_7, in lieu of both heteroatoms.[33] In other cases, one of the heteroatoms may be absent altogether e.g. Arseno-18-tungstic acid $[H_4AsW_{18}O_{62}]^{7-}$.[34] However these alternative heteroatoms accompany structural perturbations to the classical structure and hence will not be discussed in further detail.

The arrangement of metals into cap and belt regions results in several different oxygen environments, the 62 oxygen anions can be divided into eight different types. Connected to the core heteroatoms, 2 O_{a1} atoms link the heteroatom to the cap metals and 6 O_{a2} atoms link the heteroatom to the belt metals. Bridging atoms can be separated into 6 oxygen atoms that bridge the cap metals (O_{b1}), 12 oxygen atoms that link the caps to the belts (O_{b2}), 12 oxygen atoms that bridge the belt metals (O_{b3}) and 6 oxygen atoms that connect the two belts (O_{b4}). Finally, 6 terminal atoms are located on the cap metals (O_{c1}) and 12 terminal atoms are located on the belt metals (O_{c2}).

Predictably, there is rotational isomerism within the structure. Successive 60° rotations of the end caps give the α, β and γ isomers (D_{3h}, C_{3v} and D_{3h} symmetry respectively), whereas the rotation of the end caps of the staggered form (where the pyramidal heteroatoms are staggered by 180°C) give the α*, β* and γ* isomers (D_{3d}, C_{3v} and D_{3d} symmetry respectively), depicted in Figure 8.[23] The stability of these isomers follows the general trend α, β, γ, γ*, β*, α* with only the first four of these having been isolated.[35]

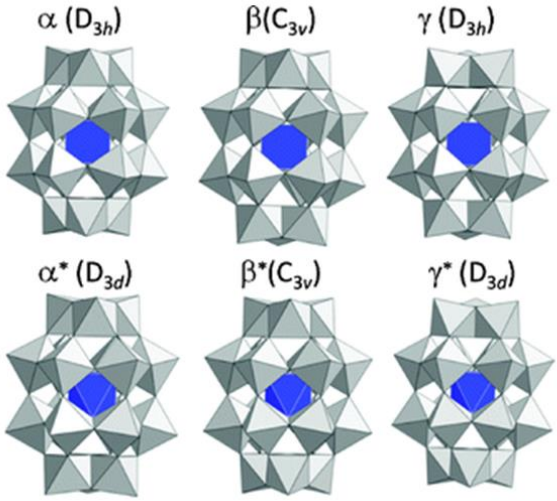


Figure 8. Six isomers of the Wells-Dawson anion, the top series is accessed through rotation of the two caps by 60°C with the core tetrahedral heteroatoms aligned whereas the bottom series is accessed through rotation of the caps by 60°C with the core tetrahedral heteroatoms misaligned by 60°C. Reproduced from [36] with permission from the Royal Society of Chemistry.

1.3.4. Lacunary anions

For some structures, chiefly the Keggin and Dawson anions, the controlled removal of one or more of the addenda atoms can be achieved through pH-controlled hydrolysis of the cluster. The resultant species are dubbed “lacunary” polyoxometalates – lacuna meaning unfilled space or gap, whist the parent polyoxometalate are referred to a “plenary” polyoxometalates. The act of removing the metal centre(s) from the cluster results in the exposure of anionic oxo ligands and an increase in the overall charge of the POM. For polyoxotungstates, these lacunary species are usually stable and isolable, whereas for molybdates these species are highly reactive and often difficult to isolate and handle without degradation occurring.[37] The lacunary species are of great importance in the functionalisation of polyoxometalate structures, as the exposed oxo- anions are capable of coordinating a wide variety of metals, essentially acting as polydentate inorganic ligands,[38] or undergo covalent organofunctionalisation with oxophilic p-block elements.[39]

For the Keggin anion, three types of lacunary structures are known through the removal of 1-3 metal centres, generating the monolacunary $[XM_{11}O_{39}]^{n-4}$, dilacunary $[XM_{10}O_{36}]^{n-4}$ and trilacunary $[XM_9O_{34}]^{n-6}$ derivatives, where n is the charge of the parent anion. The structures of the anions are depicted in Figure 9, firstly it can be seen that the increase in negative charge of the polyoxometalate corresponds directly to the number of oxo- anions that have been formed upon removal of the metal(s). Secondly, the removal of multiple atoms occurs at the same site on the POM, resulting in increasingly larger, instead of multiple isolated, lacuna. Finally, the removal of atoms on the POM can naturally generate various isomers based on the position of the atoms relative to the tetrahedral core and on the isomerism of the parent anion, and whilst over 100 permutations of mono- to trilacunary POMs exist on the basis of the 5 parent isomers, only those that are isolatable in the solid state are depicted here.

A similar family of lacunary anions can also be generated from the Wells-Dawson polyoxometalate (Figure 9), however the removal of metal centres here does not proceed in a sequential fashion from a single cap. Instead, lacunary species are formed from the removal of a single metal (monolacunary, $[X_2M_{17}O_{61}]^{n-4}$, single cap trilacunary, $[X_2M_{15}O_{56}]^{n-6}$) or single "face" (hexalacunary, $[X_2M_{12}O_{48}]^{n-8}$) of the structure. The question of isomerism here is much less complicated, as only the α-Dawson structure gives stable lacunary structures and only the monolacunary species presents positional isomerism based on the removal of a cap atom or belt atom. Given that the Dawson structure is essentially an extension of the Keggin structure through the addition of an extra belt, *α1*-$X_2M_{17}O_{61}$ is analogous to *α*-$XM_{11}O_{39}$ and *α*-$X_2M_{15}O_{56}$ is analogous to *Bα*-XM_9O_{34}.

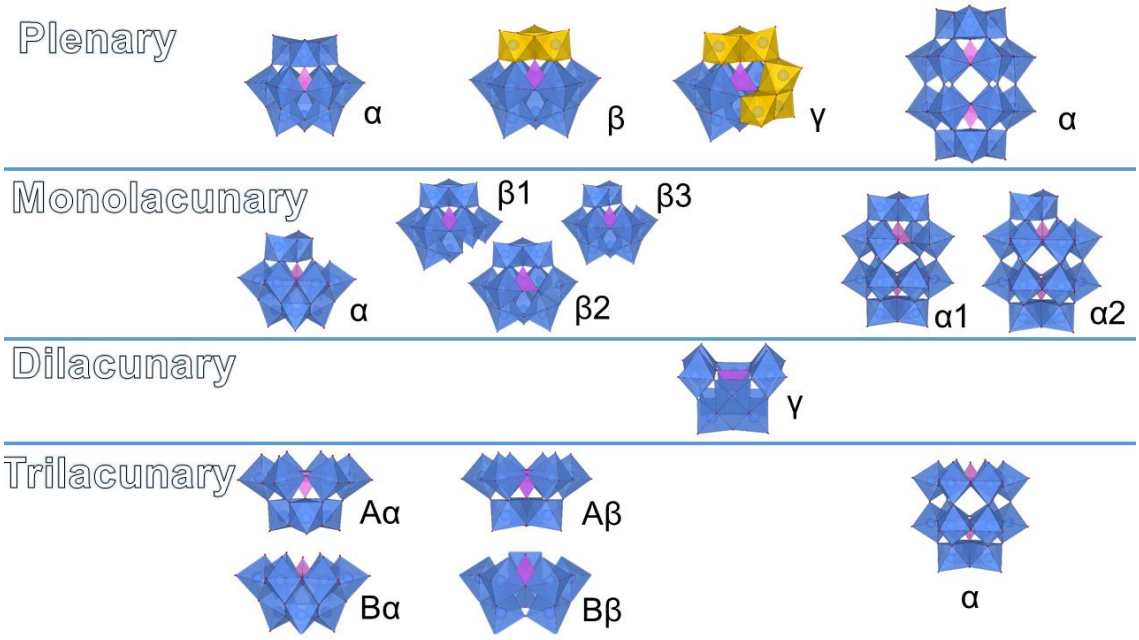


Figure 9. Stable lacunary species formed from polyoxometalates.

1.3.5. Miscellaneous anions

Whilst the following examples may not be considered archetypal POM structures in terms of their abilities as molecular building blocks and their more unusual structures, their pertinence to later literature examples and the work described here warrants their introduction.

The Anderson-Evans polyoxometalate represents an unusual variety of heteropolyoxometalate where the heteroatom is an octahedral transition metal. The structure is easily viewed as an octahedral heteroatom encompassed by a hexameric ring of equivalent edge-sharing addenda atoms (D_{3d} symmetry), giving a POM with the general formula $[H_yXM_6O_{24}]^{n-}$ (Figure 10). The addenda atoms here are commonly molybdenum, tungsten or vanadium. Three oxygen environments are present within the structure, six μ3 oxygen atoms (O_a) connect the heteroatom to each pair of adjacent addenda atoms, six μ2 oxygen atoms (O_b) connect each pair of adjacent addenda atoms to each other on the periphery of the ring and 12 terminal oxygen atoms (O_c) are located paired on each of the six addenda atoms. Whilst no isomerism occurs in this structure, there exist two classifications based on the oxidation state of the heteroatom, in high oxidation states (X^{V}, X^{VI}, X^{VII}) the structure is not protonated and is considered A-type whereas in low oxidation states (X^{II}, X^{III}, X^{IVI}) the structure is protonated and considered B-type.[40]

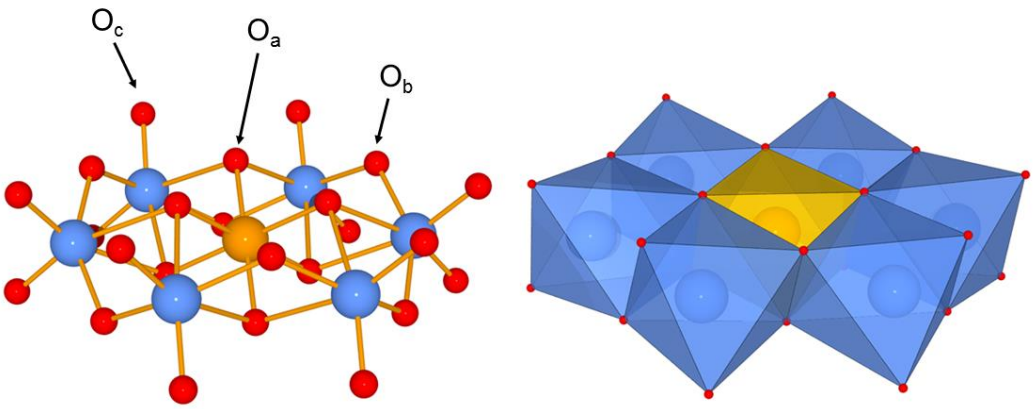


Figure 10. Ball and stick (left) and polyhedral (right) representation of the Anderson polyoxometalate (XM_6O_{24}) showing the unique oxygen atom environments within the cluster.

The decatungstate anion, $[W_{10}O_{32}]^{4-}$, is an isopolyoxotungstate that can be viewed as the condensation between two lacunary Lindqvist polyoxotungstate fragments $[W_5O_{18}]^{6-}$ through corner sharing of 4 addenda atoms (D_{4h} symmetry), the structure can therefore be described as two belts of four MO_6 units capped by two MO_6 units at each end, and therefore features two discrete metal environments (Figure 11). The oxygen atoms can be grouped into six different environments, two central μ6-oxo ligands (O_a), three different μ2-oxo atoms; eight bridging the cap and the belt (O_{b1}), eight bridging the addenda atoms

within the same belt (O_{b2}) and four bridging the two belts (O_{b3}) and finally two different terminal oxo-atoms, two on the cap (O_{c1}) and eight on the belts (O_{c2}).[41] Within the literature, the presence of "decavanadate", "decaniobate" " decatantalate" and "decamolybdate" may suggest that the structure could be considered archetypal, however, their connectivity is different with the former three examples ($[M_{10}O_{28}]^{6-}$, M = V, Nb, Ta) representing an edge-sharing fused Lindqvist structure and the latter $[Mo_{10}O_{34}]^{8-}$ consisting of molybdenum octahedra and tetrahedra.[42-44]

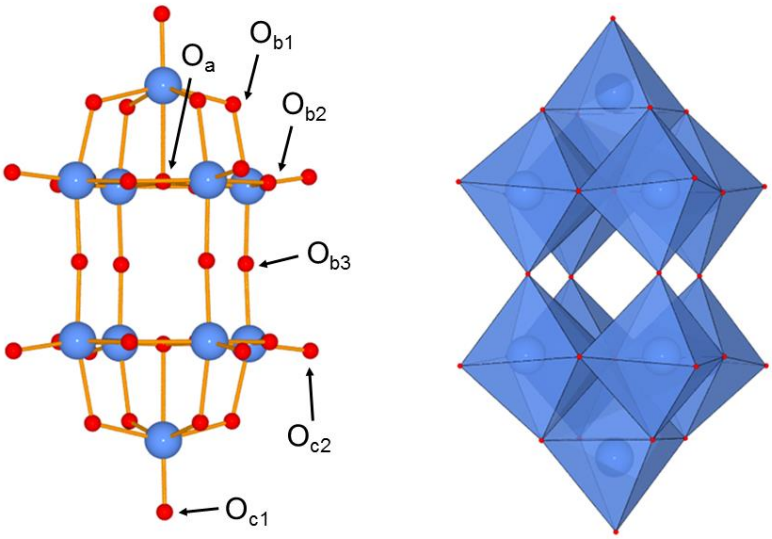


Figure 11. Ball and stick (left) and polyhedral (right) representation of the decatungstate polyoxometalate ($W_{10}O_{32}$) showing the unique oxygen atom environments within the cluster.

1.4 Electronic nature of POMs

Perhaps the most intriguing feature of polyoxometalates is their rich and complex electronic character. This single property of polyoxometalates has arguably been the most intensely studied; from their scientific origin in the nature of intense blue solutions of reduced molybdenum oxides by Scheele,[20] to the present day where the forefront of application-based POM chemistry is within fields such as photocatalysis, electrocatalysis, optics and molecular magnetism.[45]

Despite the vast variety of polyoxometalate structures ranging in size, topology and composition, the electronic properties of POMs are governed by several overarching characteristics which are a function of the electronic nature of the metal-oxo building block units. Typically, polyoxometalates are constructed from transition metals in their highest oxidation state (W^{VI}, Mo^{VI}, V^{V}, Nb^{V}), and as such, these centres can undergo reduction, allowing POMs to act as electron reservoirs. This feature is not general to all structures; however, POMs can be further classified into Class I, Class II and Class III. Class I structures are constructed from metal oxo building blocks with only one terminal M=O bond,

Class II structures feature metals with two terminal M=O bonds, and Class III systems feature both types of metal centre. From molecular orbital theory, the octahedral metal-oxo units with one terminal oxo bond (Class I and Class III) have one vacant non-bonding t_{2g} orbital that can be populated on reduction. However, anions with two terminal oxo-bonds (Class II) lack a non-bonding t_{2g} orbital because these orbitals are involved in π-bonding.[46] This means that structures such as Lindqvist, Keggin and Dawson and undergo several accessible reductions of their metal centres whilst Anderson type POMs only undergo irreversible reductions under highly forcing conditions. For Class I/III POMS, the acceptance of electrons onto the structure is accompanied by very little structural changes due to the non-bonding nature of the orbital in which these electrons reside, this results in clusters which exhibit highly reversible electron loading and unloading properties. Due to their highly interesting electronic nature, only POMs of Class I and Class III will hereon be discussed.

With regards to the electronic nature of specific structures, a widely applicable rule can be used to determine the number of electrons a fully oxidised POM structure is able to accept. This relationship was first described by Pope et al,[47] but has since been found to be general to all redox rich POMs.[48] The ability of POMs of the same addenda atoms to accept electrons, nominally the LUMO energy, is related to the ratio between the size and charge of the polyoxometalate, q/m, where q = overall negative charge and m = number of metal ions in the structure, which can be viewed as a simplified version of the charge density. Put simply, POMs that are both large and bear low negative charge are very easily reduced whereas small and highly charged polyoxometalates accept electrons less easily. Comparing POMs of the same structure but with different addenda atoms, the LUMO energies of the POMs decrease as the electronegativity of the d^0 metal ion increases ($\chi W^{6+} < \chi Mo^{6+} < \chi V^{6+}$) (Figure 12).[49] The final factor that affects the ability of a POM to accept electrons, albeit to a lesser extent and limited to heteropolyoxometalates, is the nature of the templating anion. For the Keggin structure, it has been demonstrated that a decrease in the size of the heteroatom (of the same charge) decreases the tendency of the POM to accept electrons, this is shown to be due to smaller oxyanions of the same charge possessing a more negative surface potential which decreases the ability of the neighboring metals to accept electrons.[50]

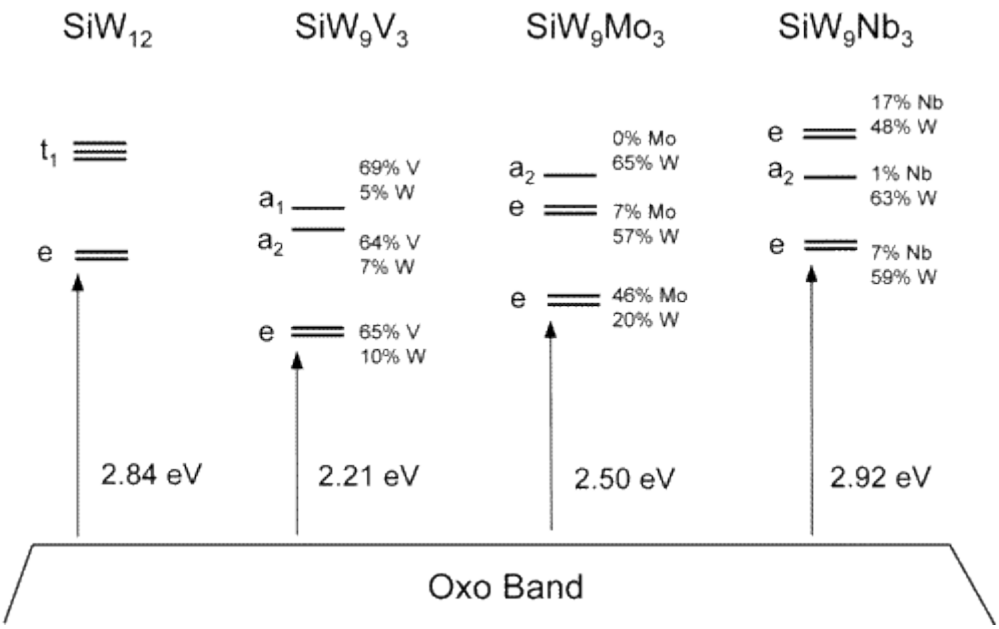


Figure 12. Calculated effect of increasing the electronegativity of the metal atom on the HOMO-LUMO gap of the POM. Reproduced from [49] with permission from the Journal of the American Chemical Society.

Upon reduction of the POM structures, a strong blue colouration, as observed by Scheele, is typically produced. This arises due to the intervalence charge transfer (IVCT) that occurs between the metal sites of the POM. This phenomenon is the rapid thermally assisted electron transfer between metal centres within the POM core, which gives rise to strong absorptions in the low energy visible and infra-red absorption spectrum of the compound (Figure 13). In highly symmetrical POMs such as the Keggin and Lindqvist ions, this corresponds to the “hopping” of the electron over the entire structure due to the equivalence of each metal sites. In structures that feature differing metal centres, such as the cap and belt regions in the Dawson ion, delocalisation occurs within regions of equivalent metal centres. These bands correlate well with the degree of reduction of the POM and the further addition of electrons to the POM result in the development of new IVCT bands at well-defined wavelengths. Overall, this makes the IVCT bands powerful diagnostic aids for monitoring the population of various reduced states of POMs within solution.

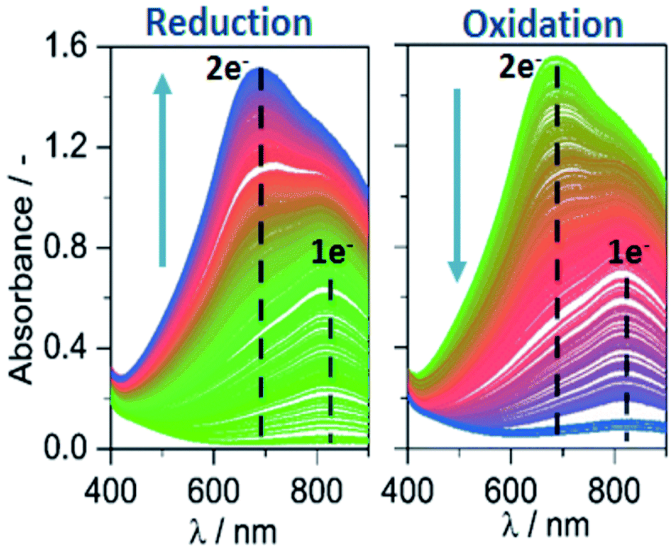


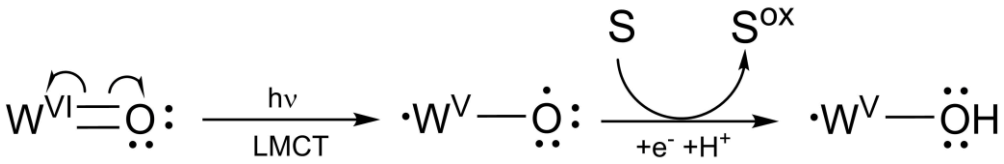
Figure 13. UV-vis spectra showing the reversible growth in IVCT bands upon reduction (and reoxidation of POMs. Reproduced from [51] with permission form the Royal society of Chemistry.

1.5 Photocatalytic properties of POMs

One of the ways in which the rich electronic properties of POMs can be accessed is through their interaction with light. Many POMs (Class I and Class III) are inherently photoactive compounds due to the ability to excite the ligand to metal charge transfer (LMCT) bands of the terminal metal-oxygen bonds. This charge transfer interaction essentially represents the HOMO-LUMO gap of the compound, as mechanistically it involves a transfer of an electron from the doubly occupied 2p orbital of the oxygen (HOMO) to the d orbitals of the metal (LUMO). These bands typically reside in the UV with minimal overlap with the visible region of the spectrum, however the LUMO energy of the POM is effectively lowered by employing more electronegative metal ions, therefore polyoxotungstates often feature higher energy LMCT bands with minimal tailing into the visible, whereas polyoxomolybdates and -vanadates exhibit lower energy bands with some tailing into the visible.[49]

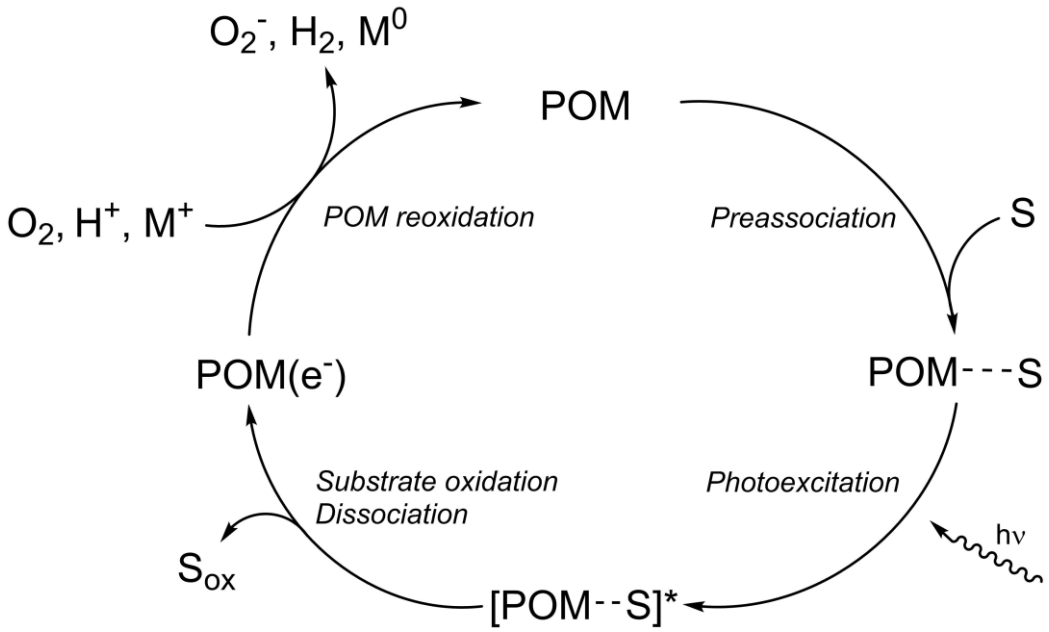
Upon excitation of the LMCT band, the transfer of an electron gives rise to a localised d^1 electron on the metal centre and an oxo-centred radical cation with a short-lived triplet state. This state is then quenched by either hydrogen atom transfer (HAT) or single electron transfer (SET), dependent on the substrate and polyoxometalate, to the oxygen radical which results in a metal-hydroxyl bond and a trapped d^1 electron on the metal, overall affording the reduction of the POM and the oxidation of the substrate (Scheme 2).[52] The trapped d^1 electron undergoes IVCT, as described previously, resulting in the blue colouration of a sample upon irradiation in the presence of a suitable substrate. It is important to note that whilst IVCT does increase the absorption profile of the POM into the visible region, this

process does not result in photosensitisation of the POM as the IVCT does not generate oxo-centred radical cations and hence is photochemically inactive. In the presence of an excess of substrate, continued irradiation can yield multiple photoreduction of the POM, with electron accumulation on the cluster much in the same way as is achieved by electrochemical methods.



Scheme 2. Mechanism of excitation of the LMCT band and subsequent photooxidation of a substrate.

Photocatalysis by POMs, the ability of POMs to catalyse the oxidation of a substrate (typically organic molecules) using light, is therefore an attractive avenue of exploration as POMs are able to accept electrons (and protons) reversibly from substrates upon irradiation. The general mechanism by which this occurs is shown in Scheme 3. Initially, POMs undergo pre-association with the substrates via hydrogen bonding (pre-association complex), either directly with the substrate or mediated by water molecules. This has been evidenced by ultra-fast electron transfer kinetics which exceed those expected for diffusion-controlled processes. Subsequently, photoirradiation results in reduction of the POM and oxidation of the substrate via either HAT or SET mechanisms, which is then followed by disassociation of the reduced POM and oxidised substrate. The cycle is then closed by reoxidation of the POM through reduction of a sacrificial electron acceptor, typically, the reduction of dioxygen to superoxide, hydroperoxide or water (dependent on the availability of protons within the system). Pertaining to this last point, the rate of reoxidation of the reduced POM, the closing of the cycle, has an inverse relationship to the rate of photoreduction of the POM, as those with higher LUMO energy are more efficient in the reduction of dioxygen. This somewhat complicates the trends observed in POM photochemistry between polyoxotungstates -molybdates and -vanadates, as whilst polyoxotungstates are more difficult to photoreduce (requires light of shorter wavelength), their corresponding reoxidations by molecular oxygen occur much faster than the corresponding polyoxomolybdate and polyoxovanadate.



Scheme 3. Catalytic cycle of POMs as photooxidation catalyst involving preassociation of the substrate and POM, photoexcitation of the complex, oxidation of the substrate and dissociation and POM reoxidation by a sacrificial oxidising agent.

As alluded to, the exact mechanism of substrate oxidation is dependent on the solvent environment. In aqueous systems the pre-association complex is between the POM and water, with photoirradiation producing hydroxyl radicals, these hydroxyl radicals are powerful oxidising agents and as such, often result in the total mineralisation of organic compounds. In non-aqueous systems, the pre-association complex forms directly between the substrate and the POM, with photoirradiation leading to the controlled oxidation of the substrate. Therefore, POM photochemistry can be divided into two regimes: indirect oxidation of substrates in aqueous systems and the direct oxidation of substrates in non-aqueous systems. Both systems have found application in the field of POM photocatalysis, the former in the degradation of organic pollutants,[53] and the latter in selective oxidation of organic molecules.[54]

1.6 Polyoxometalate hybridisation

As already mentioned, polyoxometalates are renowned for their ability to form a seemingly infinite number of structures from simple metal-oxo building blocks, resulting in a vast array of inorganic architectures ranging from the nano- to the micro-scale.[55] A new dimension is added to this field however if one considers the interaction of these clusters with other species, both to tailor the properties or add specific functionality to the POM. The hybridisation of polyoxometalates is an umbrella term that encompasses the range of methodologies for combining POMs with a variety of different inorganic and organic components to form new molecular species and materials. It is possible to classify these POM

hybrids based on the nature of the hybrid component and on the type of interactions the hybrid component forms with the POM.

Firstly, hybrid POMs may be divided into inorganic hybrid polyoxometalates and organic-inorganic hybrid polyoxometalates. Inorganic hybridisation involves the addition of transition metals or f-block metals into the structure of polyoxometalates. This is either achieved via one-pot methodologies where the polyoxometalate is synthesised in the presence of the cationic metal, or via post-synthetic addition of the cation to polyoxometalates containing one or more vacant sites to which the metal can bind. The resultant species are usually highly robust due to the ability of POMs to coordinately and electrostatically stabilise the highly charged cationic centres. Due to the difference in coordination geometry between cationic species, an even greater degree of structural diversity can be achieved based on new modes of connectivity between the inorganic components. Beyond this, the inclusion of transition metal or f-block metals into the structure can also give rise to compounds that boast powerful catalytic activities,[56] intriguing molecular magnetic properties,[57] and antiviral activity.[7] Indeed, especially with regards to catalysis, transition metal substituted POM have demonstrated exceptional performance as photocatalysts for water oxidation[58] and considerable progress towards carbon dioxide reduction,[59] where the role of the POM can be seen as a multidentate inorganic ligand housing the catalytically active metal species.

Organic hybridisation involves the association of organic components with polyoxometalates to form organic-inorganic hybrid species. These can further be classified into two distinct groups based on the nature of the interaction between the two components into Class I and Class II hybrids. Class I hybrids include any system where the polyoxometalate and organic component are associated though non-covalent interactions. Whilst this class is predominantly represented by electrostatic hybrids (i.e. the pairing of anionic polyoxometalates with organic cations), other examples include hydrogen bonding interactions,[60] with the POM able to act as a multiple hydrogen bond acceptor, or confinement of the POM in a host-guest system,[61, 62] however these will not be discussed here. Class I hybrids formed from electrostatic interactions are easily accessed synthetically through ion exchange reactions (salt metathesis) by mixing the two precursor salts in solution with molar ratios based on the desired product. Typically, salt metathesis is driven by decreased solubility or favourable lattice energy of either the POM hybrid or the waste product salt. This method provides a highly convenient route for the combination of organic and inorganic components in stoichiometry based on charge balancing, however the weak

interactions between the POM and organic moiety often leave these hybrids susceptible to further salt exchange reactions and the direct benefits obtained by having the two components in close proximity are often lost in the solution phase, mainly limiting these hybrids towards heterogeneous and materials based applications.

Conversely, Class II hybrids describe the direct covalent grafting of organic molecules to the polyoxometalate. The methods for achieving this are highly specific to both the polyoxometalate structure and the identity of the addenda atoms on the POM. Figure 14 summarises the main routes that are employed for the archetypal structures that have been described in Section 1.3. In general, the hybridisation strategies can be easily grouped based on several key motifs. Firstly, imido-functionalisation (including diazenido, hydrazido and azino) is the sole strategy used to hybridise the Lindqvist hexamolybdate. The Lindqvist hexamolybdate can react directly with primary amines through condensation reactions catalysed by diimide catalysts, which results in the substitution of one or more of the terminal oxo-groups of the POM with the primary amine, forming formal molybdenum-nitrogen triple and double bonds. Another commonly employed group are tripodal alcohols (triols), which can be used to functionalise the Anderson molybdate, Lindqvist hexavanadate and the vanadate caps of the mixed addenda Wells-Dawson polyoxometalate ($[X_2W_{15}V_3O_{62}]^{n-}$, where X is the templating atom). The tripodal alcohol arrangement is geometrically well suited to binding in a tridentate fashion on POM faces containing trigonal arrangements of bridging oxygen atoms. The reaction proceeds via a formal esterification of the protonated bridging oxo groups of the structure and the products are highly stable to hydrolysis due to the chelate effect. The related diolamide linkage has also been used on the vanadate capped tungsten Dawson anion with similar success.

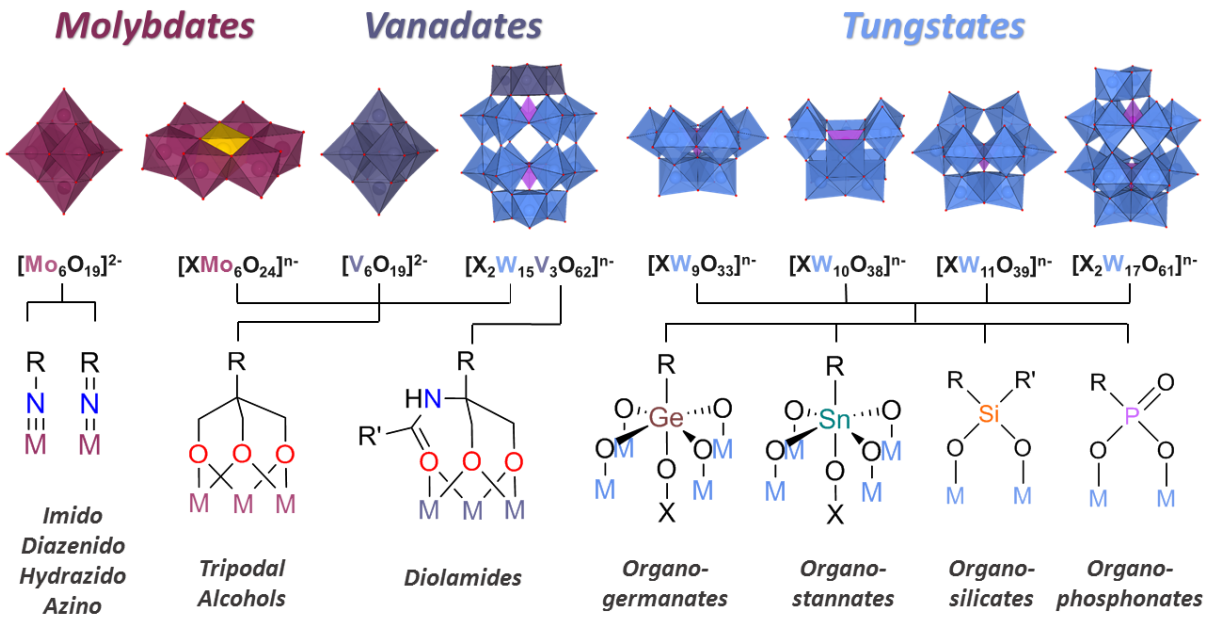


Figure 14. Covalent organofunctionalisation routes for a variety of archetypal and lacunary structures. Reproduced from [39] with permission from Elsevier.

Whilst the above methods may be used to covalently graft organic groups to the plenary structures of polyoxomolybdate and polyoxovanadate anions, the grafting of organic groups to polyoxotungstates cannot proceed directly. However, covalent hybridisation of the Keggin and Dawson polyoxotungstate anions may proceed via the lacunary species (Section 1.3.4). The removal of one or more tungsten atoms from the polyoxometalate leaves lacuna which contain negatively charged exposed oxygen atoms. These oxygen atoms are highly nucleophilic and can react with a variety of oxophilic organotin, organogermanium, organophosphorus and organosilicon reagents. These groups are typically grafted through condensation-type reactions with the anchoring atom as its oxyacid or chloro derivative. The nature of the anchoring atom has a profound role not only on the geometry and stoichiometric rations of the POM and organic moiety, but also on the extent of orbital mixing between the two species. Furthermore, many different structures are accessed by modulating both the ratios of the components and the size of the lacuna (number of removed addenda atoms) on the POM.

Given that organic chemistry offers a near-limitless number of different scaffolds featuring different physical and chemical properties, the organofunctionalisation of POMs represents an incredible opportunity to design new molecules and materials for a plethora of applications. Of themselves, POMs have already demonstrated powerful photoredox catalytic properties, however their narrow and high energy absorption windows have somewhat limited their attractiveness in the current sustainability conscious climate, where the utilisation of the abundant natural resource sunlight has become

something of a holy grail. Hereon we describe how manifold organofunctionalisation strategies have helped to revitalise the field of POM photochemistry through photosensitisation into the visible region.

1.6.1. Class 1 hybrids for photocatalytic applications

Logically, Class I hybridisation represents the easiest route to the photosensitisation of polyoxometalates, whereby anionic POMs can be combined in stoichiometric quantities with photosensitiser cations. The resultant materials typically feature wider absorption profiles through the superposition of the absorption spectrum of the two components. However, additional absorption properties may be obtained if intermolecular charge transfer interactions occur between the POM and the cation. Polyoxometalates can act as strong electron acceptors, so when paired with organic cations that are able to donate electrons, charge transfer salts are formed. These charge transfer interactions give rise to new absorption bands as a result of the electronic transition from the HOMO of the donor (organic cation) to the LUMO of the acceptor (polyoxometalate), the charge transfer band is independent of the inherent absorption bands of the molecular species and can occur within both the visible and UV regions of the electromagnetic spectrum.[63]

The cations typically paired with polyoxometalates to form photoactive Class I materials are photostable chelate complexes, cationic organic dyes and simple ammonium fragments capable of charge transfer (CT) interactions. The earliest study that recognised the enhancement of POM photochemistry through its non-covalent association with other species is by Hill and Bouchard,[64] who noted that the tailing of the absorption spectrum of $(TBA)_3PW_{12}O_{40}$ showed solvent dependence (Figure 15). It was demonstrated that when nitrogen containing solvents were employed, the tailing of the low energy absorption was shifted towards visible wavelengths. This phenomenon was ascribed to charge transfer interactions between the anionic POM and neutral solvent molecules. Interestingly, the irradiation of these CT bands, in the visible region, results in high quantum yields of polyoxometalate reduction and organic substrate oxidation, showing that these absorption features can be used to increase the photooxidation capabilities of POMs. Several subsequent studies showed that when acidic POMs are added to various amidic solvents,[65-68] coloured solids (charge transfer compounds) can be obtained which have high solvent content within the crystal structure and display short intermolecular contacts with the solvent. The first stoichiometric Class I hybrid was synthesised in earnest by Attanasio et al, through the deprotonation of phosphotungstic acid with 8-quinolinol, forming $[Hquin]_3[PW_{12}O_{40}]$. The

compound was highly insoluble and exhibited weak charge transfer behaviour based on the diffuse reflectance spectrum. In this scenario however the crystal structure revealed that no substantial structural interaction occurs between the organic cations and the POM. Whilst hybrids of this type are still of scientific interest,[69] it appears they have become somewhat unfashionable when compared with those employing inherently photoactive cations, likely due to the inability to accurately predict the energy and magnitude of their charge transfer character.

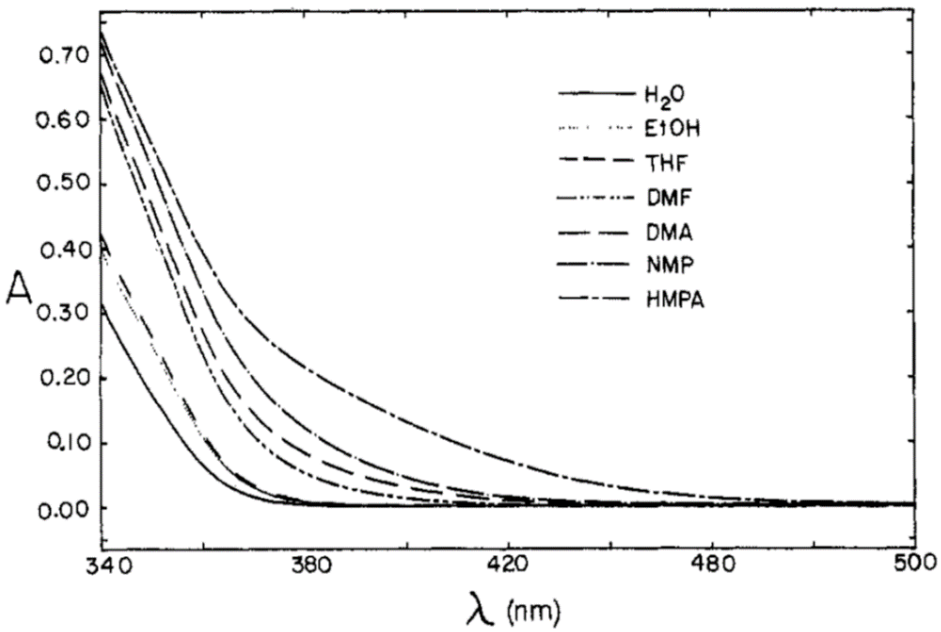


Figure 15. Enhancement of the POM absorption in the visible region through association with amine and amide containing residues. Reproduced from [64] with permission from the American Chemical Society.

Class I polyoxometalates featuring organic dye molecules were not explored until sometime later. Barring the combination of POMs with TTF, which have predominantly been explored for their magnetic properties and hence will not be discussed here,[32] the first combination of polyoxometalates with cationic dyes was contributed by Xu et al. for the 2,4,6-triphenylpyrylium cation (Figure 16) and the hexamolybdate anion.[70] This species, denoted TPPM, was compared photophysically to its precursor $[TBA]_2[Mo_6O_{19}]$ (TBAM). The solution phase photochromic properties of TPPM were found to be superior to TBAM, while the reduced state photoabsorption of the POMs (IVCT) were similar in profile, TPPM exhibited much stronger absorption and the photochromism was reversible whereas TBAM showed irreversible behaviour, due to the reversible photochromism exhibited by the dye which acts as a redox mediator between the POM acceptor and the solvent electron donor.

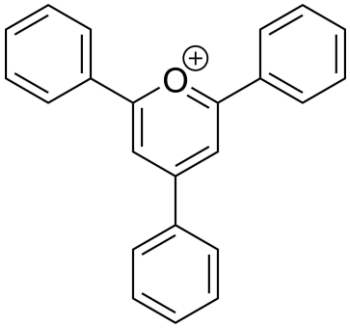


Figure 16. Structure of 2,4,6-triphenylpyrilium cation.

A pioneering study by Le Magueres et al. adopted a different approach whereby neutral dye molecules were covalently attached to tetraalkylammonium anchors which associate with the anionic POM.[71] Both the dye and POM components were modulated to isolate their influence on the properties of the overall system. For the POM, both Lindqvist and Keggin structures were investigated with either molybdenum or tungsten as the addenda atom ($[M_6O_{19}]^{2-}$ or $[SiM_{12}O_{40}]^{4-}$, where M= Mo, W). The cations employed featured anthracene or pyrene groups which were tethered to pyridinium or alkylammonium quaternised centres via aliphatic carbon chains of different lengths (Figure 17). The compounds were obtained as intensely coloured crystals which showed new strong absorption features in the diffuse reflectance spectra at $\lambda > 500$ nm, indicative of charge transfer, however upon dissolution the intense colour disappeared and the solution only gave absorption bands corresponding to the isolated components, reflecting that charge transfer is unique to the solid state species. The absorption tail edges of the compounds were correlated with the redox properties of the components, where POMs with more positively shifted reduction potentials (more powerful acceptors) gave bathochromic shifts in the absorption bands, as predicted by Mulliken's theory.[72] The charge transfer energies were not only dependent on the electronics of the system, but on the degree of contact between the donors and acceptors within the crystal lattice. This was best demonstrated by the difference in colour of two polymorphs of $[pyrene\text{-}CH_2\text{-}NMe_3][Mo_6O_{19}]$,whereby the triclinic crystal showed that the pyrene formed more favourable contacts with the POM than the monoclinic crystal (Figure 18), resulting in higher absorption between 500-600 nm (deeper red colour) in the triclinic system. It was also demonstrated for the tetrabutylammonium (λ_0 = 650 nm) anchor compared to tetramethyl- and tetraethylammonium anchors (λ_0 = 750 nm) within the same system, whereby the tetrabutylammonium compound in the crystal structure blocks more of the surface of the POM through C-H···O-M hydrogen bonds and orientates the donor away from the POM surface. Transient absorption spectra confirmed that excitation of the hybrid results in the expected generation of cation and anion radicals, with different decay kinetics

of the excited states observed based on the orientation of the donor and the strength of the charge transfer interaction.

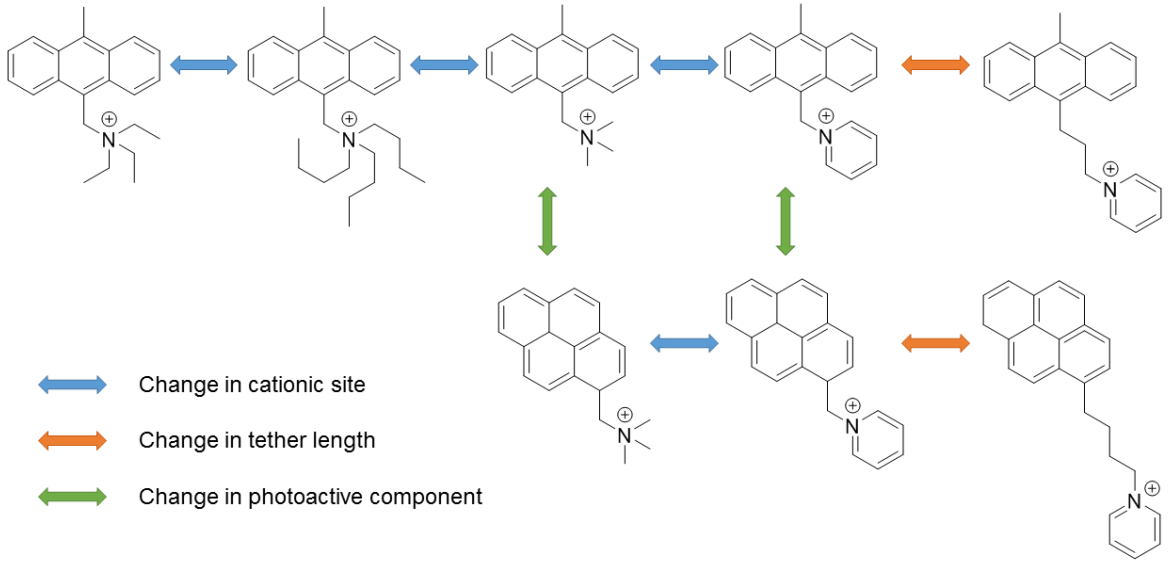


Figure 17. Cations employed by Le Magueres et al. varying the nature of the cationic site, the tether length and the chromophore. [71]

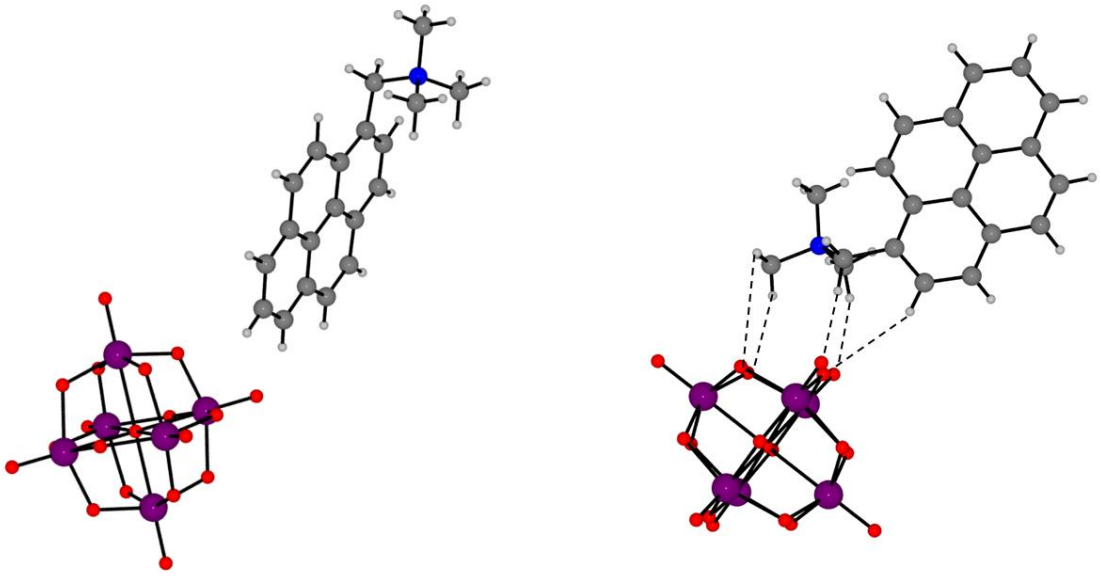


Figure 18. Two polymorphs with different photoactivities arising from the different orientations of the cation and POM in the solid state.[71]

The final family of photoactive Class I hybrids are those incorporating cationic metal complex photosensitisers. Literature examples of these hybrids are dominated by the combination of $[Ru(bpy)_3]^{2+}$ and its analogues with various polyoxometalates,[73-75] however other cationic complexes have also been explored including $[Os(bpy)_3]^{2+}$,[76] ferrocenyl,[77, 78] and metalloporphyrins have also been explored.[79, 80] The first example of this type of hybrid was demonstrated by Veya et al. for a ferrocene derivative

combined with Lindqvist hexamolybdate or hexatungstate anions ($[Fc\text{-}CH_2\text{-}NMe_3]_2[M_6O_{19}]$ where M = Mo, W). The ferrocene complex featured a N-trimethylethylammonium side group on one of the Cp rings giving it an overall monocationic charge (Figure 19). The compounds were isolated as deep red-brown salts that displayed charge transfer (evidenced from diffuse reflectance spectra) in the solid state, but not in solution. The charge transfer expectedly occurred between the POM acting as electron acceptor and the ferrocene moiety acting as electron donor, as elucidated by transient absorbance measurements and spectroelectrochemistry.

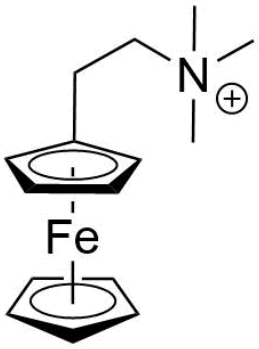


Figure 19. Structure of the tethered ferrocene cation employed by Veya et al. with Lindqvist anions.[81]

The sensitisation behaviour and electronic properties of POM salts of $[Ru(bpy)_3]^{2+}$ and its synthetic variants were well described by Fay et al. who combined both tungsten and molybdenum Dawson polyoxometalates ($[S_2M_{18}O_{62}]^{4-}$, where M = Mo, W) with $[Ru(bpy)_3]^{2+}$ cations (Figure 20) to give the stoichiometric 1:2 hybrids.[82] The hybrid compounds exhibited a new electronic transition between 470 nm and 480 nm that was assigned to charge transfer between the two species, supported by Raman spectroscopy studies. Electrochemically, the redox potentials of the POM were not significantly affected by the presence of the sensitiser ligands, in either the solid or solution state. Photochemically, the hybrids were compared to each other and their precursor tetraalkylammonium salts. The tetraalkylammonium salts when excited with 355 nm light were able to achieve the photooxidation of both DMF and benzyl alcohol, with the molybdate POM giving higher quantum yield due to its more positive reduction potential. At 420 nm illumination, the TBA molybdate POM was able to photoreduce in the presence of DMF and benzyl alcohol whereas the tungsten analogue only showed negligible photoreduction, in accordance with their absorption spectra. Conversely, when the hybrids are illuminated at 355 nm, the activity towards DMF and benzyl alcohol photooxidation decreases, likely due to interference from the strongly absorbing cations at this wavelength. Importantly though, when illuminated at 420 nm, the hybrid compounds exhibit much higher photoactivity compared to the TBA salts, especially the molybdate analogues, which were able to undergo two sequential proton coupled

2e- reductions in DMF with quantum efficiencies of 81 and 0.9, whereas the TBA salt is only able to undergo the first proton coupled $2e^-$ reduction with a quantum efficiency of 2. However, it must be noted here that the photocatalytic studies are measured in solution where the anions may be fully isolated by solvation, hence $[Ru(bpy)_3]^{2+}$ may be acting mainly as a stand-alone photosensitiser.[83, 84]

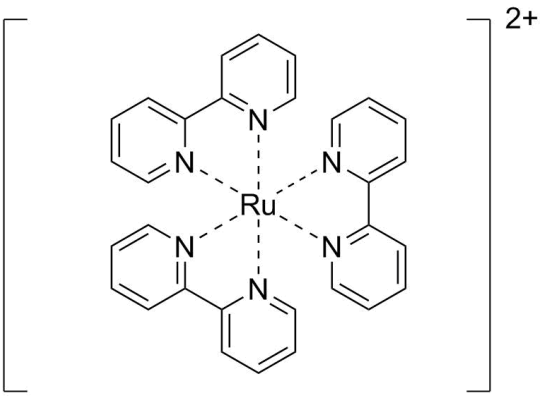
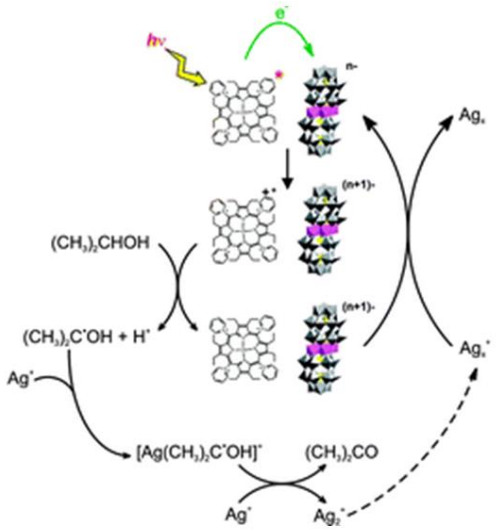


Figure 20. Structure of the photosensitiser $[Ru(bpy)_3]^{2+}$ cation.

Whilst the literature is rich with examples where these compounds have been synthesised and electronically characterised for a variety of organic cations, there are far fewer where the hybrid material has been used in a photophysical or photochemical application. In addition to the contributions mentioned above,[64, 82] there have been several more recent studies where a variety of photocatalytic transformations have been achieved using Class I type hybrids, the following examples will consider only heterogeneous systems based on the questionable nature of the system when using electrostatically linked hybrids in the solution phase. The simplest way of employing Class I materials as heterogeneous catalysts is by simply using the bulk powder as a suspension in the reaction medium, this was demonstrated by Gao et al. with hybrids formed from small molybdate clusters paired with $[Ru(phen)_3]^{2+}$ cations (phen = 1,10-phenanthroline).[85] The hybrid materials, which all showed charge transfer character, could affect the oxidation of water under visible light illumination (λ = 420 nm), with the octamolybdate derivative exhibiting the highest activity (3.75 $\mu molh^{-1}$), whilst the exact catalytic mechanism had not been elucidated, a radical scheme was proposed on the basis that radical scavengers inhibit the reaction.

Another stratagem that has shown promise is the assembly of Class I hybrids into photoactive films. Schaming et al. first explored this through the “successive dipping” of a quartz slide into solutions containing polyoxometalate anions ($[P_2W_{18}O_{62}]^{6-}$ or $[Co_4(H_2O)_2(P_2W_{15}O_{56})_2]^{16}$) and zinc porphyrin cations ($[ZnOEP(py)_4]^{4+}$ or $[ZnOEP(py)_4]^{4+}$ in a layer-by-layer approach.[86] The resultant films, formed from 60-80 nm aggregates yet exhibiting high stability and low permeability, were electroactive and showed photocatalytic activity for the reduction of silver cations under visible light irradiation (Scheme 4). The mechanism of this was suggested to be indirect and mediated by the sacrificial electron donor 2-propanol, based on thermodynamics. The films could equally be employed in the reduction of gold chloroaurate anions. Interestingly, the silver product tended towards the formation of nanowires whilst the gold product favoured nanosheets, due to the differences in the ionic feedstocks.



Scheme 4. Proposed catalytic cycle for the reduction of silver ions mediated by isopropanol in polyoxometalates encapsulated in films. Reproduced from [80] with permission from Elsevier.

The processing of Class I hybrids into films on photoanode materials, as reported by Xiang et al. can also lead to the fabrication of triad electrodes for photoelectrochemical cells.[74] The photoelectrode was constructed from SnO_2 or TiO_2, a phosphorylated $[Ru(H_4dpbpy)_2(dpbpy)]^{2+}$ complex and water oxidation catalyst $[Ru_4O_4(OH)_2(H_2O)_4(SiW_{10}O_{36})_2]^{10-}$ (Ru_4POM). The anode was constructed by sequential assembly of metal oxide, organic cation and POM anion onto the substrate (FTO or sapphire glass). The films were able to form long-lived charge separated states upon visible light illumination, the metal oxide acting as the electron carrier whereas the POM acts as the hole carrier, with the dye mediating the separation of electron and holes. The films showed superior activity towards light driven oxidation of water vs. the metal oxide organic cation bilayer (>100%) through measurement of the photocurrent,

however their long-term stability and exact mechanism of action had not been ascertained. A follow-up study further investigated the optimisation of the system by employing related phosphorylated ruthenium photosensitisers $[Ru(H_4dpbpy)(bpy)_2]^{2+}$ and a crown ether functionalised derivative $[Ru(5\text{-}crownphen)_2(H_2dpbpy)]^{2+}$.[87] Control experiments demonstrated that whilst dyads without the catalyst still give high faradaic efficiencies (80 to 94%), the inclusion of the catalyst significantly enhances the overall quantum yield. With regards to the novel crown ether derivatised sensitiser, its enhanced absorption profile coupled with superior binding to the TiO_2 surface results in a system with 270% increased O_2 quantum yields. Interestingly, the optimal operating pH of the catalyst bound to TiO_2 was significantly lower than the molecular species due to reduced dye stability, catalyst binding and less favourable electron transfer – demonstrating the non-triviality of converting between homogenous and heterogeneous systems.

Recently, the design and use of Class I hybrids as a photoanode materials with quantasome-like arrangements of carboxylate decorated perylene bis-imide cations (BPI) with the aforementioned Ru_4POM has been reported (Figure 21).[88] The material formed in 5:1 ratio of PBI to Ru_4POM as justified based on charge balancing of $[PBI]^{2+}$ and $[Ru_4POM]^{10-}$, with the POM catalyst effectively caged by the cations. The hybrid displayed several desirable properties for a photosynthetic unit including a red-shifted broad absorption cross section, favourable exciton accumulation, robust amphiphilic structure and crystalline organisation into two dimensional arrays (with analogous arrangement to that seen within PSII). When rendered onto nanostructured tungsten oxide photoelectrodes the material retains its highly organised 2D phase, the photoanode showed remarkable oxygen evolution efficiently using ‘green’ photons ($\lambda \leq 560$ nm), having quantitative faradaic yield and internal quantum efficiency up to 1.3%, in parallel with PSII bio-electrodes.

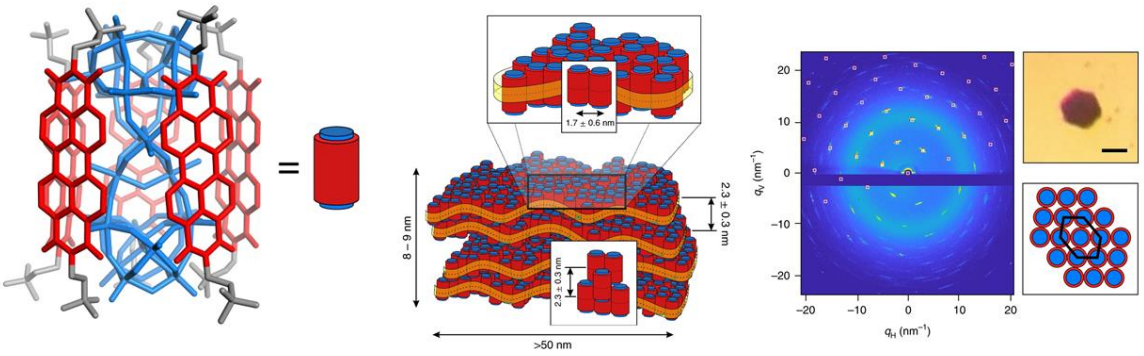


Figure 21. Quantasome arrangement of polyoxometalates and carboxylate perylene bis-imide cations into organised layers on surfaces. Reproduced from [88] with permission from Nature Publishing Group.

A recent advancement in Class I photocatalysis has been the incorporation of polyoxometalates into cationic metal organic frameworks (MOFs) formed from photoactive components (Figure 22). MOFs are a class of porous materials composed of metal nodes and organic linker arranged in a modular fashion to form multi-dimensional networks with high porosity.[89] This elegant approach was first adopted by Zhang et al.,[90] who formed a highly cationic framework with large pore sizes through the mixture of a carboxylate functionalised ruthenium photosensitiser ($[Ru(bpy)2(L)]^{2+}$ where L = 2,2'-bipyridine-5,5'-benzoic acid) with zirconium tetrachloride (which forms hexanuclear zirconium clusters in-situ). This MOF was able to encapsulate the Wells-Dawson phosphotungstate anion $[P_2W_{18}O_{62}]^{6-}$ with varied POM loadings. The POM-free framework shows phosphorescence from the excitation of the ruthenium MLCT bands, however upon introduction of the POM these were quenched suggesting excited electron transfer from the framework to the POM. The POM@MOF material showed photocatalytic activity towards H_2 evolution from acidic aqueous solution under visible light irradiation ($\lambda > 400$ nm) with turnover numbers reaching a maximum of 79 after 12 hours, the catalyst was also found to be recoverable and recyclable for at least three cycles, with the system limited by photodegradation of the ruthenium dye (5.6% leaching of Ru per run). The catalyst could also perform in an organic system using DMF/MeCN as the solvent and triethanolamine as the sacrificial electron donor, reaching TON of 307 after 14 hours (13 times higher TON than the homogeneous control). Cyclic voltammetry revealed that multielectron injection (6 or more) is necessary before the POM species are able to reduce protons catalytically, this is facilitated in the cage structure by the highly cationic environment within the pores. A similar system was reported by Paille et al. combining the well-known POM catalyst for the oxygen evolution reaction (OER) $[PW_9O_{34})_2Co_4(H_2O)_2]^{10-}$ with MOF-545,[91] a cationic MOF employing the same hexanuclear zirconium nuclei instead linked by photoactive tetracarboxylate porphyrin groups, forming

a noble-metal free architecture. Through DFT studies, the authors predicted that the POMs reside exclusively in the larger hexagonal channels, likely in the vicinity of two Zr_6 clusters connected to two porphyrin linkers stabilised by a dense hydrogen bonding network. It was also predicted that protons shuttle at the interface of the POM and the MOF, generating hydroxyl groups on both the POM and Zr_6 clusters, which are key intermediates during the OER. The material was tested for its photocatalytic oxygen evolution activity, it was found that an optimal operating pH of 8 represented a balance between POM stability and basicity needed to drive the OER. Under optimal conditions the catalyst gave a TON of 70 after 1 hour which outperformed each of the control experiments, the system was found to be stable and recyclable with only small losses of TON after each cycle attributed to local environment changes around the cobalt core within the POM. Finally, a cationic metal organic framework was synthesised by Tian et al. using a hexaarmed $[Ru(bpy)_3]^{2+}$ derivative combined with macrocyclic curcubit[8]uril.[92] This unique MOF is linked through the favourable encapsulation of the cationic arms into the cavity of the macrocycle, resulting in the first example of a water-soluble supramolecular MOF. This structure was able to encapsulate $[P_2W_{18}O_{62}]^{6-}$ anions (1 per cubic cavity) through favourable ionic interactions and large pore sizes, with electron transfer from the ruthenium sensitiser to the unit suggested by fluorescence quenching studies. The encapsulation of the POM caused a bathochromic shift in the absorption maxima of the MOF to shift from 470 nm to 500 nm, thus the materials was tested for its photocatalytic hydrogen evolution capability under irradiation at 500 nm. From acidic media (pH 1.8), the homogeneous POM@MOF catalyst achieved a turnover number of 392 after 12 hours, markedly outperforming the system reported by Xhang et al. (72 after 12 hours). The increase in performance could be due to the homogeneity of the system combined with the unique 1:1 POM to pore ratio achieved in this material, facilitating electron transfer between the components. Optimal loading was found to be 1 mM which represented the balance between excitation yield of the ruthenium sensitisers with light transmittance through the structure. It was again noted here that continued irradiation did result in partial degradation of the ruthenium sensitisers within the MOF structure. Control experiments confirmed the crucial role played by each component in the system and the catalyst was recoverable through evaporation of the solvent and could be cycled up to six times. Impressively, as a heterogeneous catalyst, the POM could also perform as a superior H_2 evolution catalyst from a

DMF/MeCN mixed solvent with triethanolamine as the electron donor with TON reaching 1820 after 14 hours irradiation (cf. 307 under the same conditions for Zhang et al.).

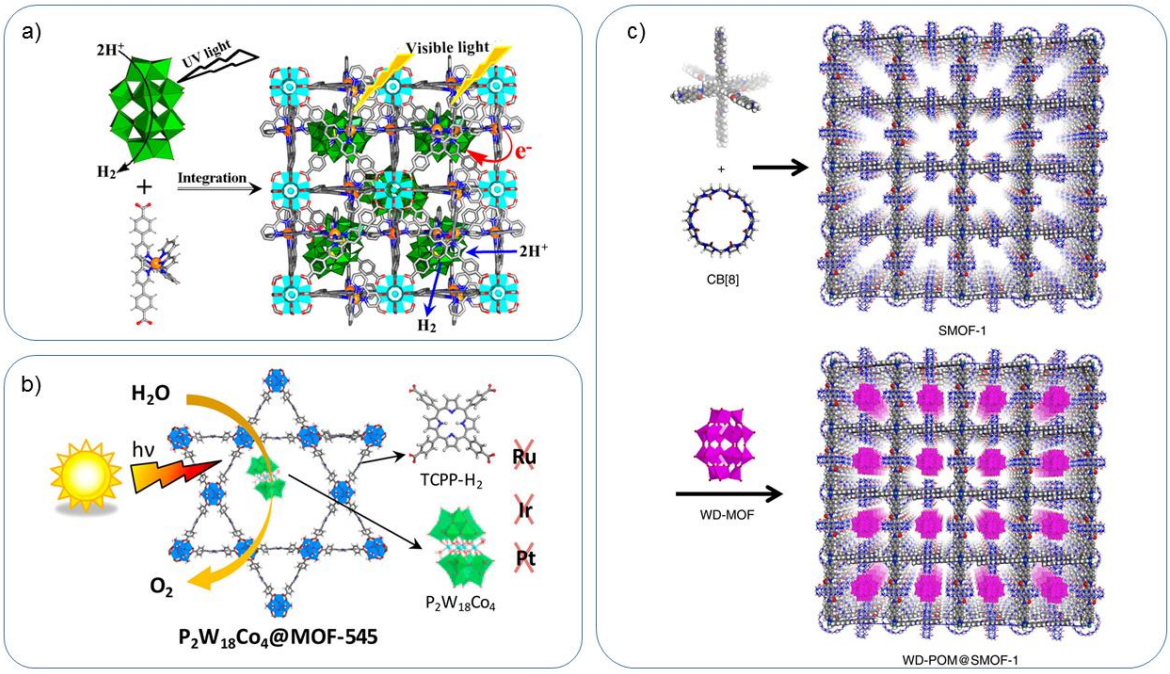


Figure 22. Strategies for the encapsulation of POMs into MOFs by a) Zhang et al. b) Paille et al. and c) Tian et al. Reproduced from [90-92] with permission from the American Chemical Society and Nature publishing Group.

1.6.2. Class 2 hybrids for photocatalytic applications

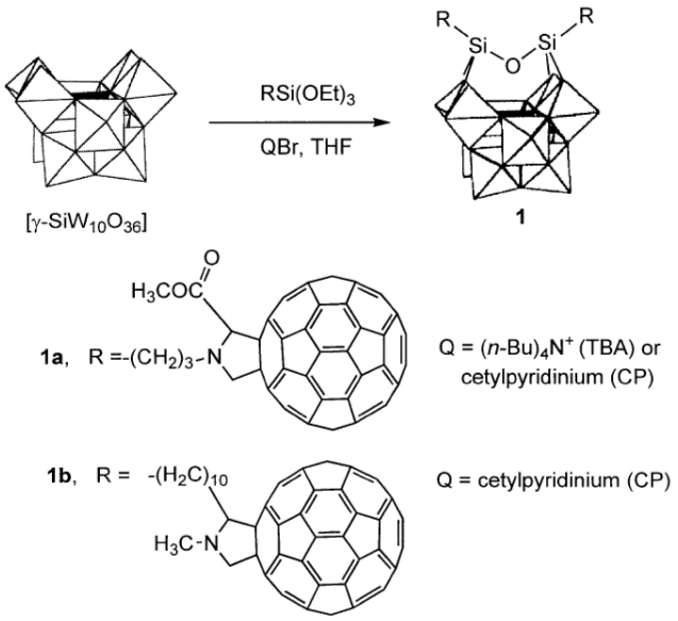
As discussed in the above section, the coupling of cationic organic dyes with anionic polyoxometalates in the Class I approach generally provides a convenient method for the widening of the absorption profile of the POM material. Although this approach has some merit, the main limitation of this hybridisation method is the lack of control over the spatial relationship and prediction of the charge transfer characteristics between the polyoxometalate and the cationic photosensitiser (unless encapsulation is achieved as in the case of cationic MOFs). Although some amount of synthetic design can be employed to influence the configuration of the organic component around the polyoxometalate (for example, stoichiometric ratio through cationic charge and use of hydrogen bond donor groups), the eventual orientation of these components will be governed by the lowest energy configuration for solid state packing, and hence will be extremely challenging to either predict or influence.

To directly counteract these issues, there has been a growing interest in the synthesis of Class II hybrid polyoxometalates for photochemical applications. Whilst synthetically more demanding, these hybrids offer key benefits over their Class I counterparts due to their tuneable solubility through the employ of suitable counter-cations and the potential for strong electronic coupling between the organic group and

the polyoxometalate, mediated by covalent bonds. The covalent approach also allows for the coupling of organic photosensitising units at predetermined sites on the polyoxometalate, and at defined distances from the polyoxometalate through the use of an appropriate spacer, giving a higher degree of geometric control over the end-product hybrid. This latter characteristic is crucial in the design of photoactive systems, where the lifetime of photo-induced charge separation is extremely sensitive to spatial configuration, not only in POM based systems,[93, 94] but other inorganic systems and natural photosystems as well.[95-97]

Of the archetypal polyoxometalates that can be functionalised in a modular approach, Keggin and Dawson polyoxotungstates have recently become one of the most intensely studies clusters for covalent organic modification. This is driven largely by their rich electrochemical properties and the variety of approaches available for their functionalisation. As had been previously discussed, multiple lacunary species are accessed through the facile treatment of either the Keggin or Dawson parent clusters with a controlled amount of base. These lacunary synthons can then be functionalised using a variety of anchoring groups (Si, Sn, P, Ge) which can be used to control the stoichiometry of organic substituents, their relative geometry and the degree of electronic interaction with the polyoxometalate platform.

It is therefore not surprising that both Keggin and Dawson polyoxotungstates have been used extensively as the basis for photoactive Class II hybrid POMs. The typical approach involves the covalent attachment of chromophores (usually metal complexes or conjugated organic molecules) to the polyoxometalate through one of the avenues described above. This was first achieved by Bonchio et al. through the grafting of organosilyl fullerene derivatives to the dilacunary Keggin silicotungstate anion $[\gamma\text{-}SiW_{10}O_{36}]^{10-}$ in a 2:1 fashion and isolating the product as TBA or cetylpyridinium salts.[98] (Scheme 5). The resultant hybrid species were shown to retain the absorption characteristic of the fullerene units with broad spectrum absorption tailing across the visible region (270-730 nm). In general, the study showed that the fullerene hybrids photocatalytic performance towards the visible light (λ > 375 nm) photooxidation of phenol in basic aqueous media was broadly comparable with that of photosensitised Class I polyoxometalates ($[Mo_6O_{19}]^{2-}$ or $[W_{10}O_{32}]^{4-}$ coupled with $[Ru(bpy)]^{2+}$ or methylene blue) under heterogeneous conditions but was inferior to that of the photosensitisers in homogeneous conditions. The mechanism of heterogeneous oxidation was also probed through the use of the known $^1O_2$ quencher sodium azide. It was found that for the Class I compound $[Ru(bpy)_3]_2[W_{10}O_{32}]$ and the title compound "**1b**", the mechanism occurs by a singlet oxygen pathway.



Scheme 5. Synthetic route towards silicokeggin derivatives functionalised with fullerene antennae by Bonchio et al. Reproduced from [98] with permission from Wiley Publishers.

Some years later, work in the field was rekindled by the contributions of Odobel, Mayer and Harriman.[99-101] This series of publications involved the functionalisation of the monolacunary Wells-Dawson phosphotungstate $K_{10}[P_2W_{17}O_{61}]$ using either phosphate or silicate linkers for the attachment of photoactive perylene monoimide, porphyrins or dendritic porphyrins, obtained as n-tetrabutylammonium salts to allow for solubility in polar organic solvents.

The first study regards the covalent attachment of perylene monoimide dyes to the polyoxometalate via two different strategies; either the employment of aryl siloxanes groups which provide a semi-rigid tether between the dye and the POM (**PSI-PER**), or the use of alkylphosphates which provides a flexible tether (**PP-PER**), see Figure 23.[101] Through UV-vis spectroscopy and electrochemical measurements, it was determined that there was no significant electronic interaction between the components as the perylene (PER) unit showed identical spectral traces and redox activity to its unfunctionalised precursor. Interestingly, the rigidity of the linker group played a vital role in determining the intramolecular electron transfer behaviour of the system. Specifically, both systems were photoactivated through the initial photoexcitation of the PER chromophore, which transfers an electron to the POM, and in both cases this electron transfer is facilitated by changes on the conformation of the hybrid which allows the units to be in close proximity. Flash photolysis experiments indicated that the phosphoryl tether allows for a greater degree of conformational flexibility and suggested that photoinduced electron transfer between the redox active species requires some orbital contact. With both hybrids, the charge shift products

were not observed as the rate of the reverse electron transfer exceeded that of the forward process, however, it was postulated that photoaccumulation could be achieved through a higher photon flux.

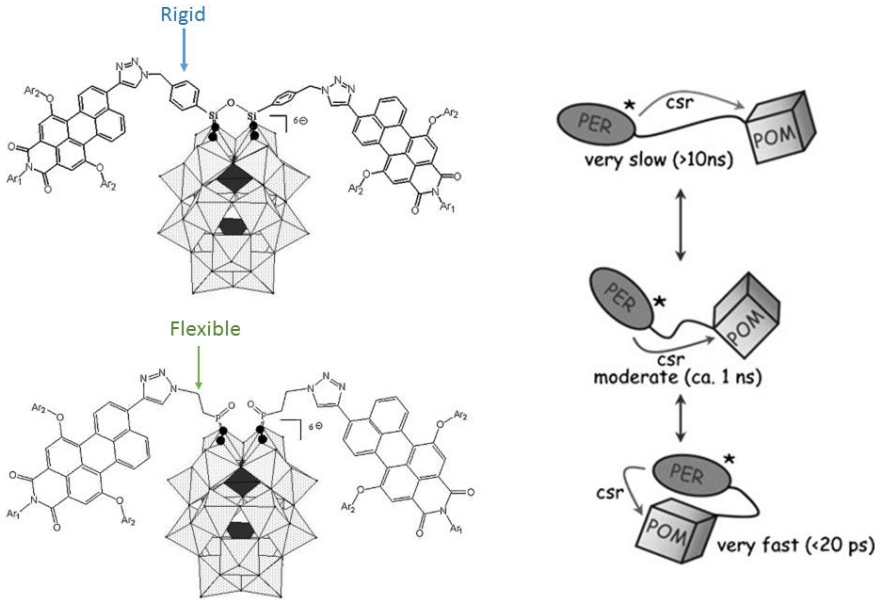


Figure 23. Change in photophysics of perylene monoimide-POM systems by employing linkers with different rigidity. Adapted from [101] with permission form Wiley Publishers.

This concept was soon expanded to the linking of the same lacunary Wells-Dawson to zinc porphyrin complexes (Harriman 09). In this study three linkages were explored, analogous flexible and semi-flexible alkylphosphate (**ZnP**-**PA**) and arylsiloxane (**ZnP**-**PSi**) as used in the previous work, and a new rigid arylphosphonate linker (**ZnP**-**PP**). Electrochemical measurements showed that the electronic properties of the POM were effectively modulated by the use of the different anchoring group following observations made by Boujita et al.[102] Specifically, the use of arylsiloxane as a tether caused the cathodic shift of the POMs first reduction potential (-0.68V vs. SCE) whereas the alkylphosphate (-0.3 V vs. SCE) and arylphosphate (-0.18 V vs. SCE) had the opposite effect. With regard to the photophysics of the systems, similar behaviour was observed between **ZnP**-**PA** and **ZnP**-**PSi** with their previously reported perylene analogues, whereby multiple conformers were observed through fluorescence and flash photolysis experiments which governed the charge separation lifetimes. **ZnP**-**PP**, as testament to its rigid linker, showed pronounced fluorescence quantum yields and lifetimes similar to unbound zinc porphyrin. Pulsed laser excitation showed that for all of the systems, the lifetime of the transient triplet states were similar, despite the fact that the driving force for the electron transfer differs between the hybrids. When **ZnP**-**PP** underwent bulk electrolysis to the monoreduced species, there was no significant reduction in the fluorescence intensity despite a strong thermodynamic driving

force for electron transfer from the reduced POM to the S_1 state of the ZnP unit (1.07 eV), indicating that the triazole group does not act as an efficient electron carrier in these systems.

The findings of these two papers cumulated in the design of a multiporphyrin cluster as a bio-inspired mimic of a photosynthetic reaction complex.[99] The system (Figure 24) comprises a 4-membered porphyrin based cluster where three Zn(II) porphyrins (ZnP) are covalently bound to a central free-base porphyrin (FbP) in a dendritic fashion, the central free-base porphyrin is then covalently bound to the lacunary Wells-Dawson phosphotungstate using the alkylphosphonate as the flexible linker in a 2:1 stoichiometry (**CL**-**POM)**. Here, the ancillary ZnP units were to function as photon collectors and transfer excitation energy to the FbP, which is then expected to donate an electron to the POM due to a high thermodynamic driving force for this process. Charge recombination should be prevented by hole transfer from the FbP to another neighbouring ZnP unit. Through UV-vis spectroscopy, it was determined that the ZnP and FbP units were able to be selectively excited through their non-overlapping Q bands. Excitation at 563 nm where the ZnP is the dominant chromophore results in only weak fluorescence from ZnP but a much stronger fluorescence from the FbP unit, indicative of electron energy transfer from the ZnP to the FbP units. With regards to the secondary electron transfer from the FbP unit to the POM, fluorescence studies showed that the POM acts as a quencher with *ca.* 14-25% efficiency through intramolecular electron transfer, time-resolved fluorescence decay curves showed monoexponential character suggesting only one conformation despite the flexible linker employed, indeed, the low rate constant for electron transfer despite the high thermodynamic driving force is consistent with through-bond electron transfer through a poor conductor (with the triazole acting as the electronic bottleneck). Nonetheless, in a charge accumulation experiment, prolonged visible light irradiation in the absence of oxygen and in the presence of the sacrificial electron donor triethanolamine, resulted in the observation of the doubly reduced POM.

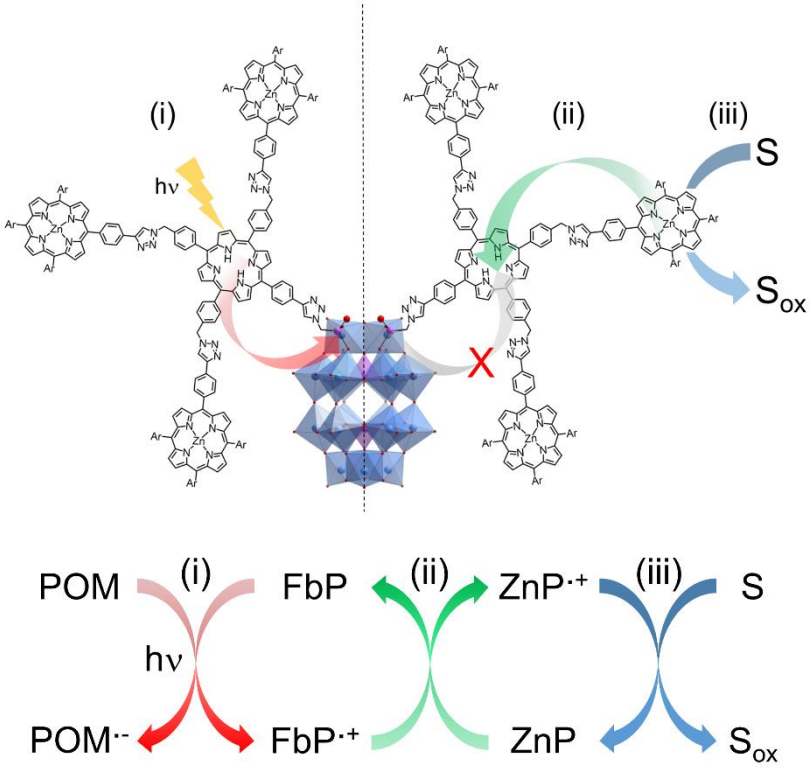


Figure 24. Configuration of dendritic polyoxometalate porphyrin hybrid featuring defined charge accumulation and separation sites for multiple electron loading onto the POM by Elliot et al.[99] Reproduced from [103] with permission from the Royal Society of Chemistry.

The systematic study of POM-photosensitiser Class II hybrids was extended to the comparison between Keggin and Dawson POM synthons and organic and inorganic photosenistisers by Matt et al.[104] In this work, Keggin and Dawson phosphotungstates were functionalised each with pyrene [Pyr] and ruthenium polypyridine [Ru] moieties using an arylsiloxane anchor, giving rise to a family of four related compounds (Figure 25). Whilst the pyrene derivatives were isolated as TBA salts, the [Ru] derivatives were isolated as 1-butyl-3-methylimidazolium (BMIM) salts as this cation was more effective at displacing the ruthenium complex-hybrid that forms post-functionalisation. The electrochemistry of both the Keggin and Dawson hybrids showed positive shifts in the first reduction process for the ruthenium complex substituent compared to the pyrene substituent due to charge mitigation. With respect to the electrochemistry of the [Ru] unit, there is only negligible differences between **Im**-**D**[**Ru**] and the [Ru] precursor suggesting that electronic interaction between the chromophore and POM units is limited. Expectedly the absorption spectra of **Im**-**K**[**Ru**] and **Im**-**D**[**Ru**] are dominated by the [Ru] chromophore in the visible region of the spectra. The fluorescence quenching rate constants for **Im**-**K**[**Ru**] and **Im**-**D**[**Ru**] ($8x10^{-6}$ and $21x10^{-6}$ s^{-1}) are modest considering the favourable thermodynamic driving force for electron transfer (-0.65 and -0.6 eV) suggesting that the high energy LUMO of the anionic

cyclometalating ligand prevents efficient through-bond electron transfer. Non-observation of the charge transfer state with transient absorption spectroscopy was attributed to extremely fast charge recombination or the inefficiency the [Ru] chromophore. When parallel studies were performed using the pyrene substituted analogues **TBA**-**K**[**Pyr**] and **TBA**-**D**[**Pyr**], remarkable similarities were observed in their photophysical behaviour; namely the dominance of the chromophore in the absorption spectra, the fluorescence quenching upon linkage of the chromophore to the POM, and the non-observation of the charge transfer state. In this case, the quenching constants of **TBA**-**K**[**Pyr**] and **TBA**-**D**[**Pyr**] were much higher than the POM-Ru systems, reflecting the higher thermodynamic driving force for the electron transfer (-1.45 eV and -1.08 eV for **TBA**-**K**[**Pyr**] and **TBA**-**D**[**Pyr**] respectively). Interestingly, the lifetime of the excited state of the [Ru] chromophore was evaluated when electrostatically combined with the POM hybrid precursors **TBA**-**K**[**I**] and **TBA**-**D**[**I**], in both cases only minimal quenching of the fluorescence was observed showing that the photoinduced electron transfer rate is faster when the photosensitiser is covalently bound to the POM than when the photosensitiser acts as an electrostatic adduct.

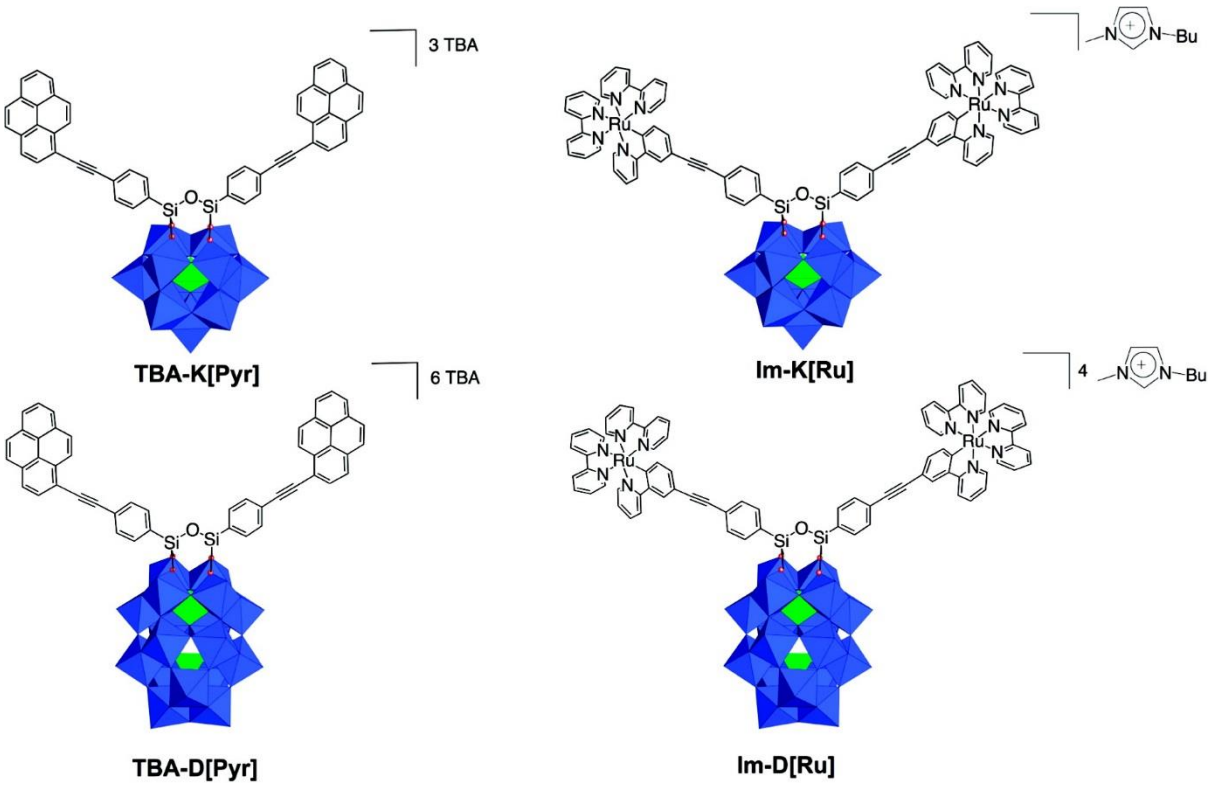


Figure 25. Related organosilyl polyoxometalate hybrids featuring remote organic or metal-based photosensitisers attached to Keggin and Dawson type polyoxometalates. Reproduced from [104] with permission from the American Chemical Society.

The groups' interest in covalently linked POM and metal photosensitiser hybrids later furnished a new system pairing Keggin and Dawson phosphotungstates with a neutral cyclometalated iridium complex

as TBA salts.[105] This study used two different anchoring methods to allow for the attachment of one (aryltin anchoring group) or two (arylsiloxane anchoring group) chromophore units to both the Keggin and Dawson POMs (Figure 26). For $\mathbf{K_{Si}[Ir]}$ and $\mathbf{D_{Si}[Ir]}$, the first reduction potential of the POM occurs at identical potentials to previously reported analogous systems with neutral chromophores (terpyridine, pyrene). More pronounced differences were observed comparing the first reduction potentials with the different POM and different linker groups, specifically, the higher the overall charge of the species the more difficult it is to reduce, giving the following series: $\mathbf{K_{Si}[Ir]}$ (-0.38 V vs. SCE, 3-) > $\mathbf{D_{Si}[Ir]}$ (-0.73 V vs. SCE, 4-) > $\mathbf{K_{Sn}[Ir]}$ (-1.09 V vs. SCE, 6-) > (-1.28 V vs. SCE, 7-) $\mathbf{D_{Sn}[Ir]}$. From transient absorption and emission spectroscopies, the charge separation times and recombination times were calculated for each species and the trend was that the electron transfer rates followed the same order as the first reduction potentials of the POM, whereby the fastest electron transfer was observed for the POMs that were the easiest to reduce (and hence had the lowest charge). Computational studies showed that the grafting of the [Ir] complex to the POM through the picolinate ligand allows facile forward electron transfer but delays charge recombination, this is because the electron donor orbital of the [Ir] complex resides on the conjugated picolinate ligand (better overlap with POM acceptor orbitals) whereas the hole resides on the phenylpyridyl ligands (poorer overlap with POM donor orbitals). Forward directionality is therefore conferred through the picolinate ligand and its proximity to the POM, this directionality was not conferred in previous systems which showed either no directionality (pyrene) or reverse directionality (Ru polypyridine).

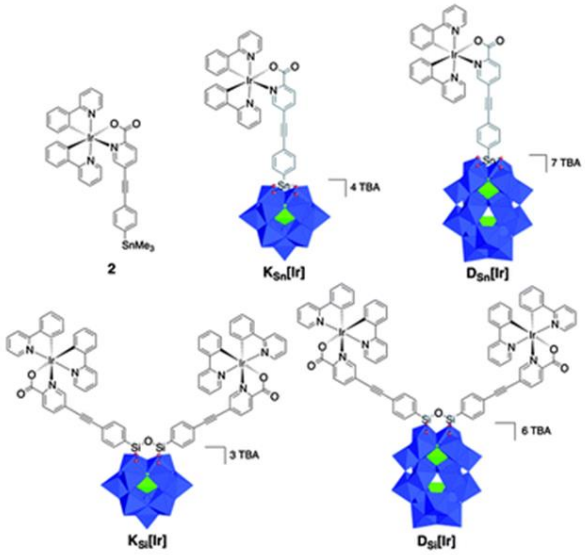
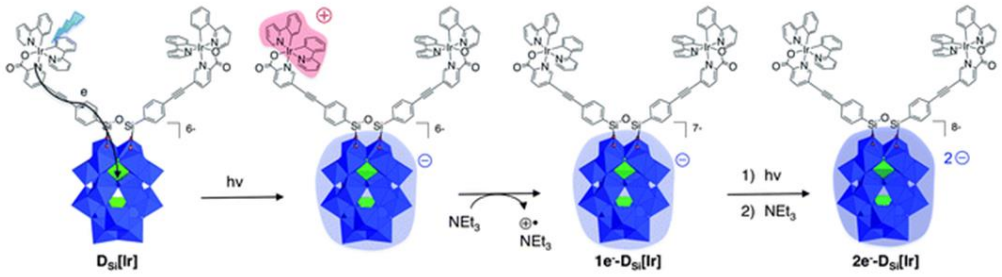


Figure 26. Related organosilyl polyoxometalate hybrids featuring remote neutral cyclometalate iridium photosensitisers attached to Keggin and Dawson type polyoxometalates either in a 1:1 or 2:1 fashion via tin or silyl linkages respectively. Reproduced from [105] with permission from the Royal Society of Chemistry.

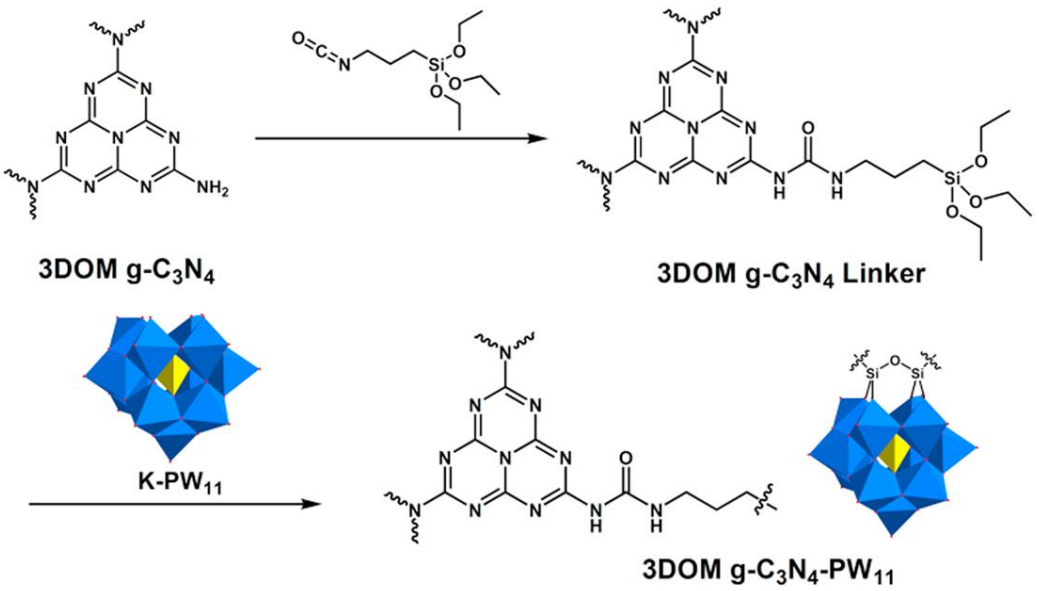
Having established the fundamental photophysics of the system, **D_{Si}[Ir]** was deemed to have the most interesting photophysical properties since it exhibits a very effective charge separation which is theoretically long enough to allow redox chemistry with external substrates to occur. This compound was thus tested for its charge photo-accumulation abilities and photocatalytic hydrogen evolution activity in a follow-up study by the same authors.[106] Monitoring the evolution of the absorption spectrum upon visible light irradiation (λ > 400 nm), the monoreduced species formed quickly ($\tau_{1/2}$, = 43 s, $\varphi_{400\ nm}$ = 10.5 ± 1%) whereas the doubly reduced species more slowly ($\tau_{1/2}$ = 270 s, $\varphi_{400\ nm}$ = 2.3 ± 0.5). Photoirradiation experiments in the presence of acetic acid showed little influence on the evolution of the monoreduced species ($\tau_{1/2}$ = 37 s) but did show a dramatic acceleration of the evolution of the doubly reduced species ($\tau_{1/2}$ = 60 s). As a H_2-evolving catalyst, the hybrid sustained H_2 evolution at a TOF of 0.25 h^{-1} over 7 days in the presence of acetic acid and trimethylamine (Scheme 6). No activity was seen when triethylamine was omitted or the precursor POM hybrid **D_{Si}[I]** was used instead, and only trace amounts of H_2 were observed when [Ir] was employed as the photocatalyst, when **D_{Si}[I]** was employed in the presence of 2 equivalents of [Ir], the TOF was halved, thus demonstrating the beneficial effect offered through the covalent tethering of the POM and photosensitiser units.



Scheme 6. Proposed mechanism for enhancement of the photoreduction of iridium tethered Dawson polyoxometalate in the presence of trimethylamine and acetic acid. Reproduced from [106] with permission from the Royal Society of Chemistry.

Karimian et al. investigated the use of hybrid photosensitser POMs as both the photoanode material and sensitiser in the construction of a dye-sensitised solar cell (DSSC).[107] The POM selected was the lacunary Keggin silicotungstate and the dye selected was D35 (see Scheme 7) which was anchored to the POM in a 2:1 fashion using an alkylsilicate group. Curiously, the inclusion of this hybrid into a DSSC required a non-conventional synthetic route. Firstly, the lacunary silicotungstate was prepared as a thin film on fluorine-doped tin oxide glass (FTO), this was followed by heterogeneous surface functionalisation of the glass via treatment with the anchoring tether (3-aminopropyl)trimethoxysilane

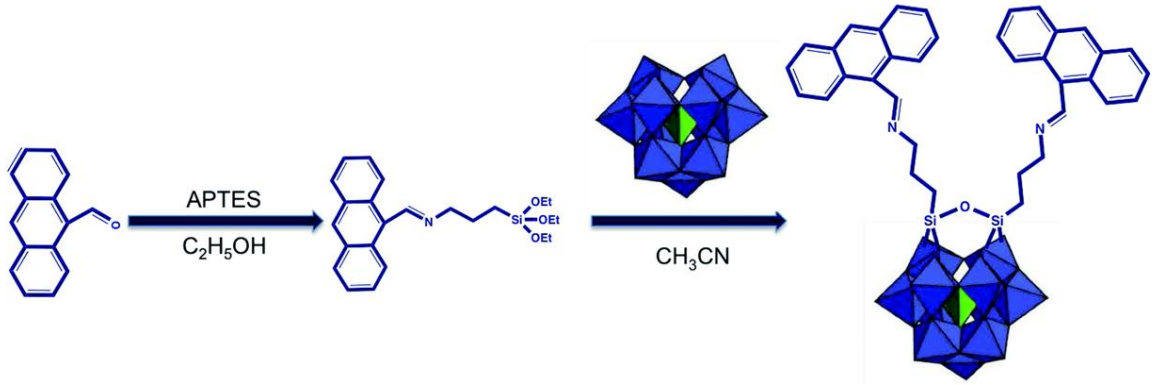
(APTES), this was then heterogeneously post-functionalised with the dye D35 to form the material as a functionalised layer. The absorption properties of the layer were probed using UV-vis reflectance spectroscopy, where upon covalent addition of the dye, an extra reflection occured at 510-700 nm related to the broad absorption of D35 at 530 nm. Despite this, it appeared that the solid-state band gap of the material remained unchanged at 3.3 eV based on an indirect transition. From the reflectance spectrum it was also calculated that the refractive index is 1.35 which is lower than that of the bulk standard POM (2). The dye coverage on the surface of the layer was determined to be 2.5 x 10^{-7} molcm^{-2} and the dye occupied an area on the polyoxometalate of 0.66 nm^2. Once fabricated into a DSSC device, the hybrid material showed superior photovoltage values (+55 mV), short circuit current density, incident photon to current conversion efficiency (ICPE) (+30%) and transient electron lifetimes (τ_e = 0.5 - 3.2 s *cf.* <0.3 s) compared to similar devices based on mesoporous titania, which could be directly related to the higher electron transport in the photoanode layer.



Scheme 7. Synthetic strategy for the tethering of POMs to a photoactive heterogeneous surface using oranosilicon linkers. Reproduced from [108] with permission from the Royal Society of Chemistry.

Using the same molecular design approach, Karimian et al. also tethered anthracene units to the lacunary Keggin silicotungstate (Scheme 8) and tested its capabilities towards the photocatalytic aerobic oxidation of alcohols.[108] As expected, the attachment of anthracene moieties to the POM served to widen its absorption profile when measured in the solution phase. From the solid-phase diffuse reflectance spectrum, the band gap was estimated at 2.28 eV which represents a significant decrease compared to its synthetic precursor (3.76 eV) thus suggesting that the hybrid has been photosensitised.

The hybrid indeed showed high activity for the selective oxidation of benzylic alcohols and moderate activity towards cyclic and aliphatic alcohols with good recyclability.



Scheme 8. Organofunctionalisation strategy for the tethering of anthracene dyes to the lacunary Keggin silicotungstate. Reproduced from [108] with permission from the Royal Society of Chemistry.

A series of phosphate tethered hybrid POMs have been investigated by Wong, Du and co-workers, where the organic group linked the polyoxometalate to remote metal complexes; namely Pt(II) and Hg(II) acetylene complexes and a Zn(II) porphyrin complex,[109-111] the former two forming oligomeric hybrid species. The absorption spectra of the compounds are mainly dictated by the chromophoric nature of the metal complex, the Zn-porphyrin complex having the most features. It is interesting to see here that the Q-band of the Zn-porphyrin complex upon hybridisation has shifted bathochromically, indicative of delocalisation between the two units. This is markedly different from previous examples of metalloporphyrin hybrid POMs where the two components are completely decoupled. The three metallocomplex hybrids were tested for their conductive and photocurrent responses as LB layers analogously to the previously described naphthyl hybrid. In general, photocurrents were generated upon excitation by UV-vis light and were highest in the blue region, with the zinc metalloporphyrin hybrid being the best performer (7.9 μV @ 471 nm), their conductivity was comparable with each able to perform as a semiconductor.

A recent approach by Zhao et al. involved the covalent grafting of a hybrid polyoxometalate to the surface of the semiconductor graphitic carbon nitride (g-C_3N_4) for photodriven H_2O_2 production from water and dioxygen in the absence of organic electron donors.[112] The material (g-C_3N_4-PW_{11}) was synthesised by first functionalising the g-C_3N_4 so that it had pendant siloxane groups, and then coupling this with the lacunary Keggin phosphotungstate. g-C_3N_4-PW_{11} was found to be highly active towards H_2O_2 production as both a water oxidation catalyst and an oxygen reduction catalyst and performed over twice as efficiently as the non-covalently attached analogue (g-C_3N_4-PW_{11}IMP) with the same components. The hybrid material was also efficient at stabilising the H_2O_2 produced (17%

decomposition after 1 hour) and did not catalyse the back-reaction whereas its components, and the non-covalent analogue, did to varying degrees (>62% for g-C_3N_4, PW_{11} and g-C_3N_4-PW_{11}IMP cf. native H_2O_2 degradation rate: 35%). When characterised as a film on FTO, g-C_3N_4-PW_{11} showed larger photocurrent densities and lower resistances than g-C_3N_4 and better charge separation as detected by a reduction in its photoluminescence spectrum. From Tauc plots and Mott-Schottky diagrams, the valence band positions of the hybrid material were both estimated to be more positive than g-C_3N_4. This proves to be beneficial for the production of H_2O_2 as it aids in overcoming the kinetic barrier of oxygen evolution and prevents the undesirable one electron reduction pathway. A follow-up study showed that substituting the Keggin phosphotungstate for the Keggin silicotungstate (which has a more negative conduction band level),[113] resulted in photocatalytic performance that relied on the presence of sacrificial electron donors (methanol) and was significantly hampered with UV light was precluded from the spectrum, also it was unable to completely suppress the one-electron oxygen reduction pathway.

Whilst the attachment of chromophores to the polyoxometalate gives a highly controlled approach towards photoactive POM materials, it is evident that the synthetic demand of such a route hinders its practical application in industrial settings. Chromophores themselves are often laborious to synthesise and purify, compounded with the fact that the POM chemist must design a covalent tethering approach that does not negatively impact its photoabsorbing properties and gives the desired amount of distance, electronic coupling and stoichiometry between the components.

It is also especially important to note that the mechanism of photoexcitation in all of the above scenarios differs from the conventional photoexcitation of polyoxometalates as described in Section 1.5. In these examples, the polyoxometalate retains the role of the electron reservoir but does not act as the chromophore, instead, the POM must rely on inter-or intramolecular charge transfer from the photoexcitation of the appended chromophore. Whereas in conventional POM photochemistry, the polyoxometalate is directly excited through the LMCT band and itself acts as the chromophore. The former example may be described as a "*Vis-exo*" excitation (visible light activation via an external chromophore) and the latter as "UV-endo" (UV light activation via an internal mechanism). Fundamentally, the origin of the excitation results in completely contrasting photochemistry of the system. The *UV-endo* approach, generating the oxo-cation radical as previously discussed, allows the POM to abstract a hydrogen atom (a proton and an electron) from a substrate and thus the POM acts as a potent photooxidation catalyst. Conversely, in the *Vis-exo* approach, the chromophore undergoes

photoexcitation and subsequently donates electrons to the POM via charge transfer, the POM is then able to donate these electrons to a substrate and thus act as a photoreduction catalyst. Thus, whilst photosensitisation via covalent attachment of chromophores has shown to be effective for proton reduction,[106] and chromophore-POM donor-acceptors compounds in photoelectronics,[108, 111] their ability to perform visible light photooxidations has not been unequivocally proven.

A major goal within the field is to therefore find simple and controllable ways to increase the photoabsorption properties of the polyoxometalate core itself through the tuning of the LMCT band (i.e. a *Vis-endo* photosensitisation). Recently, a pioneering study by Cameron et al. adopted an "orbital engineering" approach to the photoactivation of the Dawson phosphotungstate (Figure 27a).[114] They postulated that if a sufficiently electron withdrawing moiety is attached to the polyoxometalate, the LUMO energy may be decreased to affect the visible light photoactivation of the LMCT band. The organic group thus chosen was 4-carboxyphenyl phosphonic acid, bearing an electron withdrawing carboxyl group opposite the anchoring group. Electrochemical measurements showed a dramatic positive shift in the first reduction potential versus the parent anions (~400 mV and ~500 mV vs. "W_{18}" and "W_{17}" respectively) suggesting a change in the electronic structure on the POM and a lowering of the LUMO energies (Figure 27b). Interestingly, the absorption spectra of the hybrid compound show very similar features to those of W_{18} and W_{17}, with only a slight bathochromic shift of the absorption maxima and more pronounced tailing into the visible region. Despite this, photoreduction experiments using visible light ($\lambda > 420$ nm) in the presence of a sacrificial electron donor (DMF) showed that the hybrid species underwent time dependent photoreduction whereas neither the lacunary nor plenary POM showed any activity. When the irradiation was blue-shifted to $\lambda > 390$ nm, the activity of the hybrid and "W_{18}" both increased; the former reaching full saturation of the monoreduced species and the latter only undergoing partial 2-electron reduction in the timeframe of the experiment (1 hour), "W_{17}" showed no activity (Figure 27c). These results indicate that photochemical behaviour of POMs cannot always be predicted from their absorption spectra and are dependent on both the optical (HOMO-LUMO gap) and electronic (LUMO energy) properties of the POM. This photoactivity was then tested towards the photooxidation of model pollutant indigo dye ($\lambda > 390$ nm) and followed predicted reactivities based on the photoreduction studies; in fact, the hybrid POM was over 4 times more active than "W_{18}" ($k_{obs} = 6 \times 10^{-4}$ s^{-1} vs. 1.4×10^{-4} s^{-1}) whereas "W_{17}" showed no appreciable activity. At $\lambda > 420$ nm only the hybrid POM showed any activity (1×10^{-4} s^{-1}) (Figure 27d). These experimental findings were

supported by computational studies, where the HOMO-LUMO electron density maps of the hybrid show significant electron delocalisation between the ligand π* orbitals and the POM core. The LUMO energy of 1 appears to be lowered and there is a smaller HOMO-LUMO gap compared with "W_{18}". The observed and calculated effects result from a combination of the inductive and resonance effects exerted by the carboxyphenyl phosphonate groups, the former stabilising both the HOMO and LUMO levels (sigma contribution) and the latter destabilising the HOMO and stabilising the LUMO (pi contribution). The enhanced photooxidative capabilities of the hybrid are therefore attributed to both an increase in visible light photosensitisation (smaller HOMO-LUMO gap) and a more oxidising (lower) LUMO energy.

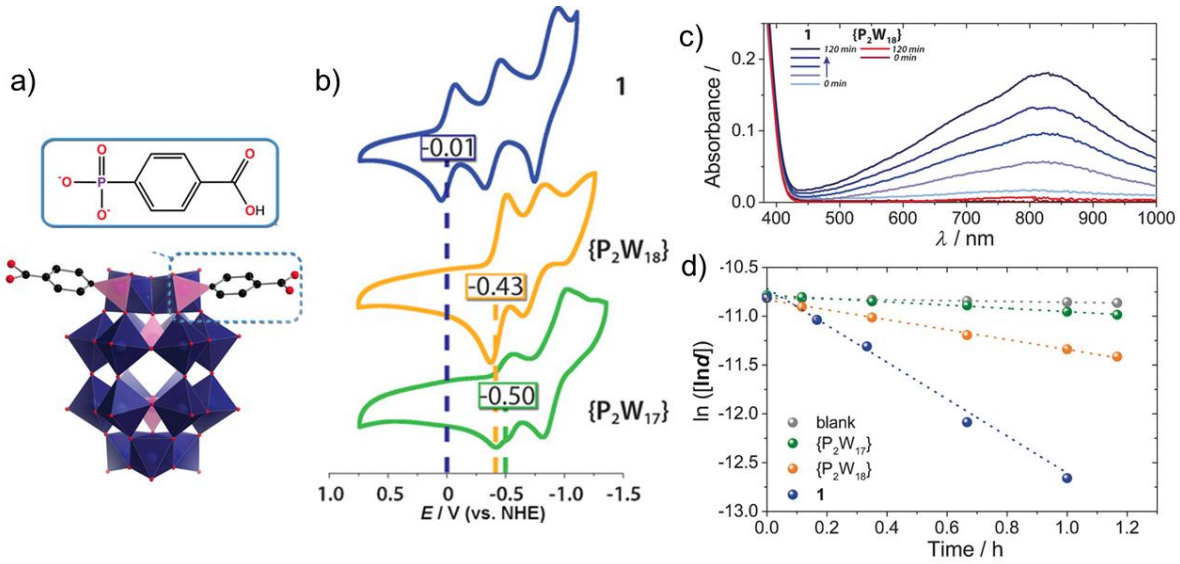


Figure 27. Orbital engineering approach to the lowering of the POM LUMO energy through electron withdrawing carboxyphenylphosphate ligands, resulting in rapid photoreduction behaviour and improved efficiency for organic dye degradation. Reproduced from [114] with permission form Wiley Publishers.

Shortly after, this study was elaborated and extended to investigate the nature of this phenomenon with different organophosphonate substituents. Three phenylphosphoryl moieties with different electron natures (4-carboxyphenyl-, 4-methoxyphenyl- and phenylphosphonates) were coupled with the lacunary Dawson phosphotungstate (Figure 28a). Computational studies showed that the substituents did have a clear and predictable effect on the frontier molecular orbitals. Whilst all of the phenylphosphonate groups showed a stabilisation of the LUMO and destabilisation of the HOMO compared to W_{18} commensurate with the inductive and resonance effects exhibited by all phenylphosphonate moieties, the HOMO-LUMO gap (and LUMO energies) showed a clear dependence on the substituent with W_{17}PhOMe having the largest gap (and highest LUMO energy) and W_{17}PhCOOH having the smallest gap (and lowest LUMO energy) in agreement with their relative electronic effects (Figure 28b). The electrochemistry of the three hybrids mimicked the trends observed

from the computational studies, whereby more electron donating substituents on the ring destabilise the LUMO on the POM which manifests as more negative first redox potentials. A fourth species was also synthesised and analysed bearing all inorganic phosphonic acid groups ("$W_{17}H$"), this hybrid was to aid in the deconvolution of the electronic effects that tune the photoactivity of the POM as it was expected to exert an electron withdrawing inductive effect on the POM with minimal resonance effects. Hence, the photocatalytic properties of the four named compounds were explored using the same set-up as in the previous communication (photooxidation of indigo dye with visible light (λ > 420 nm) or UV-visible light (λ > 390 nm)) (Figure 28c), the four hybrids all showed activity commensurate with their measured and calculated electronic properties; $W_{17}H$ > $W_{17}PhCOOH$ > $W_{17}Ph$ > $W_{17}PhOMe$ > W_{18}. In fact, the rate constants calculated from the dye degradation studies showed a linear correlation with the first redox potentials of the POMs (Figure 28d), specifically, the more positive the first reduction potential of the POM, the higher the observed logarithmic rate constant. This demonstrates that the first reduction potential may be the most indicative parameter for estimating the photocatalytic activities of hybrid POMs.

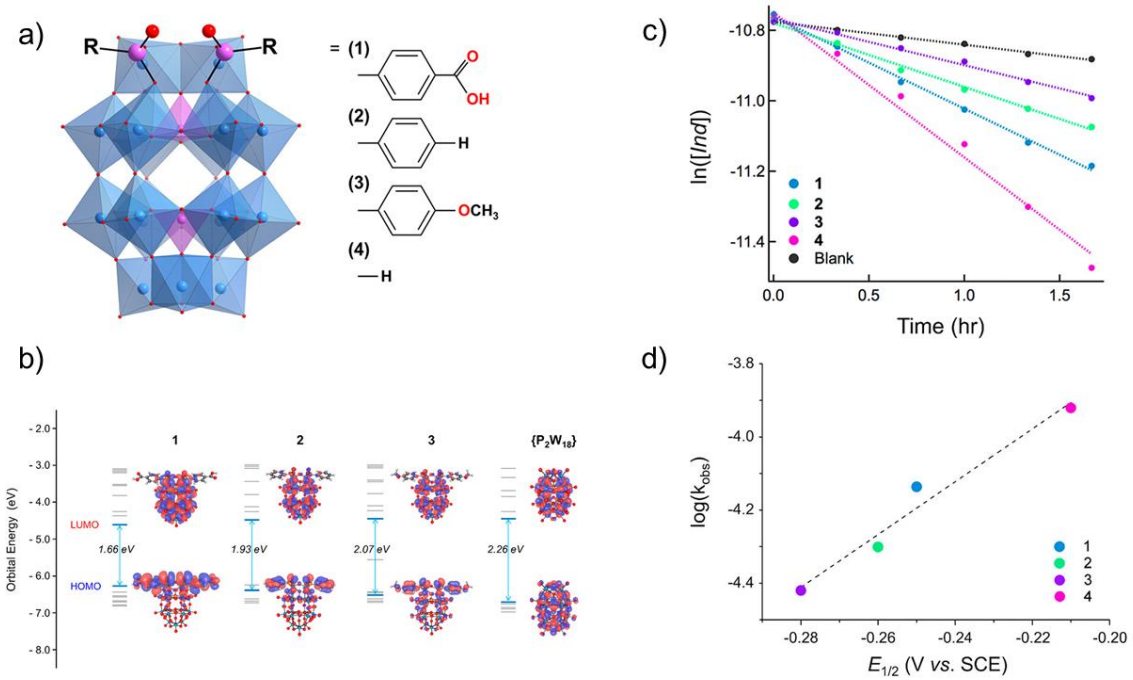


Figure 28. Controllable orbital engineering through modulation of the electronics of phenylphosphonate organic groups for the predictable lowering of the LUMO and enhancement of the photocatalytic activity. Reproduced from [115] with permission form the American Chemical Society.

1.7 References

1. S. S. Wang and G. Y. Yang, *Chem. Rev.*, 2015, **115**, 4893-4962.
2. J. J. Walsh, A. M. Bond, R. J. Forster and T. E. Keyes, *Coord. Chem. Rev.*, 2016, **306**, 217-234.
3. Y. Ji, L. Huang, J. Hu, C. Streb and Y.-F. Song, *Energy Environ. Sci.*, 2015, **8**, 776-789.
4. L. Chen, W.-L. Chen, X.-L. Wang, Y.-G. Li, Z.-M. Su and E.-B. Wang, *Chem. Soc. Rev.*, 2019, **48**, 260-284.
5. Q. Y. Li, L. Zhang, J. L. Dai, H. Tang, Q. Li, H. G. Xue and H. Pang, *Chem. Eng. J.*, 2018, **351**, 441-461.
6. J. M. Clemente-Juan, E. Coronado and A. Gaita-Ariño, *Chem. Soc. Rev.*, 2012, **41**, 7464-7478.
7. J. T. Rhule, C. L. Hill and D. A. Judd, *Chem. Rev.*, 1998, **98**, 327-357.
8. C. G. Lin, J. Hu and Y. F. Song, in *Advances in Inorganic Chemistry, Vol 69: Polyoxometalate Chemistry*, eds. R. VanEldik and L. Cronin, 2017, vol. 69, pp. 181-212.
9. L. C. W. Baker and D. C. Glick, *Chem. Rev.*, 1998, **98**, 3-50.
10. W. N. Lipscomb, *Inorg. Chem.*, 1965, **4**, 132-&.
11. J. J. Borrás-Almenar, E. Coronado, A. Müller and M. Pope, *Polyoxometalate Molecular Science*, Springer Netherlands, 2003.
12. S. Herrmann, *New Synthetic Routes to Polyoxometalate Containing Ionic Liquids: An Investigation of their Properties*, Springer Fachmedien Wiesbaden, 2015.
13. R. Dronskowski, S. Kikkawa and A. Stein, *Handbook of Solid State Chemistry, 6 Volume Set*, Wiley, 2017.
14. D.-L. Long, R. Tsunashima and L. Cronin, *Angew. Chem., Int. Ed.*, 2010, **49**, 1736-1758.
15. I. Lindqvist, *Arkiv for Kemi*, 1953, **5**, 247-250.
16. M. Nyman, *Dalton Trans.*, 2011, **40**, 8049-8058.
17. B. C. Bunker and W. H. Casey, *The Aqueous Chemistry of Oxides*, Oxford University Press, 2016.
18. J. Li, *J. Cluster Sci.*, 2002, **13**, 137-163.
19. J. F. Keggin, *Proceedings of the Royal Society of London A: Mathematical, Physical and Engineering Sciences*, 1934, **144**, 75-100.
20. P. Gouzerh and M. Che, *Actual Chim.*, 2006, 9-22.
21. A. Kondinski and T. N. Parac-Vogt, *Front. Chem.*, 2018, **6**, 346-346.
22. M. Nyman, F. Bonhomme, T. M. Alam, J. B. Parise and G. M. B. Vaughan, *Angew. Chem. Int. Ed.*, 2004, **43**, 2787-2792.
23. M. Yuan, Y. G. Li, E. B. Wang, C. G. Tian, L. Wang, C. W. Hu, N. H. Hu and H. Q. Jia, *Inorg. Chem.*, 2003, **42**, 3670-3676.
24. J. Canny, A. Teze, R. Thouvenot and G. Herve, *Inorg. Chem.*, 1986, **25**, 2114-2119.
25. L. Cronin, *ChemInform*, 2004, **35**, 1-56.
26. W. A. Neiwert, J. J. Cowan, K. I. Hardcastle, C. L. Hill and I. A. Weinstock, *Inorg. Chem.*, 2002, **41**, 6950-6952.
27. I. A. Weinstock, J. J. Cowan, E. M. G. Barbuzzi, H. D. Zeng and C. L. Hill, *J. Am. Chem. Soc.*, 1999, **121**, 4608-4617.
28. A. Tézé, E. Cadot, V. Béreau and G. Hervé, *Inorg. Chem.*, 2001, **40**, 2000-2004.
29. J. Rowsell and L. F. Nazar, *J. Am. Chem. Soc.*, 2000, **122**, 3777-3778.
30. D. Sloboda-Rozner, K. Neimann and R. Neumann, *J. Mol. Catal. A Chem.*, 2007, **262**, 109-113.
31. B. Dawson, *Act. Cryst.*, 1953, **6**, 113-126.
32. E. Coronado and C. J. Gómez-García, *Chem. Rev.*, 1998, **98**, 273-296.
33. U. Kortz and M. T. Pope, *Inorg. Chem.*, 1994, **33**, 5643-5646.
34. I.-M. Mbomekalle, B. Keita, Yu W. Lu, L. Nadjo, R. Contant, N. Belai and Michael T. Pope, *Eur. J. Inorg. Chem.*, 2004, **2004**, 4132-4139.
35. F.-Q. Zhang, W. Guan, L.-K. Yan, Y.-T. Zhang, M.-T. Xu, E. Hayfron-Benjamin and Z.-M. Su, *Inorg. Chem.*, 2011, **50**, 4967-4977.

36. L. Vila-Nadal, S. G. Mitchell, D.-L. Long, A. Rodriguez-Fortea, X. Lopez, J. M. Poblet and L. Cronin, *Dalton Trans.*, 2012, **41**, 2264-2271.
37. A. Hashikawa, M. Fujimoto, Y. Hayashi and H. Miyasaka, *Chem. Commun.*, 2011, **47**, 12361-12363.
38. J. Server-Carrió, J. Bas-Serra, M. E. González-Núñez, A. García-Gastaldi, G. B. Jameson, L. C. W. Baker and R. Acerete, *J. Am. Chem. Soc.*, 1999, **121**, 977-984.
39. A. J. Kibler and G. N. Newton, *Polyhedron*, 2018, **154**, 1-20.
40. A. Blazevic and A. Rompel, *Coord. Chem. Rev.*, 2016, **307**, 42-64.
41. J. P. Martínez, E. Rivera-Avalos, S. Vega-Rodríguez and D. de Loera, *Res. Chem. Intermed.*, 2018, **44**, 2061-2073.
42. H. T. Evans, *Inorg. Chem.*, 1966, **5**, 967-977.
43. E. J. Graeber and B. Morosin, *Acta Cryst. B*, 1977, **33**, 2137-2143.
44. J. L. Garin and J. A. Costamagna, *Acta Cryst. C*, 1988, **44**, 779-782.
45. D. E. Katsoulis, *Chem. Rev.*, 1998, **98**, 359-388.
46. N. I. Gumerova and A. Rompel, *Nat. Rev. Chem.*, 2018, **2**, 0112.
47. M. T. Pope, *Heteropoly and isopoly oxometalates*, Springer-Verlag, 1983.
48. X. López, J. A. Fernández and J. M. Poblet, *Dalton Trans.*, 2006, DOI: 10.1039/B507599H, 1162-1167.
49. X. López, C. Bo and J. M. Poblet, *J. Am. Chem. Soc.*, 2002, **124**, 12574-12582.
50. I.-M. Mbomekallé, X. López, J. M. Poblet, F. Sécheresse, B. Keita and L. Nadjo, *Inorg. Chem.*, 2010, **49**, 7001-7006.
51. K. Kastner, A. J. Kibler, E. Karjalainen, J. A. Fernandes, V. Sans and G. N. Newton, *J. Mater. Chem. A*, 2017, **5**, 11577-11581.
52. V. D. Waele, O. Poizat, M. Fagnoni, A. Bagno and D. Ravelli, *ACS Catal.*, 2016, **6**, 7174-7182.
53. P. Lei, C. Chen, J. Yang, W. Ma, J. Zhao and L. Zang, *Environ. Sci. Technol.*, 2005, **39**, 8466-8474.
54. M. D. Tzirakis, I. N. Lykakis and M. Orfanopoulos, *Chem. Soc. Rev.*, 2009, **38**, 2609-2621.
55. D. L. Long, R. Tsunashima and L. Cronin, *Angew. Chem. Int. Ed.*, 2010, **49**, 1736-1758.
56. H. Lv, Y. V. Geletii, C. Zhao, J. W. Vickers, G. Zhu, Z. Luo, J. Song, T. Lian, D. G. Musaev and C. L. Hill, *Chem. Soc. Rev.*, 2012, **41**, 7572-7589.
57. F. Luis and M. Evangelisti, in *Molecular Nanomagnets and Related Phenomena*, ed. S. Gao, 2015, vol. 164, pp. 431-460.
58. X.-B. Han, Z.-M. Zhang, T. Zhang, Y.-G. Li, W. Lin, W. You, Z.-M. Su and E.-B. Wang, *J. Am. Chem. Soc.*, 2014, **136**, 5359-5366.
59. A. M. Khenkin, I. Efremenko, L. Weiner, J. M. L. Martin and R. Neumann, *Chem. Eur. J.*, 2010, **16**, 1356-1364.
60. M. Stuckart and K. Y. Monakhov, *Chem. Sci.*, 2019, **10**, 4364-4376.
61. J. W. Jordan, G. A. Lowe, R. L. McSweeney, C. T. Stoppiello, R. W. Lodge, S. T. Skowron, J. Biskupek, G. A. Rance, U. Kaiser, D. A. Walsh, G. N. Newton and A. N. Khlobystov, *Adv. Mater.*, **2019**, 1904182.
62. M. Stuckart and K. Y. Monakhov, *J. Mater. Chem. A*, 2018, **6**, 17849-17853.
63. A. Das and S. Ghosh, *Angew. Chem. Int. Ed.*, 2014, **53**, 2038-2054.
64. C. L. Hill and D. A. Bouchard, *J. Am. Chem. Soc.*, 1985, **107**, 5148-5157.
65. J. A. Schmidt, E. F. Hilinski, D. A. Bouchard and C. L. Hill, *Chem. Phys. Lett.*, 1987, **138**, 346-351.
66. C. M. Prosser-McCartha, M. Kadkhodayan, M. M. Williamson, D. A. Bouchard and C. L. Hill, *J. Chem. Soc., Chem. Commun.*, 1986, DOI: 10.1039/C39860001747, 1747-1748.
67. M. M. Williamson, D. A. Bouchard and C. L. Hill, *Inorg. Chem.*, 1987, **26**, 1436-1441.
68. C. L. Hill, *Chem. Rev.*, 1998, **98**, 1-2.
69. J. A. F. Gamelas, F. M. Santos, V. Felix, A. M. V. Cavaleiro, E. de Matos Gomes, M. Belsley and M. G. B. Drew, *Dalton Trans.*, 2006, DOI: 10.1039/B508986G, 1197-1203.
70. X. X. Xu, X. Z. You and X. Wang, *Acta Chem. Scand.*, 1996, **50**, 1-5.

71. P. Le Maguerès, S. M. Hubig, S. V. Lindeman, P. Veya and J. K. Kochi, *J. Am. Chem. Soc.*, 2000, **122**, 10073-10082.
72. R. S. Mulliken, *J.Phys. Chem.*, 1952, **56**, 801-822.
73. V. M. Hultgren, A. M. Bond and A. G. Wedd, *J. Chem. Soc., Dalton Trans.*, 2001, DOI: 10.1039/B008682G, 1076-1082.
74. X. Xiang, J. Fielden, W. Rodriguez-Cordoba, Z. Huang, N. Zhang, Z. Luo, D. G. Musaev, T. Lian and C. L. Hill, *J. Phys. Chem. C*, 2013, **117**, 918-926.
75. H. Ye, R. Sun, J. Qi, L. Gao and K. Wang, *J. Solid State Electrochem.*, 2019, **23**, 227-235.
76. A. Kuhn and F. C. Anson, *Langmuir*, 1996, **12**, 5481-5488.
77. B. Artetxe, A. Iturrospe, P. Vitoria, E. Ruiz-Bilbao, J. S. Garitaonandia and J. M. Gutiérrez-Zorrilla, *Molecules*, 2018, **23**, 3150.
78. H. Xu, L. Zhang, Z. Li, X. Liu, H. Hu and G. Xue, *Solid State Sci.*, 2010, **12**, 1332-1336.
79. C. Costa-Coquelard, S. Sorgues and L. Ruhlmann, *J. Phys. Chem. A*, 2010, **114**, 6394-6400.
80. D. Schaming, C. Costa-Coquelard, S. Sorgues, L. Ruhlmann and I. Lampre, *Appl. Catal. A Gen.*, 2010, **373**, 160-167.
81. P. L. Veya and J. K. Kochi, *J. Organomet. Chem.*, 1995, **488**, C4-C8.
82. N. Fay, V. M. Hultgren, A. G. Wedd, T. E. Keyes, R. J. Forster, D. Leane and A. M. Bond, *Dalton Trans.*, 2006, DOI: 10.1039/B605663F, 4218-4227.
83. R. Ballardini, M. T. Gandolfi and V. Balzani, *Inorg. Chem.*, 1987, **26**, 862-867.
84. M. Orlandi, R. Argazzi, A. Sartorel, M. Carraro, G. Scorrano, M. Bonchio and F. Scandola, *Chem. Commun.*, 2010, **46**, 3152-3154.
85. J. Gao, S. Cao, Q. Tay, Y. Liu, L. Yu, K. Ye, P. C. S. Mun, Y. Li, G. Rakesh, S. C. J. Loo, Z. Chen, Y. Zhao, C. Xue and Q. Zhang, *Sci. Rep.*, 2013, **3**, 1853.
86. D. Schaming, R. Farha, H. Xu, M. Goldmann and L. Ruhlmann, *Langmuir*, 2011, **27**, 132-143.
87. J. Fielden, J. M. Sumliner, N. Han, Y. V. Geletii, X. Xiang, D. G. Musaev, T. Lian and C. L. Hill, *Chem. Sci.*, 2015, **6**, 5531-5543.
88. M. Bonchio, Z. Syrgiannis, M. Burian, N. Marino, E. Pizzolato, K. Dirian, F. Rigodanza, G. A. Volpato, G. La Ganga, N. Demitri, S. Berardi, H. Amenitsch, D. M. Guldi, S. Caramori, C. A. Bignozzi, A. Sartorel and M. Prato, *Nat.*, 2019, **11**, 146-153.
89. X. Han, S. Yang and M. Schröder, *Nat. Rev. Chem.*, 2019, **3**, 108-118.
90. Z.-M. Zhang, T. Zhang, C. Wang, Z. Lin, L.-S. Long and W. Lin, *J. Am. Chem. Soc.*, 2015, **137**, 3197-3200.
91. G. Paille, M. Gomez-Mingot, C. Roch-Marchal, B. Lassalle-Kaiser, P. Mialane, M. Fontecave, C. Mellot-Draznieks and A. Dolbecq, *J. Am. Chem. Soc.*, 2018, **140**, 3613-3618.
92. J. Tian, Z.-Y. Xu, D.-W. Zhang, H. Wang, S.-H. Xie, D.-W. Xu, Y.-H. Ren, H. Wang, Y. Liu and Z.-T. Li, *Nat. Comm.*, 2016, **7**, 11580.
93. M. Janjua, M. U. Khan, B. Bashir, M. A. Iqbal, Y. Z. Song, S. A. R. Naqvi and Z. A. Khan, *Comput. Theor. Chem.*, 2012, **994**, 34-40.
94. H. N. Wu, T. Zhang, C. X. Wu, W. Guan, L. K. Yan and Z. M. Su, *Dyes Pigm.*, 2016, **130**, 168-175.
95. M. Gilbert and B. Albinsson, *Chem. Soc. Rev.*, 2015, **44**, 845-862.
96. C. O. Obondi, G. N. Lim, B. Churchill, P. K. Poddutoori, A. van der Est and F. D'Souza, *Nanoscale*, 2016, **8**, 8333-8344.
97. T. Cardona, A. Sedoud, N. Cox and A. W. Rutherford, *Biochim. Biophys. Acta*, 2012, **1817**, 26-43.
98. M. Bonchio, M. Carraro, G. Scorrano and A. Bagno, *Adv. Synth. Catal.*, 2004, **346**, 648-654.
99. K. J. Elliott, A. Harriman, L. Le Pleux, Y. Pellegrin, E. Blart, C. R. Mayer and F. Odobel, *Phys. Chem. Chem. Phys.*, 2009, **11**, 8767-8773.
100. A. Harriman, K. J. Elliott, M. A. H. Alamiry, L. L. Pleux, M. Séverac, Y. Pellegrin, E. Blart, C. Fosse, C. Cannizzo, C. R. Mayer and F. Odobel, *J. Phys. Chem. C*, 2009, **113**, 5834-5842.
101. F. Odobel, M. Severac, Y. Pellegrin, E. Blart, C. Fosse, C. Cannizzo, C. R. Mayer, K. J. Eliott and A. Harriman, *Chem. Eur. J.*, 2009, **15**, 3130-3138.

102. M. Boujtita, J. Boixel, E. Blart, C. R. Mayer and F. Odobelc, *Polyhedron*, 2008, **27**, 688-692.
103. J. M. Cameron, D. J. Wales and G. N. Newton, *Dalton Trans.*, 2018, **47**, 5120-5136.
104. B. Matt, C. Coudret, C. Viala, D. Jouvenot, F. Loiseau, G. Izzet and A. Proust, *Inorg. Chem.*, 2011, **50**, 7761-7768.
105. B. Matt, X. Xiang, A. L. Kaledin, N. Han, J. Moussa, H. Amouri, S. Alves, C. L. Hill, T. Lian, D. G. Musaev, G. Izzet and A. Proust, *Chem. Sci.*, 2013, **4**, 1737-1745.
106. B. Matt, J. Fize, J. Moussa, H. Amouri, A. Pereira, V. Artero, G. Izzet and A. Proust, *Energy Environ. Sci.*, 2013, **6**, 1504-1508.
107. D. Karimian, B. Yadollahi, M. Zendehdel and V. Mirkhani, *RSC Adv.*, 2015, **5**, 76875-76882.
108. D. Karimian, B. Yadollahi and V. Mirkhani, *Dalton Trans.*, 2015, **44**, 1709-1715.
109. L. Liu, L. Hu, Q. Liu, S.-Z. Liu, F.-B. Li, L. Li, L. Peng, D.-H. Yao, W.-Y. Wong and Z.-L. Du, *J. Organomet. Chem.*, 2015, **792**, 102-108.
110. L. Liu, L. Hu, Q. Liu, Z.-L. Du, F.-B. Li, G.-H. Li, X.-J. Zhu, W.-Y. Wong, L. Wang and H. Li, *Dalton Trans.*, 2015, **44**, 306-315.
111. S. X. Zhang, L. Liu, F. B. Li and Z. L. Du, *Inorg. Chim. Acta*, 2016, **453**, 179-185.
112. S. Zhao, X. Zhao, H. Zhang, J. Li and Y. F. Zhu, *Nano Energy*, 2017, **35**, 405-414.
113. S. Zhao, X. Zhao, S. Ouyang and Y. Zhu, *Catal. Sci. Technol.*, 2018, **8**, 1686-1695.
114. J. M. Cameron, S. Fujimoto, K. Kastner, R. J. Wei, D. Robinson, V. Sans, G. N. Newton and H. H. Oshio, *Chem. Eur. J.*, 2017, **23**, 47-50.
115. S. Fujimoto, J. M. Cameron, R.-J. Wei, K. Kastner, D. Robinson, V. Sans, G. N. Newton and H. Oshio, *Inorg. Chem.*, 2017, **56**, 12169-12177.

2. Combining POMs with cationic dyes for photocatalytic small molecule activation

2.1 Introduction

In Section 1.6, surveying the literature revealed that the use of organic-inorganic hybrid POMs for photochemical applications is a vibrant field due to the highly tuneable nature of the absorptive properties of photosensitiser molecules. Class 1 hybrids have remained extremely attractive in this regard, as the POM can be easily paired with photoactive cationic d- and f-block complexes which are easily modulated through the design of the organic ligand system.[1-3] Comparatively, there is a dearth of literature describing combinations of POMs with photosensitiser cations where the composition of the cation is entirely organic, despite the fact that these too can be easily tuned through functional group modulation on the photosensitising core.[4] POMs have been successfully paired with cations bearing polycyclic aromatic hydrocarbons (PACs), commercial cationic dyes, azo compounds and fused heterocycles to yield charge transfer complexes with wide absorption windows across the visible region.[5-7] Very recently, these species have been of interest as heterogeneous photocatalysts (either as a powder or film) for reactions such as hydrogen evolution and dye degradation.[8, 9] Thus, the exploration of hitherto unused photoactive organic cations with polyoxometalates could yield extremely interesting materials.

2,1,3-Benzothiadiazoles (BTDs) are a class of fused heterocyclic compounds comprising a benzene ring fused with a 1,2,5-thiadiazole ring. Early interest in this molecule was focused on their ability to increase disease resistance in plants and as an anti-viral agent,[10-13] and this sparked a desire to improve the synthetic protocol for substitution reactions at the core on the four benzyl positions (Figure 29).

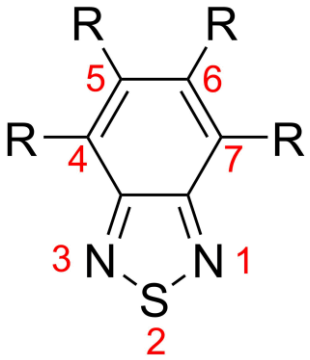
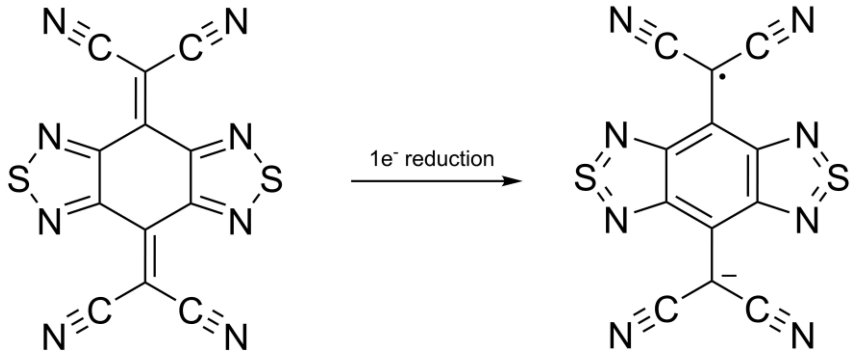


Figure 29. Structure of 2,1,3-Benzothiadiazole, illustrating the available sites for functionalisation.

Earlier syntheses relied on the substitution of the o-phenylenediamine, which is used as a precursor, but this only occurs at the 1 and 2 positions on the ring (5 and 6 positions on the BTD ring).[14, 15] Pilgram et al.[16, 17] developed methodologies for the controlled successive direct bromination (specifically at the 4 and 7 positions) and nitration of the benzene ring of BTD. The disubstituted 4,7-dibromo-2,1,3-benzothiadiazole described here is inarguably the most commonly employed synthon for the design of functionalised BTD derivatives. Indeed dibromo derivatives were used by both Ghosh[18] and Uno[19, 20] to synthesise a range of bisfurazano-BTD derivatives, but it was the synthesis of benzothiadiazole derivatives flanked by dicyanomethylene groups in the 4- and 7- positions that ignited interest in the BTD unit. These were first synthesised by Yamashita et al.[21] for the bis-2,1,3-thiadiazole and naphthothiadiazole units. The compound was intriguing due to its high planarity, symmetry and the ability of the thiadiazole ring(s) to stabilise the anion radical (Scheme 9) which can easily be prepared by reaction with alkali metal iodide salts. It was also found that when paired with planar aromatic electron donors, charge transfer complexes of high conductivity were produced. Crystallographic studies on the bis-2,1,3-thiadiazole revealed that the sulfur atom forms an extremely short contact with the nitrogen atom of the cyano side-groups (3.03Å), which causes the molecule to assemble in sheet-like networks.



Scheme 9. Structure of 4,7-dicyanomethylbis-2,1,3-benzothiadiazole demonstrating stabilisation of the radical anion through electronic rearrangement to form a new aromatic sextet upon reduction.

Suzuki et al.[22] demonstrated that radical anion salts of these molecules paired with simple alkylammonium salts formed salts with high temperature dependent electrical conductivity, here it was found that higher conductivities were exhibited by salts that formed 2-dimensional networks via the S-N contacts, as revealed by X-ray crystallography. Similar compounds bearing bis(1,3-dithiole) groups were also of interest due to their analogous structural motif (Figure 30a), these too exhibited high conductivities due to short S-S contacts between the dithiolane and thiadiazole rings forming sheet like networks (Figure 30b) and readily formed charge transfer complexes, however here the molecule acts as a donor.[23] These findings propagated a wealth of research in the structural and electronic

optimisation of benzothiadiazole dicyanomethylene and dithiolane derivatives for their electronic conductivities and use as acceptor and donor units respectively in charge transfer salts.[24-26] A particularly curious feature of these materials, taking advantage of their capacity to form various types of inclusion lattices in the crystal phase, is their molecular recognition between substituted aromatic hydrocarbons isomers, for example p-xylene and 2,6-dimethylnaphthalene, which could be separated from the isomer mixtures due to the sensitivity of the compounds towards lattice interactions.[27]

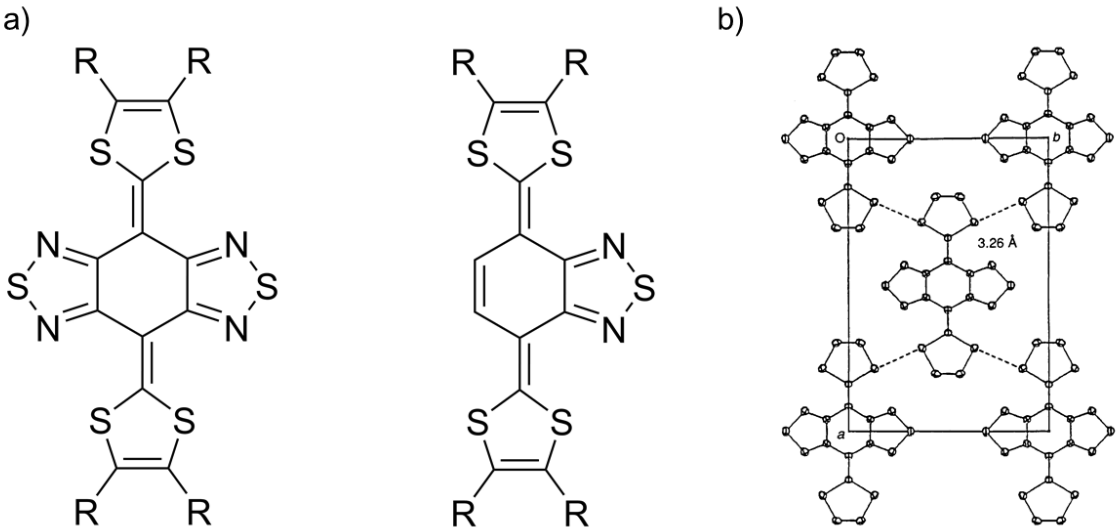


Figure 30. a) General structure of 4,7-dithiolenebis-2,1,3-benzothiadiazoles and 4,7-dithiolene-2,1,3-benzothiadiazoles. b) Crystallographic packing arrangement of 4,7-dithiolenebis-2,1,3-benzothiadiazole showing short S-N intramolecular contacts. Reproduced from [23] with permission from The Royal Society of Chemistry.

A more topical field related to the benzothiadiazole molecule is their use as monomers for the formation of various types of homo- and co-polymers which can exhibit extraordinary electronic and photonic properties. Kanbara et al.[28] first synthesised poly(2,13-benzothiadiazole-4,7-diyl) as a reddish brown powder through the dehalogenation polycondensation of 4,7-dibromo-2,1,3-benzothiadiazole with zero valence $Ni(cod)_2$ as a catalyst (Figure 31a). Electrochemical analysis agreed with previous molecular orbital calculations on related benzazole compounds, confirming that the molecular units act as electron acceptors. Karikomi et al.[29] shortly after designed narrow band gap polymers based on the polymerisation of benzo- or bisbenzothiadiazoles flanked by thiophene units in the 4- and 7 position (Figure 31b). The copolymerisation of donor and acceptor units in an alternating fashion is an effective strategy for the formation of small band gap polymers in which benzothiadiazole units act as the acceptor unit whereas thiophene is the electron donor. Crystallography of the monomer species revealed a highly planar structure mediated by strong intramolecular contact between the sulphur on the thiophene and the nitrogen of the thiadiazole moiety. Polymerisation was achieved directly from the

monomer solution by applying an oxidising potential which causes oxidation and subsequent coupling of thiophene units. Absorption spectroscopy revealed that the bisbenzo- polymer had an incredibly low band gap (<0.5 eV) likely due to the high electron affinity of the BTD units coupled with the rigid planar structure of the polymer which is reinforced through short intramolecular contacts. The benzo- derivative had a larger band gap of 1.1 eV due to the inclusion of only one thiadiazole unit per benzene ring but remained much easier to modulate through functionalisation on the 5- and 6- positions. However, it was the pioneering work of He et al.[30] in which a benzothiadiazole polymer was used for the first time in an OLED device. By combining benzothiadiazole units with 9,9-dicotylfluorene as an alternating copolymer, dubbed F8BT or PFBT (Figure 31c), an electroluminescent compound with strong green emission is generated. This compound can be fabricated into an OLED device when combined with a hole-transporting polymer (amine-fluorene) and sandwiched between a transparent indium-tin oxide (ITO) anode and a stable aluminium cathode. The device exhibited high brightness, good emission and luminous efficiency, a large external quantum efficiency and a reasonable forward-to-reverse bias current rectification ratio, giving an overall device efficiency that was unparalleled to any other polymer OLEDs reported at the time. From here, an explosion in the interest and use of benzothiadiazole based polymers ensued, with a clear paradigm shift towards device-based research. In addition to fundamental polymer design[31-36] and new polymerisation approaches[37-39], BTD based polymers were now of interest in fields such as organic light emitting diode (OLED) devices[40-43], plastic solar cells[44-48], field-effect transistors (FETs)[49-52], small molecule sensors[53-56], biosensors[57-62] and photodetectors.[63]

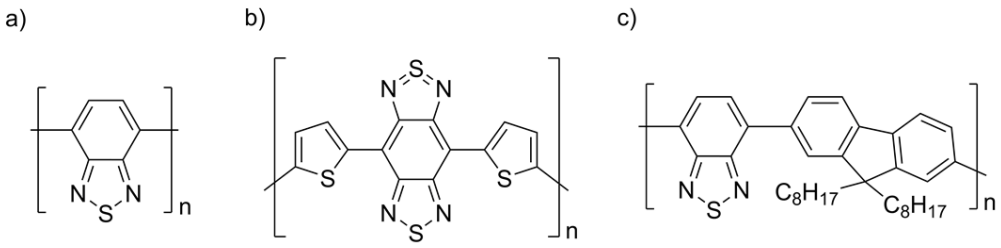


Figure 31. Repeating unit of BTD based polymers; a) poly(benzimidazole-4,7-diyl). b) poly(4,7dithienyl(3-diyl)-2,1,3-benzothiadiazole. c) F8BT – poly(9,9-dioctylfluorene-alt-benzo[2,1,3]thiadiazole)

Parallel to this, interest in BTD-based molecular analogues was also burgeoning, due to the unique advantages offered by molecular species. Photoactive materials formed from small molecule or oligomeric species pose several advantages such as solution processability, flexibility, defined molecular structure, intrinsic monodispersity, high purity, negligible batch-to-batch variations, and reproducible performance compared to polymer analogues.[64] As such, these BTD-containing molecular

compounds have been equally prominent in solar cell[65-68], OLED[69-71] and FET[72-74] devices. The move from material to molecular also opened up a new avenue of photonic research on BTD compounds. Raimudo et al.[75] first recognised that the flanking of benzothiadiazole units in the 4- and 7 positions by aryl or thiophene species gave fluorescent compounds with moderate fluorescence quantum yields (Φ_f = 0.73-0.8). Akhtaruzzaman et al.[76] also investigated several permutations on BTD functionalised in the 4- and 7- positions by pyridine groups, including the effect of an ethylene spacer, functionalisation position on the pyridine ring, the number of BTD cores, and quaternisation of the pyridine groups. It appeared that the former two factors had no impact on the high fluorescent quantum yield of the compounds (Φ_f = 0.68-0.9) whereas the latter two factors significantly decreased the fluorescent quantum yield (Φ_f = 0.08-0.26), see Figure 32a. The crystal structure revealed that the ionic species tended to form dimers in the solid-state (Figure 32b) whereas the neutral compounds showed only weak π-stacking interactions (Figure 32c), possibly explaining the weaker fluorescence exhibited in the ionic species. Zhang et al.[77] also demonstrated the tuneability of these systems by employing different combinations of phenyl, thienyl and alkenyl groups with BTD to form linear penta-aromatic arrays which exhibit fluorescence ranging from green to magenta. When dispersed in MLC-2039, the compounds exhibited dichroic ratio values up to 12.3, giving them potential applications in liquid crystal display technologies.

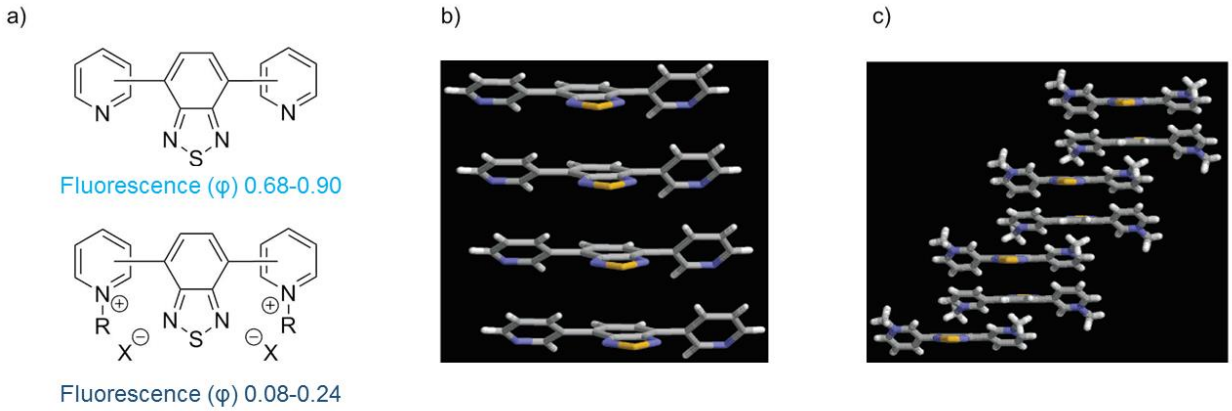
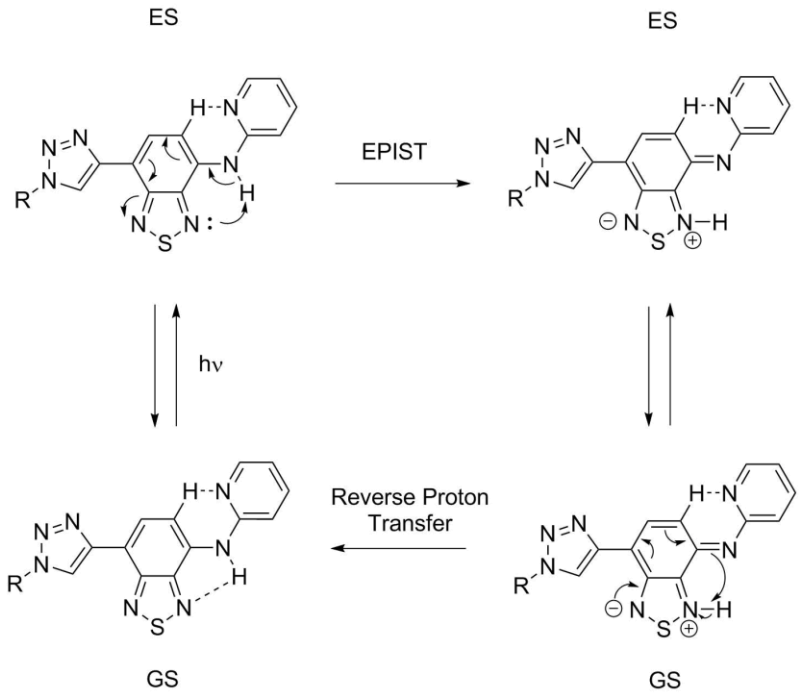


Figure 32. a) Structure of 4,7-pyridine/pyridinium-2,1,3-benzothiadiazoles with fluorescent yield ranges. b) Crystal structure of 4,7-(3-pyridine)-2,1,3-benzothiadiazole showing weak intramolecular interactions. c) Crystal structure of 4,7-(N-methyl-3-pyridinium)-2,1,3-benzothiadiazole showing anion assisted dimer formation. Crystal Structures reproduced from [76] with permission from the American Chemical Society

Several groups have aided in the theoretical prediction and design molecular BTD fluorophores with combined computational and experimental approaches. Li et al.[78] identified that in D-A and D-A-D configurations (A is BTD) the HOMO is delocalised over both the donor and acceptor unit(s) but the

LUMO is located only on the acceptor, consistent with intramolecular charge transfer occurring upon excitation. Furthermore, comparing models of the ground state with the excited state, the molecules in the ground state are generally more twisted (larger dihedral angle between D and A) whilst still retaining strong π-conjugation over the entire molecule. The molecules which have larger geometric differences between the ground and excited state had larger stokes shifts due to the longer relaxation times, all the above ratified the experimental work performed within the same study. Da Cruz et al.[79] also highlighted through combined theoretical and experimental studies that the fluorescence efficiencies of molecules may be reinforced through other short range contacts and processes such as excited-state intramolecular proton transfer (EPIST), where the N on the thiadiazole moiety is capable of accepting a proton in the excited state (Scheme 10). Through a proximal proton donor (secondary amine) at an optimised orientation, stabilisation of the excited state may be achieved.



Scheme 10. Proposed role of the EPIST mechanism for stabilisation of the excited state – photoexcitation is followed by proton transfer between proximal nitrogen atoms with resonance stabilisation, upon relaxation reverse proton transfer occurs to regenerate the original configuration.

Not only are the fluorescence properties of benzothiadiazole derivatives dependent on their structure, but also on their chemical environment. Perhaps the most obvious example of this is the solvent dependence on the lifetime and emission of π-extended BTD structures, or indeed any fluorophores, which has been noted extensively throughout the literature.[78, 80, 81] The sensitivity of fluorescence towards the molecular environment can be harnessed however for the selective detection of species in solution. As has been demonstrated for polymeric materials, monomer BTD analogues can too be used

as fluorescent sensors for small ions if appended to a suitable coordinating group such as cyclodextrin[82], amino acids[83], dimesitylboranes[84] and dicyanovinyls groups[85], or even directly as a ligand through the thiadiazole functionality.[86]

Perhaps more impressively, fluorescent BTD based molecules have shown excellent compatibility with biological systems for sensing, imaging and selective staining. Neto et al.[87] first designed an asymmetric benzothiadiazole fluorophore bearing an electron donating 4-methoxyphenyl moiety to induce a charge transfer state and an aryl acetylene group to encourage the binding with DNA (Figure 33). Upon binding to DNA, the fluorophore exhibited a blue shifting and exponential decay of the fluorescence which was concentration sensitive. Ab initio modelling revealed that the ethynyl phenyl group preferentially binds to the DNA which means the distal 4-methoxyphenyl derivative is unperturbed and can perform intramolecular charge transfer. This model was later verified with docking and molecular dynamics simulations.[88] The compounds developed were found to be highly selective towards DNA over phosphorylase enzymes, could detect DNA down to ~1 ppm and be utilised in Realtime PCR. The same molecules were also found to be effective mitochondrial stains for live cell imaging proves due to their long-lived and stable excited states.[89]

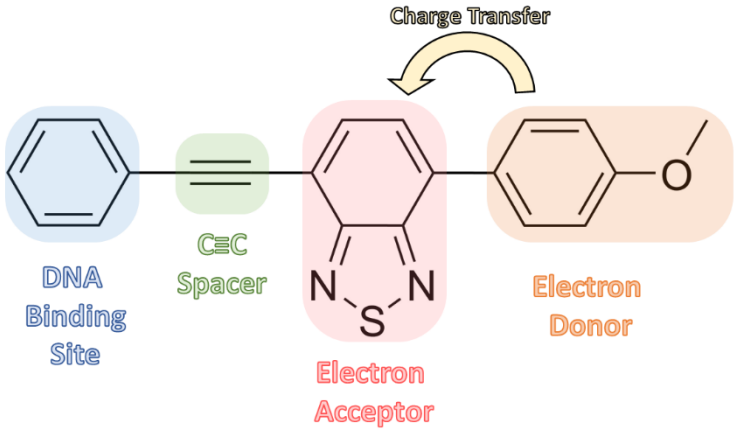


Figure 33. Structure of 4-(phenylacetylenyl)-7(p-anisole)-2,1,3-benzothiadiazole showing the role of each component for the fluorescent imaging of DNA.

In addition to this asymmetric architecture, other bespoke BTD based fluorescent imaging probes have been developed. For example, hypoxic tumour cell imaging by nitro derivatives[90], low temperature imaging probes with lipophilic BTD derivatives bearing a long alkyl chain[91], highly pH stable probes employing BTDs with ESIPT sites[92, 93] and polycyclic aromatic functionalised BTD as long-term cancer cell probes.[94] A recent approach in this field is the work from Neto, Dupont and coworkers[95] in the development of BTD ionic liquids as live cell imaging probes, these compounds (Figure 34a) feature novel imidazole flanking groups on the BTD core which were then protonated or quaternised with

methylene or acetic acid residues giving fluorescent IL materials. These ionic species were able to traverse the cell membrane and the acetic acid derivative showed high lysosomal preference with emissive behaviour in both blue and green channels (Figure 34b).

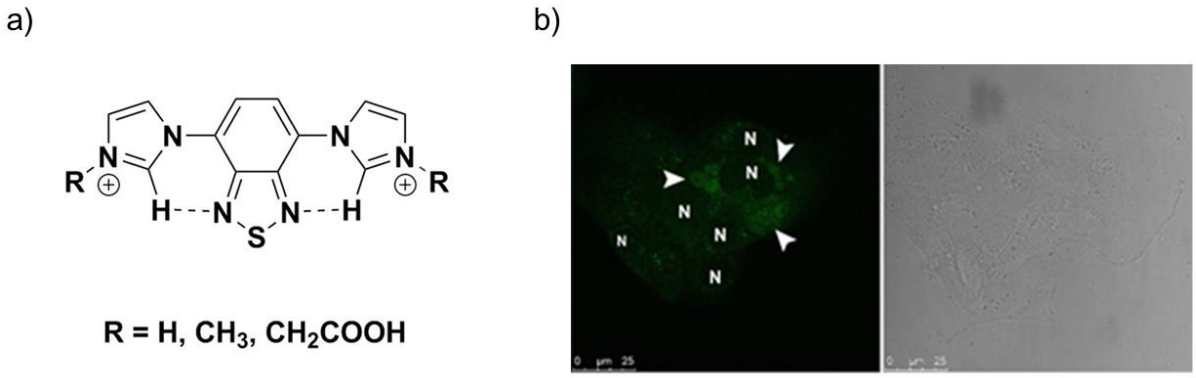


Figure 34. a) General structure of 4,7-(3-imidazol-1-ium)-2,1,3-benzothiadiazole. b) Selective cell staining preferences for lysosomal sites near the nuclei sites (N). Reproduced with permission form the corresponding author.[95]

From the above, it is clear than benzothiadiazole-containing structures are versatile platforms for a vast array of photonic applications. Given the intriguing properties of Class I hybrid polyoxometalate materials formed by ion pairing with photoactive cations, it is surprising that these two components have not yet been combined to form photo- and electroactive materials. One highly impactful field in which polyoxometalate chemistry is flourishing is in the photocatalytic transformation of small molecules for the production of solar fuels (i.e. the valorisation of H_2O and CO_2). This concept has previously been explored for polyoxometalates, especially with regards to the aforementioned photoactivation of water mediated by hydrogen bonding to the polyoxometalate (Section 1.5). POM based water-oxidation is a flourishing field due to the ability to form a pre-association complex coupled with their ability to act as proton and electron reservoirs, extremely high activities can be attained when other catalytically active metals are incorporated in the structure, acting as catalytic sites.[96] Carbon dioxide reduction remains a much more challenging area of work, with POM-CO_2 interactions exclusively occurring at non-addenda transition metal atoms that have been substituted into the framework.[97] To our knowledge, the ability of Class I type hybrids to achieve the latter transformation has not yet been explored, despite the ability of certain functional groups, such as the imidazolium fragment, to act as organocatalysts for carbon dioxide, and hence this combination may provide synergic advantages for the coordination and photoreduction of CO_2.This chapter will therefore explore the combination of photoactive π-extended benzothiadiazole cations featuring imidazolium fragments with electron rich Wells-Dawson

polyoxotungstate anions and their potential application as heterogeneous photocatalysts for small molecule transformations.

2.2 Aims

The aim of this project was to synthesise novel Class I hybrids formed from the Wells-Dawson phosphotungstate anion and three benzothiadiazole cations (Figure 35). The cations showed distinct functionalities (H, Me, Ac) yielding different protic and aprotic environments which could be used to tune the redox behaviour of the polyoxometalate and lead to the formation of different architectures in the solid-state. Furthermore, the π-extended BTD framework with absorbance in the visible range of the electromagnetic spectrum serves to increase the absorption profile of the materials and hence makes the resultant hybrids of interest in photocatalytic applications.

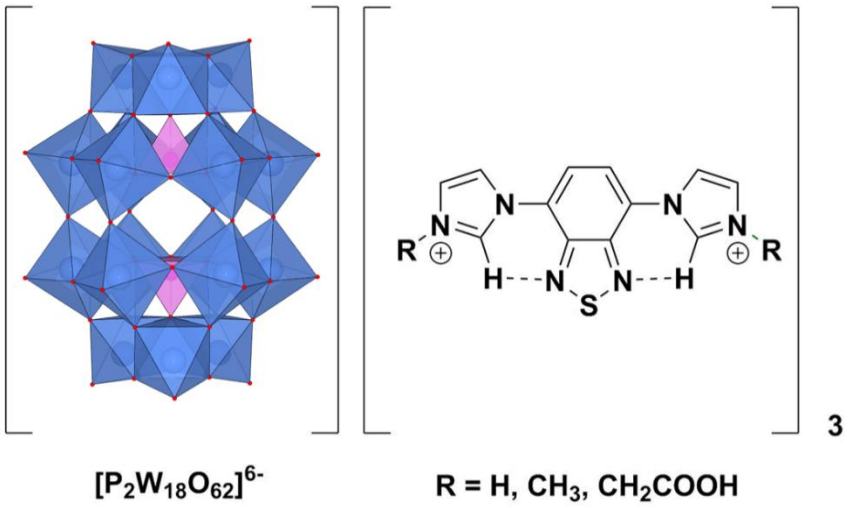


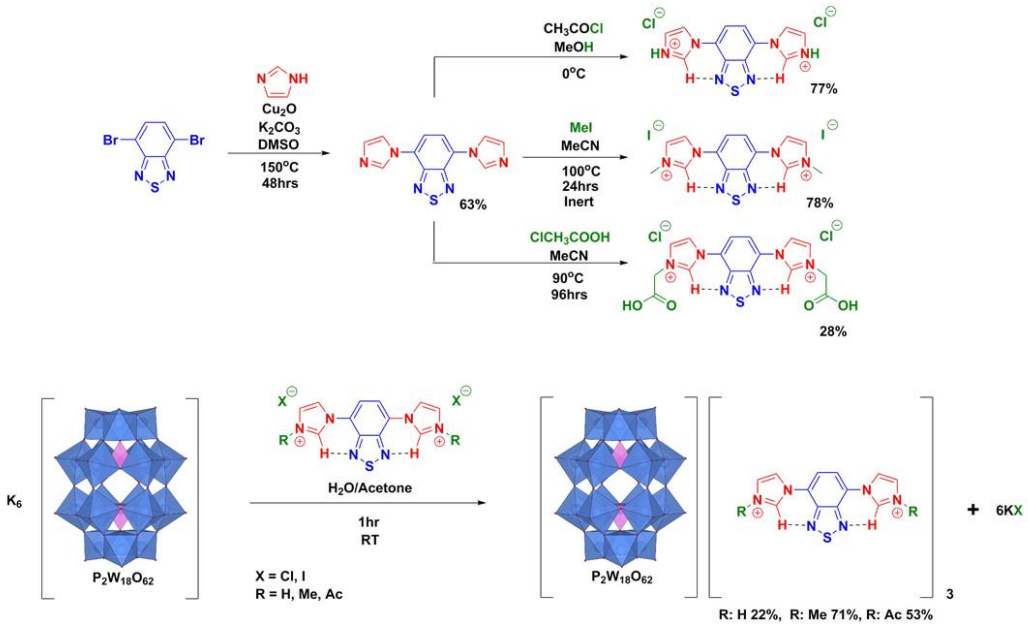
Figure 35. Structure of the polyoxometalate anion and BTDIm based cations to be used in this study.

The target materials will be synthesised and structurally characterised with specific focus on the pairing nature of the ionic components. The electronic nature of the hybrids will be assessed and compared to their precursor salts to assess whether any synergic electronic coupling between the two components is occurring and to determine the extent of redox tuning that the different functionalities on the cations evoke. Lastly, the lead materials will be assessed for their photocatalytic performance for small molecule activation reactions.

2.3. Results and discussion

2.3.1 Synthetic development

The synthetic pathway for obtaining the target hybrid species is shown in Scheme 11. First, it was necessary to prepare the separate anionic and cationic components as their simple alkali metal and halide salts. The former, $K_6[P_2W_{18}O_{62}]$ (hereon referred to as $[W_{18}]$), was formed in high yields in a simple one step procedure according to the literature report.[98] The latter, $[BTDImH]Cl_2$, $[BTDImMe]I_2$ and $[BTDImAc]Cl_2$, were prepared in a divergent two step synthesis, starting with the coupling of the imidazolium rings to the benzothiadiazole core via an Ullmann-type copper catalysed cross-coupling reaction to form the extended aromatic dye scaffold.[99] The imidazole basic nitrogen atoms were then either protonated or alkylated via treatment with HCl, methyl iodide or chloroacetic acid to give the above compounds respectively. The coupling step proceeded in good yields (63%) and pure compound could be obtained by either column chromatography or recrystallisations from either EtOH or DCM. For the N-quaternisation step, the methylation reaction proceeded in high yield (78%), methyl iodide is a highly active methylating agent as iodide is an excellent leaving group and the reagent is sterically unhindered towards nucleophilic attack. The S_N2 reaction with chloroacetic acid proceeded with a much lower yield (28%), potentially due to the interference of acid-base interactions with the mechanism and the poorer chloride leaving group.



Scheme 11. Synthesis pathway for the formation of the target hybrid materials.

The N-protonation was synthetically more challenging. Following the guidance of Souza *et al*.[95] the reaction was to be performed by bubbling dry HCl gas into a methanolic solution of BTDIm which causes precipitation of the product. Aqueous HCl cannot be used to protonate BTDIm as it is not soluble in aqueous environments. Given the obvious safety implications of using a high pressure dry HCl gas cylinder, it was instead decided to generate the HCl gas via the addition of conc. HCl to conc. H_2SO_4. This commonly used method takes advantage of the higher affinity of conc. H_2SO_4 (98%) for water than conc. HCl (30%), upon addition of HCl to H_2SO_4, a dehydration reaction takes place which causes the liberation of HCl gas. This method, whilst somewhat successful (34% yield), suffered from the drawback that without specialised piping and connectors between the gas generator and reaction vessels, the generated gas was able to leak from the system which decreased the positive pressure and allowed the highly corrosive reagent to escape from the system. To circumvent these issues, a new method was devised to generate HCl directly within the reaction flask containing BTDIm, involving the dropwise addition of acetyl chloride to the methanolic solution of BTDIm. The system works through the near-immediate esterification reaction between acetyl chloride with methanol, which generates stoichiometric quantities of methyl acetate and HCl. This method precluded the use of hazardous gaseous HCl gas and allowed the yield to increase to 77%.

The final step was then to combine [W_{18}] with the cationic BTD species to form the desired products. The ion exchange reaction was performed through the simple addition of the two reagents together at room temperature in a 1:3 ratio (based on charge balancing) in water. In each case, the combination of the two reagents resulted in the immediate precipitation of the products as yellow or orange powders. The products were obtained in high purity as the starting materials and potassium halide side-product remained in the aqueous phase and could be removed from the product by washing with copious water. Interestingly, the yields of the reaction varied between the three cations, likely due to their different acidity within the aqueous solvent. Through the course of analysing the products, it was found that the three species exhibited extremely poor solubilities in water, non-polar solvents (hydrocarbons, diethyl ether, chlorinated solvents), polar protic solvents (methanol, ethanol, isopropanol) and the majority of polar aprotic solvents (ethyl acetate, acetone, acetonitrile). In fact, the compounds only exhibited modest solubility in DMSO, N-methylpyrrolidone and DMF. In each case the integrity of the ionic components were verified via ^{1}H and ^{31}P NMR spectroscopies and purity analysed by CHN elemental analysis.

2.3.2 Structural characterisation

Given the non-covalent interaction between the polyoxometalate anion and the BTD cations, and the lack of any comparable nuclei that the two components share, NMR spectroscopy could only be used as a tool to verify that the ion exchange had not caused any structural changes amongst the two species. The ^{31}P NMR in DMSO-d_6 shows a single peak between -13.5 and -13.6 which is diagnostic for the Dawson polyoxotungstate anion, confirming its integrity. The ^{1}H NMR for the hybrids displays several peaks corresponding to the various aromatic environments on the core of the molecule and different environments associated with the R-groups, whose peaks have shifted upfield compared to the cationic starting material (Figure 36).

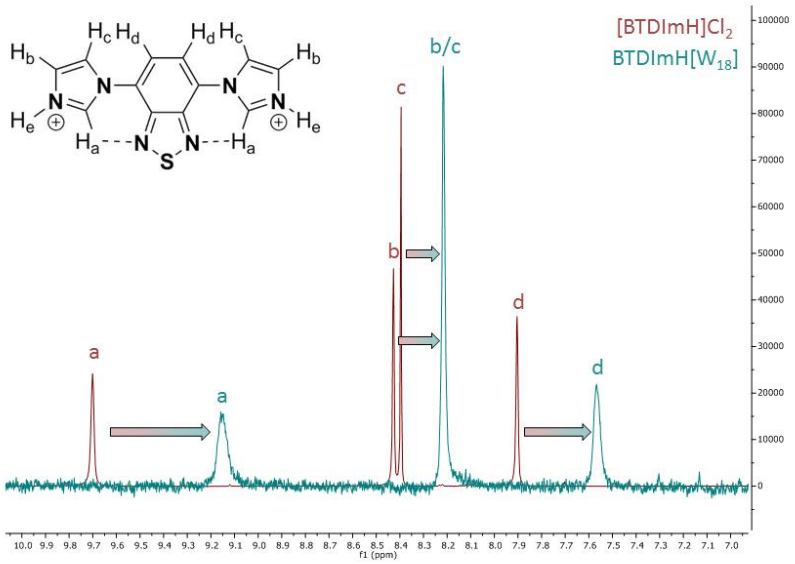


Figure 36. ^{1}H NMR spectrum of [BTDImH]Cl_2 (maroon) compared with BTDImH]W_{18} (teal) showing the relative peak shifts of the aromatic signals associated with the cation.

To accurately confirm the ratio of the ions and the purity of the sample, CHN microanalysis was employed to calculate the proportion of the organic component. The results (Table 1) show that for each compound, the measured weight % of C and H are generally close to the predicted formula, however for N they are consistently lower than expected, although, only by a maximum deviation of ~1% demonstrating that the cation generally pairs in a 3:1 fashion with the POM. Attempts to rationalise the observed %C, H and N through the addition of potassium halides, [W_{18}] and water to the structural formula did not give good agreement with the obtained values, neither did partial exchange of K^+ in the formula for organic cations, as in the case of a mixed salt or non-stoichiometric compound. Furthermore, given that no fragmentation of the cation is seen and no non-product (solvents, grease, starting

materials etc.) based peaks are present in the 1H NMR experiments, and that this problem occurs with all three samples, it can be surmised that this is likely due to a measurement based error. Nonetheless, despite these small discrepancies, the elemental analysis is highly suggestive of full cation exchange.

	BTDImH[W_{18}]			BTDImMe[W_{18}]			BTDImAc[W_{18}]		
	%C	%H	%N	%C	%H	%N	%C	%H	%N
Predicted	8.357	0.584	4.873	9.594	0.805	4.795	10.44	0.767	4.566
Observed	8.01	0.77	4.29	9.38	0.60	4.18	9.17	0.50	3.61
	7.92	0.57	4.17	9.24	0.60	4.23	9.32	0.46	3.70

Table 1. Results obtained for CHN elemental analysis compared to the predicted values based on the empirical formulae (green – within 0.3% experimental error, lime – within 0.4% experimental error, red exceeds 0.4% experimental error).

Infra-red (IR) spectroscopy was also employed to ascertain the structural integrity of the two components through the observation of peaks that are characteristic to the two species. Furthermore, IR spectroscopy can also yield information about the local environment around the bonds of interest, which may give information on the nature of association between the two ions. Firstly, the hybrid materials can be compared to their starting materials, as exemplified in Figure 37 for BTDImH[W_{18}]. For each of the hybrid species, features that pertain to the anionic polyoxometalate and the organic dye cation are present. Particularly prominent are the C-H stretching modes at >3000 cm^{-1} (cation), C=C stretch at ~1540 cm^{-1} and C=N stretch at ~1370 cm^{-1} (cation) and P-O, W=O_d and W-O_b-W vibrational modes at ~1085 cm^{-1}, ~955 cm^{-1} and ~730 cm^{-1} respectively (anion). Curiously, when the hybrid species are compared to their precursors, there is a consistent blue shifting of the characteristic peaks. This effect is most pronounced for the C-H stretching and W-O_b-W bending modes (see Figure 38a and 38b). It has previously been demonstrated that the shift of C-H stretching modes of imidazolium species correlates directly with the magnitude of hydrogen bonding between the donor cation and the acceptor anion.[100, 101] The observed blue shift could be therefore a direct result of the weaker hydrogen bonding exhibited between the cation and the polyoxometalate vs. the halide anions as the POM is a much weaker hydrogen bonding acceptor. However, it is prudent to note that this is only reliable when the samples are of comparable morphologies with similar refractive indices, as the observed wavelength given by ATR techniques is dependent on the penetration depth of the evanescent wave which is related to the materials refractive index.[102] This blue-shift could also be a direct result of the materials inherent

physical properties, which is supported by the non-specific blue shifting of all of the different C-H stretching modes.

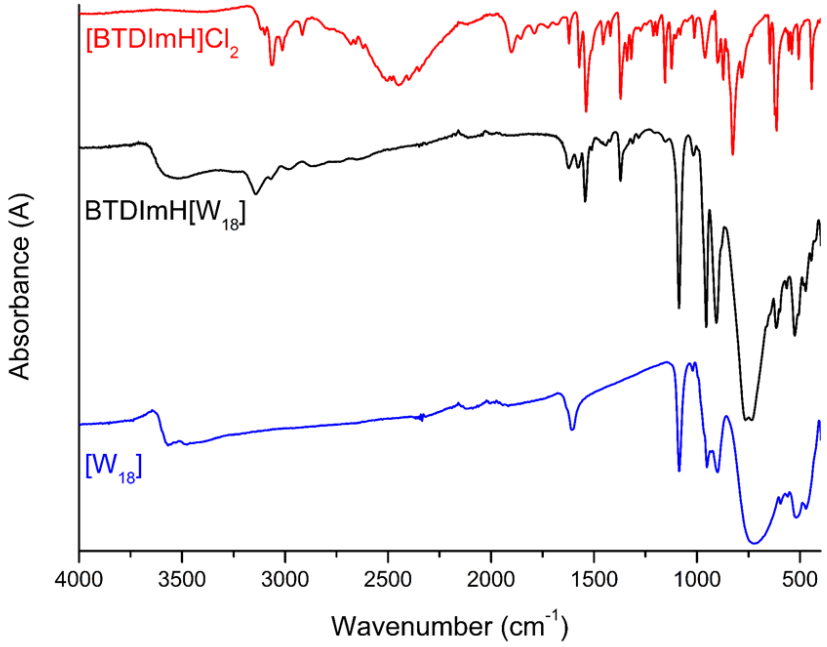
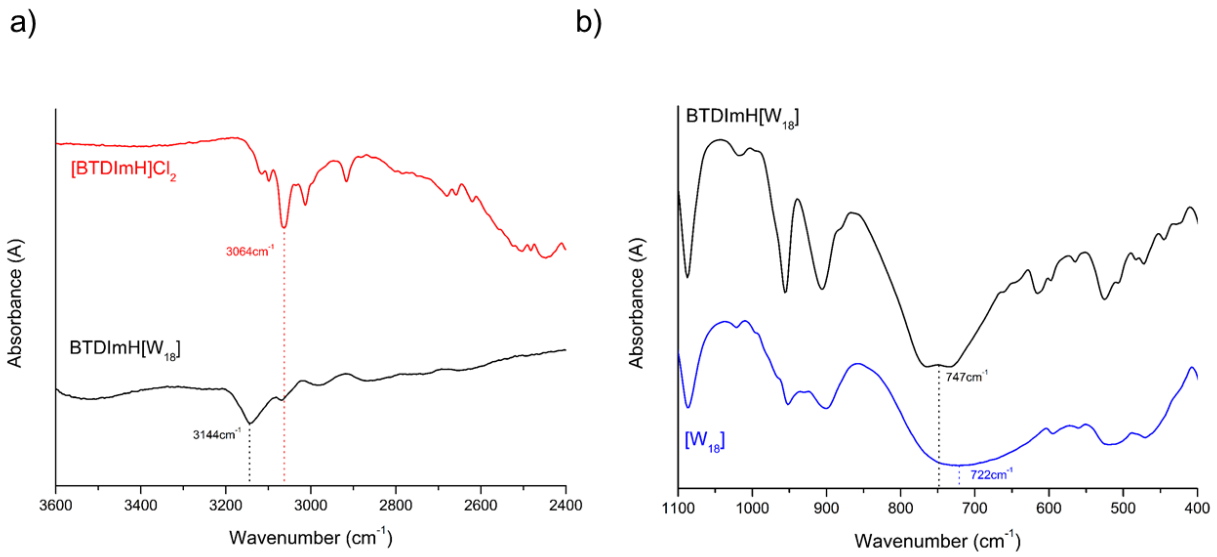


Figure 37. IR spectrum comparing BTDImH[W_{18}] (black) to its precursor salts; [W_{18}] (blue) and [BTDImH]Cl_2



(red).

Figure 38. a) Comparison of the C-H stretching modes between BTDImH[W_{18}] and [BTDImH]Cl_2. b) Comparison of the W-O-W bending modes between BTDImH[W_{18}] and [W_{18}].

A better comparison is given between the three hybrid materials. Immediately it can be seen that the difference in the R-group on the imidazolium moieties gives rise to distinctive spectral features for each hybrid (Figure 39). Whilst many of these reside in the fingerprint region and are heavily obscured by features pertaining to the POM, there are some features that can be easily assigned. For example

BTDImMe[W_{18}] shows a weak peak at 1243 cm^{-1} that corresponds to the C-H methylene bend, whereas BTDImAc[W_{18}] shows several peaks including a broad peak at 3363 cm^{-1} for the carboxylic O-H stretch, a sharp peak at 1732 cm^{-1} for he carboxylic C=O stretch and a medium peak at 1239 cm^{-1} corresponding to the C-O stretch. These peaks are absent in BTDImH[W_{18}], suggesting that they arise from the R-groups specifically, and confirming that the three hybrids contain different structural residues.

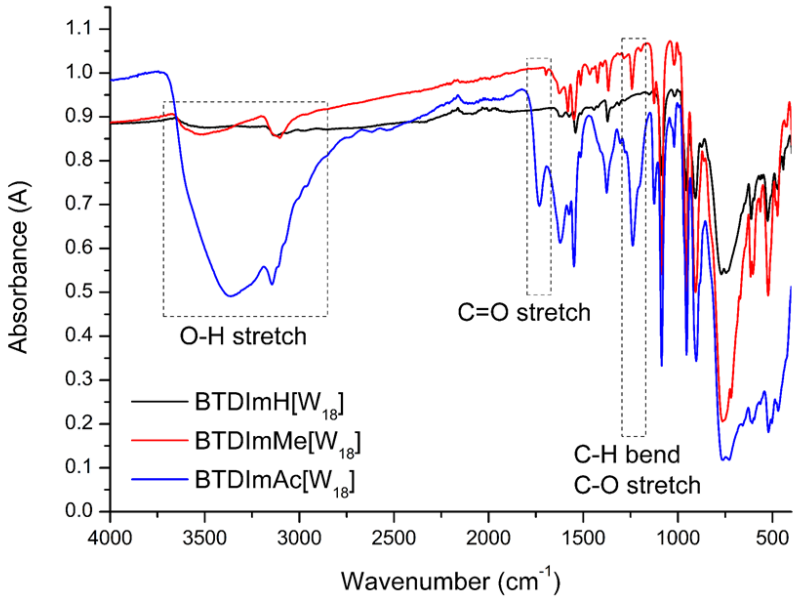


Figure 39. IR spectrum comparing the three hybrid materials displaying characteristic vibrational modes that correlate to the R-groups of the imidazolium ring.

Fortunately, single crystals of BTDImH[W_{18}] could be obtained through the layering of $K_6P_2W_{18}O_{62}$ in DMF with [BTDImH]Cl_2 in methanol. The yellow needle crystals were suitable for single crystal X-ray diffraction and revealed that BTDImH[W_{18}] crystallises in a triclinic crystal system corresponding to the P-1 space group. Collection and refinement details, bond length, bond angle and hydrogen bonding tables can be found in the methods and appendix sections respectively. The asymmetric unit of the structure is composed of one complete Dawson-type polyoxometalate $[P_2W_{18}O_{62}]^{6-}$, three $[BTDImH]^{2+}$ cations and three DMF solvent molecules that have been assigned. The residual electron density that could not be sensibly modelled was calculated as 8 DMF molecules per asymmetric unit with PLATON SQUEEZE. Whilst the three cations are in non-identical positions, two of the cations lie closer to the belt regions of the POMs and lie sandwiched between two POMs (BTD2, BTD3) whereas the other cation is situated closer to the cap region (BTD1) (Figure 40). No π-π stacking is observed between the cations, likely due to cationic repulsion, however several hydrogen bonding contacts are formed between the BTDImH cation and both the solvent molecules and the POM. Surveying the list of

crystallographically recognised hydrogen bonds (see Section 6.1), it is possible to identify several short contacts with near linear bonding angles (Table 2). The shortest hydrogen bonds are formed from the acidic imidazolium protons of BTD1 and amidic oxygen of the solvent (N12-O11S, N17-O6S). The same BTD1 residue also makes a near linear hydrogen bonding contact with the POM from the acidic "C-2" position of the imidazolium species to the terminal oxo group at a cap-based tungsten centre. BTD2 also makes several hydrogen bonding contacts between imidazolium based C-H groups with the same DMF and POM based acceptor atoms (C38-O1S, C39-O10, C39-O46) albeit with less linear contacts. BTD3 only makes one strong hydrogen bonding contact with the POM (C59-O14). It is prudent to mention that although many more hydrogen bonds are reported in the Appendix, those that are longer and less linear are more likely to be crystallographically imposed. The three dye cations also differ from one another with respect to the ring torsion of the imidazolium fragments with respect to the BTD core. BTD1 features the most twisted ring, whereby the imidazolium with the two strongest contacts has the largest torsion angle of 37.3° (C3-C4-N10-C11). The second ring which only makes one strong hydrogen bonding contact through the acidic imidazolium proton shows less twisting with an angle of 28.4° (C8-C7-N16-C16). BTD2 has slightly less torsion in its imidazolium rings, with the ring featuring more optimal external hydrogen bonding contact lengths and angles having greater torsion angles (35.2°, C28-C27-N35-C36) versus the other ring (28.0°, C23-C24-N30-C31). Finally, BTD3 with the weakest contacts has the lowest torsion angles (25.7°, C48-C47-N55-C56, 19.8°, C43-C44-N50-C51). This demonstrates that the degree of torsion correlates strongly with the extent of external hydrogen bonding with solvent and POM molecules. Indeed, Souza et al.[95] demonstrated that when [BTDImMe]I_2 is crystallised in the absence of strong hydrogen bond acceptors, the cation adopts an almost completely planar structure that is reinforced through internal hydrogen bonding of the "C(2)-H" donor on the imidazolium with the N acceptor atom within the thiadiazole ring (Figure 41). It can therefore be summarised that both the polyoxometalate and the solvent molecules are capable of interacting with, and altering the structure of, the associated cationic dyes, which may affect their intrinsic properties.

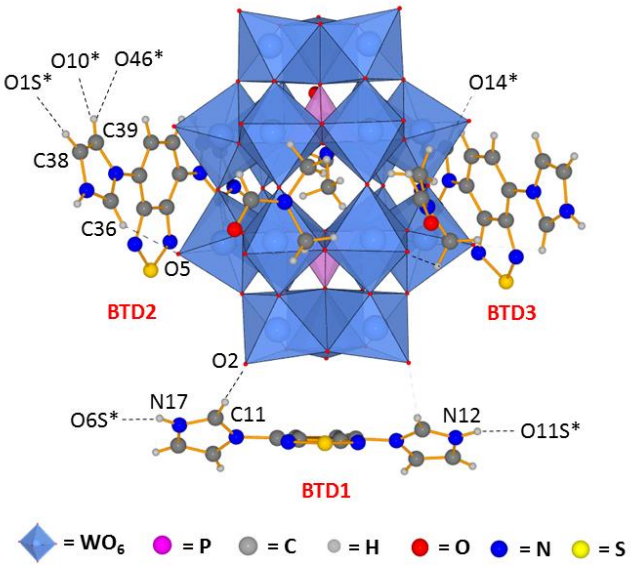


Figure 40. Asymmetric unit of BTDImH[W_{18}], showing that the BTDImH cations reside in three distinct environments based on their hydrogen bonding contacts with the POM and solvent molecules and display different extents of imidazolium-benzothiadiazole ring torsions. Dashed lines indicate hydrogen bonding interaction with those to atom labels only showing hydrogen bonds between molecules in different asymmetric units.

D	H	A	d(D-H)/Å	d(H-A)/Å	d(D-A)/Å	D-H-A/°
N(12)	H(12)	O(11S)	0.88	1.66	2.54(5)	176.7
N(17)	H(17)	O(6S)	0.88	1.81	2.67(6)	165.3
C(11)	H(11)	O(2)	0.95	2.11	3.06(4)	176.6
C(36)	H(36)	O(5)	0.95	2.33	3.11(4)	138.3
C(38)	H(38)	O(1S)	0.95	1.88	2.77(4)	156.7
C(39)	H(39)	O(10)	0.95	2.23	3.11(4)	153.9
C(39)	H(39)	O(46)	0.95	2.45	3.18(3)	134.4
C(59)	H(59)	O(14)	0.95	2.24	3.16(3)	163.5
C(2S)	H(2S)	O(15)	0.95	2.37	3.15(5)	139.2
C(9S)	H(9SA)	O(7)	0.98	2.30	3.11(6)	139.4

Table 2. Selected hydrogen bonding interactions between donor (D) and acceptor (A) atoms within the structure (only D-A < 3.2 Å and D-H-A > 130°). d(D-H) are the donor hydrogen bond lengths, d(H-A) are the acceptor to hydrogen atom distances, d(D-A) are the donor to acceptor distances and D-H-A are the hydrogen bonding angles.

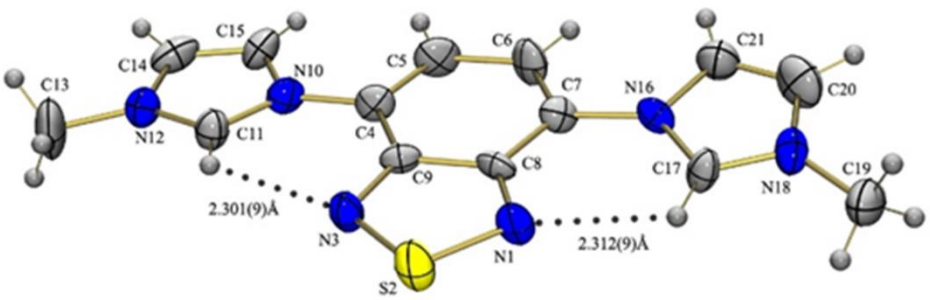


Figure 41. Crystal structure of [BTDImMe]I_2 showing the intramolecular hydrogen bonding interactions of the cation that reinforces planarity within the structure. Reproduced with permission from the corresponding author.[95]

2.3.3 Thermophysical characterisation

The materials were further characterised through thermophysical techniques to gain insight into both their stability and phase behaviour. Thermogravimetric analysis (TGA) is a commonly employed technique that can find the thermal limit of a sample, verify the ratio between components with different decomposition temperatures and assess its relative hygroscopicity. The samples were heated at 10°C per minute from 25°C to 1000°C under an inert atmosphere. The TGA curves for the three hybrid compounds are presented in Figures 42-44. Initially, for each species, there is a small weigh loss event (1-4%) occurring below 60°C which corresponds to the loss of adsorbed water. Beyond this, for BTDImH[W_{18}] and BTDImMe[W_{18}], the materials undergo no weight loss events until the onset of degradation occurring at 402°C and 422°C respectively. For BTDImH[W_{18}], the derivative of the weight loss curve reveals two merged weight loss events centred at 423°C and 600°C (with an instrumental blip at 518°C) which correspond to a 10.5% weight loss, followed by a second sharp weight loss event at 843°C with a 17.9% weight loss which leaves a final residue of 66.8%. The first weight loss event most likely corresponds to the partial decomposition of the cation (full decomposition would correspond to 15.7%), whereas the second event at high temperatures corresponds to the total decomposition of the organic components and structural collapse of the Dawson anion, which may be cooperative as BTD based components have been shown to decompose at high temperatures and the POMs decomposition appears to be highly dependent on the cation and influences the decomposition pathway and the molecular fate of the templating atoms.[103] BTDImMe[W_{18}] shows a similar complex weight loss profile with several discrete events that are elucidated from the derivative curve with events at 447°C, 513°C and 621°C. The peaks when combined show a total weight loss of 17.67% which matches well with the calculated weight loss for the three cations (17.0%), this leaves a final residue of 80.3%. Finally, BTDImAc[W_{18}] shows a contrasting thermal profile to the other hybrids, its thermal stability is limited by an event at 288°C which exactly matches the predicted weight loss from decarboxylation of the two acid groups (4.9%), this then continues into a decomposition event with maximal rate of loss at 548°C and 598°C which corresponds to the complete decomposition of the cation and structural collapse of the Dawson cage, leaving a final residue of 73.0%. The observation that BTDImH[W_{18}] and BTDImAc[W_{18}] exhibit decomposition events associated with the POM as well as the cation, whereas BTDImMe[W18] shows only decomposition of the cation within the temperature limits of the

experiments, demonstrates that the presence of acidic sites may aid in the thermal decomposition of the POM structure.

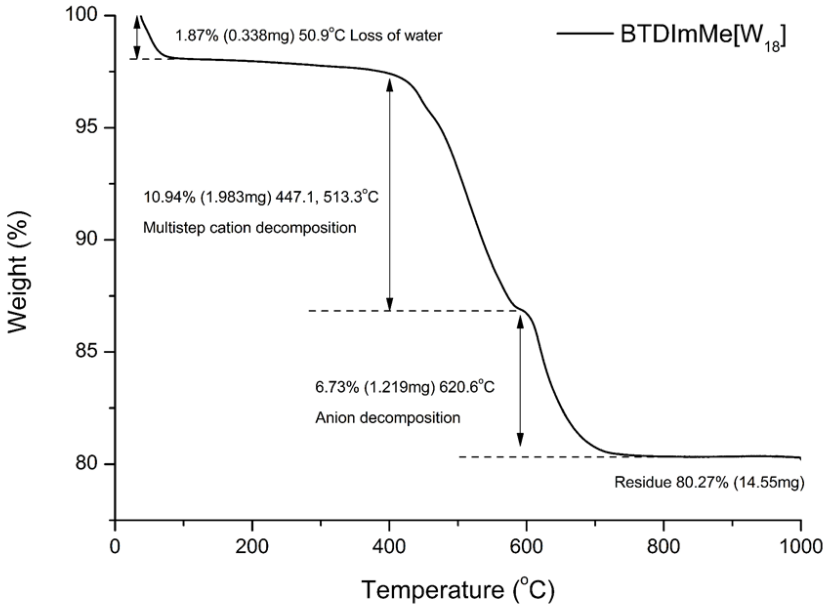


Figure 42. TGA curve for BTDImH[W_{18}] showing initial loss of adsorbed water (3.61%, 39.6°C) followed by multistep cation decomposition (10.52%, 422.9 and 600°C) and anion decomposition (17.93%, 843.3°C).

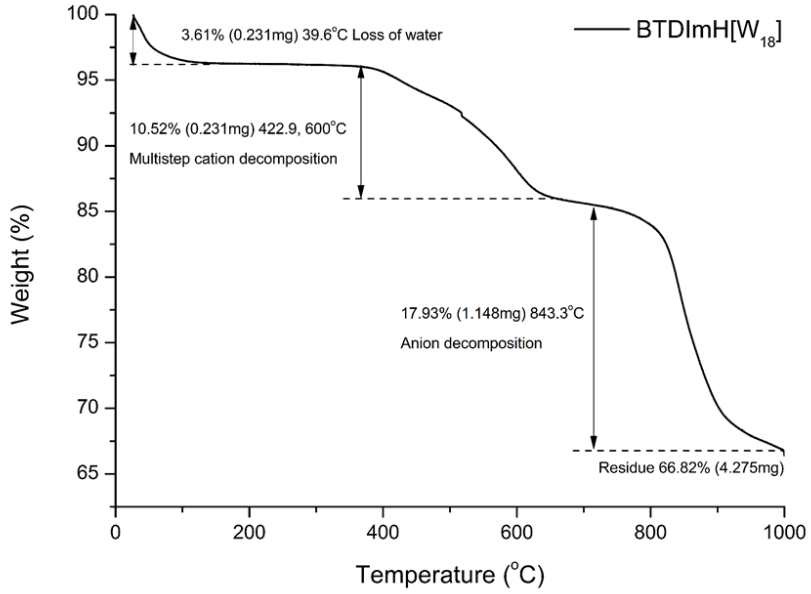


Figure 43. TGA curve for BTDImMe[W_{18}] showing initial loss of adsorbed water (1.87%, 50.9°C) followed by multistep cation decomposition (10.94%, 447.1 and 513.3°C) and anion decomposition (6.73%, 620.6°C).

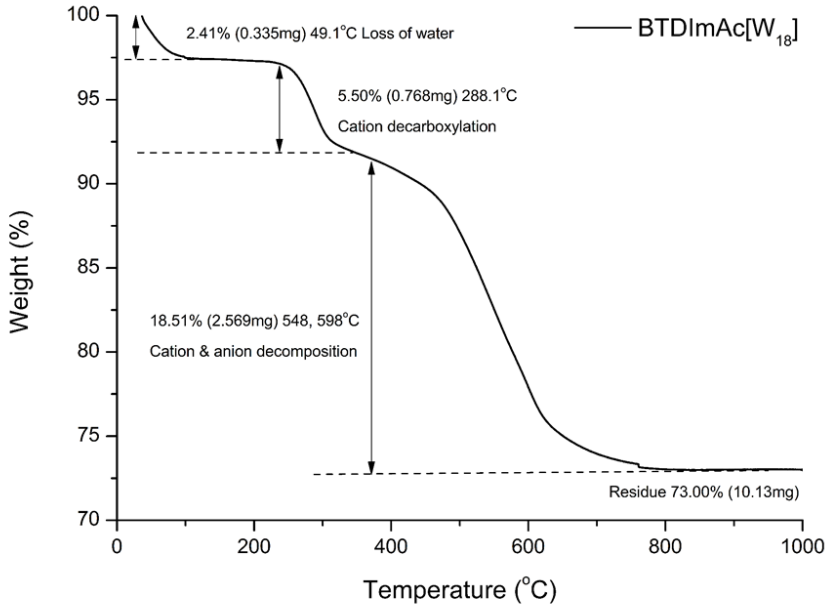


Figure 44. TGA curve for BTDImAc[W_{18}] showing initial loss of adsorbed water (2.41%, 49.1°C) followed by cation decarboxylation (5.50%, 288°C) and cation and anion decomposition (18.51%, 548 and 598°C).

Differential scanning calorimetry was subsequently used to investigate the melting temperatures of the hybrid materials. Whilst the structure contains imidazolium residues which are a common component of ionic liquids, the symmetrical nature of the cation containing little steric bulk combined with the highly symmetrical and diffuse electronic nature of the polyoxoanion suggests that these materials will not have depressed melting temperatures. The DSC traces of the three compounds, shown in Figure 45, demonstrates that none of the materials shows any phase change behaviour within the temperature limits of the experiment, as demonstrated by a complete absence of peaks. This confirms that the materials show no phase changes prior to the onset of decomposition.

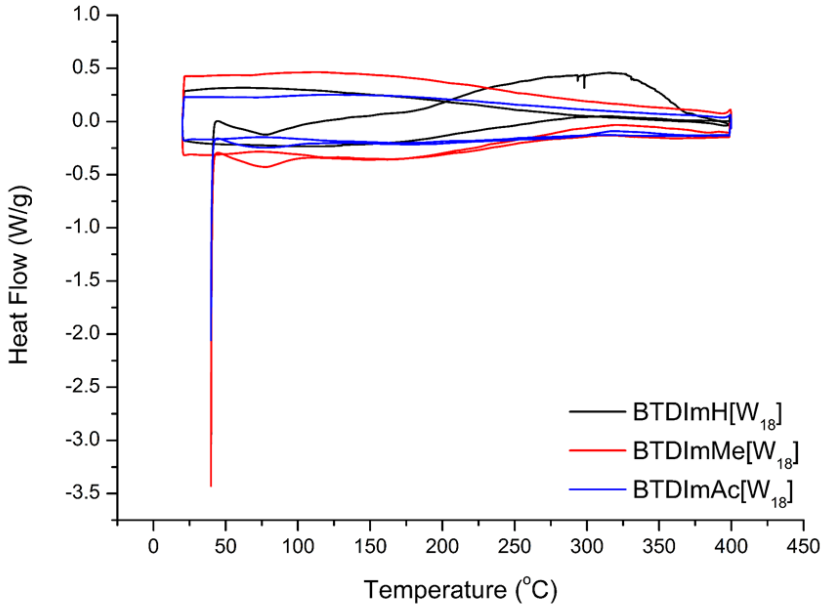


Figure 45. DSC traces for BTDImH[W_{18}], BTDImMe[W_{18}] and BTDImAc[W_{18}] showing no discernible phase transitions within the window of the experiment.

2.3.4 Electronic characterisation

The electronic nature of each of the materials were probed using common solution-based techniques. Firstly, UV-vis spectroscopy was employed to find whether the employ of organic dye cations served to increase the absorptive properties of the POM material. Due to the extremely limited solubility of these materials in a variety of solvents, DMSO was employed despite its limited UV-vis cut-off window of 270 nm (cf. NMP = 285 nm). Firstly, comparing the polyoxometalates to their precursor components (Figure 46, Table 3), it is evident that the spectral profile of the hybrids is a superposition of the excitations of the photoactive components, namely, the tailing of the O→W LMCT band of the polyoxometalate and the π-π* transitions of the aromatic cation, however, whilst the hybrid materials do not feature new absorption bands or significant bathochromic shifts, the absorption coefficient of the hybrids species were consistently larger than their precursor compounds, reflecting the fact that each component of the salt contributes to the photo absorption profile. Comparing directly the three hybrids (Figure 47), BTDImH[W_{18}] has a superior overall absorption profile courtesy of a lower energy absorption feature that is enhanced in the protonated cation versus the quaternised cations. This gives BTDImH[W_{18}] a wider overall absorption profile with significantly higher absorption in the visible region.

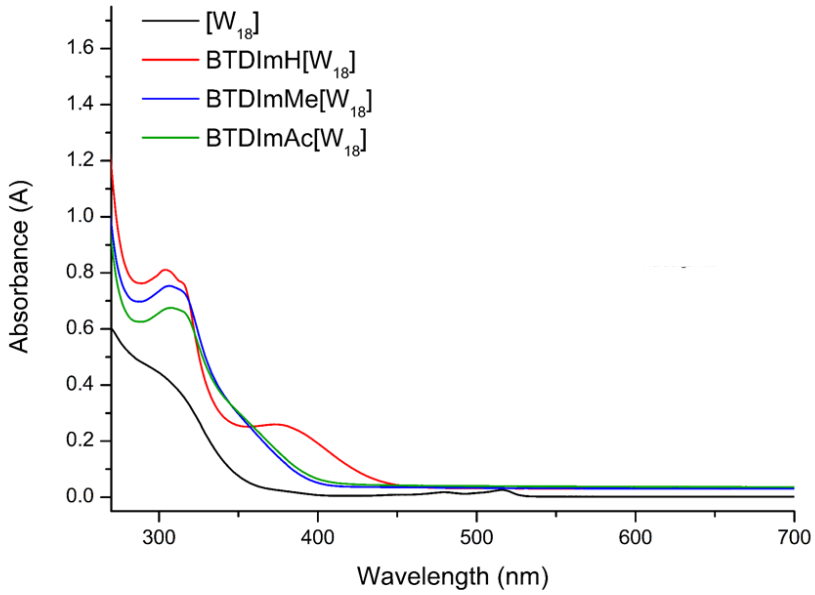


Figure 46. UV-vis spectra of a) BTDImH[W_{18}] b) BTDImMe[W_{18}] c) BTDImAc[W_{18}] compared with their susbstituent starting materials at 1 x 10^{-5} M in DMSO. The hybrid materials (blue) can be accurately described as a superposition of the cationic precursors (red) and [W_{18}] (black).

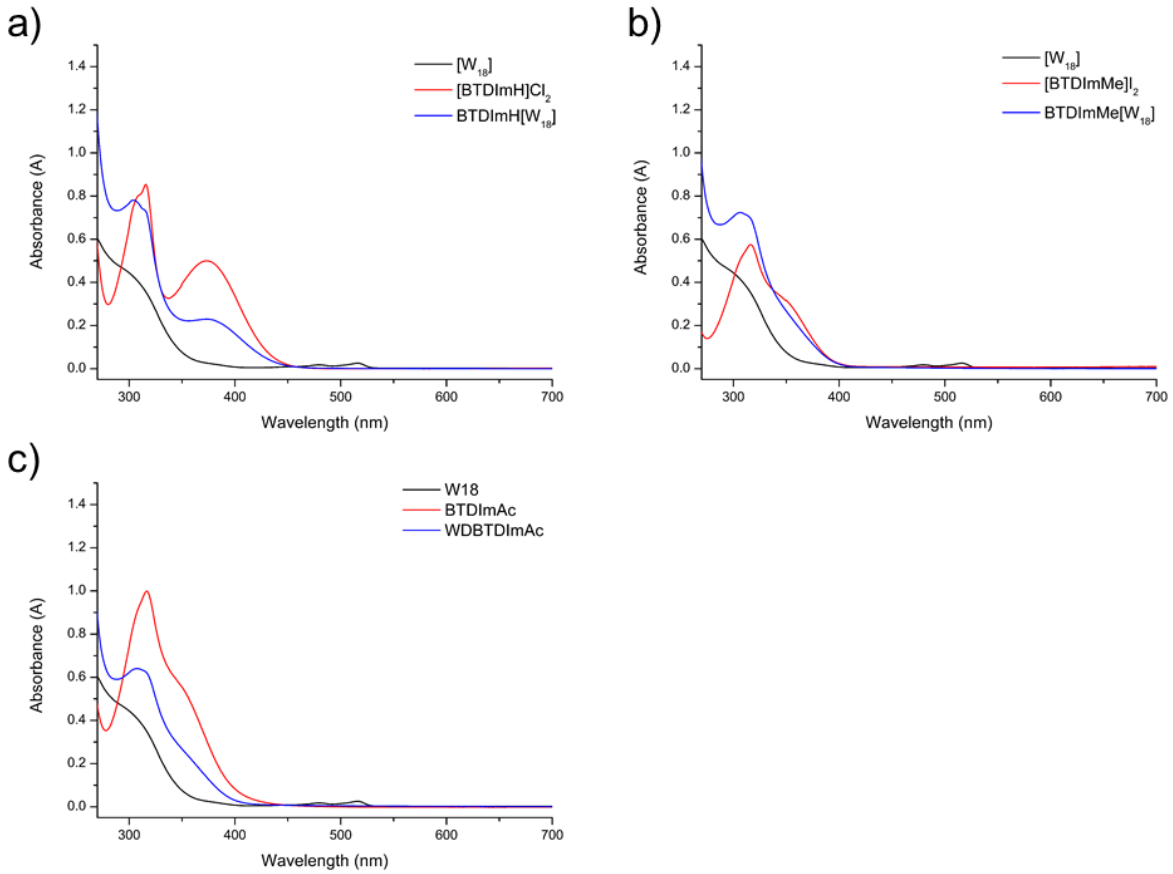


Figure 47. Overlay of the UV-vis spectra of BTDImH[W_{18}] (red), BTDImMe[W_{18}] (blue) and BTDImAc[W_{18}] (green) with [W_{18}] (black), showing the enhanced visible profile of BTDImH[W_{18}].

	λ_{max} (nm)	Extinction Coefficient (ε)
$[W_{18}]$	261	6631
$[BTDImH]Cl_2$	316	8540
	373	5000
$[BTDImMe]I_2$	316	5749
$[BTDImAc]Cl_2$	317	9990
$BTDImH[W_{18}]$	304	8107
	373	2597
$BTDImMe[W_{18}]$	305	7522
$BTDImAc[W_{18}]$	308	6754

Table 3. Absorption maxima (λ_{max}) in nm and extinction coefficients (ε) in $M^{-1}cm^{-1}$ for the hybrid materials and their precursor salts.

Cyclic voltammetry was next employed to probe the redox character of the material, this technique was expected to be particularly informative as both the cation and anion are expected to be redox active. Initially the electrochemical system was tested in both DMSO and DMF, as these solvents can dissolve the hybrids to an appreciable degree and possess wide electrochemical windows, especially in the negative region where the polyoxometalate usually exhibits multiple redox processes. However, initial testing of these materials in those solvent encountered issues of electrodeposition on the electrode which obscured the solution based signals. To counteract these issues, the hybrids were instead measured in an ionic liquid solvent. Ionic liquids possess a host of advantages that make them excellent alternative solvents for electrochemical applications – these include ionic conductivity, high solvation ability, negligible vapour pressure and wide potential windows to name a few.[104] For the measurement of the hybrid species, 1-ethyl-3-methyl imidazolium ethylsulphate ([EMIM][$EtSO_4$]) was found to be an excellent IL solvent, balancing lower viscosities, a wide electrochemical window and good solubilisation of the hybrids. A three-electrode set-up was employed with a glassy carbon working electrode, (d = 3 mm), Pt wire counter-electrode and a Ag-wire pseudo-reference electrode, with Fc^+/Fc redox couple as an internal reference.

Figure 48 shows the redox behaviour of the hybrids, in addition to $[W_{18}]$ for comparison, as 1 mM solutions in [EMIM][$EtSO_4$] as both the solvent and supporting electrolyte at 100 mV/s scan rate. It is immediately clear that the electrochemistry of each hybrid material is both complex and distinct. Each hybrid exhibits two well-defined quasi-reversible reductions which are likely the $POM^{6-/7-}$ and $POM^{7-/8-}$ redox couples based on similar behaviour observed in the parent anion. When considering the half-wave potentials of the first and second processes (Table 4), the hybrids generally show redox potentials

matching those of TBA[W_{18}], with the exception of BTDImMe[W_{18}] for which a significant positive peak shift is observed (~ +150 mV vs. TBA[W_{18}]), this effect may be due to the difference in ion pairing exhibited by the aprotic BTDImMe cation compared to the protic BTDImH and BTDImAc cations.[105] Interestingly, the peak to peak separation of the first two redox processes for the hybrid species approach the value expected for electrochemical reversibility (57-79 mV cf. 59 mV as expected for a one electron process) whereas under the same conditions, TBA[W_{18}] exhibits peak to peak separations exceeding 100 mV. Whilst the accurate measurement of peak area, and therefore electrons transferred, is frustrated by the large amount of capacitive charging in all cases, it seems that the return oxidation is more supressed in TBA[W_{18}] compared with the hybrid materials. These together suggest that the electrochemical reversibility of the first two redox processes of the POM are enhanced when coupled with the BTD cations. This may be rationalised by considering the ion pairing with the solvent that may occur. For TBA[W_{18}], the bulky tetrabutylammonium cation has a much lower ionic potential than the EMIM cation. Imidazolium-based cations have theoretically demonstrated a high tendency to form strong ion pairs with polyoxometalates, therefore it is likely that the EMIM cations of the solvent/electrolyte will form ion pairs with the POM upon reduction.[106] Ion pairing with the electrolyte means that the initial reduction product is rapidly consumed, thus back electron transfer is hampered and the reduction becomes rate determining. This converts a reversible process to an irreversible process governed by the association and dissociation kinetics of the ion pair.[107] For the hybrid species, the thermodynamic driving force for ion pairing with the solvent upon reduction may be limited, as the BTD salt, which strongly associates with the POM, provides similar ion contact opportunities as the EMIM electrolyte, therefore it is possible that the BTD ions are strongly associated with the POM even in solution and could limit the ability of the POM to form ion pairs with the EMIM cations.

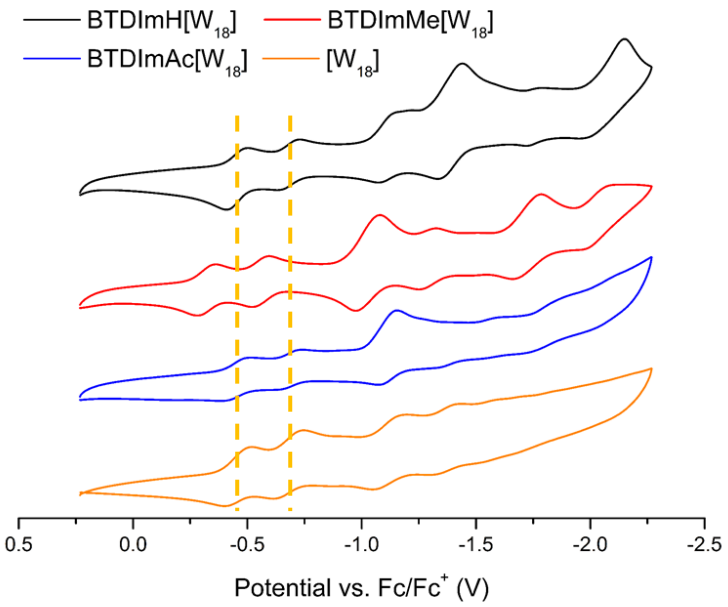


Figure 48. Cyclic voltammograms of BTDImH[W_{18}] (black), BTDImMe[W_{18}] (red) and BTDImAc[W_{18}] (blue) compared to [W_{18}] (yellow), demonstrating the positive shift of the first two redox couples of BTDImMe[W_{18}] compared with [W_{18}].

	Reduction processes vs. Fc/Fc+ (V)					
	1	2	3	4	5	6
[W_{18}]	-0.466(q)	-0.503(q)	-1.135(q)	-1.362(q)	-	-
[BTDImH]Cl_2	-2.031(i)	-	-	-	-	-
BTDImH[W_{18}]	-0.471	-0.699(q)	-1.127	-1.385(q)	-2.193(i)	
BTDImMe[W_{18}]	-0.322	-0.565	-1.028(q)	-1.299(q)	-1.733(q)	-2.047(q)
BTDImAc[W_{18}]	-0.459	-0.696(q)	-1.116(q)	-1.472(q)	-1.797(q)	

Table 4. Redox potentials for [W_{18}], [BTDImH]Cl_2, BTDImH[W_{18}], BTDImMe[W_{18}] and BTDImAc[W_{18}] given as the half wave potential ($E_{1/2}$) for reversible and quasireversible (q) processes and the peak maximum (E_p) for irreversible (i) processes. Ascending numbered processes refer to sequential reductions of the analyte scanning from positive to negative, all values are given in volts (V) referenced to Fc/Fc^+ redox couple as an external standard.

Beyond the first two redox processes, TBA[W_{18}] exhibits two further reduction processes which is typical for the Dawson phosphotungstate anion. It appears that the signal from the 3rd and 4th reduction peaks are supressed (based on the peak area) as it is expected that the peaks correspond to four single-electron reductions (1:1:1:1 ratio) based on previous analysis of the anion in aprotic ionic liquid media[108], this again is likely due to the increase in capacitive current at more negative potentials as IR compensation was not used. The hybrid species each show multiple complex redox processes beyond the first and second reduction. Direct comparison of the hybrids with their precursor salts, as exemplified in Figure 49 for BTDImMe[W_{18}], reveals that the hybrid species shows redox behaviour beyond that of the molecular components. For example, [W_{18}] shows four quasi-reversible processes between

-0.45 V and -1.1 V as previously mentioned, and [BTDImMe]Cl_2 shows one main non-reversible process at extremely low potentials (-2.026 V), however BTDImMe[W_{18}] shows 6 quasi-reversible peaks, some of which appear to show multi-electron character. BTDImH[W_{18}] and BTDImAc[W_{18}] similarly exhibit noncombinatorial redox processes. The complex electrochemistry is likely to arise from synergic effects between the two components, and confirms that even when solvated, the components are interacting strongly such that electronic transfer processes can occur. In this regime, it would be likely that the polyoxometalate is initially reduced but is then able to shuttle its electrons to the three BTD cations allowing for more POM based reductions to take place. The observation that functionalisation by different groups causes large differences in the CV profile at more reducing potentials suggests that the first two processes are likely to be solely POM based reductions whereas the following processes involve electron transfer between the POM and the BTD cations.

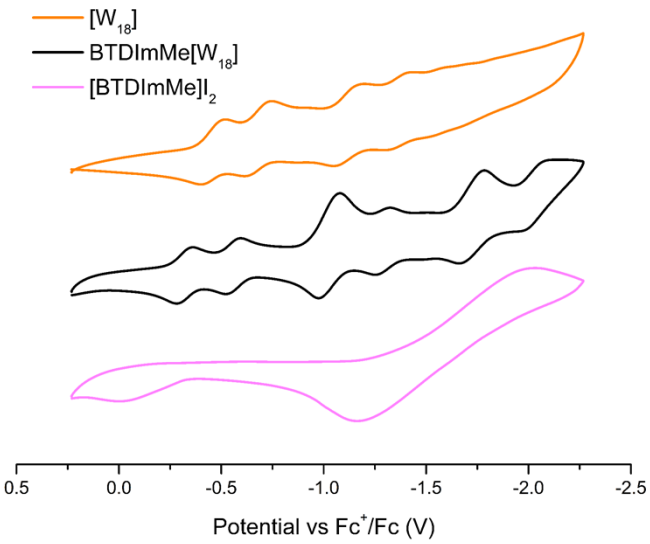


Figure 49. Cyclic voltammograms of BTDImMe[W_{18}] (black), [BTDImMe]I_2 (pink) and [W_{18}] (orange). Demonstrating the non-superimposed nature of the hybrid material.

2.3.5 Solid-state electronic characterisation

The electronic characterisation presented in Section 2.3.4, in conjunction with the structural characterisation, confirmed that the components of the hybrid were intact and retained their electro- and photoactivity. However, solution state measurements do not allow for the direct investigation of the overall material properties, as in each case the effect of solvation must be considered and the degree and effect of ion pairing in solution cannot be directly determined.

To address this, electronic characterisation was repeated directly on the solid-state materials to investigate the mutual electronic influence of the ions and to characterise the materials as whole entities. Firstly, the electrochemical characterisation was repeated by preparing the analyte as a solid-state layer on the electrode. Each of the hybrids (10 mg) were dissolved as saturated solutions in DMSO and subsequently drop cast onto glassy carbon electrodes (d = 1.6 mm), these were then dried over 2 weeks to ensure full evaporation of the solvent. The prepared electrodes were then utilised in a three-electrode set up using an AgCl/Ag reference electrode and a platinum counter electrode. Acetonitrile was selected as the electrochemistry solvent due to its wide electrochemical window, relatively low vapour pressure and its inability to dissolve the analyte and the electrolyte selected was tetrabutylammonium tetrafluoroborate ($TBABF_4$). Figure 50 show the electrochemical profile of the hybrid materials as measured by this technique. It is immediately evident that the voltammograms measured by the drop casting method have very weak current responses, however, a closer inspection of the voltammogram reveals that the peaks corresponding to the predicted first and second reduction of the polyoxometalate, especially evident in the voltammogram of BTDImH[W_{18}], appear to be diffusional in nature, with peak separation exceeding 59 mV between the reduction and oxidation peaks. For an ideal reversible solid-state electrochemical process, peak to peak separation should be 0 as the analyte is in direct contact with the electrode and so there should be no diffusional contributions. The above suggests that either the hybrid materials show extremely low solubility in acetonitrile or that upon reduction there is electrodissolution of the species. Given the potential complexity of the system which is in a mixture of states and the extremely weak contribution from the solution state species, square wave voltammetry was performed and compared with the obtained cyclic voltammetry. Square wave voltammetry is a voltammetric technique that combines square wave modulation with a staircase waveform to obtain current responses with increased sensitivity and mitigation of background currents, allowing for the detection of analytes at lower concentrations and more facile calculation of the number of electrons involved in a process.[109]

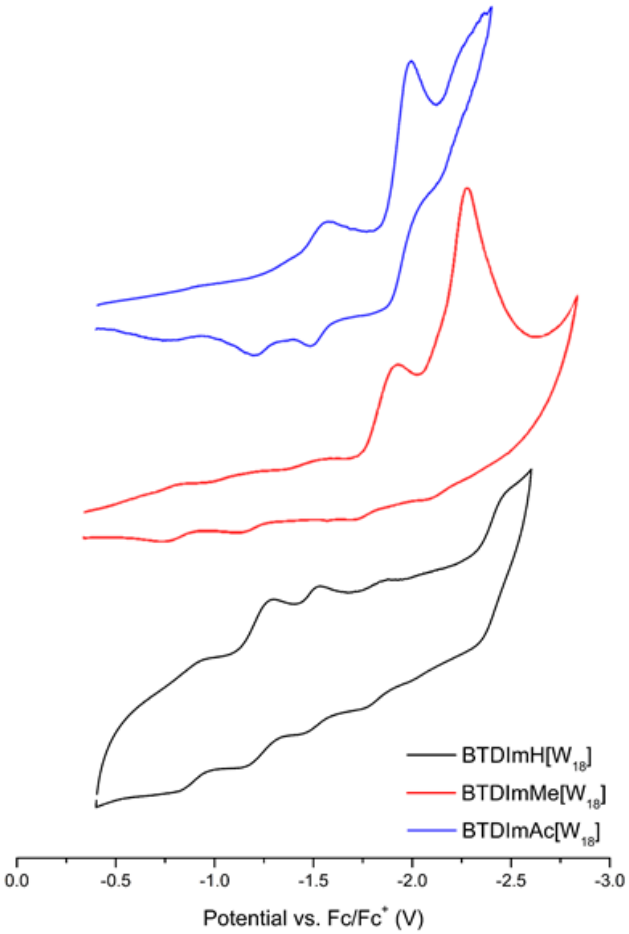


Figure 50. Cyclic voltammograms of BTDImH[W_{18}] (black), BTDImMe[W_{18}] (red) and BTDImAc[W_{18}] (blue) as measured by the dropcasting method.

Figure 51 show the cyclic voltammogram and the square wave voltammogram scanning from positive to negative obtained for BTDImH[W_{18}], with peak positions and areas reported in Table 5. The cyclic voltammogram shows four apparent quasi-reversible redox couples: 1a/9a, 2a/8a, 3a/7a and 4a/6a, with one irreversible reduction 5a. The square voltammogram shows seven major peaks, five of which match extremely well with the potentials of the peaks in the cyclic voltammogram, two peaks of smaller magnitude have also been elucidated due to the increased sensitivity of the technique. Analysis of the conflicting peak areas, which are usually indicative of the number of electrons within a process, has been avoided given the inherent complexity of the system (presence of two distinct electroactive ions within the system coupled with a mixture of phases). It is important to note here that for chemically reversible yet electrochemically irreversible processes (i.e. processes with large peak separations), square wave voltammetry may produce misleading signals, which makes their interpretation challenging.[110] Nonetheless, it is clear that the first two redox couples are reminiscent of the voltammograms obtained in the solution phase measurements, likely corresponding to the first and

second reduction of the POM core. The peaks measured in ionic liquid are cathodically shifted by >400 mV showing the strong dependence on POM reduction potentials on the solvent polarity.[108]

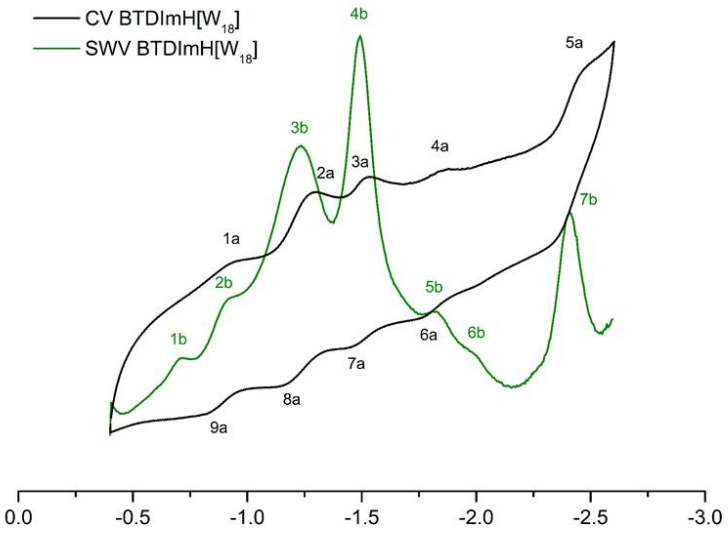


Figure 51. Cyclic (black) and square-wave (green, scanning from positive to negative) voltammogram of BTDImH[W_{18}].

BTDImH[W_{18}] CV		**BTDImH[W_{18}] SWV**	
Peak	Potential vs. Fc/Fc^+ (V)	Peak	Potential vs. Fc/Fc^+ (V)
-	-	1b	-0.702
1a/9a	-0.871	2b	-0.899
2a/8a	-1.213	3b	-1.212
3a/7a	-1.496	4b	-1.493
4a/6a	-1.821	5b	-1.835
-	-	6b	-2.001
5a	-2.464	7b	-2.409

Table 5. Redox potentials for BTDImH[W_{18}] given as the half wave potential ($E_{1/2}$) for quasireversible redox couples in the CV and the peak maximum (E_p) for irreversible processes and SWV peaks. All values are given in volts (V) referenced to Fc/Fc+ redox couple as an external standard.

The cyclic and square wave voltammograms of BTDImMe[W_{18}] are shown in Figure 52 with parameters given in Table 6. The analysis reveals the familiar appearance of two quasi reversible redox processes followed by a series of irreversible reduction processes. The first two redox processes (1a/10a and 2a/9a) correlate well in terms of their reversibility and half wave potentials with the first two redox potentials of BTDImH[W_{18}], suggesting that these are the first and second POM based reductions. Beyond this the voltammogram is dominated by irreversible processes. The square wave voltammetry again showed excellent agreement with the peak positions, however the peak area for the second

reduction, nominally having the same electron count as the first reduction, is massively augmented. This phenomenon again reinforces the complexity of the system.

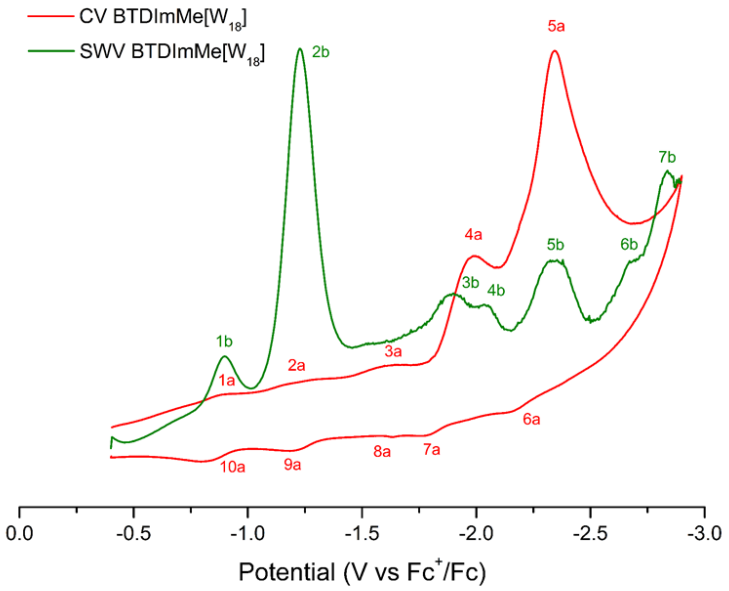


Figure 52. Cyclic (red) and square-wave (green, scanning from positive to negative) voltammogram of BTDImMe[W_{18}].

BTDImMe[W_{18}] CV		**BTDImMe[W_{18}] SWV**	
Peak	Potential vs. Fc/Fc^+ (V)	Peak	Potential vs. Fc/Fc^+ (V)
1a/9a	-0.846	1b	-0.893
2a/8a	-1.236	2b	-1.226
3a	-1.599	-	-
4a	-1.968	3b	-1.875
		4b	-2.052
5a	-2.343	5b	-2.324
-		6b	-2.671
-		7b	-2.827
6a*	-2.163	-	-
7a*	-1.792	-	-

Table 6. Redox potentials for BTDImMe[W_{18}] given as the half wave potential ($E_{1/2}$) for quasireversible redox couples in the CV and the peak maximum (E_p) for irreversible processes and SWV peaks. All values are given in volts (V) referenced to Fc/Fc+ redox couple as an external standard. Peaks with an asterisk denote irreversible oxidations occurring on the return scan of the cyclic voltammogram.

Finally, analysing BTDImAc[W_{18}] through the same methods (Figure 53, Table 7), some marked differences are observed. Firstly, the cyclic voltammogram does not show the typical solution state electrochemistry of the polyoxometalate anion, suggesting that this hybrid exhibits much lower solubility (or does not undergo electrodissolution) in acetonitrile. In addition, it appears that there is a large

increase in current within the system before the formal potential limit for acetonitrile, this may be due to the presence of a strong proton source within the cation (acetic acid groups) and hence the signals could be due to electrocatalytic hydrogen reduction, multiple proton coupled reduction processes of the analyte, or the proton assisted early onset of solvent reduction. In the absence of dissolution processes, it can be determined that the first reduction of the material is peak 8a at -1.56 V which is non-reversible in nature, suggesting that the material has a high lying LUMO energy, however it is worth noting that the irreversible oxidation processes may have reduction counterparts that are barely discernible from the baseline.

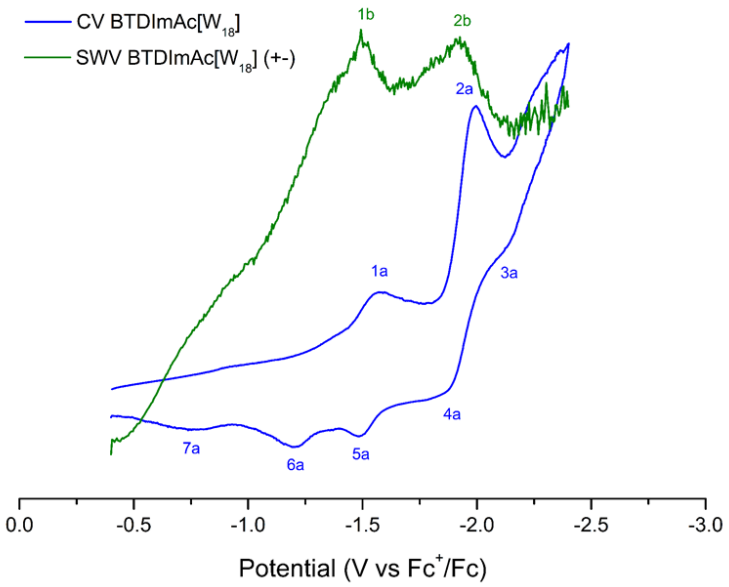


Figure 53. Cyclic (blue) and square-wave (green, scanning from positive to negative) voltammogram of BTDImAc[W_{18}].

BTDImMe[W_{18}] CV		**BTDImMe[W_{18}] SWV**	
Peak	Potential vs. Fc/Fc^+ (V)	Peak	Potential vs. Fc/Fc^+ (V)
1a/5a	-1.529	1b	-1.493
2a/4a	-1.930	2b	-1.926
3a*	-2.163	-	-
6a*	-1.191	-	-
7a*	-0.737	-	-

Table 7. Redox potentials for BTDImAc[W_{18}] given as the half wave potential ($E_{1/2}$) for quasireversible redox couples in the CV and the peak maximum (E_p) for irreversible processes and SWV peaks. All values are given in volts (V) referenced to Fc/Fc+ redox couple as an external standard. Peaks with an asterisk denote irreversible oxidations occurring on the return scan of the cyclic voltammogram.

Following this, UV-vis spectroscopy was also reinvestigated in the solid-state. Solution-state measurements gives information on the different electronic transitions within a compound, including their absorption maxima and extinction coefficients. However, solid-state UV-vis spectroscopy operates

on the basis of diffuse reflectance, which can be quantitatively transformed into an absorption spectrum through the Kubelka-Munk equation (Equation 1), this function acts to linearly relate the analyte concentration with the reflectance characteristics of the sample, this is achieved by supressing weaker bands with high reflectance and enhancing stronger bands with lower reflectance, the output of this does not give details on specific transitions, but can be used to extract information such as the absorption maximum, absorption edge and band gap of the material.[111]

$$\frac{k}{s} = \frac{(1 - R_\infty)^2}{2R_\infty}$$

Equation 1. The Kubelka-Munk function for diffuse reflectance. Where k is the absorption coefficient of the sample, s is the scattering coefficient and R∞ is the diffuse reflectance

Figure 54 shows the solid-state absorption profiles for the three materials. Absorption maxima for BTDImH[W_{18}], BTDImMe[W_{18}] and BTDImAc[W_{18}], were observed at 305 nm, 304 nm and 303 nm. These correlate closely with the maxima obtained from the solution based studies which is composed of π-π* transitions of the organic cations augmented by tailing of the W→O LMCT bands of the polyoxometalate (304 nm, 305 nm and 308 nm). Surprisingly the intense LMCT band of the POM, which absorbs more strongly than the cations, is somewhat reduced in the solid-state. To calculate the absorption band edge, the linear part of the spectrum where the absorption decays towards the baseline is fitted and the intersection of this line with the x-axis (y=0) gives the absorption edge. BTDImH[W_{18}], BTDImMe[W_{18}] and BTDImAc[W_{18}] show absorption edges of 409 nm, 422 nm and 413 nm respectively. These values indicate that the solid-state materials absorb primarily in the UV with minor visible light absorption. The absorption edge of BTDImH[W_{18}] does not seem significantly enhanced despite the extra absorption component (λ_{max} = 373 nm) that is visible in the UV-vis spectrum in DMSO, demonstrating that solution state absorption profiles may not always correlate to the solid-state absorption properties of materials due to effects such as solvatochromism and molecular packing.

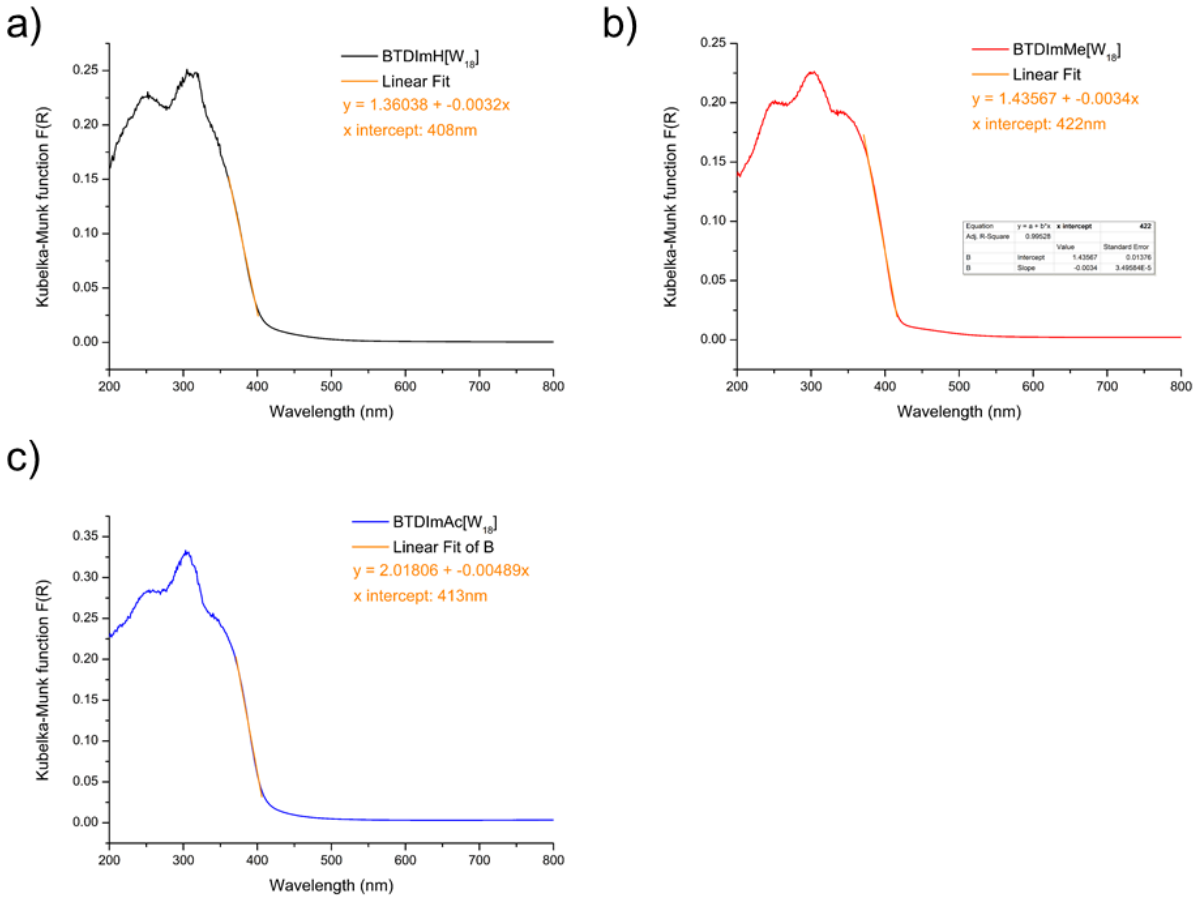


Figure 54. Diffuse reflectance UV-vis spectra of a) BTDImH[W_{18}] b) BTDImMe[W_{18}] a) BTDImAc[W_{18}]. Fitting and extrapolation of the linear portion of the curve to the x-axis (orange) gives the absorption edge.

To estimate the band gap of the materials, the data must be replotted in the form of a Tauc plot. The Tauc plot allows the band gap to be determined through the dependence of the optical absorption strength on the difference between the photon energy and the band gap, according to the Tauc equation (Equation 2).[112]

$$(\propto h\nu)^{1/n} = A(h\nu - E_g)$$

Equation 2. The Tauc equation relating absorbance to the band gap. Where α is the absorption coefficient, h is Planck's constant, v is photon frequency, A is the proportionality constant and Eg is the band gap energy. The value of the exponent, n, depends on the nature of the transition, where n = 1/2 is direct allowed, n = 3/2 is direct forbidden, n = 2 is indirect allowed and n = 3 is indirect forbidden

By plotting $(\alpha h\nu)^{1/n}$ vs. hv, the optical band gap (E_g) can be determined by extrapolating the linear portion of the graph to the x-axis (y=0). The Tauc plots for the three compounds are presented in Figure 55 with Table 8 summarising the parameters obtained from the solid-state absorption studies.

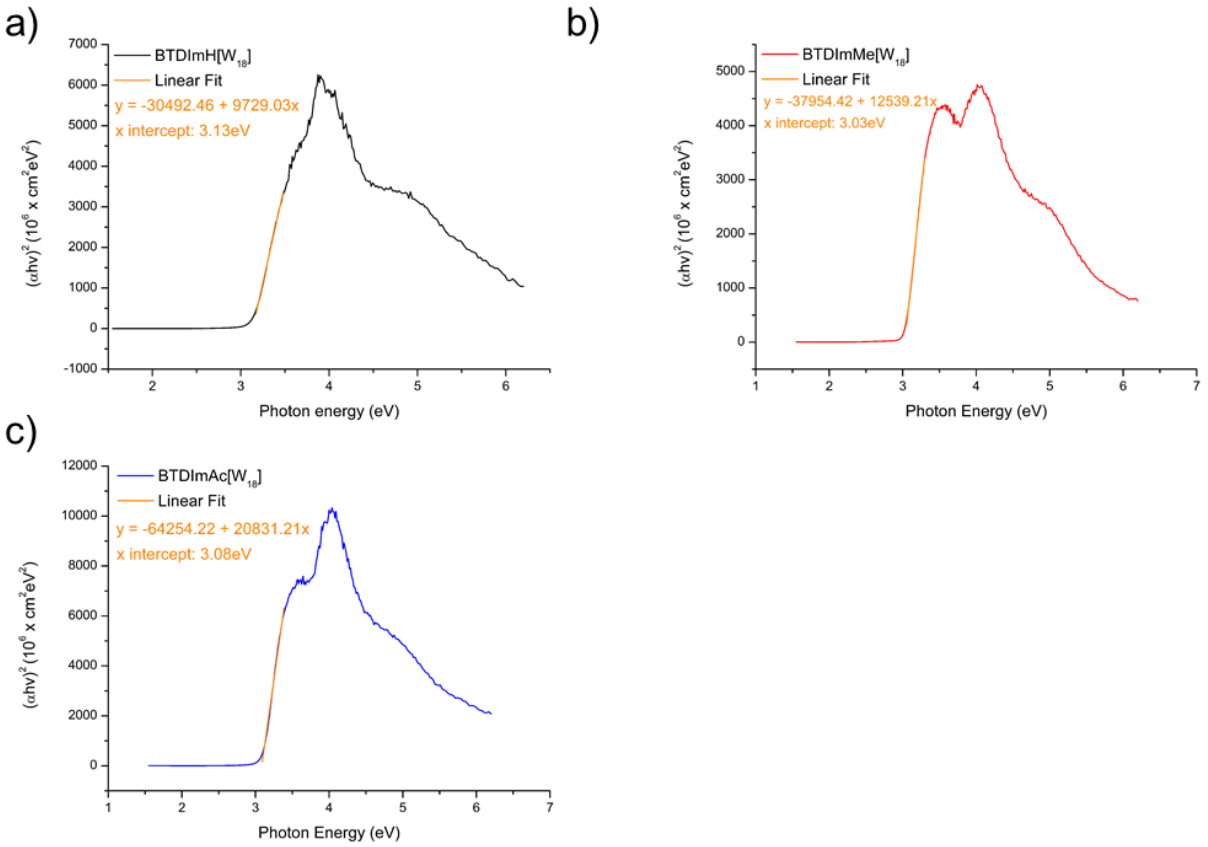


Figure 55. Tauc plot of a) BTDImH[W_{18}] b) BTDImMe[W_{18}] a) BTDImAc[W_{18}]. Fitting and extrapolation of the linear portion of the curve to the x-axis (orange) gives the optical band gap.

	λ_{max} (nm)	λ_{edge} (nm)	E_g (eV)
BTDImH[W_{18}]	305	409	3.13
BTDImMe[W_{18}]	304	422	3.03
BTDImAc[W_{18}]	303	413	3.08

Table 8. Absorption properties of the three hybrid materials obtained from solid state UV-vis measurements – absorption maxima (λ_{max}), absorption edge (λ_{edge}) and optical band gap (eV).

Initially, when constructing Tauc plots for a material, it is necessary to model the data for all possible transitions (direct allowed, direct forbidden, indirect allowed, indirect forbidden) using the Tauc equation. When plotted, only one scenario will exhibit a linear dependence of the absorption edge, corresponding to the correct transition for the material. For all the POM hybrids, the band gap was direct with an allowed transition. The photon energies of the materials (Table 8), are extremely similar and are clearly dominated by the core structures of the POM and the cations. The band gap energy of the hybrids ranged between 3 and 3.15 eV which corresponds to the violet portion of the visible spectrum, indicating that the materials may be able to act as visible light photocatalysts. These large band gaps are sufficient to span water oxidation and carbon dioxide reduction potentials and thus be of interest as artificial photocatalysts. To investigate the origin of the band behaviour for the hybrids, the

measurements were employed on $[W_{18}]$ and $[BTDImH]Cl_2$ and compared directly with their hybrid product $BTDImH[W_{18}]$.

Figures 56 and 57 show the UV-vis spectra and Tauc plots for $BTDImH[W_{18}]$ with its starting materials, Table 9 gives the respective photophysical characteristics. The main observations are that the absorption maximum and edge of the hybrid material is blue-shifted and the band gap has increased compared to the starting materials. The band gaps for the materials correlate well with their absorption maxima, suggesting that the parent $[W_{18}]$ should be easiest to excite with visible light, completely contradicting the observations in the solution state. The superior reflectance of the hybrid suggests that the material may be a stronger overall photon absorber and exhibit higher quantum yields upon excitation, however this postulation must be treated with caution given the different morphological nature of the samples (crystallinity and particle size) which will affect their specular and diffuse reflectance behaviours.[113]

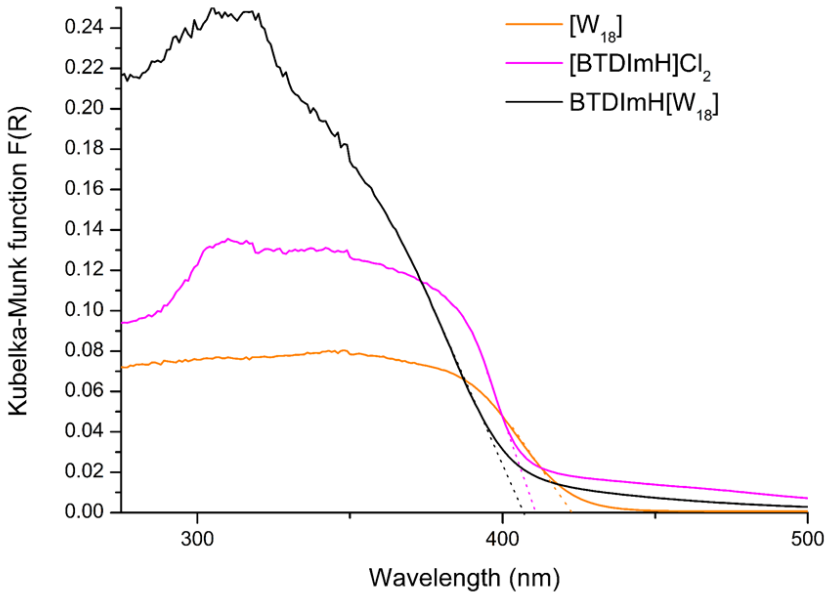


Figure 56. Diffuse reflectance UV-vis spectra of $BTDImH[W_{18}]$ (black), $[BTDImH]Cl_2$ (pink) and $[W_{18}]$ (orange) with X-axis intercepts shown with dashed lines.

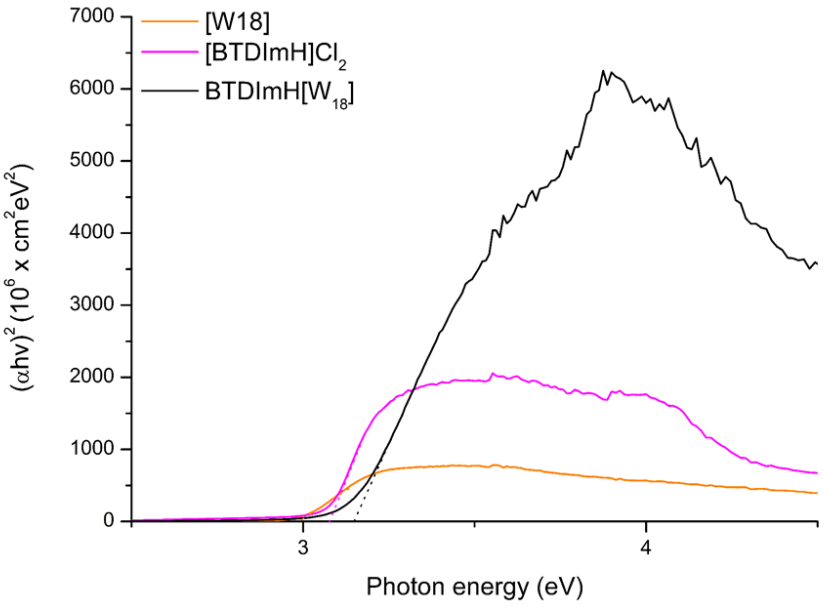


Figure 57. Tauc plot of BTDImH[W_{18}] (black), [BTDImH]Cl_2 (pink) and [W_{18}] (orange) with X-axis intercepts shown with dashed lines.

	λ_{max} (nm)	λ_{edge} (nm)	E_g (eV)
[W_{18}]	348	427	2.98
[BTDImH]Cl_2	310	414	3.05
BTDImH[W_{18}]	305	409	3.13

Table 9. Absorption properties of BTDImH[W_{18}], [BTDImH]Cl_2 and [W_{18}] obtained from solid state UV-vis measurements – absorption maxima (λ_{max}), absorption edge (λ_{edge}) and optical band gap (eV).

Recalling the original application of the benzothiadiazole cations, Souza et al.[95] described the strong fluorescence characteristics of all three cations as their halide salts in the solution phase in a variety of solvents with emissions ranging from 400 to 550 nm. It was therefore interesting to explore whether the hybrid materials retained any fluorescence behaviour in the solid-state. For this, BTDImH[W_{18}] was selected as the lead compound as this material is the most well characterised in the solid-state through X-ray crystallography. From the solid-state UV-vis measurements, the absorption maximum of the material was calculated to be 305 nm, therefore this was selected as the excitation wavelength. Figure 58 shows the fluorescence emission spectrum for BTDImH[W_{18}] compared with [BTDImH]Cl_2, [W_{18}] showed no solid-state fluorescence. The emission spectrum for the two species clearly demonstrates that [BTDImH]Cl_2 is highly fluorescent in the solid-state with an emission wavelength of 435 nm, whereas BTDImH[W_{18}] is only weakly fluorescent with an emission wavelength of 502 nm. Although a reduction in the fluorescence could be expected purely based on the reduced amount of fluorescent species in the hybrid versus the starting material (79 wt% vs. 16 wt%), this does not explain the approximately 200-fold reduction in the signal. From the X-ray crystal structure of BTDImH[W_{18}], the

imidazolium rings of the BTDImH cation are twisted from planarity, to varying degrees, due to hydrogen bond forming contacts with the polyoxometalate and solvent molecules. One theory is that these interactions could provide extra scope for relaxation mechanisms when compared to the native cation which is reinforced by internal hydrogen bonding.[95] This is supported by the larger stokes shift exhibited by the hybrid material when compared to $[BTDImH]Cl_2$ (Table 10), which is indicative of more vibrational relaxation pathways in the fluorophore. Another explanation for the reduction of fluorescence is that the excited electron is undergoing electron transfer from the BTD to the POM upon excitation; as has been previously alluded to from the solution state electrochemistry with the evolution of several new peaks, whether via photoexcitation or electroreduction, electrons may be able to transfer between the two electroactive species when they are in high energy LUMO states.

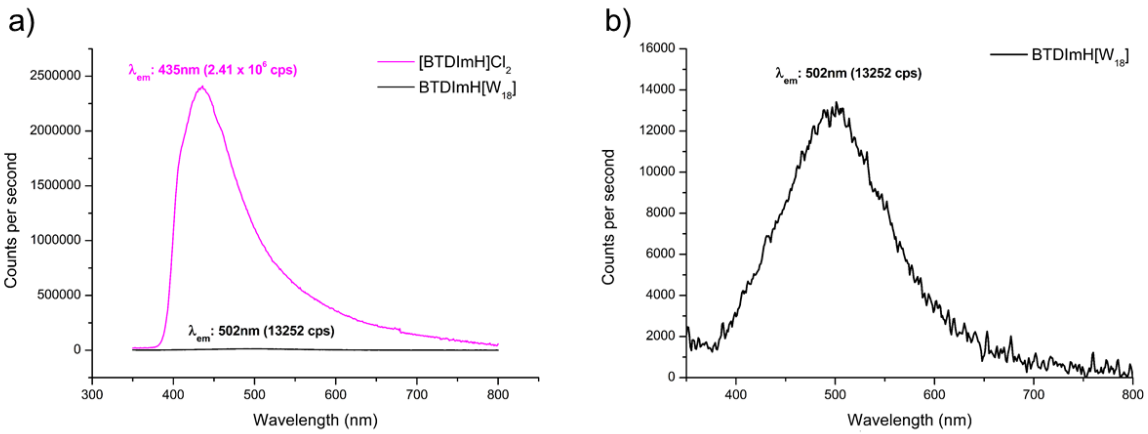


Figure 58. a) Fluorescence emission spectrum of $BTDImH[W_{18}]$ (black) compared to $[BTDImH]Cl_2$ (pink) b) Zoomed in fluorescence emission spectrum of $BTDImH[W_{18}]$. Measured at 305nm irradiation

	$\lambda_{max\ abs}$ (nm)	$\lambda_{max\ em}$ (nm)	Obs fluorescence (cps)	Stokes Shift (nm)
$[W_{18}]$	300-350	-	-	-
$[BTDImH]Cl_2$	310	435	2.41×10^{-6}	125
$BTDImH[W_{18}]$	305	502	1.33×10^{-4}	197

Table 10. Absorption and emission properties of $BTDImH[W_{18}]$, $[BTDImH]Cl_2$ and $[W_{18}]$ obtained from solid state UV-vis measurements and fluorimetry studies – absorption maxima ($\lambda_{max\ abs}$), absorption edge ($\lambda_{max\ em}$), optical fluorescence and Stokes shift.

2.3.6 Photocatalytic studies

Having extensively characterised the materials both physically and electronically and ensuring that the hybrids exhibit high thermal stability and photoactivity, the final phase of the project was to test these materials for their photocatalytic capabilities towards redox transformations of small molecules. The catalyst selected was $BTDImH[W_{18}]$, again due to the deeper understanding of the structure of the

hybrid. The reactions that were selected were the two half-reactions that comprise artificial photosynthesis, water oxidation and carbon dioxide reduction, due to their high relevance and obvious impact in sustainable fuel production. Initial tests were performed with water oxidation in a heterogeneous solution regime and carbon dioxide reduction directly at the solid-gas interface. Whilst the former showed no activity for the evolution of oxygen, the latter reaction showed evidence of carbon dioxide reduction using hydrogen as a sacrificial electron donor by the appearance of carbon monoxide in the headspace of the photoreactor. A photocatalysis reaction was therefore conducted to quantify the conversion of CO_2 to CO in the presence of BTDImH[W_{18}]. The experiment was performed by placing 50 mg of the catalyst into the photoreactor, purging the vessel with carbon dioxide and charging to 1 bar, then charging the vessel further with hydrogen until a total pressure of 4 bar was obtained. The reaction vessel was then illuminated with a 200 W mercury arc lamp with no agitation. The reactor was connected to a gas chromatograph that was calibrated for the detection of lightweight molecular species operating with both FID and TCD detectors. Samples were taken at regular intervals and then a final measurement after 24 hours. The amount of carbon monoxide produced was quantified by integration of the area underneath the GC peak at 1.14 minutes, which had been calibrated and confirmed as the retention time for carbon monoxide. Figure 59a shows the carbon monoxide FID peak at each interval and Figure 59b shows the time dependent evolution of carbon monoxide, the kinetic data is given in Table 11.

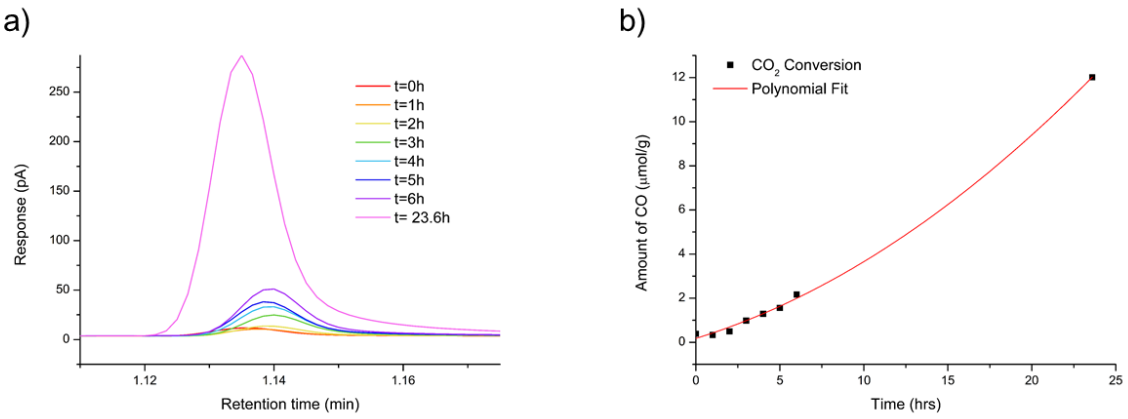


Figure 59. a) Evolution of the FID peak corresponding to CO over the course of the experiment. b) Rate of CO evolution plotted from volumes calculated using the area of the TCD peaks, fitted to a polynomial.

Time (hrs)	%mol/mol (CO/CO_2)	% Conversion	Amount of CO/catalyst (µmol/g)	TON	TOF
0	2.35×10^{-4}	1.52×10^{-3}	0.384	-	-
1	2.00×10^{-4}	1.20×10^{-3}	0.324	-	-
2	3.01×10^{-4}	1.78×10^{-3}	0.493	-	-
3	6.00×10^{-4}	3.53×10^{-3}	0.984	-	-
4	7.90×10^{-4}	4.63×10^{-3}	1.292	-	-
5	9.51×10^{-4}	5.58×10^{-3}	1.56	-	-
6	1.32×10^{-3}	7.72×10^{-3}	2.16	-	-
23.6	7.34×10^{-3}	4.27×10^{-2}	12.0	0.0654	0.00278

Table 11. Obtained CO conversion and rate parameters based on GC-FID measurements of CO concentration in the gas headspace of the photoreactor.

The results show that the hybrid is capable of photo-reducing carbon dioxide to carbon monoxide in the presence of H_2 as a sacrificial electron donor in a solid-gas regime. Sampling occurred every hour for the first 6 hours and then a final measurement was taken after the reaction had reached 24 hours. At the final measurement, a turnover number of 6.54×10^{-2} was attained which correlated to a turnover frequency of 2.78×10^{-3} $\mu molh^{-1}$, this indicates that the hybrid was able to activate CO_2 towards photoreduction but did not display catalytic activity within the confines of the experiment as TON < 1. From the polynomial fitting of the conversion curve, there appears to be an initial induction period of 2 hours before conversion starts, this could be due to the need for thermal activation, as no cooling apparatus was used within the set-up so the reaction temperature increases during irradiation. Interestingly, after 24 hours a small amount of methane was detected (retention time 1.05), suggesting that the hybrid may be able to facilitate $8e^-$ reductions either in a concerted or stepwise manner. When the reaction is repeated in the dark or in the absence of hybrid or using $[W_{18}]$ or $[BTDImH]Cl_2$ as catalysts under the same conditions, no CO is detected. Although the TON and TOF of the reaction are extremely low, there is immense scope for optimisation, especially with regards to the distribution of the photocatalyst within the reactor to ensure maximum illumination, which is expected to dramatically increase the TON.

With regards to the unique reactivity of the hybrid material compared to the precursor salts, a synergic effect is obtained when the two photoactive components are combined. The observed activity may arise from the unique photochemistry of the hybrid system; however, it may also be a function of the chemical activities of the components. POMs can act as substrates for the adsorption of CO_2[114] and as efficient proton and electron reservoirs[115], whereas imidazolium species can act as proton donors and CO_2

binding sites through the N-heterocyclic carbene species.[116] Furthermore, crystallographic evidence reveals hydrogen bonding between the C2-H of the imidazolium and the POMs, suggesting that the POM or its reduced forms could act as a base for the acidic proton. Due to the photoexcitation of both components being accessible with broad UV-vis irradiation, it is likely that both molecules are simultaneously excited. From UV-vis and electrochemical measurements, the orbital levels of the components can be approximated by correlating the first reduction potentials to the LUMO energy and the lowest energy electron transition the HOMO-LUMO gap through the use of Equations 3 and 4.[117] By performing the cyclic voltammetry of $[W_{18}]$ and $[BTDImH]Cl_2$ in DMSO to mitigate any solvent effects, orbital levels were able to estimated and mapped. Figure 60 demonstrates that energetically the polyoxometalate and BTDImH may exhibit a synergic effect through the ability of excited state electron transfer, here it is tentatively suggested that the POM and BTDImH may both undergo photoexcitation, this is followed by photooxidation of hydrogen by the polyoxometalate with generates the reduced species. This may then undergo intermolecular charge transfer with the photoexcited BTDImH molecule to occupy the photogenerated hole, finally, this entraps a high energy electron on the BTDImH molecule which is then able to reduce carbon dioxide. The phenomena of electron transfer between the two molecules in excited states has been previously suggested from both electrochemical and fluorescence studies however further investigation, including time-resolved spectroscopies (IR and UV-vis), mechanistic studies, isotopic labelling and specific wavelength excitation studies would be instrumental in substantiating these postulations.

$$E_{LUMO}(eV) = -(E_{onset}(red) - 4.8)$$

Equation 3. Estimation of the LUMO energy through correlation with the energy levels of ferrocene in a vacuum, E_{onset}(red) is the onset of the first reduction wave obtain from cyclic voltammetry.

$$E_g(eV) = {}^{1240}/_{\lambda_{onset}}$$

Equation 4. Estimation of the band gap from the onset of absorption of the lowest energy absorption feature in the UV-vis spectrum.

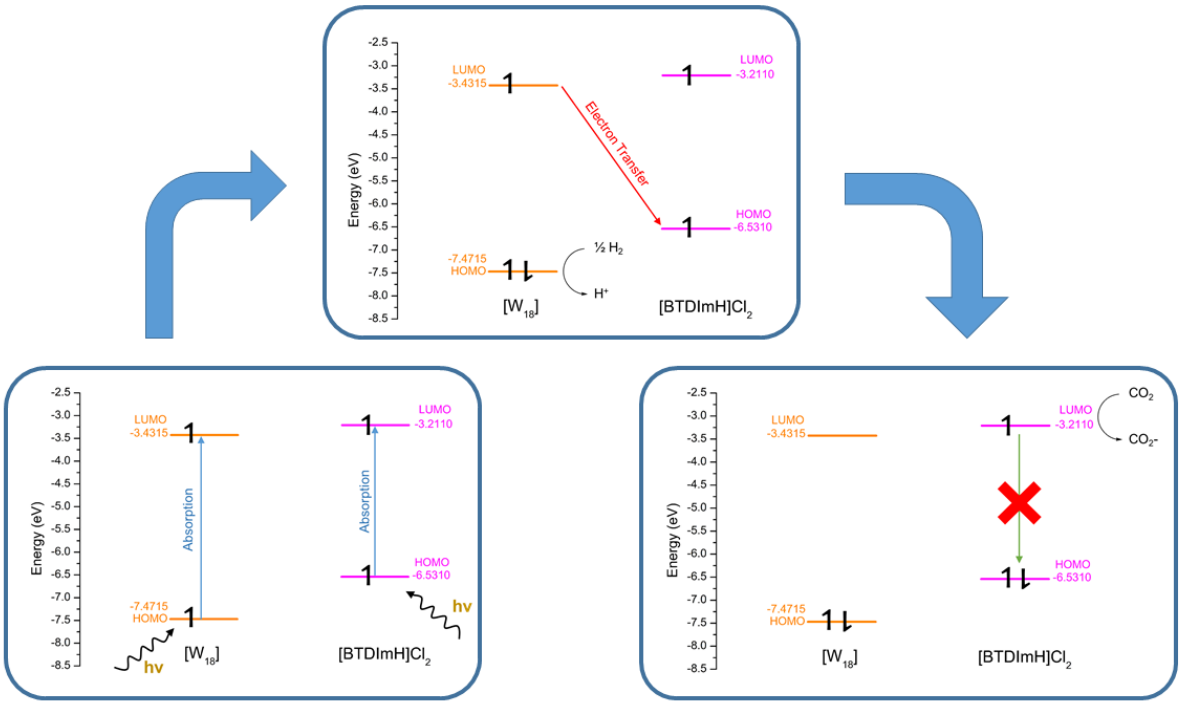


Figure 60. Possible photoexcitation mechanism for the photocatalytic system: photoexcitation of POM leads to oxidation of H2, the reduced POM is then able to transfer its electron to the photoexcited BTDImH cation, the entrapped excited electron on BTDImH can then photoreduce CO_2.

2.4 Conclusion

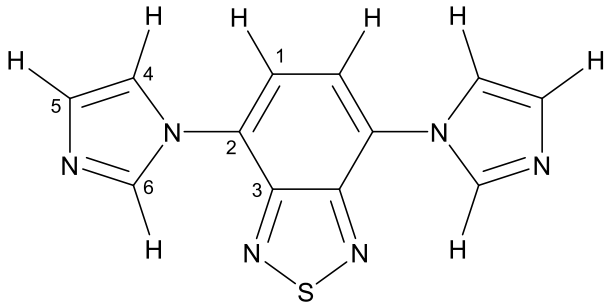
In conclusion, the first example of Class I hybrids featuring polyoxometalates paired with benzothiadiazole-imidazolium cations have been reported. Three distinct materials were produced which featured different cationic functionalities, namely protic, methylene and acetic acid. The hybrids were easily prepared from their salt precursors through metathesis reactions. The hybrids were confirmed to be composed of three of the BTDImR dications paired with the hexaanionic polyoxometalate as expected from charge balancing. The compounds were extensively characterised structurally by ^{1}H and ^{31}P NMR, IR spectroscopy and X-ray crystallography, thermophysically via TGA and DSC and electronically with UV-vis, cyclic voltammetry and fluorimetry. X-ray crystallography revealed that for BTDImH[W_{18}], there is significant ring torsion between the benzothiadiazole and imidazolium units, whereas the halide salts of these cations are highly planar due to internal hydrogen bonding between the C2-H and nitrogen on the thiadiazole unit. Challenges were encountered with electrochemical analysis, as the compounds underwent undesirable electrodissolution processes or exhibited highly complex redox behaviour.

The UV-vis spectra of the compounds were measured in both solid and solution phases. In solution, it appeared that the cations that absorbed at longer wavelengths served to increase the absorption profiles of the hybrids and showed distinctive differences based on the cation. In the solid-state however, the hybrids showed little variation between different BTDIm derivatives and were large band gap materials. The solid-state fluorescent properties of the BTDImH cation were quenched on pairing with the polyoxometalate, due to conformational changes of the fluorophore induced by intermolecular hydrogen bonding interactions in the solid-state, excited electron transfer from the organic dye molecule to the POM, or a combination of the two. BTDImH[W_{18}] was selected as the lead material for testing in the photoactivation of small molecules. The material was inactive towards water oxidation but showed activity towards the photoconversion of CO_2 to CO with H_2 as a sacrificial electron donor. Parallel experiments testing the reactions in the dark, in the absence of catalyst or with the precursor salts as catalyst confirmed that a synergic effect is exhibited by the hybrids which invokes activity towards CO_2 photoreduction. The TON and TOF numbers obtained after 24 hours of reaction were low but could be improved through set up and reactor design.

The project showed significant promise for further development, especially with regards to true solid-state electrochemical measurement of the hybrid species, for example by exploring different methods of material immobilisation such as carbon paste or vitreous reticulated carbon electrodes. Furthermore, the photocatalytic work can be expanded by trialling all the hybrid materials and fully determining the role of the two ions in the photocatalytic cycle through aforementioned techniques and studies. In general, the area of POM cationic dye Class I hybrids represents an underrepresented yet intriguing field within POM photocatalysts, where the further development of these species could involve the tailoring of the cation to control its specific interactions with each other, with the POM core, and with substrates in a photocatalytic system.

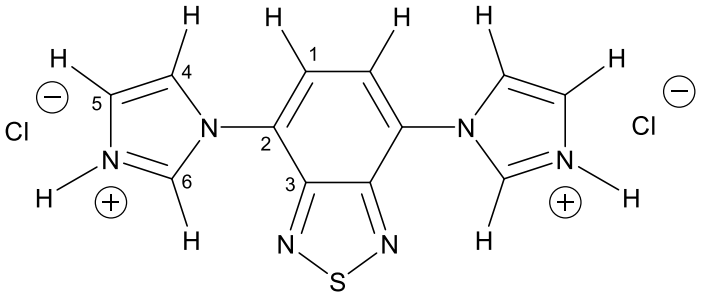
2.5 Experimental

Synthesis of 4,7-Diimidazole-2,1,3-benzathiadiazole "BTDIm"



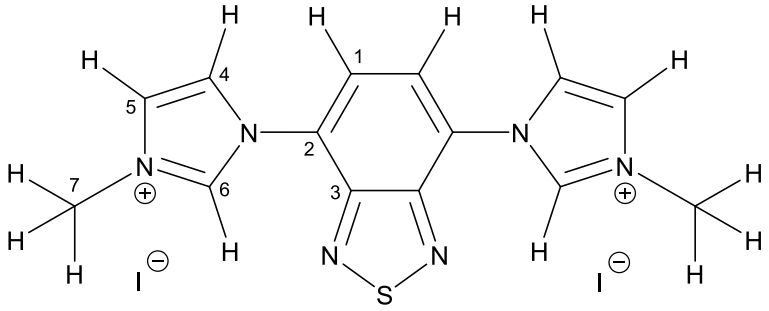
4,7-Dibromo-2,1,3-benzathiadiazole (6 g, 0.020 mol), K_2CO_3 (6 g, 0.043 mol), Cu_2O (0.16 g, 0.002 mol) and imidazole (3.6 g, 0.053 mol) were dissolved in anhydrous DMSO (30 ml) under an inert atmosphere giving a pale red solution. This was then heated at 150°C for 48 hrs, upon heating the reaction mixture immediately turned dark brown and after 48 hrs a black suspension had formed. The reaction mixture was then Buchner filtered and the solid was washed copious DCM, the filtrate was then concentrated under reduced pressure to give the crude product as an orange-brown powder. The product was purified with silica column chromatography (EtOAc/MeOH 9:1) and solvent removed *in vacuo* to give the final product as an orange powder (3.41 g, 63%), the product may also be obtained as orange needle like crystals through slow evaporation of the solvent (DCM). ^{1}H NMR (DMSO-d_6, 400MHz, ppm): δ = 8.58 (C6-Hs, 2H), 8.06 (C4/5-H, s, 4H), 7.24 (C1-H, s, 2H). *m/z* 269.06 (M^+ + H, 100%). ^{13}C NMR (DMSO-d_6, 400MHz, ppm): δ = 159.9 (C3), 149.2 (C6), 127.6 (C1), 121.3 (C5), 115.1 (C4), 108.5 (C2). ATR-IR (cm^{-1}): 3137, 1608, 1514, 1479, 1317, 1251, 1103, 1077, 1015, 824, 753, 650, 605, 543. λ_{max} (DMSO): 307nm (sh), 316nm (ε = 4630 $dm^3mol^{-1}cm^{-1}$), 380nm (ε = 2850 $dm^3mol^{-1}cm^{-1}$). *Anal.* Calcd. for $C_{12}H_8N_6S$ (268.30): C 53.72, H 3.01, N 31.32. Found: C 53.55, H 2.88, N 30.78.

Synthesis of 4,7-Diimidazolium-2,1,3-benzathiadiazole dichloride "[BTDImH]Cl_2"



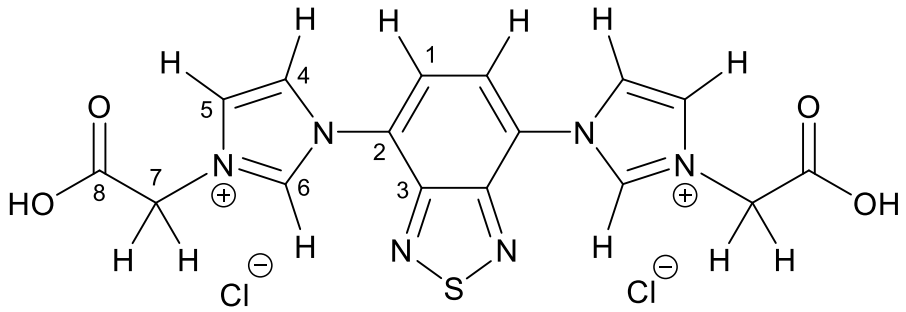
BTDIm (0.25 g, 0.932 mmol) was dissolved in methanol (12 ml). The solution was then cooled to 0°C and acetyl chloride was added dropwise with stirring until a creamy orange precipitate had formed. This was then filtered and washed several times with ethyl acetate to give the final product as a pale orange solid (0.25 g, 77%). ^{1}H NMR (DMSO-d_6, 500MHz, ppm): δ = 9.70 (C6-H, s, 2H, CH_{Im}), 8.43 (C5-H, t, J=2.1Hz, 2H, CH_{Im}), 8.40 (C1-H, s, 2H, CH_{Ar}), 7.90 (C4-H, s, 2H, CH_{Im}). ^{13}C NMR (DMSO-d_6, 500MHz, ppm): δ = 148.9 (C3), 137.3 (C6), 127.4 (C1), 124.0 (C5), 123.0 (C4), 122.5 (C2). *m/z* 135.04 (M^{2+}, 100%). ATR-IR (cm^{-1}): 3059, 3012, 1902, 1621, 1571, 1538, 1370, 1155, 960, 826, 613, 506, 443. λ_{max} (DMSO): 306nm (sh), 316nm (ε = 8540 $dm^3mol^{-1}cm^{-1}$), 373nm (ε = 5000 $dm^3mol^{-1}cm^{-1}$). *Anal.* Calcd. for $C_{12}H_{10}N_6SCl_2$ (341.22): C 42.24, H 2.95, N 24.63. Found: C 42.19, H 2.91, N 23.78.

Synthesis of 4,7-Di(3-methylimidazolium)-2,1,3-benzathiadiazole diiodide "[BTDImMe]I_2"



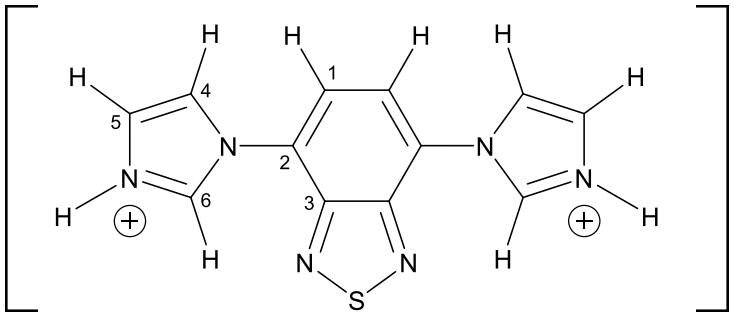
BTDIm (0.45 g, 1.68 mol) and iodomethane (0.75 g, 5.28 mmol) were dissolved in acetonitrile (10 ml) under an inert atmosphere. The solution was then refluxed at 100°C for 24 hours, which formed a bright orange precipitate. This was then filtered and washed several times with ethyl acetate to give the final product as an orange powder (0.72 g, 78%). ^{1}H NMR (DMSO-d_6, 500MHz, ppm): δ = 10.14 (C6-H, m, 2H, CH_{Im}), 8.55 (C5-H, t, J=1.9Hz, 2H, CH_{Im}), 8.47 (C1-H, s, 2H, CH_{Ar}), 8.14 (C4-H, t, J=1.9Hz, 2H, CH_{Im}), 4.10 (C7-H, s, 6H, CH_3). ^{13}C NMR (DMSO-d_6, 500MHz, ppm): δ = 148.7 (C3), 138.3 (C6), 127.1 (C1), 124.9 (C5), 124.1 (C4), 123.9 (C2), 37.1 (C7). m/z 149.09 (M^{2+}, 100%). ATR-IR (cm-1): 3053, 3022, 1902, 1623, 1576, 1538, 1366, 1243, 1132, 1115, 1012, 874, 814, 769, 748, 609, 550, 535, 503. λ_{max} (DMSO): 306nm (sh), 316nm (ε = 5749 $dm^3mol^{-1}cm^{-1}$), 352nm (sh). *Anal.* Calcd. for $C_{14}H_{14}N_6SI_2$ (552.17): C 30.45, H 2.56, N 15.22. Found: C 26.99, H 2.05, N 13.66.

Synthesis of 4,7-Di(3-acetylimidazolium)-2,1,3-benzathiadiazole dichloride "[BTDImAc]Cl_2"



BTDIm (0.497 g, 1.69 mmol) and chloroacetic acid (0.435 g, 4.60 mmol) were dissolved in acetonitrile. The reaction mixture was heated at reflux (90°C) for 96 hrs which produced a pale orange precipitate. This was then isolated by Buchner filtration and washed with acetonitrile giving the product as a pale orange powder (0.216 g, 28%). ^{1}H NMR (DMSO-d_6, 500MHz, ppm): δ = 10.35 (C6-H, m, 2H, CH_{Im}), 8.64 (C5-H, t, J=1.8Hz, 2H, CH_{Im}), 8.56 (C1-H, s, 2H, CH_{Ar}), 8.21 (C4-H, t, J=1.7Hz, 2H, CH_{Im}), 5.36 (C7-H, s, 4H, CH_2). ^{13}C NMR (DMSO-d_6, 500MHz, ppm): δ = 168.19 (C8), 148.6 (C3), 139.0 (C6), 127.1 (C1), 125.2 (C5), 124.1 (C4), 122.7 (C2), 51.0 (C7). *m/z* 193.03 (M^{2+}, 100%). ATR-IR (cm^{-1}): 3059, 2917, 1727, 1621, 1571, 1538, 1370, 1317, 1243, 1122, 1013, 845, 826, 777, 664, 607, 504, 443. λ_{max} (DMSO): 305nm (sh), 317nm (ε = 9990 $dm^3mol^{-1}cm^{-1}$), 353nm (sh). *Anal.* Calcd. for $C_{16}H_{14}N_6O_4SCl_2$ (457.29): C 42.02, H 3.09, N 18.38. Found: C 38.87, H 3.16, N 16.66.

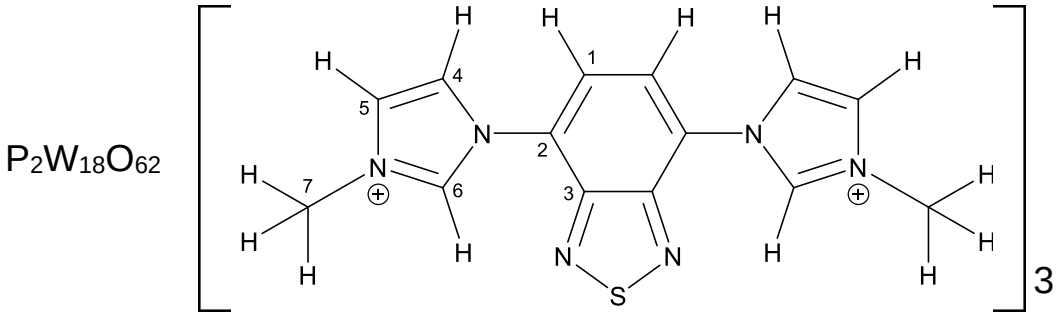
Synthesis of $(BTDImH)_3[P_2W_{18}O_{62}]$ "BTDImH[W_{18}]"

$P_2W_{18}O_{62}$  3

[BTDImH]Cl_2 (0.44 g, 1.29 mmol) was dissolved in deionised water (15 ml). This was added dropwise to a stirring solution of $K_6P_2W_{18}O_{62}$ (2.09 g, 0.430 mmol) in deionised water (15 ml) which caused the immediate formation of a fine yellow precipitate. The reaction mixture was stirred overnight, and the fine yellow precipitate was collected by Buchner filtration. The precipitate was washed with deionised

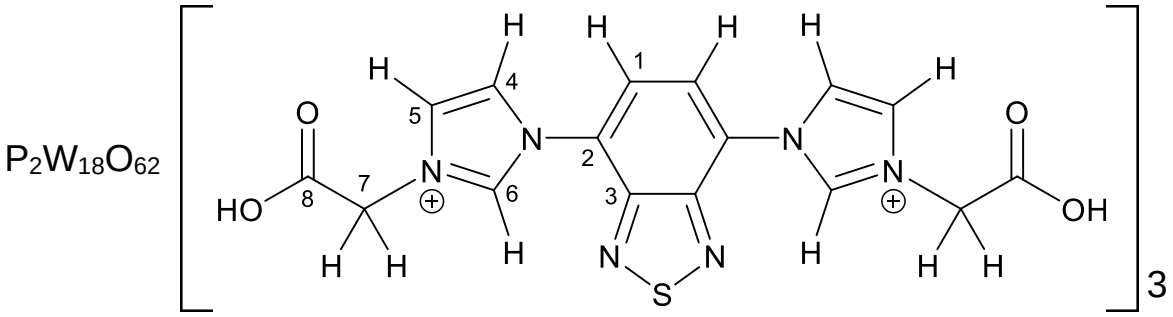
water and ethyl acetate to yield the final product as a yellow powder (0.737 g, 22%). ^{1}H NMR (DMSO-d_6, 400MHz, ppm): δ = 9.15 (C6-H, s, 2H, CH_{Im}), 8.22 (C4/5-H, s, 4H, CH_{Im}), 7.57 (C1-H, s, 2H, CH_{Ar}). ^{31}P NMR (DMSO-d_6, 202MHz, ppm): δ = -13.08. ATR-IR (cm^{-1}): 3133 (CH stretch aliphatic, w), 1540 (C=N stretch aromatic, w) 1370 (C=C stretch aromatic, w), 1085 (P-O stretch, s), 954 (W=O_d stretch, s), 901 (W-O_b-W, s), 730 (W-O_c-W, b). λ_{max} (DMSO): 304nm (ε = 8107 $dm^3mol^{-1}cm^{-1}$), 317 (sh) 373nm (ε = 2597 $dm^3mol^{-1}cm^{-1}$). *Anal.* Calcd. for $C_{36}H_{30}N_{18}S_3P_2W_{18}O_{62}$ (5173.97): C 8.36, H 0.58, N 4.87. Found: C 8.01, H 0.77, N, 4.29.

Synthesis of $(BTDImMe)_3[P_2W_{18}O_{62}]$ "BTDImMe[W_{18}]"



[BTDImMe]I_2 (0.60 g, 1.29 mmol) was dissolved in a mixture of deionised water (20 ml) and acetone (10 ml). This was added dropwise to a stirring solution of $K_6P_2W_{18}O_{62}$ (2.09 g, 0.430 mmol) in deionised water (10 ml) which caused the immediate formation of a creamy orange precipitate. The reaction mixture was stirred overnight, and the orange precipitate was collected by Buchner filtration. The precipitate was washed with deionised water and ethyl acetate to yield the final product as an orange powder (1.69 g, 71%). ^{1}H NMR (DMSO-d_6, 400MHz, ppm): δ = 10.06 (C6-H, m, 2H, CH_{Im}), 8.52 (C5-H, m, 2H, CH_{Im}), 8.44 (C1-H, s, 2H, CH_{Ar}), 8.08 (C4-H, s, 2H, CH_{Im}), 4.11 (C7-H, s, 6H, CH_3). ^{31}P NMR (DMSO-d_6, 202MHz, ppm): δ = -13.15. ATR-IR (cm^{-1}): 3105 (CH stretch aliphatic, w), 1582 (C=N stretch aromatic, w) 1549 (C=C stretch aromatic, w), 1088 (P-O stretch, s), 954 (W=O_d stretch, s), 907 (W-O_b-W, s), 763 (W-O_c-W, b). λ_{max} (DMSO): 305nm (ε = 7522 $dm^3mol^{-1}cm^{-1}$), 317 (sh). *Anal.* Calcd. for $C_{42}H_{42}N_{18}S_3P_2W_{18}O_{62}$ (5258.13): C 9.594, H 0.805, N 4.795. Found: C 9.32, H 0.46, N 3.70.

Synthesis of $(BTDImAc)_3[P_2W_{18}O_{62}]$ "BTDImAc[W_{18}]"



[BTDImAc]Cl_2 (0.59 g, 1.29 mmol) was dissolved in a mixture of deionised water (10 ml) and acetone (10 ml). This was added dropwise to a stirring solution of $K_6P_2W_{18}O_{62}$ (2.09 g, 0.430 mmol) in deionised water (10 ml) which caused the immediate formation of a pale yellow precipitate. The reaction mixture was stirred overnight, and the pale yellow precipitate was collected by Buchner filtration. The precipitate was washed with deionised water and ethyl acetate to yield the final product as a pale yellow powder (1.34 g, 53%). ^{1}H NMR (DMSO-d_6, 400MHz, ppm): δ = 10.15 (C6-H, m, 2H, CH_{Im}), 8.58 (C5-H, m, 2H, CH_{Im}), 8.51 (C1-H, s, 2H, CH_{Ar}), 8.13 (C4-H, s, 2H, CH_{Im}), 5.36 (C7-H, s, 4H, CH_2). ^{31}P NMR (DMSO-d_6, 202MHz, ppm): δ = -13.13. ATR-IR (cm^{-1}): 3363 (O-H stretch, b), 1732 (C=O stretch, m), 1621 (O-H bend, m), 1549 (C=N aromatic stretch, s), 1085 (P-O stretch, s), 954 (W=O_d stretch, s), 903 (W-O_b-W, s), 761 (W-O_c-W, s). λ_{max} (DMSO): 308nm (ε = 6754 $dm^3mol^{-1}cm^{-1}$), 317 (sh). *Anal.* Calcd. for $C_{48}H_{42}N_{18}S_3P_2W_{18}O_{62}$ (5330.19): C 10.82, H 0.79, N 4.73. Found: C 9.38, H 0.60, N 4.18.

2.6 References

1. V. M. Hultgren, A. M. Bond and A. G. Wedd, *J. Chem. Soc., Dalton Trans.*, 2001, DOI: 10.1039/B008682G, 1076-1082.
2. T. E. Keyes, E. Gicquel, L. Guerin, R. J. Forster, V. Hultgren, A. M. Bond and A. G. Wedd, *Inorg. Chem.*, 2003, **42**, 7897-7905.
3. K. Heussner, K. Peuntinger, N. Rockstroh, L. C. Nye, I. Ivanovic-Burmazovic, S. Rau and C. Streb, *Chem. Commun.*, 2011, **47**, 6852-6854.
4. N. Sakai, J. Mareda, E. Vauthey and S. Matile, *Chem. Commun.*, 2010, **46**, 4225-4237.
5. P. Le Maguerès, S. M. Hubig, S. V. Lindeman, P. Veya and J. K. Kochi, *J. Am. Chem. Soc.*, 2000, **122**, 10073-10082.
6. S. Gao, R. Cao and C. Yang, *J. Colloid Interface Sci.*, 2008, **324**, 156-166.
7. J.-D. Compain, P. Mialane, A. Dolbecq, J. Marrot, A. Proust, K. Nakatani, P. Yu and F. Sécheresse, *Inorg. Chem.*, 2009, **48**, 6222-6228.

8. M. Bonchio, Z. Syrgiannis, M. Burian, N. Marino, E. Pizzolato, K. Dirian, F. Rigodanza, G. A. Volpato, G. La Ganga, N. Demitri, S. Berardi, H. Amenitsch, D. M. Guldi, S. Caramori, C. A. Bignozzi, A. Sartorel and M. Prato, *Nat. Chem.*, 2019, **11**, 146-153.
9. A. Tian, H. Ni, X. Ji, Y. Tian, G. Liu and J. Ying, *RSC Adv.*, 2017, **7**, 30573-30581.
10. H. Koopman, J. J. van Daalen and J. Daams, *Weed Res.*, 1967, **7**, 200-207.
11. L. Friedrich, K. Lawton, W. Ruess, P. Masner, N. Specker, M. G. Rella, B. Meier, S. Dincher, T. Staub, S. Uknes, J. P. Metraux, H. Kessmann and J. Ryals, *Plant J.*, 1996, **10**, 61-70.
12. J. Gorlach, S. Volrath, G. KnaufBeiter, G. Hengy, U. Beckhove, K. H. Kogel, M. Oostendorp, T. Staub, E. Ward, H. Kessmann and J. Ryals, *Plant Cell*, 1996, **8**, 629-643.
13. K. Ijichi, M. Fujiwara, H. Nagano, Y. Matsumoto, Y. Hanasaki, T. Ide, K. Katsuura, H. Takayama, S. Shirakawa, N. Aimi, S. Shigeta, K. Konno, M. Matsushima, T. Yokota and M. Baba, *Antiviral Res.*, 1996, **31**, 87-94.
14. O. Hinsberg, *Ber. Dtsch. Chem. Ges.*, 1889, **22**, 2895-2902.
15. A. Michaelis, *Justus Liebigs Ann. Chem.*, 1893, **274**, 200-266.
16. K. Pilgram, M. Zupan and R. Skiles, *J. Heterocycl. Chem.*, 1970, **7**, 629-633.
17. K. Pilgram and M. Zupan, *J. Org. Chem.*, 1971, **36**, 207-209.
18. P. B. Ghosh and B. J. Everitt, *J. Med. Chem.*, 1974, **17**, 203-206.
19. T. Uno, K. Takagi and M. Tomoeda, *Chem. Pharm. Bull.*, 1978, **26**, 3896-3901.
20. T. Uno, K. Takagi and M. Tomoeda, *Chem. Pharm. Bull.*, 1980, **28**, 1909-1912.
21. Y. Yamashita, T. Suzuki, T. Mukai and G. Saito, *J. Chem. Soc., Chem. Commun.*, 1985, DOI: 10.1039/C39850001044, 1044-1045.
22. S. Takanori, K. Chizuko, Y. Yoshiro and M. Toshio, *Bull. Chem. Soc. Jpn.*, 1987, **60**, 2111-2115.
23. Y. Yoshiro, T. Shoji, I. Kenichi and I. Hiroo, *Chem. Lett.*, 1991, **20**, 1213-1216.
24. Y. Yamashita, K. Saito, T. Suzuki, C. Kabuto, T. Mukai and T. Miyashi, *Angew. Chem. Int. Ed. Engl.*, 1988, **27**, 434-435.
25. A. Ugawa, K. Iwasaki, A. Kawamoto, K. Yakushi, Y. Yamashita and T. Suzuki, *Phys. Rev.*, 1991, **43**, 14718-14721.
26. T. Suzuki, Y. Yamashita, C. Kabuto and T. Miyashi, *J. Chem. Soc., Chem. Commun.*, 1989, DOI: 10.1039/C39890001102, 1102-1103.
27. T. Suzuki, H. Fujii, Y. Yamashita, C. Kabuto, S. Tanaka, M. Harasawa, T. Mukai and T. Miyashi, *J. Am. Chem. Soc.*, 1992, **114**, 3034-3043.
28. K. Takaki and Y. Takakazu, *Chem. Lett.*, 1993, **22**, 419-422.
29. M. Karikomi, C. Kitamura, S. Tanaka and Y. Yamashita, *J. Am. Chem. Soc.*, 1995, **117**, 6791-6792.
30. Y. He, S. Gong, R. Hattori and J. Kanicki, *Appl. Phys. Lett.*, 1999, **74**, 2265-2267.
31. Y. P. Shi, G. L. Xue, H. M. Hu, F. Fu and J. W. Wang, *J. Coord. Chem.*, 2006, **59**, 1739-1747.
32. W.-Y. Wong, X.-Z. Wang, Z. He, A. B. Djurišić, C.-T. Yip, K.-Y. Cheung, H. Wang, C. S. K. Mak and W.-K. Chan, *Nat. Mater.*, 2007, **6**, 521.
33. L. Yang, J.-K. Feng and A.-M. Ren, *J. Mol. Struc. Theochem*, 2007, **816**, 161-170.
34. Y. Hou, Y. Chen, Q. Liu, M. Yang, X. Wan, S. Yin and A. Yu, *Macromolecules*, 2008, **41**, 3114-3119.
35. P. M. Beaujuge, W. Pisula, H. N. Tsao, S. Ellinger, K. Müllen and J. R. Reynolds, *J. Am. Chem. Soc.*, 2009, **131**, 7514-7515.
36. C. Duan, K. Zhang, X. Guan, C. Zhong, H. Xie, F. Huang, J. Chen, J. Peng and Y. Cao, *Chem. Sci.*, 2013, **4**, 1298-1307.
37. H. Yan, P. Lee, N. R. Armstrong, A. Graham, G. A. Evmenenko, P. Dutta and T. J. Marks, *J. Am. Chem. Soc.*, 2005, **127**, 3172-3183.
38. M. A. Karim, Y.-R. Cho, J. S. Park, S. C. Kim, H. J. Kim, J. W. Lee, Y.-S. Gal and S.-H. Jin, *Chem. Commun.*, 2008, 1929-1931.
39. R. C. Coffin, J. Peet, J. Rogers and G. C. Bazan, *Nat. Chem.*, 2009, **1**, 657.

40. G. L. Frey, K. J. Reynolds, R. H. Friend, H. Cohen and Y. Feldman, *J. Am. Chem. Soc.*, 2003, **125**, 5998-6007.
41. C. D. Müller, A. Falcou, N. Reckefuss, M. Rojahn, V. Wiederhirn, P. Rudati, H. Frohne, O. Nuyken, H. Becker and K. Meerholz, *Nature*, 2003, **421**, 829-833.
42. Q. Fang, B. Xu, B. Jiang, H. Fu, X. Chen and A. Cao, *Chem. Commun.*, 2005, DOI: 10.1039/B417810F, 1468-1470.
43. Y. Yang, Y. Zhou, Q. He, C. He, C. Yang, F. Bai and Y. Li, *J. Phys. Chem. B*, 2009, **113**, 7745-7752.
44. J. Y. Kim, K. Lee, N. E. Coates, D. Moses, T.-Q. Nguyen, M. Dante and A. J. Heeger, *Science*, 2007, **317**, 222.
45. J. Peet, J. Y. Kim, N. E. Coates, W. L. Ma, D. Moses, A. J. Heeger and G. C. Bazan, *Nat. Mater.*, 2007, **6**, 497.
46. S. H. Park, A. Roy, S. Beaupré, S. Cho, N. Coates, J. S. Moon, D. Moses, M. Leclerc, K. Lee and A. J. Heeger, *Nat. Photonics*, 2009, **3**, 297.
47. J. You, L. Dou, K. Yoshimura, T. Kato, K. Ohya, T. Moriarty, K. Emery, C.-C. Chen, J. Gao, G. Li and Y. Yang, *Nat. Commun.*, 2013, **4**, 1446.
48. Y. Liu, J. Zhao, Z. Li, C. Mu, W. Ma, H. Hu, K. Jiang, H. Lin, H. Ade and H. Yan, *Nat. Commun.*, 2014, **5**, 5293.
49. M. Zhang, H. N. Tsao, W. Pisula, C. Yang, A. K. Mishra and K. Müllen, *J. Am. Chem. Soc.*, 2007, **129**, 3472-3473.
50. W. Zhang, J. Smith, S. E. Watkins, R. Gysel, M. McGehee, A. Salleo, J. Kirkpatrick, S. Ashraf, T. Anthopoulos, M. Heeney and I. McCulloch, *J. Am. Chem. Soc.*, 2010, **132**, 11437-11439.
51. H. N. Tsao, D. M. Cho, I. Park, M. R. Hansen, A. Mavrinskiy, D. Y. Yoon, R. Graf, W. Pisula, H. W. Spiess and K. Müllen, *J. Am. Chem. Soc.*, 2011, **133**, 2605-2612.
52. J. D. Yuen and F. Wudl, *Energy Environ. Sci.*, 2013, **6**, 392-406.
53. Q. Zou and H. Tian, *Sens. Actuators B Chem.*, 2010, **149**, 20-27.
54. Y. Dong, B. Koken, X. Ma, L. Wang, Y. Cheng and C. Zhu, *Inorg. Chem. Commun.*, 2011, **14**, 1719-1722.
55. X. Ma, F. Song, L. Wang, Y. Cheng and C. Zhu, *J. Polym. Sci., Part A: Polym. Chem.*, 2012, **50**, 517-522.
56. Y. Lei, H. Li, W. Gao, M. Liu, J. Chen, J. Ding, X. Huang and H. Wu, *J. Mater. Chem. C*, 2014, **2**, 7402-7410.
57. B. Liu and G. C. Bazan, *J. Am. Chem. Soc.*, 2004, **126**, 1942-1943.
58. L. An, Y. Tang, F. Feng, F. He and S. Wang, *J. Mater. Chem.*, 2007, **17**, 4147-4152.
59. K.-Y. Pu and B. Liu, *Macromolecules*, 2008, **41**, 6636-6640.
60. D. Yu, Y. Zhang and B. Liu, *Macromolecules*, 2008, **41**, 4003-4011.
61. K.-Y. Pu and B. Liu, *J. Phys. Chem. B*, 2010, **114**, 3077-3084.
62. H. Dzudzevic Cancar, S. Soylemez, Y. Akpinar, M. Kesik, S. Göker, G. Gunbas, M. Volkan and L. Toppare, *ACS Appl. Mater. Interfaces*, 2016, **8**, 8058-8067.
63. X. Gong, M. Tong, Y. Xia, W. Cai, J. S. Moon, Y. Cao, G. Yu, C.-L. Shieh, B. Nilsson and A. J. Heeger, *Science*, 2009, **325**, 1665.
64. M. P. Nikiforov, B. Lai, W. Chen, S. Chen, R. D. Schaller, J. Strzalka, J. Maser and S. B. Darling, *Energy Environ. Sci.*, 2013, **6**, 1513-1520.
65. H. Shang, H. Fan, Y. Liu, W. Hu, Y. Li and X. Zhan, *Adv. Mater.*, 2011, **23**, 1554-1557.
66. A. Yella, C. L. Mai, S. M. Zakeeruddin, S. N. Chang, C. H. Hsieh, C. Y. Yeh and M. Gratzel, *Angew. Chem. Int. Ed.*, 2014, **53**, 2973-2977.
67. Y. Wu, M. Marszalek, S. M. Zakeeruddin, Q. Zhang, H. Tian, M. Grätzel and W. Zhu, *Energy Environ. Sci.*, 2012, **5**, 8261-8272.
68. M. Zhang, Y. L. Wang, M. F. Xu, W. T. Ma, R. Z. Li and P. Wang, *Energy Environ. Sci.*, 2013, **6**, 2944-2949.
69. G. Qian, Z. Zhong, M. Luo, D. Yu, Z. Zhang, Z. Y. Wang and D. Ma, *Adv. Mater.*, 2009, **21**, 111-116.

70. P. Moonsin, N. Prachumrak, S. Namuangruk, S. Jungsuttiwong, T. Keawin, T. Sudyoadsuk and V. Promarak, *Chem. Commun.*, 2013, **49**, 6388-6390.
71. N. J. Findlay, B. Breig, C. Forbes, A. R. Inigo, A. L. Kanibolotsky and P. J. Skabara, *J. Mater. Chem. C*, 2016, **4**, 3774-3780.
72. Y. Zhang, C. Kim, J. Lin and T.-Q. Nguyen, *Adv. Funct. Mater.*, 2012, **22**, 97-105.
73. G. Yang, C.-a. Di, G. Zhang, J. Zhang, J. Xiang, D. Zhang and D. Zhu, *Adv. Funct. Mater.*, 2013, **23**, 1671-1676.
74. N. M. Tucker, A. L. Briseno, O. Acton, H.-L. Yip, H. Ma, S. A. Jenekhe, Y. Xia and A. K. Y. Jen, *ACS Appl. Mater. Interfaces*, 2013, **5**, 2320-2324.
75. J.-M. Raimundo, P. Blanchard, H. Brisset, S. Akoudad and J. Roncali, *Chem. Commun.*, 2000, DOI: 10.1039/B002369H, 939-940.
76. M. Akhtaruzzaman, M. Tomura, J.-i. Nishida and Y. Yamashita, *J. Org. Chem.*, 2004, **69**, 2953-2958.
77. X. Zhang, R. Yamaguchi, K. Moriyama, M. Kadowaki, T. Kobayashi, T. Ishi-i, T. Thiemann and S. Mataka, *J. Mater. Chem.*, 2006, **16**, 736-740.
78. Y. Li, L. Scudiero, T. Ren and W.-J. Dong, *J. Photochem. Photobiol. A Chem.*, 2012, **231**, 51-59.
79. E. H. G. da Cruz, P. H. P. R. Carvalho, J. R. Corrêa, D. A. C. Silva, E. B. T. Diogo, J. D. de Souza Filho, B. C. Cavalcanti, C. Pessoa, H. C. B. de Oliveira, B. C. Guido, D. A. da Silva Filho, B. A. D. Neto and E. N. da Silva Júnior, *New J. Chem.*, 2014, **38**, 2569-2580.
80. T. Ishi-i, M. Sakai and C. Shinoda, *Tetrahedron*, 2013, **69**, 9475-9480.
81. T. E. A. Frizon, J. C. Valdivia Martínez, J. L. Westrup, R. d. C. Duarte, E. Zapp, K. G. Domiciano, F. S. Rodembusch and A. G. Dal-Bó, *Dyes Pigm.*, 2016, **135**, 26-35.
82. S. Maisonneuve, Q. Fang and J. Xie, *Tetrahedron*, 2008, **64**, 8716-8720.
83. Y.-B. Ruan, S. Maisonneuve, C. Li, J. Tang and J. Xie, *Front. Chem. Chin.*, 2010, **5**, 208-213.
84. B. Wang, H. Pan, J. Jia, Y.-Q. Ge, W.-Q. Cai, J.-W. Wang and C.-H. Zhao, *Tetrahedron*, 2014, **70**, 5488-5493.
85. Q. Zhang, J. Zhang, H. Zuo, C. Wang and Y. Shen, *Tetrahedron*, 2016, **72**, 1244-1248.
86. Y. Yu, N. Bogliotti, S. Maisonneuve, J. Tang and J. Xie, *Tetrahedron Lett.*, 2013, **54**, 1877-1883.
87. B. A. D. Neto, A. A. M. Lapis, F. S. Mancilha, E. L. Batista Jr, P. A. Netz, F. Rominger, L. A. Basso, D. S. Santos and J. Dupont, *Mol. Biosyst.*, 2010, **6**, 967-975.
88. P. A. Netz, *Int. J. Quantum Chem.*, 2012, **112**, 3296-3302.
89. B. A. D. Neto, J. R. Corrêa, P. H. P. R. Carvalho, D. C. B. D. Santos, B. C. Guido, C. C. Gatto, H. C. B. d. Oliveira, M. Fasciotti, M. N. Eberlin and E. N. d. Silva Jr., *J. Braz. Chem. Soc.*, 2012, **23**, 770-781.
90. Q. Jiang, Z. Zhang, J. Lu, Y. Huang, Z. Lu, Y. Tan and Q. Jiang, *Biorg. Med. Chem.*, 2013, **21**, 7735-7741.
91. A. A. R. Mota, P. H. P. R. Carvalho, B. C. Guido, H. C. B. de Oliveira, T. A. Soares, J. R. Corrêa and B. A. D. Neto, *Chem. Sci.*, 2014, **5**, 3995-4003.
92. F. F. D. Oliveira, D. C. B. D. Santos, A. A. M. Lapis, J. R. Corrêa, A. F. Gomes, F. C. Gozzo, P. F. Moreira, V. C. de Oliveira, F. H. Quina and B. A. D. Neto, *Bioorg. Med. Chem. Lett.*, 2010, **20**, 6001-6007.
93. B. A. D. Neto, P. H. P. R. Carvalho, D. C. B. D. Santos, C. C. Gatto, L. M. Ramos, N. M. d. Vasconcelos, J. R. Corrêa, M. B. Costa, H. C. B. de Oliveira and R. G. Silva, *RSC Adv.*, 2012, **2**, 1524-1532.
94. W. Qin, K. Li, G. Feng, M. Li, Z. Yang, B. Liu and B. Z. Tang, *Adv. Funct. Mater.*, 2014, **24**, 635-643.
95. J. R. C. Virginia S. Souza, Pedro H. P. R. Carvalho, Gabriela I. Matiello, Patrícia C. Ferreira, Kelly G. Magalhães, Heibbe C. B. de Oliveira, Claudia C. Gatto, Gunter Ebeling, Jairton Dupont,Brenno A. D. Neto, unpublished work.
96. H. Lv, Y. V. Geletii, C. Zhao, J. W. Vickers, G. Zhu, Z. Luo, J. Song, T. Lian, D. G. Musaev and C. L. Hill, *Chem. Soc. Rev.*, 2012, **41**, 7572-7589.

97. Y. W. Cao, Q. Y. Chen, C. R. Shen and L. He, *Molecules*, 2019, **24**.
98. C. R. Graham and R. G. Finke, *Inorg. Chem.*, 2008, **47**, 3679-3686.
99. R. A. Altman, E. D. Koval and S. L. Buchwald, *J. Org. Chem.*, 2007, **72**, 6190-6199.
100. S. Cha, M. Ao, W. Sung, B. Moon, B. Ahlström, P. Johansson, Y. Ouchi and D. Kim, *PCCP*, 2014, **16**, 9591-9601.
101. S. Cha, T. Shim, Y. Ouchi and D. Kim, *J. Phys. Chem. B.*, 2013, **117**, 10818-10825.
102. D. J. Rowe, D. Smith and J. S. Wilkinson, *Sci. Rep.*, 2017, **7**, 7356.
103. L. E. Briand, G. T. Baronetti and H. J. Thomas, *Appl. Catal. A. Gen.*, 2003, **256**, 37-50.
104. M. J. A. Shiddiky and A. A. J. Torriero, *Biosens. Bioelectron.*, 2011, **26**, 1775-1787.
105. B. Chen and R. Neumann, *PCCP*, 2016, **18**, 22487-22493.
106. Y. Zheng, J. Liu, X. Yang and J. Wang, *J. Mol. Model.*, 2014, **20**.
107. J.-M. Savéant, *J Phys. Chem. B.*, 2001, **105**, 8995-9001.
108. G. Bernardini, C. Zhao, A. G. Wedd and A. M. Bond, *Inorg. Chem.*, 2011, **50**, 5899-5909.
109. V. Mirceski, S. Komorsky-Lovric and M. Lovric, *Square-Wave Voltammetry: Theory and Application*, Springer Berlin Heidelberg, 2007.
110. C. R. Guy and B. C. E, *Understanding Voltammetry (2nd Edition)*, World Scientific Publishing Company, 2010.
111. F. M. Mirabella, *Modern Techniques in Applied Molecular Spectroscopy*, Wiley, 1998.
112. B. D. Viezbicke, S. Patel, B. E. Davis and D. P. Birnie III, *Phys. Status Solidi B*, 2015, **252**.
113. G. Balcerowska, R. Siuda, J. Skrzypczak, A. Łukanowski and C. Sadowski, *Food Addit Contam. A*, 2009, **26**, 726-732.
114. S. Barman, S. S. Sreejith, S. Garai, R. Pochamoni and S. Roy, *ChemPhotoChem*, 2019, **3**, 93-100.
115. R. Liu, G. Zhang, H. Cao, S. Zhang, Y. Xie, A. Haider, U. Kortz, B. Chen, N. S. Dalal, Y. Zhao, L. Zhi, C.-X. Wu, L.-K. Yan, Z. Su and B. Keita, *Energy Environ. Sci.*, 2016, **9**, 1012-1023.
116. P.-C. Chiang and J. W. Bode, *Org. Lett.*, 2011, **13**, 2422-2425.
117. A. Riaño, P. Mayorga Burrezo, M. J. Mancheño, A. Timalsina, J. Smith, A. Facchetti, T. J. Marks, J. T. López Navarrete, J. L. Segura, J. Casado and R. Ponce Ortiz, *J. Mater. Chem. C*, 2014, **2**, 6376-6386.

3. Electronic structure and photocatalytic abilities of organoarsenic hybrid POMs

3.1 Introduction

Class II hybrids, as discussed in section 1.6.2, represents an exciting new avenue of exploration for the synthesis of well-defined and photoactive POM molecular catalysts and materials. Not only does the organofunctionalisation via anchoring groups give the POM chemist control over their structural properties, but the choice of anchoring group and organic components give a subtle yet powerful control over the POM's redox and optical properties, which is especially desirable for the design and optimisation of POMs in photocatalysis. This is exemplified best by the works of Newton, Oshio and co-workers,[1, 2] whereby the use of arylphosphonate linkers with different R-groups results in hybrids with predictable electronic properties that correlate directly with their photocatalytic performance. It is interesting that the phosphorus linker plays two key roles. Firstly, irrespective of the organic group, the phosphonate is able to withdraw electron density from the POM due to its electron withdrawing inductive effect. Secondly, when the organic substituent is conjugated, the ligand can withdraw electron density through resonance effects mediated by the phosphonate group, allowing the fine-tuning of the redox properties through modulation of the electron deficiency of the conjugated system.[3] These effects are not replicated with other linker systems employed for Keggin and Dawson polyoxotungstates (Si, Sn, Ge) due to their lack of resonance groups, and is in fact reversed due to their electron donating character.[4]

Spurred by this recent discovery of the *vis-endo* approach to the photosensitisation of POMs, we were interested in exploring new anchoring groups that could permit the electronic coupling of the organic group and the POM such that we could fine tune the redox properties of the POM in an analogous, or superior fashion as to that described above. We decided that a bonding format similar to phosphonic acids (i.e. possession of X=O bonding and two binding sites for condensation with the polyoxometalate) would provide the desired influence with good hydrolytic stability. Thus, we turned our attention to the isoelectronic arylarsonic acids. Arylarsonic acids comprise a pentavalent As(V) atom covalently bound to an aryl ring, two hydroxyl groups and a double bond to an oxygen atom (Figure 61). This small family

of compounds have been known and studied for over a century,[5, 6] with their historical uses focused on medicinal, veterinary and agricultural disciplines.[7, 8] Despite their toxicity, interest in organoarsenic compounds is burgeoning due to their diverse biochemical, biological and organometallic reactivities.[9] Of particular interest to us is the potential of organoarsenic acids to form strong bonds with metal oxide surfaces (TiO_2 and SiO_2) as was demonstrated by LaFranzo and Maurer et al.,[10] in this study it was shown that alkyl arsonates could be employed as 2D self-assembled monolayers on the surface of TiO_2 and SiO_2 and were more reactive than their alkyl phosphonate analogues – resulting in more robust coatings with superior wear-protection abilities. Ahn et al also demonstrated the robust binding properties of arylarsonic acids in the stabilisation of Fe_3O_4 nanoparticles, here arylarsonic acids acted as novel anchor groups that could be chemically post-functionalised via click chemistry and gave superior surface coverage, binding affinity and pH stability than the commonly employed anchors catechol and carboxylic acids.[11]

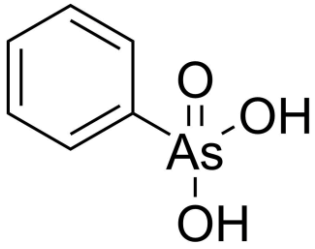


Figure 61. General structure of arylarsonic acids, with derivatives usually obtained through functionalisation of the phenyl ring.

Whilst the use of inorganic arsenates as templating atoms is relatively well-explored,[12-16] the use of organoarsenates as ligands and anchoring groups is much more esoteric. Firstly, it seems that polyoxovanadate and polyoxomolybdate hybrids dominate the literature whereas only a sparse number of polyoxotungstate hybrids have been reported. Furthermore, examples in the literature are typically centred on the structural (and superstructural) characterisation of hybrids formed from organoarsenates and monomeric metal oxoanion precursors with the adventitious one-pot approach. This has resulted in the synthesis of an impressive array of hybrid structures, however the degree of molecular design offered is somewhat limited and the exploration of their innate properties is often overlooked. Nonetheless, several exceptional papers highlight some of the interesting features of organoarsenate hybrids specifically featuring arylarsonic acids as the organic component. An early report by Khan et al.[17] synthesised two organoarsenic hybrid polyoxovanadates $(TBA)_2[V_6O_{18}(AsPh)_6]$ and $(TBA_2)(NH_4)_2[V_{10}O_{33}(AsPhNH_2)_3]$ from $(NH_4)_2Na_2K_2[V_{10}O_{28}]$ and arylarsonic acids with addition of TBABr. Curiously, identical reaction conditions for phenylarsonic acid and arsanilic acid led to

completely different hybrid structures with different oxidation states (Figure 62). These compounds were shown to be redox active, with $(TBA)_2(NH_4)_2[V_{10}O_{33}(AsPhNH_2)_3]$ undergoing both a proton decoupled reduction and several proton coupled oxidations, whereas $(TBA)_2[V_6O_{18}(AsPh)_6]$ undergoes two reversible one-electron oxidations.

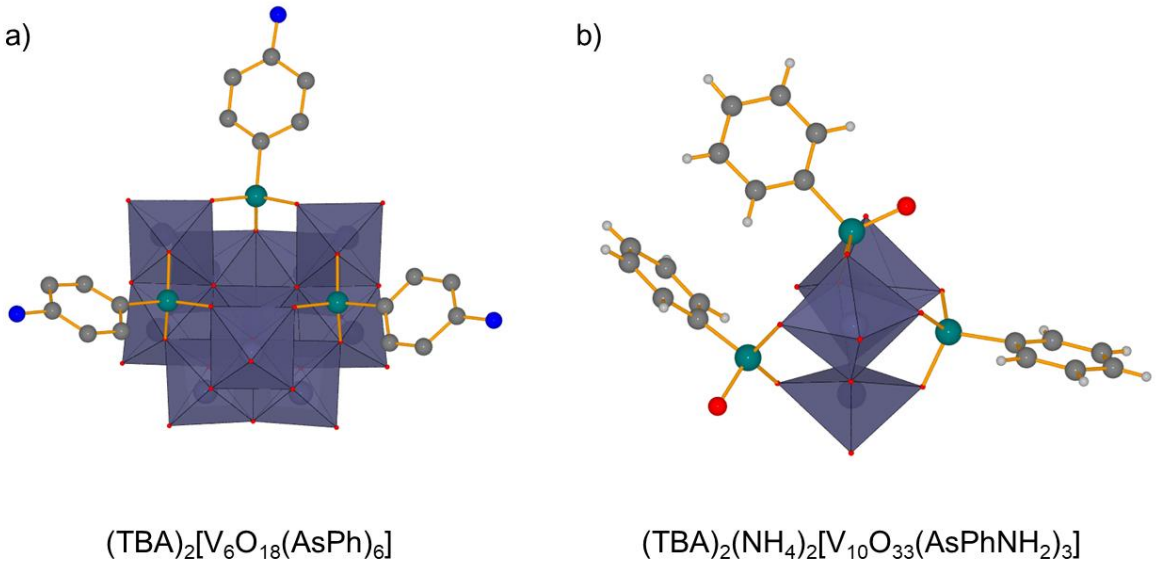


Figure 62. a) Structure of $(TBA)_2[V_6O_{18}(AsPh)_6]$. b) Structure of $(TBA)_2(NH_4)_2[V_{10}O_{33}(AsPhNH_2)_3]$. POM hybrids obtained under the same reaction conditions by employing phenylarsonic and p-arsanilic acid ligands respectively.[4]

A more recent report gives a systematic study on the effect of phenylarsonic acid when used as a ligand compared to phenylphosphonic acid within the structure of $PPh_4[V_4O_{18}(XPh)_4F]$, where X = P or As (denoted VPF and VAsF respectively).[18] Structurally, the two hybrids were found to be extremely similar – belonging to the same crystal system and space group and showing very similar connectivity (Figure 63). The influence of the anchoring atom could be seen clearly in NMR studies, where the decreased electronegativity of As vs. P (2.18 vs. 2.19 eV) results in the shielding of both the ^{51}V and ^{19}F nuclei and hence a downfield chemical shift. The UV-vis spectra of the two compounds showed that VAsF had a blue-shifted LMCT energy compared with VPF (331 nm vs. 343 nm) meaning that it is higher energy, this corroborated nicely with the NMR data as the amount of deshielding is inversely proportional to the energy of the LMCT. Cyclic voltammetry and linear sweep voltammetry was employed for the two species showing that VPF showed one reversible electron reduction at +0.164 V (vs. Fc^+/Fc) whereas VAsF had a negatively shifted reversible first reduction peak at -0.141 V (Figure 63c), both species also showed irreversible reduction features at potentials beyond -0.3 V, however the onset of these features was more negatively shifted in VAsF suggesting it is more stable. The difference in half wave potentials for the first reduction indicates that phenylarsonate moieties do not decrease the

electron density around vanadium as effectively as phenylphosphonates and hence is more difficult to reduce. These experimental findings were also reinforced with computational studies, where the first and second electron affinities were calculated and agreed with observations from the electrochemical data; namely, the POMs can only uptake 1 electron reversibly and the uptake of the 1st and 2nd electron occurs more readily in VPF than in VAsF.

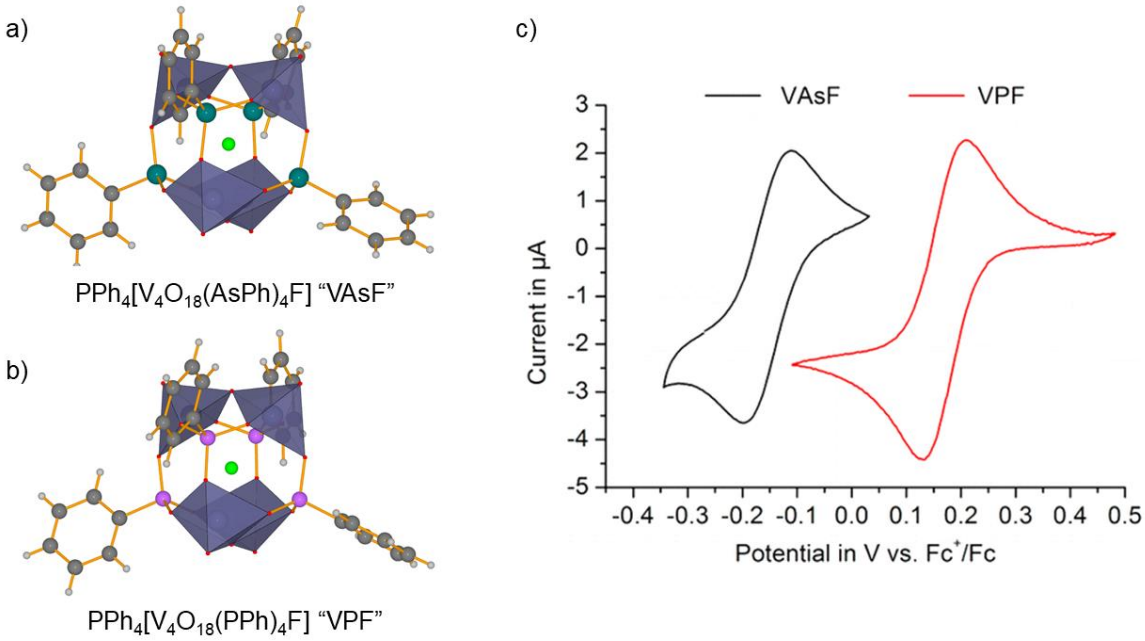
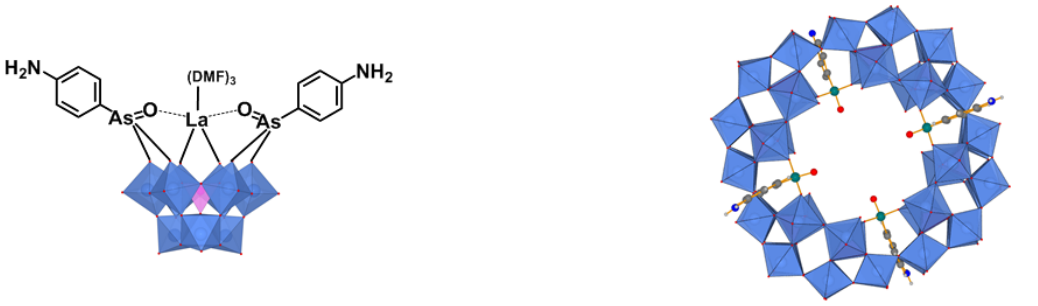


Figure 63. a) Structure of $PPh_4[V_4O_{18}(AsPh)_4F]$ "VAsF". b) Structure of $PPh_4[V_4O_{18}(PPh)_4F]$ "VPF" c) Cyclic voltammetry of VasF and VPF. Despite being isostructural, the electron withdrawing effects of the two pnictogen ligands results in contrasting electrochemical behaviour.[18] Cyclic voltammogram reproduced from [18] with permission from the American Chemical Society.

Structurally, there are very few examples of organoarsenic hybrid polyoxotungstate POMs formed from the building block approach with organoarsenates and lacunary polyoxotungstates, and of these, none contain any electronic characterisation of the hybrid. Nevertheless, hybridisation of trilacunary and monolacunary Keggins and superlacunary macrocyclic $[H_7P_8W_{48}O_{184}]^{33-}$ with phenylarsonic acid or arsanilic acid has been successfully achieved (Figure 64).[19-21] This clearly indicates that the binding of arylarsonic acids to redox active clusters such as the Wells-Dawson polyoxotungstate may not only be possible, but could also offer exciting opportunities for the intricate tailoring of the POMs electronic properties towards bespoke catalysis and materials applications.



$[PW_9O_{34}(AsOC_6H_4p\text{-}NH_2)_2(La(dmf)_3(H_2O)_2)]^{2-}$ $[(RAsO)_4P_8W_{48}O_{184}]^{32-}$ (R =C_6H_5, C_6H_4p-NH_2)

Figure 64. Structure of polyoxotungstate organoarsenic hybrids that have been reported including lanthanide complexed trilacunary Keggin di(*p*-arsanilic acid) hybrid (left),[20] and tetra-functionalisation of wheel-type P8W48 polyoxotungstates (right).[21]

3.2 Aims

As discussed above, the combination of monolacunary Wells-Dawson polyoxotungstates and arylarsonic fragments to form a new family of organic-inorganic POM hybrids could provide an alternative route to the synthesis of electronically tuneable POM (photo)redox catalysts. To investigate this, we aimed to synthesise two families of structurally related hybrid compounds. The first series, which would isolate the influence that the covalent anchoring group exhibited on the POM, would compare a phenylarsonic hybrid with isostructural phenylphosphonic and structurally related phenylsiloxane hybrids. Whereas the second series, which would determine the extent of orbital tuning that arylarsonic acids allow, would compare the phenylarsonic hybrid with contrasting para-substituted arylarsonic hybrids employing an amino electron donating group and a nitro electron-withdrawing group (summarised in Figure 65).

The synthesised arsenic compounds would then be structurally characterised, mainly to confirm the proposed binding motif and compare the bonding environment around arsenic. Subsequently, electronic characterisation would be instrumental in determining the redox capabilities of the species. Finally, with the electronics of the system determined, the photoreduction of these compounds would be studied to gauge their potential photocatalytic activity for the transformation of organic substrates to value-added compounds.

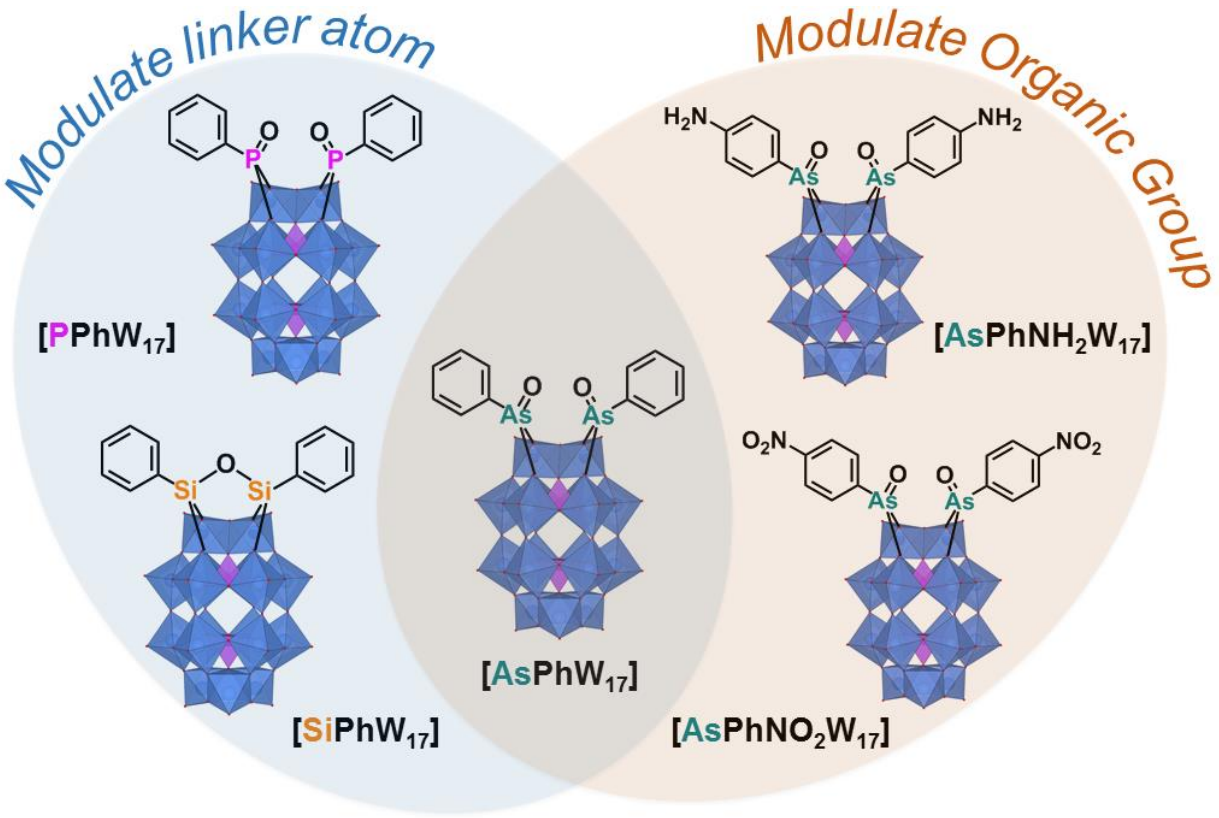


Figure 65. Diagram of the two families of related compounds synthesised in this study, through the modulation of the linker atom (left) or the aromatic ring (right) from [$AsPhW_{17}$].

3.3. Results and discussion

3.3.1 Synthetic development

The first synthesis of the organoarsenic hybrid Wells-Dawson polyoxometalate was attempted by following the procedures previously described in our group for the coupling of organophosphonates to the lacunary Wells-Dawson structure and isolating the hybrid as the potassium salt.[2, 22] The ligand with which we chose to optimise the synthetic procedure was arsanilic acid due to its lower cost and toxicity than phenylarsonic acid and p-nitarsone. Specifically, p-arsanilic acid and $K_{10}[P_2W_{17}O_{61}]$ are combined in a 2.5:1 ratio in DMF, a catalytic amount of 12M HCl is then added and the reaction mixture is heated at 90°C for 24 hours. The addition of acid caused the immediate dissolution of the reagents and the solution turned orange. Upon heating, the orange solution progressed to a deep red colour. After 24 hours, the reaction is then allowed to cool to room temperature which caused the precipitation of a fine white powder (unreacted $K_{10}[P_2W_{17}O_{61}]$). This is removed by filtration and the solvent is removed in vacuo to give a deep red crystalline powder. Dissolution of the crude product into acetonitrile and

filtering removed any unreacted ligand and yielded the product as a red-brown powder after removal of the solvent in moderate yield (65%). Functionalisation was confirmed through ^{1}H and ^{31}P NMR spectroscopy where we can observe the downfield shift of the aromatic H signals from the organo-group and the negative shift of the templating phosphate that resides closest to the lacuna as the functionalisation decreases the high amount of negative charge at that site and thus the phosphate signal becomes less deshielded. Whilst the functionalisation appeared successful and the yield of the reaction satisfactory, it was observed that the sample underwent physical changes when stored under atmospheric conditions over time; namely darkening and progression towards a liquid phase. When the structural integrity of the sample was investigated over time using ^{1}H and ^{31}P NMR, we found that it had partially degraded as seen by the evolution of new peaks in the aromatic portion of the ^{1}H NMR spectrum and in the negative portion of the ^{31}P NMR spectrum. This indicated that the hybrid species may be both hygroscopic and hydrolytically unstable due to the fact that it was isolated as its K^{+} salt and that arsonate esters are less stable than phosphonate esters,[23] and hence may bind less strongly to the POM. Whilst it may also have been possible that O_2 had caused the degradation of the POM, this is much more unlikely as both the W^{VI} addenda atoms of the POM and the As^{V} atoms of the organic group are in their highest oxidation state, hence they should be resistant to oxidative degradation by O_2. Nonetheless, to prove the detrimental effect of water on the system, we performed the ^{1}H and ^{31}P NMR experiments of the freshly prepared hybrid $K_6[P_2W_{17}O_{61}(AsOC_6H_4NH_2)_2]$ ($K_6[AsPhNH_2W_{17}$) in D_2O and immediately observed the evolution of several new peaks within both spectra, specifically new aromatic signals in the ^{1}H and new ^{31}P peaks in the negative region. The new peaks did not correspond to either the free ligand or $[P_2W_{17}O_{61}]^{10-}$, indicating that the organic groups had not fully hydrolysed, nonetheless, several peaks in the ^{1}H and ^{31}P NMR spectra are indicative of partial hydrolysis (Figure 66).

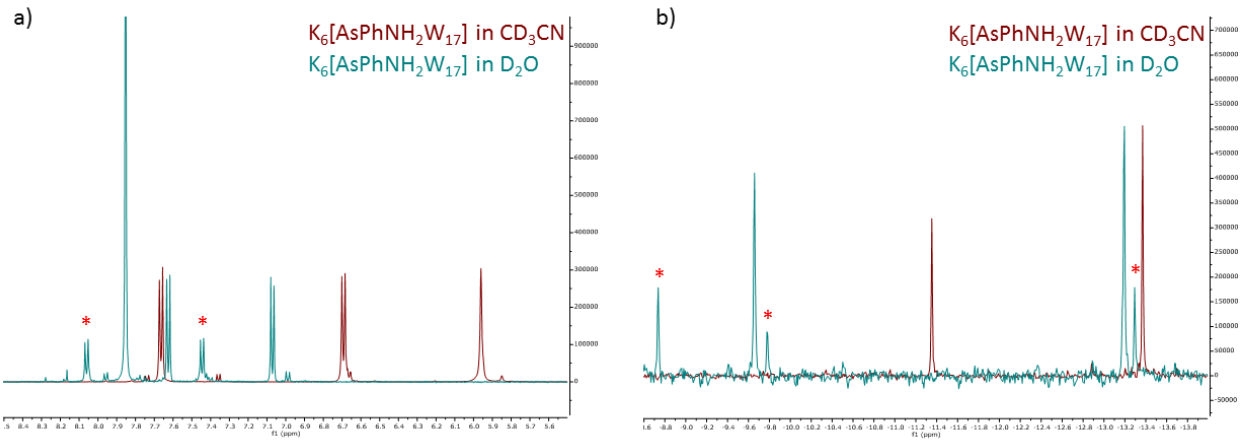
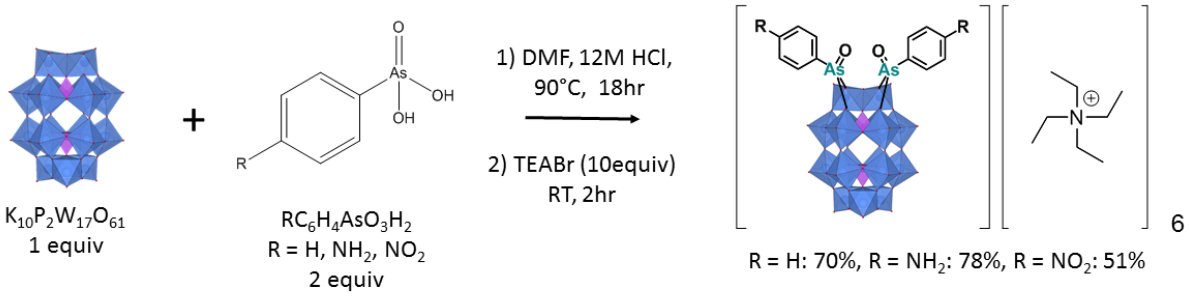


Figure 66. a) ^{1}H NMR and b) ^{31}P NMR of $K_6[AsPhNH_2W_{17}]$ in acetonitrile (maroon) and water (teal), demonstrating that in water the evolution of new peaks (indicated by asterisks) indicates partial hydrolysis.

To counteract the hydrolytic instability of the system, the synthesis of the same hybrid was attempted but with isolation of the TBA salt instead. When employed as a counterion for polyoxometalates, TBA causes the POM to be soluble in a wider range of organic solvent but insoluble in water. It was hoped that TBA may be able to hinder the accessibility of water to the cluster through both sterically crowding and creating a hydrophobic environment around the POM. Following reports on the synthesis of TBA salts of organophosphonate hybrids, the same conditions were used as above but with the addition of TBABr to the initial reaction mixture before heating. Unfortunately, it was found that this method resulted in the isolation of a miniscule amount of unknown product. The lack of reactivity may have been due to the cation exchange of $K_{10}[P_2W_{17}O_{61}]$ with TBABr, which was used in excess. This could then prevent the reaction of the highly polar arsanilic acid with the lacunary POM due to the effects of TBA as a cation as described above. We therefore modified the procedure so that TBABr was added post-reaction to the mother liquor once cooled and filtered. After stirring the solution at room temperature for at least 1hr, the solvent was removed in vacuo and the TBA salt was purified by multiple reprecipitations from acetonitrile using $CHCl_3$. Purity of the hybrid was confirmed by ^{1}H and ^{31}P NMR spectroscopy by monitoring the characteristic peaks earlier. Furthermore, using TBA as a cation means that we can also confirm that the charge is balanced as the expected 6:1 (TBA:POM), through integration of the aromatic organoarsonate ^{1}H NMR signals with the aliphatic ^{1}H NMR signals of TBA.

With a general method in hand, we applied this to the synthesis of the three organoarsenic hybrids. One major change made from this point onwards was the switch of TBA as the cation to N-tetraethylammonium (TEA). The reason behind this was that tetraethylammonium, whilst still able to provide a hydrophobic environment around the POM and usable in confirming the ionic ratios of the

hybrid, is much more compatible with mass spectrometry and could facilitate the growth of single crystals for X-ray diffraction by encouraging ordered packing. Thus, the three organoarsenic hybrids were synthesised as their TEA salts using a similar procedure to above, outlined in Scheme 12. Serendipitously, it was found that the TEA salts of the hybrid POMs were insoluble in acetonitrile but soluble in DMF; acetonitrile was found to be a better washing and precipitating solvent for the purification of the hybrids as the organoarsenic precursors were much more soluble in this solvent. As outlined in the aims section, we also synthesised phenylphosphonate and phenylsiloxane hybrids and these were too isolated as their TEA salts. We achieved this by first synthesising them as their stable potassium salts, following literature procedures,[4, 24] and then performing cation exchange with TEABr in water, with high yields. Overall this gave us the five target hybrids as their TEA salts in moderate to high yields and in high purity as determined by ^{1}H and ^{31}P NMR spectroscopy and CHN elemental analysis.

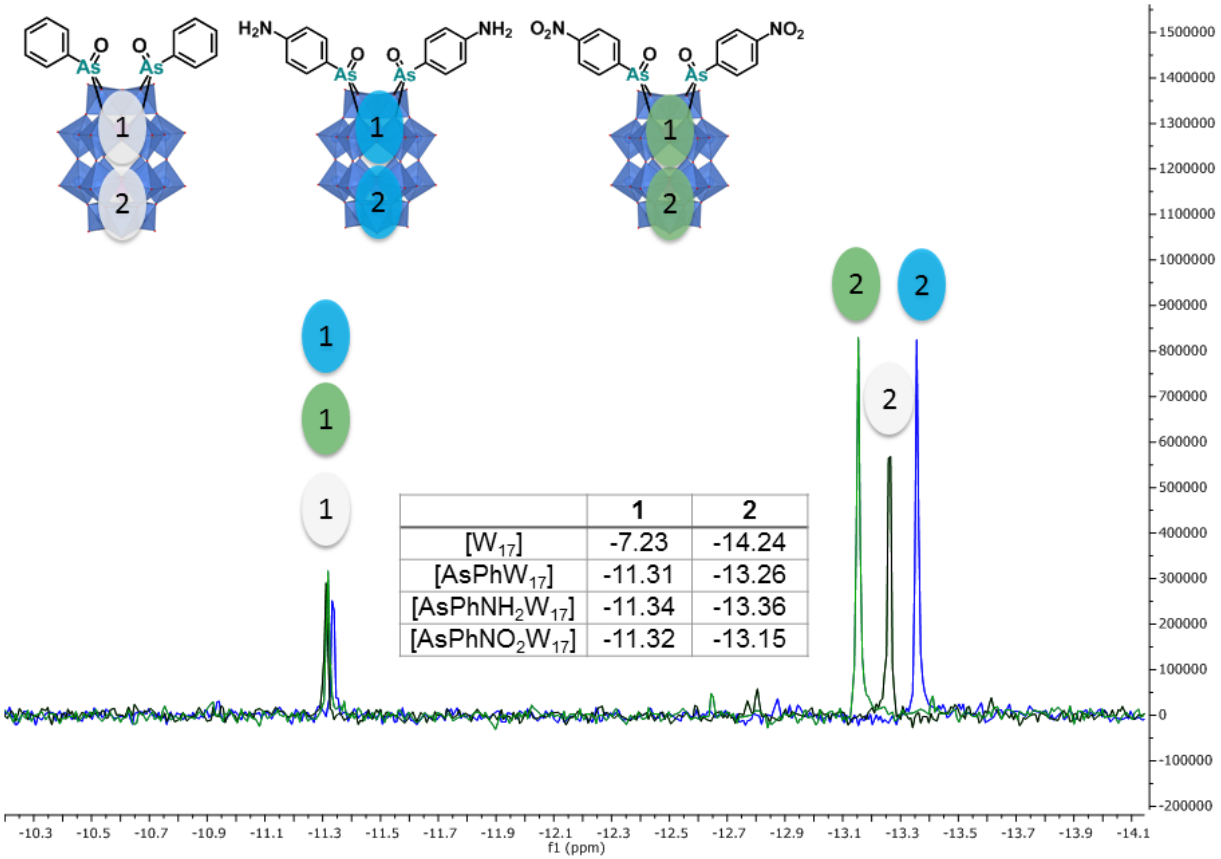


Scheme 12. Synthetic route to N-tetraethylammonium organoarsenic hybrid polyoxometalates.

3.3.2 Structural characterisation

As alluded to in the previous section, both ^{1}H and ^{31}P NMR spectroscopies were instrumental in initially confirming the composition of the hybrid species formed. The first evidence of hybridisation was given by the shifts in the ^{31}P NMR (Figure 67), in the lacunary precursor $K_{10}[P_2W_{17}O_{61}]$, we observe two discrete peaks corresponding to the two non-equivalent templating P atom at -7.23 ppm and -14.24 ppm, the former peak (P1) is the phosphorus environment lying closest to the lacuna, which is deshielded due to the localised negative oxo-anions at the lacuna, and the latter peak (P2) obviously is more shielded by being further from the lacuna and thus its peak is further upfield. Upon hybridisation, each arylarsonic hybrid shows shifts in both peaks- whereby P1 is shifted downfield (~4 ppm) as the localised negative charge has now been removed through covalent bonding to the oxophilic arsenic atom, P2 is shifted slightly upfield (~1ppm) due to the redistribution of negative charge upon

hybridisation. It is interesting to observe that between the three arylarsonic hybrids, P1 occurred at almost the same shift, whereas the shift of P2 was dependent on the electronics of the aryl ring – despite residing further from the site of functionalisation than P1. The shift has trends that can be rationalised based on the electronics of the different arylarsonic rings, where the p-nitro group which removes electron density from the POM, causes the deshielding and downfield shift of P2 compared to [$AsPhW_{17}$] (-13.15 ppm vs. -13.26 ppm), conversely, the p-amino group donates electron density to the POM which causes the opposite shielding and upfield shift of P2 compared to [$AsPhW_{17}$] (-13.36 ppm vs. -13.26 ppm). The fact that the effect of the aryl ring is influential on the shift of distal P2 is already supportive that there is strong orbital mixing between the organic and inorganic components and suggests that hybridisation has been successful.



	1	2
[W_{17}]	-7.23	-14.24
[$AsPhW_{17}$]	-11.31	-13.26
[$AsPhNH_2W_{17}$]	-11.34	-13.36
[$AsPhNO_2W_{17}$]	-11.32	-13.15

Figure 67. Overlaid ^{31}P NMR spectra of [$AsPhW_{17}$] (white), [$AsPhNH_2W_{17}$] (blue) and [$AsPhNO_2W_{17}$] (green).

This technique is complemented by ^{1}H NMR spectroscopy, where we can probe both the nature of both the aromatic H atoms contributed from the grafted organic rings and the aliphatic H atoms from the organic cation. Regarding the aromatic peaks, upon hybridisation an upfield shift is observed as the electron withdrawing arsonic acid become much less deshielding upon hybridisation (Figure 68), this can be attributed directly to the effect of hybridisation as the shift is less pronounced as we move from ortho to meta and para (for [$AsPhW_{17}$]). The aliphatic signals that originate from the cations are an

extremely useful tool for determining the cationic ratio as they can be integrated against the aryl signals on the POM. It is observed that full exchange occurs in each scenario giving hybrids POMs that are charge balanced by six TEA counterions. The integration of these peaks also reinforces the assumption that the arylarsonic moieties bind to the POM in the expected 2:1 fashion based on the binding of the isoelectronic phenylphosphonic acids.

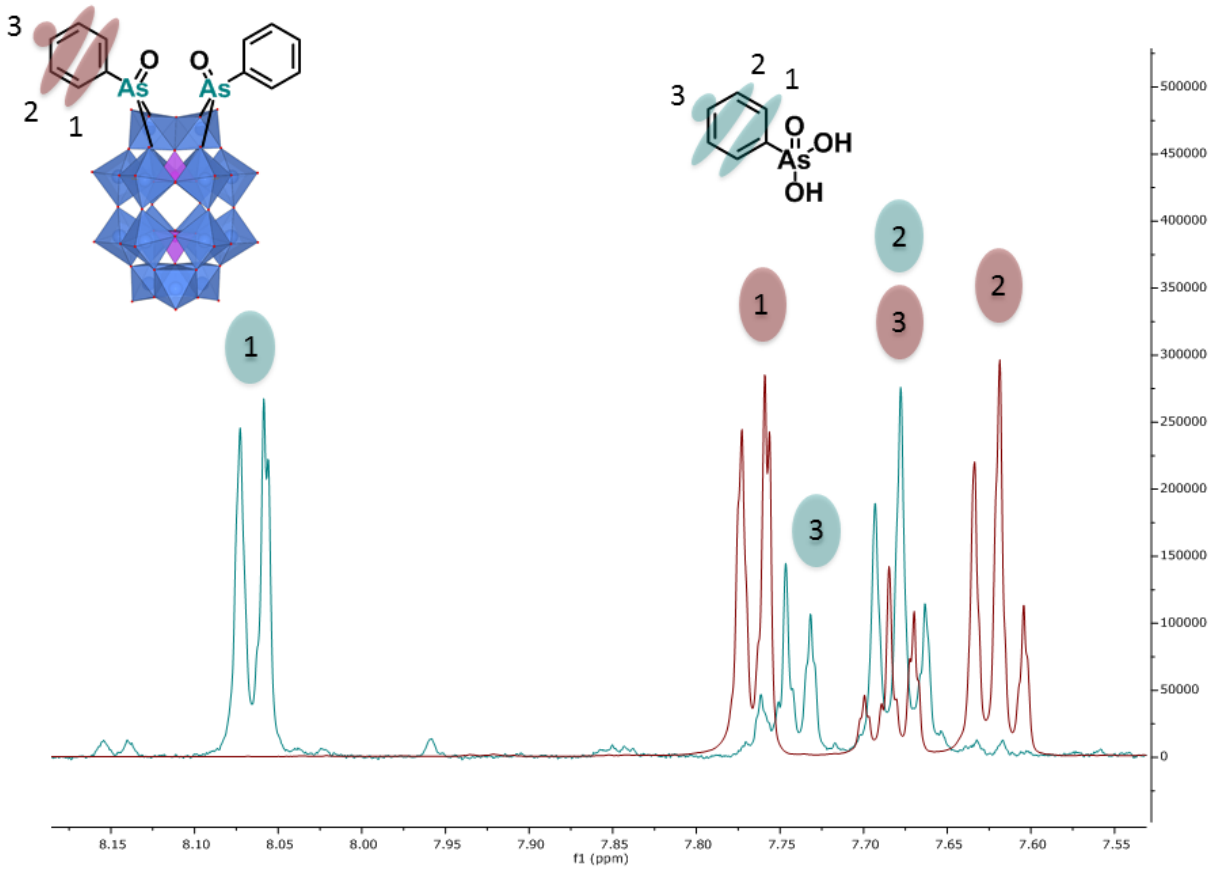


Figure 68. ^{1}H NMR of [AsPhW$_{17}$] (teal) compared to phenylarsonic acid (maroon) showing a clear upfield shift of aromatic signals upon hybridisation.

Mass spectrometry was also used to verify the structure of the arylarsonic hybrids. For [AsPhW$_{17}$], there are three discrete populated regions which roughly correspond to [AsPhW$_{17}$]$^{2-}$, [AsPhW$_{17}$]$^{3-}$ and [AsPhW$_{17}$]$^{4-}$ species, within these regions, various peaks correspond to the different cationic combinations that occur between the original paired cation (TEA) with small cationic fragments present in the mobile phase. Figure 70 and Table 12 show that within the high m/z region, peaks correspond to [AsPhW$_{17}$]$^{2-}$ fragments with four corresponding cations. There are 5 main peaks which are very broad due to each of the seventeen tungsten atoms existing in 4 relatively abundant isotopes (^{182}W 26.5%, ^{183}W 14.3%, ^{184}W 30.6%, ^{186}W 28.4%) this incidentally helps differentiate the high nuclearity tungsten

clusters from other artefacts within the spectrum and the peak separation helps identify the charge of each species. These peaks correspond nicely to the intact cluster with the composition $(TEA)_wH_xNa_yK_z[AsPhW_{17}]^{2-}$ (where w+x+y+z=4), with the higher extreme corresponding to $(TEA)_3H_1[AsPhW_{17}]^{2-}$ at 2445.64 m/z and the lower extreme corresponding to $(TEA)_1H_2Na_1[AsPhW_{17}]^{2-}$ at 2326.96 m/z. Considering now the mid-region containing $[AsPhW_{17}]^{3-}$ signals, again 5 main peaks are observed corresponding to $(TEA)_wH_xNa_yK_z[AsPhW_{17}]^{3-}$ (where w+x+y+z=3), ranging from $(TEA)_2H_1[AsPhW_{17}]^{3-}$ at 1586.71 m/z to $H_1Na_2[AsPhW_{17}]^{3-}$ at 1507.93 m/z. The lower region contains only one $[AsPhW_{17}]^{4-}$ species which corresponds to $(TEA)_1H_1[AsPhW_{17}]^{4-}$ at 1157.49 m/z. It is also interesting to observe peaks that correspond to dimeric species within the mass spectrum, especially prominent is a small series of 3 peaks between 1950-1875 m/z, which correspond to $TEA_xH_yK_z[(AsPhW_{17})_2]^{5-}$ species (where x+y+z=7). Thus, given the array of peaks that correspond to the parent ion (and its dimers), the presence of the intact cluster can be confirmed. Analogously, mass spectrometry of $[AsPhNH_2W_{17}]$ and $[AsPhNO_2W_{17}]$ yielded confirmation of the molecular species through similar families of peaks corresponding to the parent ions with different charges, cation combinations and as monomeric and dimeric species (see Figure 69-71 and Table 12-14).

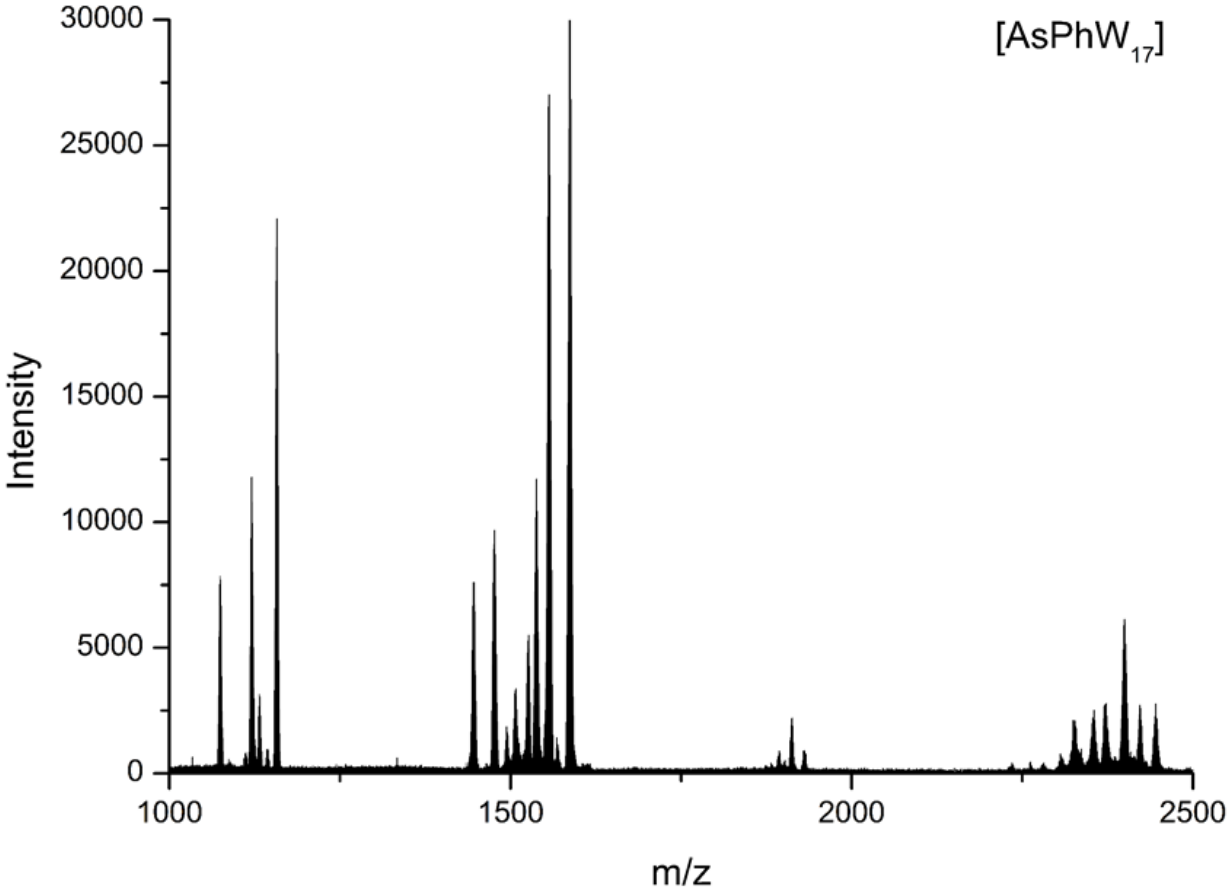


Figure 69. ESI mass spectrum of $[AsPhW_{17}]$.

m/z(obs)	Z	Assignment	m/z(calc)
2455.64	2	$(TEA_3H_1[P_2W_{17}O_{61}(AsOC_6H_5)_2])$	2445.60
2422.34	4	$(TEA_5K_1[(P_2W_{17}O_{61}(AsOC_6H_5)_2)_2])$	2422.30
2400.05	2	$(TEA_2H_1K_1[P_2W_{17}O_{61}(AsOC_6H_5)_2])$	2400.00
2373.06	2	$(TEA_1K_3[P_2W_{17}O_{61}(AsOC_6H_5)_2])$	2373.38
2354.49	2	$(TEA_1H_1K_2[P_2W_{17}O_{61}(AsOC_6H_5)_2])$	2354.45
2326.96	2	$(TEA_1H_2Na_1[P_2W_{17}O_{61}(AsOC_6H_5)_2])$	2326.94
1930.29	5	$(TEA_5H_2[(P_2W_{17}O_{61}(AsOC_6H_5)_2)_2])$	1930.25
1912.05	5	$(TEA_4H_1K_2[(P_2W_{17}O_{61}(AsOC_6H_5)_2)_2])$	1912.01
1893.81	5	$(TEA_3H_2K_2[(P_2W_{17}O_{61}(AsOC_6H_5)_2)_2])$	1893.77
1586.71	3	$(TEA_2H_1[P_2W_{17}O_{61}(AsOC_6H_5)_2])$	1586.68
1556.64	3	$(TEA_1H_1K_1[P_2W_{17}O_{61}(AsOC_6H_5)_2])$	1556.62
1538.99	3	$(K_3[P_2W_{17}O_{61}(AsOC_6H_5)_2])$	1538.87
1526.64	3	$(H_1K_2[P_2W_{17}O_{61}(AsOC_6H_5)_2])$	1526.22
1507.93	3	$(H_1Na_2[P_2W_{17}O_{61}(AsOC_6H_5)_2])$	1507.91
1157.49	4	$(TEA_1H_1[P_2W_{17}O_{61}(AsOC_6H_5)_2])$	1157.47

Table 12. Mass spectrum peaks corresponding to $[AsPhW_{17}]^{n-}$ ions

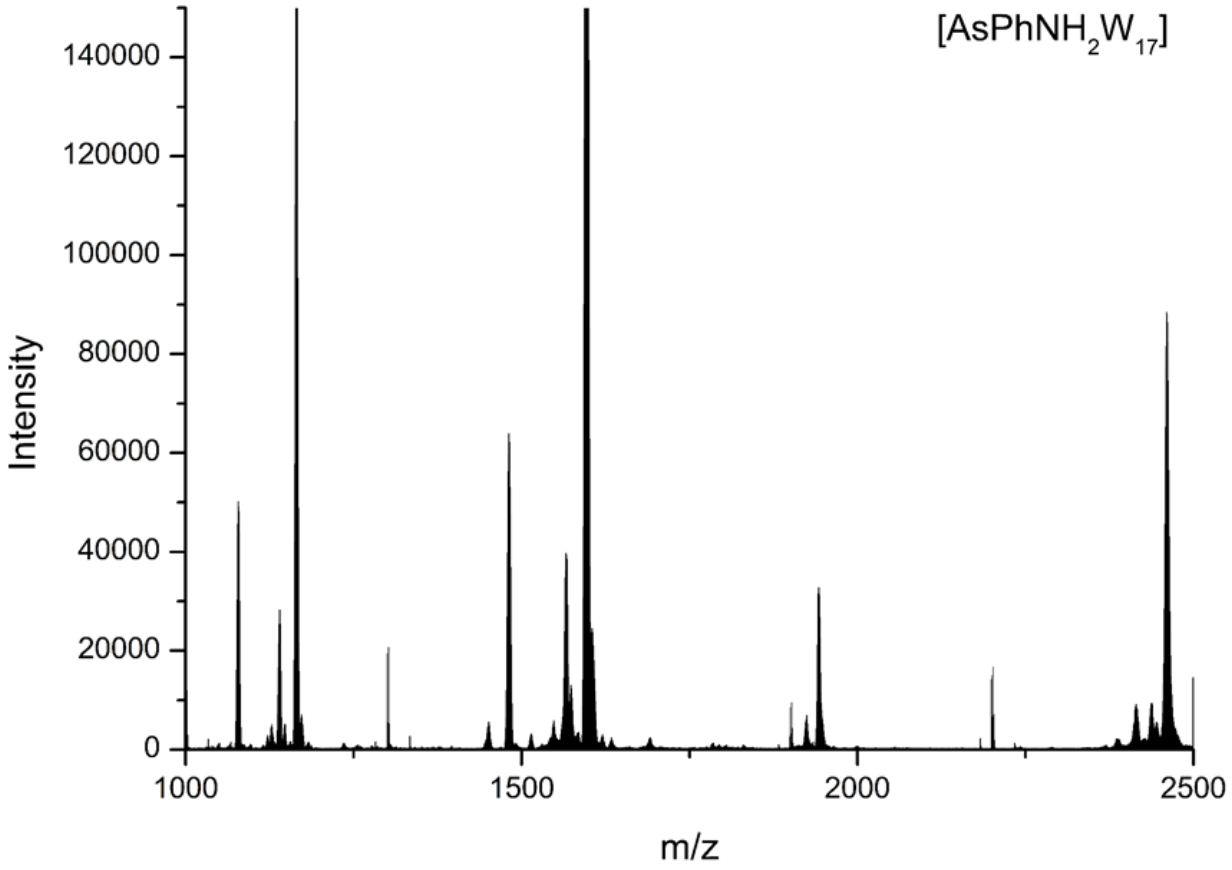


Figure 70. ESI mass spectrum of $[AsPhNH_2W_{17}]$.

m/z(obs)	Z	Assignment	m/z(calc)
2460.63	2	$(TEA_3H_1[P_2W_{17}O_{61}(AsOC_6H_4NH_2)_2])$	2460.62
1942.06	5	$(TEA_5H_1[(P_2W_{17}O_{61}(AsOC_6H_4NH_2)_2)_2])$	1942.06
1923.83	5	$(TEA_4H_1K_1[(P_2W_{17}O_{61}(AsOC_6H_4NH_2)_2)_2])$	1923.82
1596.69	3	$(TEA_2H_1[P_2W_{17}O_{61}(AsOC_6H_4NH_2)_2])$	1596.69
1566.63	3	$(TEA_1H_1K_1[P_2W_{17}O_{61}(AsOC_6H_4NH_2)_2])$	1566.62

Table 13. Mass spectrum peaks corresponding to $[AsPhNH_2W_{17}]^{n-}$ ions

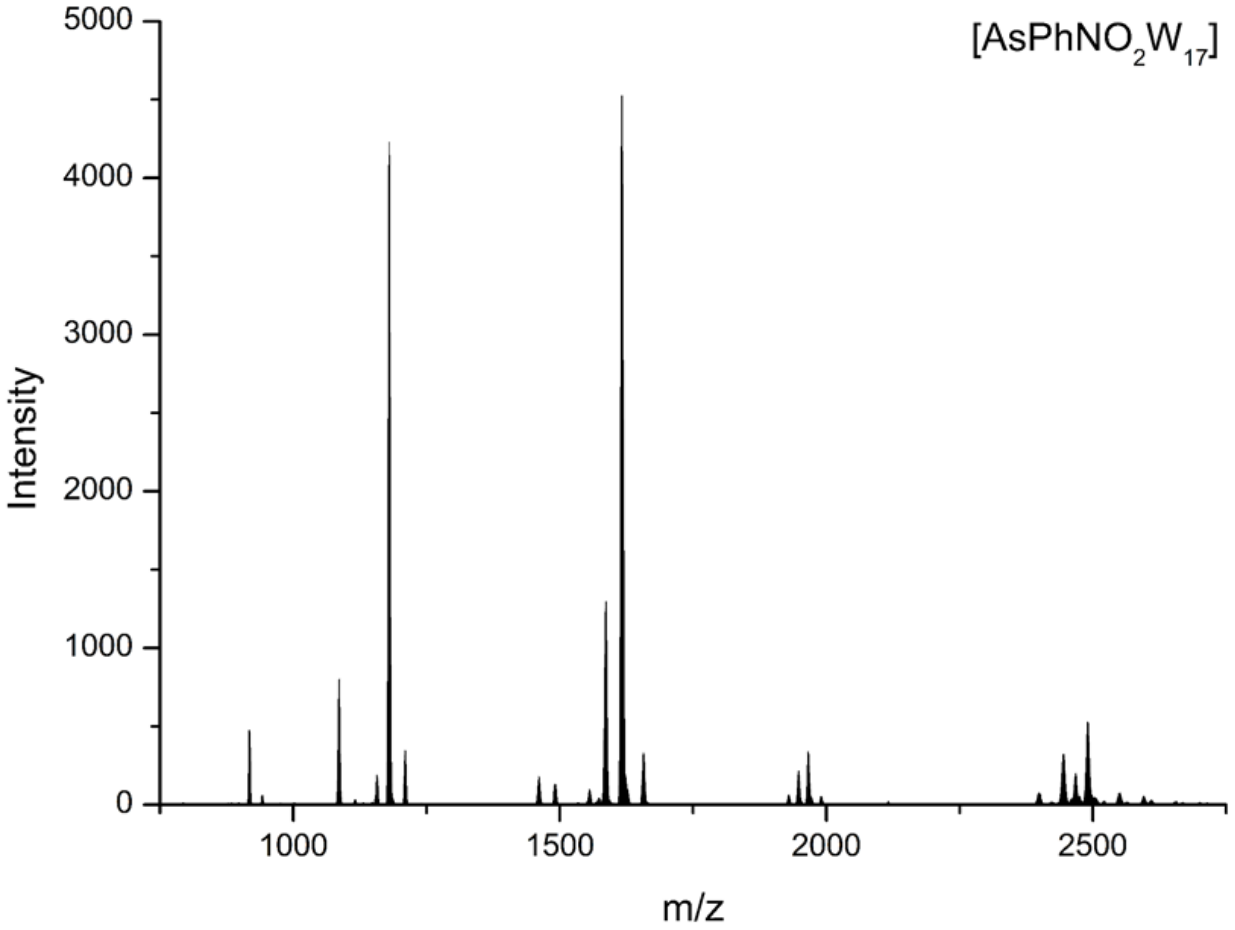


Figure 71. ESI mass spectrum of $[AsPhNO_2W_{17}]$

m/z(obs)	Z	Assignment	m/z(calc)
2490.59	2	$(TEA_3H_1[P_2W_{17}O_{61}(AsOC_6H_4NO_2)_2])$	2490.59
2467.79	4	$(TEA_5H_2K_1[P_2W_{17}O_{61}(AsOC_6H_4NO_2)_2]_2)$	2467.80
2444.99	2	$(TEA_2H_1K_1[P_2W_{17}O_{61}(AsOC_6H_4NO_2)_2])$	2444.99
2399.39	2	$(TEA_1H_1K_2[P_2W_{17}O_{61}(AsOC_6H_4NO_2)_2])$	2399.40
1966.24	5	$(TEA_5H_2[(P_2W_{17}O_{61}(AsOC_6H_4NO_2)_2)_2])$	1966.24
1950.00	5	$(TEA_4K_1H_2[(P_2W_{17}O_{61}(AsOC_6H_4NO_2)_2)_2])$	1950.00
1929.96	5	$(TEA_3K_2H_2[(P_2W_{17}O_{61}(AsOC_6H_4NO_2)_2)_2])$	1929.97
1617.01	3	$(TEA_2H_1[(P_2W_{17}O_{61}(AsOC_6H_4NO_2)_2)])$	1617.00
1586.61	3	$(TEA_1H_1K_1[P_2W_{17}O_{61}(AsOC_6H_4NO_2)_2])$	1586.61
1179.96	4	$(TEA_1H_1[P_2W_{17}O_{61}(AsOC_6H_4NO_2)_2])$	1179.97
917.54	5	$(H_1[P_2W_{17}O_{61}(AsOC_6H_4NO_2)_2])$	917.54

Table 14. Mass spectrum peaks corresponding to $[AsPhNO_2W_{17}]^{n-}$ ions

To further investigate the structural relationship between the organic and inorganic components in the hybrid poloyoxometalates, infra-red spectroscopy was employed on the five compounds. Firstly, we investigated the characteristic peaks of the known compounds $[SiPhW_{17}]$ and $[PPhW_{17}]$. The prominent features common to both spectra were the symmetric and asymmetric C-H stretching modes

contributed from both the aromatic organic groups and the aliphatic countercations between 3000 and 2900 cm^{-1}, the C-H bends also contributed to by the same groups occur at *ca.* 1483 and 1392 cm^{-1}. At lower wavenumbers, characteristic peaks corresponding to the POM core can be observed with the P-O-W bends occurring at ~1086 cm^{-1} and ~910 cm^{-1}, the W=O stretches of the terminal oxo groups are seen at ~950 cm^{-1} and the W-O-W bends of the bridging oxygens occurring as a broad band between 800 and 700 cm^{-1}, Features unique to the siloxane and phosphorus hybrids obviously occur with bands associated with the bonding of the functionalisation group. In the former case, this is the band occurring at 1128 cm^{-1}, which corresponds to the Si-O-Si bending mode, the band occurring at 1040 cm^{-1} due to the Si-O-W bending mode and the sharp band at 697 cm^{-1} due to the Si-C stretching mode. For the phosphonate hybrid, only one diagnostic peak can be observed for the anchoring group at 1135 cm^{-1} which corresponds to the P=O stretch.

When comparing the above peaks to the organoarsenic hybrid POMs (Figure 72), several key similarities and differences can be observed. Firstly, the peaks corresponding to the POM core, phenyl ring and organic cation are all present with minimal shifts, suggesting, in line with NMR characterisation, that the bonding environment between the arylarsonate and POM is very similar to that observed for the phenylphosphonate and phenylsiloxane POMs and that the POM core has retained its structure. For the phenylarsonic hybrid, [$AsPhW_{17}$], a new weak band is observed at 1739 cm^{-1} which may corresponds to the overtone of the As=O stretching frequency, the original band for this stretching mode cannot be observed as it is obscured by the strong POM based bands. Expectedly, for the para-substituted arylarsonic hybrids, bands can be observed related to the para substituent. For example, [$AsPhNH_2W_{17}$] shows bands at 3353 cm^{-1} and 1593 cm^{-1} which correspond to the N-H stretching and bending modes respectively, whereas [$AsPhNO_2W_{17}$] shows a pair of peaks at 1663 and 1527 cm^{-1} due to N-O stretching modes. The above indicates that the phenylarsonic moieties forms a covalent linkage to the polyoxometalate and that the three substituents retain their organic structure post-functionalisation.

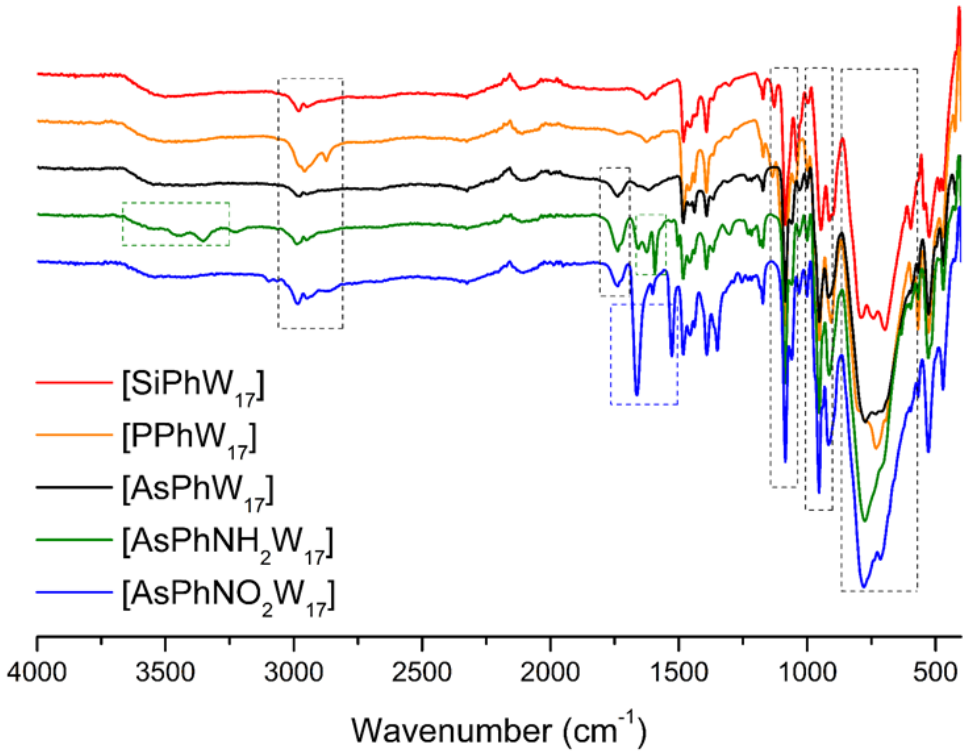


Figure 72. ATR-IR spectrum of [$SiPhW_{17}$] (red), [$PPhW_{17}$] (orange), [$AsPhW_{17}$] (black), [AsPhNH2W_{17}] (green) and [$AsPhNO_2W_{17}$] (blue) with characteristic bands highlighted.

We were further able to explore the structural features of the organoarsenic hybrid POMs by X-ray crystallography. Fortunately, we were able to grow single crystals of [$AsPhW_{17}$] through the vapour diffusion method, where the diffusion of the antisolvent EtOAc into a saturated solution of [$AsPhW_{17}$] in DMSO afforded single crystals as colourless parallelepipeds. [$AsPhW_{17}$] crystallises in the orthorhombic system with the space group Pnma with the unit cell containing 4 hybrid POM moieties; further crystallographic details including cell dimensions and volume, refinement and data parameters may be found in Section 7.2. The structure was found to be compositionally disordered, in that the hybrid has co-crystallised with a minor component of [W_{18}]. Both species overlapped within the crystal structure such that the only atoms close to the site of functionalisation differed. Structure refinement was achieved when the major (hybrid) and minor (plenary) components had occupancy values of 0.84(1) and 0.16(1) respectively. Regarding the structure of the hybrid POMs, we can see that two phenylarsonate moieties have condensed onto the POM in a 2:1 fashion, analogous to that of the previously reported isoelectronic phenylphosphonate hybrid Dawson POM (Figure 73).[2] Direct comparison of the bonding environment around the As^V centre with the P^V centre in said report reveals that the As atom resides in the same tetrahedral geometry, however the As centre is spatially further from the POM core due to the longer As-O bond lengths (the W-O bond lengths are approximately the same), this is due to poorer orbital overlap which is to be expected given that the 4p orbitals of arsenic

are more diffuse than the 3p orbitals of phosphorus. The As=O (1.652 Å) and As-O bonds (1.662 Å, 1.668 Å) are *ca.* 0.12 Å longer than the P=O (1.526 Å) and P-O bonds (1.536 Å, 1.541 Å) and the As-C bond (1.904 Å) is *ca.* 1.1 Å longer than the P-C bond (1.791 Å), reflecting the nature of the As atoms frontier orbitals. Interestingly, despite this structural differences, the bond angle between the two oxo-groups and arsenic (O-As-O) is nearly identical to that observed with phosphorus (O-As-O =110° vs. O-P-O = 111.8°), indicating that it is the geometry of the lacuna that dictates the geometry around the organic groups anchoring atom. This is particularly evidenced when we compare our crystallographic data with that of the previously mentioned macrocyclic organoarsenic polyoxotungstate hybrid, whereby the organic functionalisation group is the same but the lacuna of the polyoxometalate is completely different.[21] Here we observe that the bond lengths between arsenic and carbon (1.904 Å cf. 1.891 Å) and arsenic and oxygen (1.651 Å cf. 1.661 Å) are extremely similar however the O-As-O angle is markedly different ([$AsPhW_{17}$] = 111° vs. [$AsPhW_{48}$] = 102.6°). The above comparisons are summarised in Table 15. Whilst we were unable to obtain crystallographic data for [$AsPhNH_2W_{17}$] and [$AsPhNO_2W_{17}$], we can now assert that these two hybrids most likely adopt a similar structural configuration upon hybridisation with the polyoxometalate, due to the similarities observed in the ^{31}P NMR shifts of the polyoxometalate, the ratio of aryl and alkyl peaks observed within the ^{1}H NMR spectrum (indicating that there are two aryl rings for every six tetraethylammonium cations) and the similarities between the infra-red As=O overtone bands between the three hybrids.

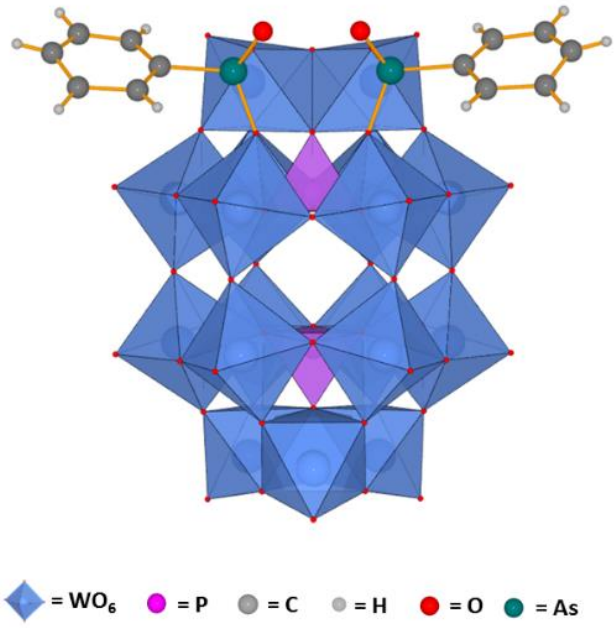
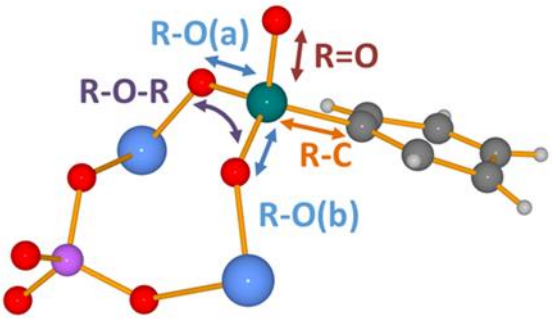


Figure 73. Crystal structure of [$AsPhW_{17}$] with solvent molecules omitted for clarity. Organoarsenic groups bind to the POM in a 2:1 fashion analogous to known organophosphorus analogues.



	[AsPhW$_{17}$]	[P$_2$W$_{17}$O$_{61}$(POC$_6$H$_5$)$_2$]$^{6-}$	[(C$_6$H$_5$AsO)$_4$P$_8$W$_{48}$O$_{184}$]$^{32-}$
R=O	1.651(17) Å	1.526(9) Å	1.661(15) Å
R-O(a)	1.668(14) Å	1.536(8) Å	1.683(12) Å
R-O(b)	1.662(19) Å	1.541(8) Å	1.718(12) Å
R-C	1.904(23) Å	1.791(13) Å	1.891(9) Å
R-O-R	110.0(14)°	111.8(5)°	102.5(6)°

Table 15. Comparison of the bond lengths and geometries around the anchoring atom with the analogous phenylphosphonate structure [PPhW$_{17}$] (Fujimoto) and related organoarsenate polyoxotungstate [P$_8$W$_{48}$O$_{184}$(OAsPhNH$_2$)]$^{32-}$.

3.3.3 Electronic Characterisation

Having confirmed the binding motif of the arylarsonic groups with the polyoxometalate, we then embarked on a study of the electronic properties of these hybrids. Firstly, we employed UV-vis spectroscopy for the 5 synthesised hybrids. UV-vis spectroscopy is often employed as an invaluable tool for investigating the change in the optical properties of POMs upon hybridisation, typically it allows us to observe changes to the LMCT band, the appearance of organic group-based absorption bands and the calculation of the HOMO-LUMO gap. Whilst this technique has been widely employed for POM hybrids which employ the vis-exo approach towards photosensitisation, resulting from the discrete and non-overlapping absorbances of the chromophore with the polyoxometalate,[25-27] UV-vis spectroscopy has proven to be less diagnostic for hybrids which employ the vis-endo approach.[2] The vis-endo approach changes the fundamental HOMO-LUMO energies of the POM core, which should manifest as a predictable shifting of the LMCT band. As Fujimoto et al. found, due to the broad and complex nature of the multiple O→W LMCT transitions within this region, it is often difficult to observe any effect of hybridisation on the HOMO-LUMO gap despite the demonstrated ligand mediated effects on the orbitals from computational and electrochemical studies.[2] Figure 74 shows the ground state absorption spectra of the synthesised hybrid compounds recorded in DMF at 4x10^{-5} M analyte concentration

between 275 and 1100 nm. Unfortunately, due to the absorption solvent window of DMF being limited at lower wavelengths (<270 nm), it is not possible to observe the entirety of the LMCT band. However, we can observe that the general absorption profile of the 5 hybrids follows a similar trend whereby there are strong LMCT absorbances >350 nm which rapidly tail-off to negligible absorbance across the visible region. Interestingly, when comparing the three arylarsonic hybrids (Figure 75) we observe that the intensity of the O→W LMCT band, which is partially visible at the upper limit of the experimental window, differs considerably between the three molecules and follows the trend [$AsPhNH_2W_{17}$] > [$AsPhNO_2W_{17}$] > [$AsPhW_{17}$]. An increase in the molar extinction coefficient of the LMCT band for para-derivatised species versus the unfunctionalised aryl derivative may arise from the extension of the conjugated system by employing both strong resonance electron donors "NH_2" or acceptors "NO_2" para to the anchoring group and could indicate strong electronic coupling between the organic and inorganic components. Curiously, compound [$AsPhNH_2W_{17}$] showed both a dramatic enhancement of the O→W LMCT band and a significant tailing across the visible region of the spectra (up to 750 nm). These superior absorption properties could be photoinduced proton transfer from the amine residues to the polyoxometalate (either via intramolecular or intermolecular mechanisms) which has been prolifically observed when polyoxometalates are paired with protic amine countercations.[28]

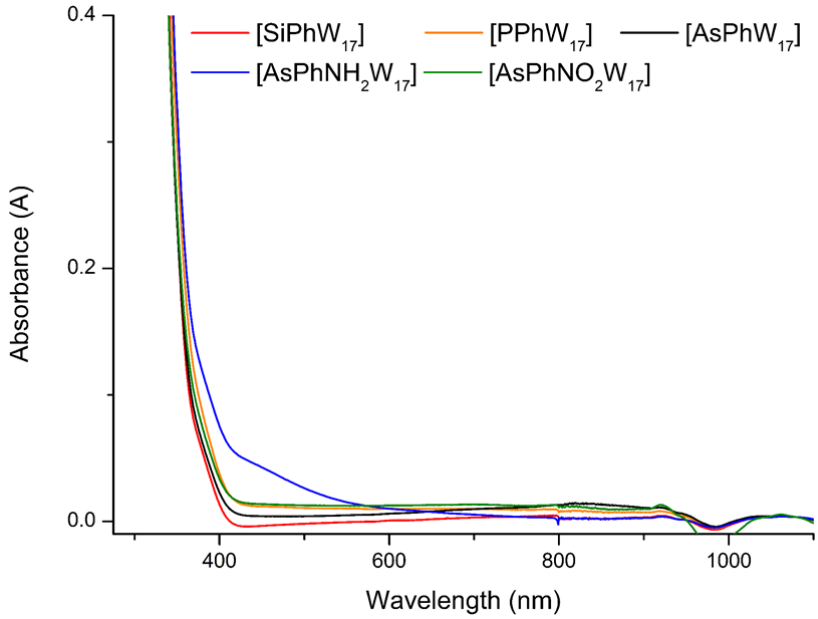


Figure 74. UV-vis spectra of [$SiPhW_{17}$] (red), [$PPhW_{17}$] (orange), [$AsPhW_{17}$] (black), [AsPhNH2W_{17}] (blue) and [$AsPhNO_2W_{17}$] (green) in DMF at 4 x 10^{-5} M concentration. Only [AsPhNH2W_{17}] shows significant tailing into the visible region of the spectrum.

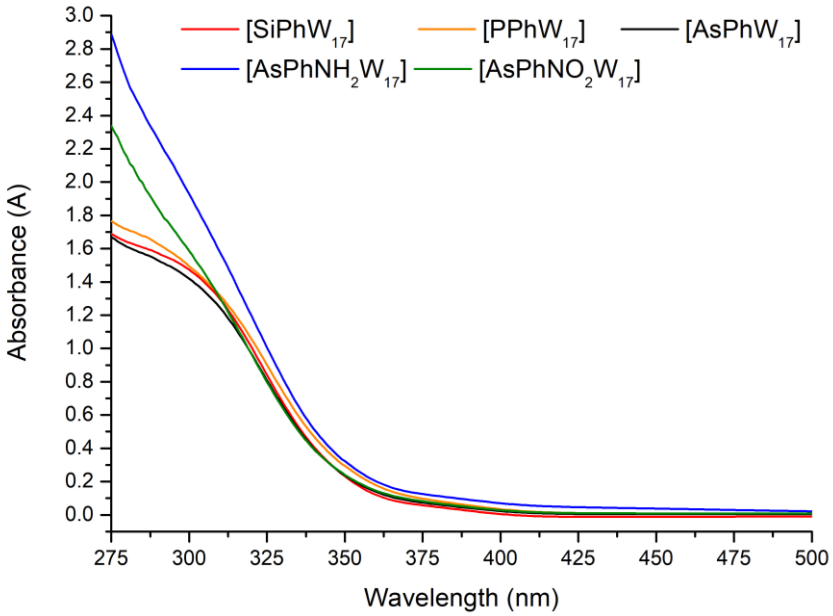


Figure 75. UV-vis spectra of $[SiPhW_{17}]$ (red), $[PPhW_{17}]$ (orange), $[AsPhW_{17}]$ (black), $[AsPhNH_2W_{17}]$ (blue) and $[AsPhNO_2W_{17}]$ (green) in DMF at 4 x 10^{-5} M concentration. $[AsPhNH_2W_{17}]$ and $[AsPhNO_2W_{17}]$ show considerably higher absorptions as they approach the solvent cut-off.

In addition, electrochemical measurements have been extensively used to accurately predict the LUMO energies of many organic-inorganic hybrid polyoxometalates and observed electrochemical trends have shown to strongly correlate with catalytic and photocatalytic activity.[2, 25, 29] We therefore employed cyclic voltammetry on the hybrids (0.5 mM) in anhydrous DMF with 0.1 M $TBAPF_6$ as electrolyte, at 100 mV/s scan rate under a positive argon pressure. A three-electrode set-up was employed with a glassy carbon working electrode, (d = 3 mm), Pt wire counter-electrode and a Ag-wire pseudo-reference electrode, with Fc^+/Fc redox couple as an internal reference. $[SiPhW_{17}]$ and $[PPhW_{17}]$, whose TBA salts have been electrochemically analysed in the literature, were used as comparative references.

To first isolate the influence that the arsenic linker exhibits on the POM, we first compared the reduction behaviours of $[SiPhW_{17}]$ and $[PPhW_{17}]$ with $[AsPhW_{17}]$, we observe that the phenylarsonic hybrid retains the electrochemical behaviour of the parent polyoxometalate by exhibiting two reversible one electron reductions within the potential window of the experiment. Comparing the half wave potential of the first reduction between the three species (Figure 76), we see that the phenylarsonic acid hybrid's first reduction ($E_{1/2}$ = -0.775 V) lies at a similar potential to the phenylphosphonic hybrid's first reduction ($E_{1/2}$ = -0.741 V), which are both considerably positive shifted versus the phenylsiloxane hybrid ($E_{1/2}$ = -1.170 V). The behaviour of $[SiPhW_{17}]$ and $[PPhW_{17}]$ matched well with that previously reported for the TBA salts, the electron withdrawing arylphosphonate moiety removes electron density from the POM whereas the arylsiloxane moiety exhibits the opposite effect by donating electron density to the

POM. As expected, the phenylarsonic moiety exhibits an electron withdrawing effect on the polyoxometalate, by decreasing the electron density based on the cluster and thus facilitating the acceptance of electrons onto the W^{VI} centres. From the first reduction potentials, it appears that the phenylarsonic groups have a slightly weaker electron withdrawing effect than the phenylphosphonate groups which is most likely due to poorer orbital overlap between arsenic and the oxo groups of the polyoxometalate and the carbon of the phenyl ring, thus lessening the extent of orbital mixing between the organic and inorganic components, this is supported by the previously described longer bond lengths of arsenic observed in the crystal structure.

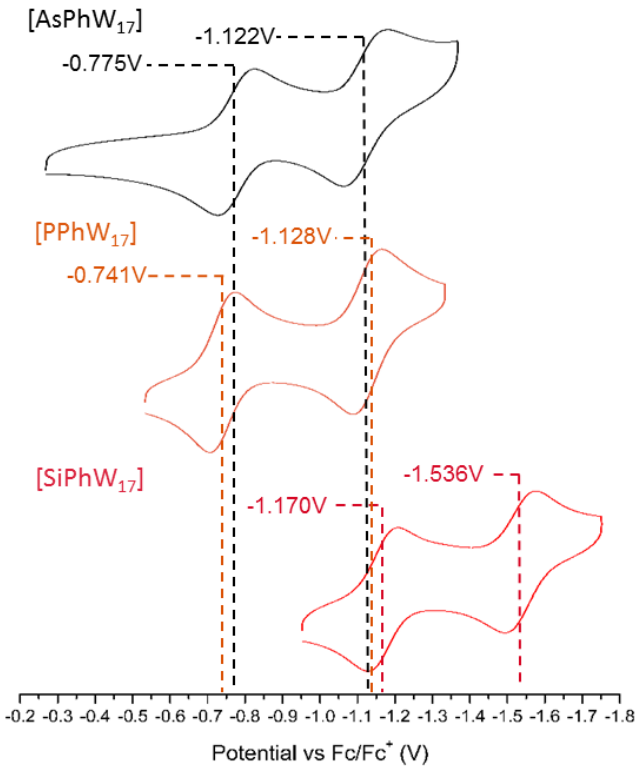


Figure 76. Cyclic voltammograms of $[SiPhW_{17}]$ (red), $[PPhW_{17}]$ (orange) and $[AsPhW_{17}]$ (black) with potentials referenced vs. Fc^{+}/Fc internal reference, demonstrating that the electronic nature of the anchoring atom has a profound role on the redox properties of the POM core.

We then investigated the effect that the electronic nature of the ring exhibits on the organoarsenic hybrid POMs electrochemical nature by comparing $[AsPhW_{17}]$ with $[AsPhNH_2W_{17}]$ and $[AsPhNO_2W_{17}]$ (Figure 77). This study mirrors that shown by Fujimoto et al where the employment of para-substituted electron donating and electron withdrawing groups was shown to have a powerful effect on the reduction potentials of the POM. Specifically, the use of the strong resonance electron donor, NH_2, at the para position causes the negative shift of the first two reduction potentials compared to $[AsPhW_{17}]$, whereas

the use of the strong resonance electron acceptor (NO_2) in the same position causes the positive shift of the first two reduction potentials. This indicates that the arylarsonate groups permit significant orbital mixing between the organic and inorganic components such that changes to the electronic structure of the aryl component results in significant and predictable shifts in the electrochemical behaviour of the POM. This behaviour was also alluded to in the initial ^{31}P NMR characterisation, where the shift of the templating phosphorus atom furthest from the site of functionalisation shows chemical shifts agreeing with the electrochemical trend. We observe that the p-nitro aryl group causes a downfield shift of the P signal, suggesting that the site has become more deshielded by the removal of electron density compared with [$AsPhW_{17}$], whereas the p-amino group causes an upfield shift of the signal, indicating a more shielded environment by the donation of electron density to the P atom. That this effect is observed for the templating P atom that is distal from the site of functionalisation is indicative that the influence of the organic group modulates the orbitals over the entire polyoxometalate structure. Overall, this indicates that the electronic nature of arylarsonate POMs can be effectively tuned and influenced through employment of appropriate substituents on the organic group.

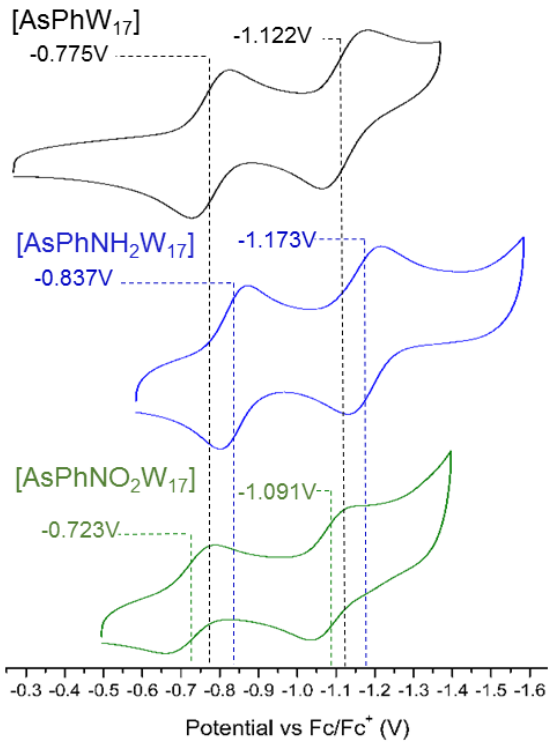


Figure 77. Cyclic voltammograms of [$AsPhW_{17}$] (black), [$AsPhNH_2W_{17}$] (blue) and [$AsPhNO_2W_{17}$] (green) with potentials referenced vs. Fc^+/Fc internal reference, demonstrating that the electronic nature of the aryl ring can be used to influence the redox properties of the POM core.

Given that the full redox chemistry of the [$SiPhW_{17}$] and [$PPhW_{17}$] anions has already been described,[4] we could confirm the structural and electronic integrity of the same polyoxoanions as synthesised in this study. It is observed that [$SiPhW_{17}$] features three reversible and three quasi-reversible redox processes within the potential window of the experiment (Figure 78a). The first three redox processes can be ascribed as two successive one-electron reductions followed by a two-electron reduction based on peak area. This follows the CV reported for [$SiPhW_{17}$] which shows the same three redox events. In our case, the electrochemistry of [$SiPhW_{17}$] at more reductive potentials (-2.3 V to -3.0 V vs. Fc^+/Fc) shows three more quasi-reversible reductions which were not reported by Boujtita et al.[4], as the use of DMF as a solvent has allowed us to increase the electrochemical window by a further ~1000 mV. Concerning [$PPhW_{17}$], we observe four reversible one electron reductions within the potential window of the experiment (Figure 78b), which mirrors the reported voltammetry by Boujtita et al.[4], here when we attempt to extend the potential window beyond -2.5 V vs. Fc^+/Fc, we encounter a large increase in current suggesting that either the solvent, or more likely the analyte, is decomposing. Directly comparing the redox potentials of the same processes observed in this study with those that have been reported, there is a consistent negative shift of each peak by ~150 mV, which may be a result of several differing factors between the experiments such as the solvent, the electrolyte and the POM counterion.

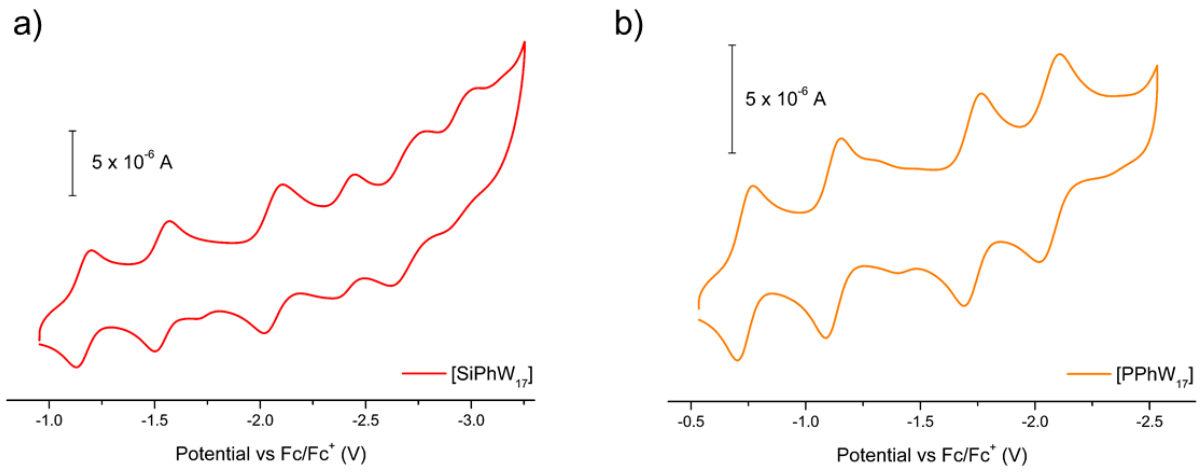


Figure 78. a) Cyclic voltammogram of [$SiPhW_{17}$] showing three reversible reductions followed by three quasi-reversible reductions b) Cyclic voltammogram of [$PPhW_{17}$] showing four reversible reductions, both referenced vs. Fc^+/Fc internal reference.

Concerning the arylarsonic derivatives, pushing the experimental window to more negative reduction potentials reveals that there is a disparity in the redox behaviour between the organoarsenic and the organophosphorus/organosilicon hybrids. Cycling each of the organoarsenic hybrid polyoxometalates within the full potential window allowed by the solvent shows that beyond the first two redox processes,

the electrochemical profile is dominated by non-reversible behaviour (Figure 79). Clearly, the use of organoarsenic as a linker atom has a profound effect on the electrochemical reversibility of the system. To investigate the limits of the reversibility of the system, we conducted experiments where the potential window was increased incrementally for both [$AsPhW_{17}$] without cleaning the electrode between scans. According to Figure 80, it seems that when the third reduction is accessed at ca. -1.6 V vs. Fc^+/Fc (by pushing the potential window to ca. -1.9 V vs. Fc^+/Fc), the reoxidation processes become ill defined and the current density of the second reduction and its corresponding reoxidation increases. When the potential is pushed even further (ca. -2.4 V vs Fc^+/Fc), the reductive behaviour becomes extremely ill-defined and broad and again the second redox waves seem to grow in intensity. Beyond this potential we observe a large increase in the current most likely resulting from breakdown of the analyte. Given that the only difference between [$AsPhW_{17}$] and [$PPhW_{17}$] is the identity of the pnictogen linker, we can surmise that the chemistry of arsenic is responsible for the irreversible behaviour. The most intuitive explanation for this behaviour is the difference in redox chemistry between arsenic and phosphorus. Both arsenic and phosphorus compounds share four common redox states (5+, 3+, 0 and -3), however, the reduction of P^V to P^{III} is highly endergonic and hence extremely difficult,[30] whereas the reduction of As^V to As^{III} is much easier to achieve.[31] It is therefore possible that the As^V centres in the hybrid can be electrochemically reduced to As^{III}, this would then cause a structural rearrangement around arsenic from trigonal pyramidal to trigonal planar which may or may not cause cleavage of the As-O bonds either due to structural strain or due to reduced oxophilicity of As^{III} vs. As^V.

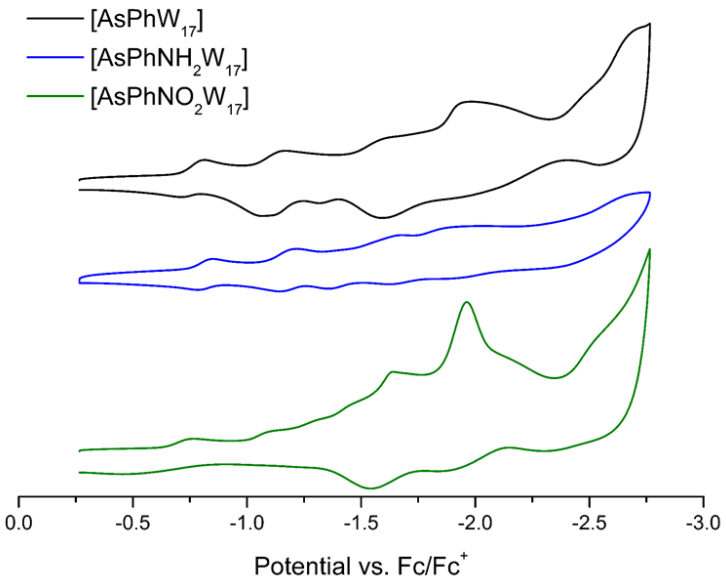


Figure 79. Cyclic voltammograms of [$AsPhW_{17}$] (black), [$AsPhNH_2W_{17}$] (blue), [$AsPhNO_2W_{17}$] (green), showing that beyond the first two reversible reductions, the voltammogram is dominated by non-reversible behaviour.

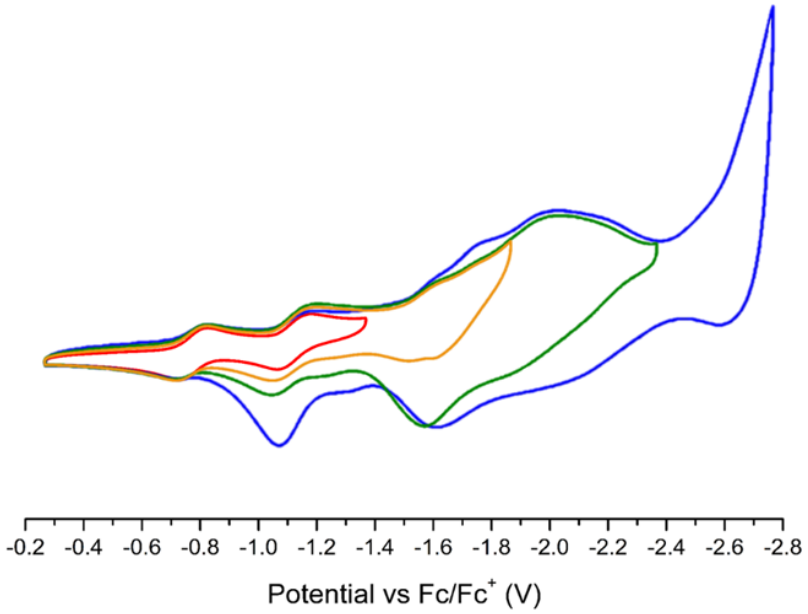


Figure 80. Cyclic voltammograms of [AsPhW$_{17}$] at increasingly negative potential windows (red→yellow→green→blue), showing that the reversibility of the first two reduction processes, and the system in general, decreases at more reducing potentials.

To investigate whether this irreversible behaviour is destructive to the sample, cycling studies were performed between -0.265 V and -2.765 V vs. Fc+/Fc. Figure 81 shows that over the course of 10 cycles, evanescence of the first three POM-based redox waves occurs until completely merging with the baseline, whereas at more reducing potentials (<-1.25 V) the subsequent evolution of oxidation peaks at -1.94 V and -2.38 V and reduction peaks at -1.31 V, -1.66 V and -2.05 V occurs. The reason for this behaviour can be explained by two contrasting theories. Firstly, supporting the above proposition, the reduction in the POM-based redox waves could indicate destruction of the sample (mediated by the redox activity of arsenic), which would mean that the evolving currents at more negative potential would correspond to the electroactive species that are formed from the breakdown of the hybrid. On the other hand, it could also be proposed that upon the third reduction of the POM, electrodeposition of the POM starts to occur on the electrode; the material deposited on the electrode exhibits different redox properties to the POMs in solution causing the evolution of new redox processes upon each successive cycle, and as the material builds on the electrode, the surface accessible to the solution decreases which causes the disappearance of the solution phase redox peaks. Whilst either theorem supports the observed behaviour, it seems logical to ascribe the difference in redox chemistry to the unique electrochemical properties of arsenic and seems a more likely reason for the large difference in behaviour exhibited by the nearly structural identical clusters [AsPhW$_{17}$] and [PPhW$_{17}$].

The latter theorem could be disproved by cycling the solution beyond the third reduction and then removing the working electrode and placing it into fresh electrolyte solution and scanning the potential window, where an observation of redox events would indicate that electroactive material is adhered to the electrode.

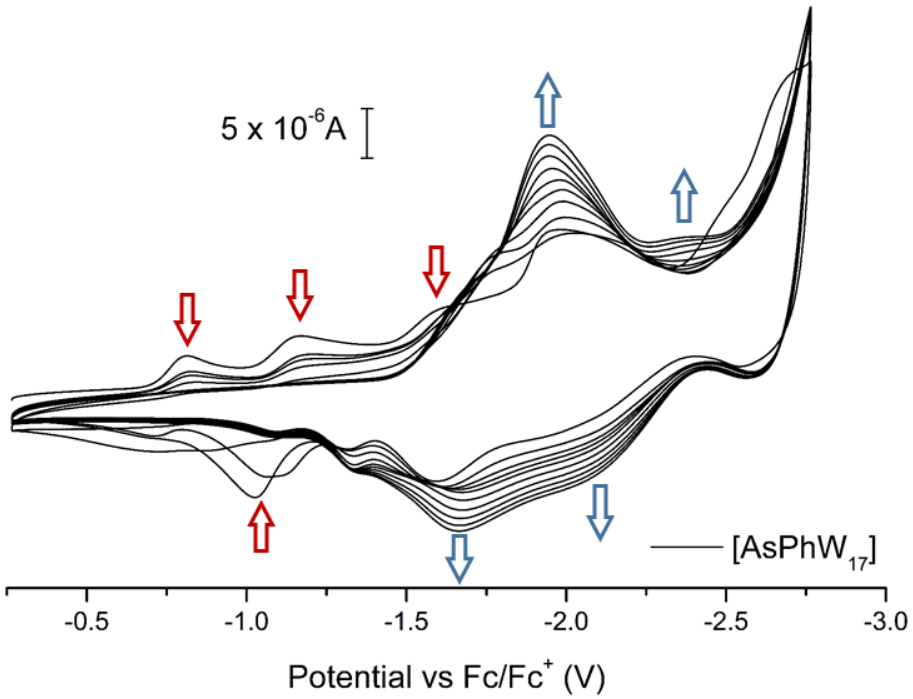


Figure 81. Cyclic voltammogram of [$AsPhW_{17}$] over 10 cycles showing the evanescence of the characteristic first and second reduction potential and the evolution of new peaks at more negative potentials.

Usually, from a combination of electrochemical and absorption measurements, it is possible to fully map the frontier molecular orbital energies of an analyte. However, given that the lowest energy transition in these compounds are the broad and complex LMCT bands (which have previously shown to be poor indicators of the true HOMO-LUMO gap), and the complete absence of oxidation processes exhibited by these POMs, it is extremely challenging to calculate the values of the HOMO and LUMO using practical experimental techniques. It was therefore decided that computational methods would be invaluable in determining these energies, hence, time-dependent density functional theory (TD-DFT) was employed for the *in silico* calculation of the HOMO, LUMO and HOMO-LUMO gap. DFT calculations were performed using geometry optimisation with BP86/LANL2DZ and energy refinement with BP86/CRENBL. Each of the 5 synthesised hybrids were analysed with this approach, where the frontier molecular orbitals of the POM were taken as the LUMO and the highest energy HOMO with a significant degree of POM-based orbital character. Higher energy HOMO energies were almost entirely

ligand centred and therefore non-contributing to the energy of the POM-centred LMCT band as no intramolecular charge transfer is expected to occur in these species, as the UV-vis spectra feature no discernible charge transfer bands. The HOMO-LUMO orbital diagrams and energies are given in Figure 82. Looking at the charge density diagrams generated from the calculations, the LUMO energies in each case appear to be POM centred and delocalised across the entire structure, this is expected as the first reduction of many POMs typically involves reduction of the metal centre which then undergoes IVCT between the many equivalent/near equivalent metal centres of the POM. The HOMO-X, where X= 2, 4 or 6 depending on the specific cluster (lowest energy HOMO with significant POM contributions), shows greater differences between the 5 species. Most notable perhaps is that the HOMO-4 for [$SiPhW_{17}$] is unique in that it shows very little orbital mixing between the phenyl ring and POM, with the orbitals delocalised across the POM in a similar manner as in the LUMO. Whereas the HOMO-X for the arylphosphonate and arylarsonate hybrids all show significant orbital mixing between the aryl rings and the POM, with the POMs orbital distribution being confined to the northern hemisphere of the structure, proximal to the site of functionalisation. This clearly supports the experimental and reported literature observations that the silyl group prevents orbital mixing whereas the phosphoryl and arsonyl promotes it through a mixture of inductive and resonance effects.

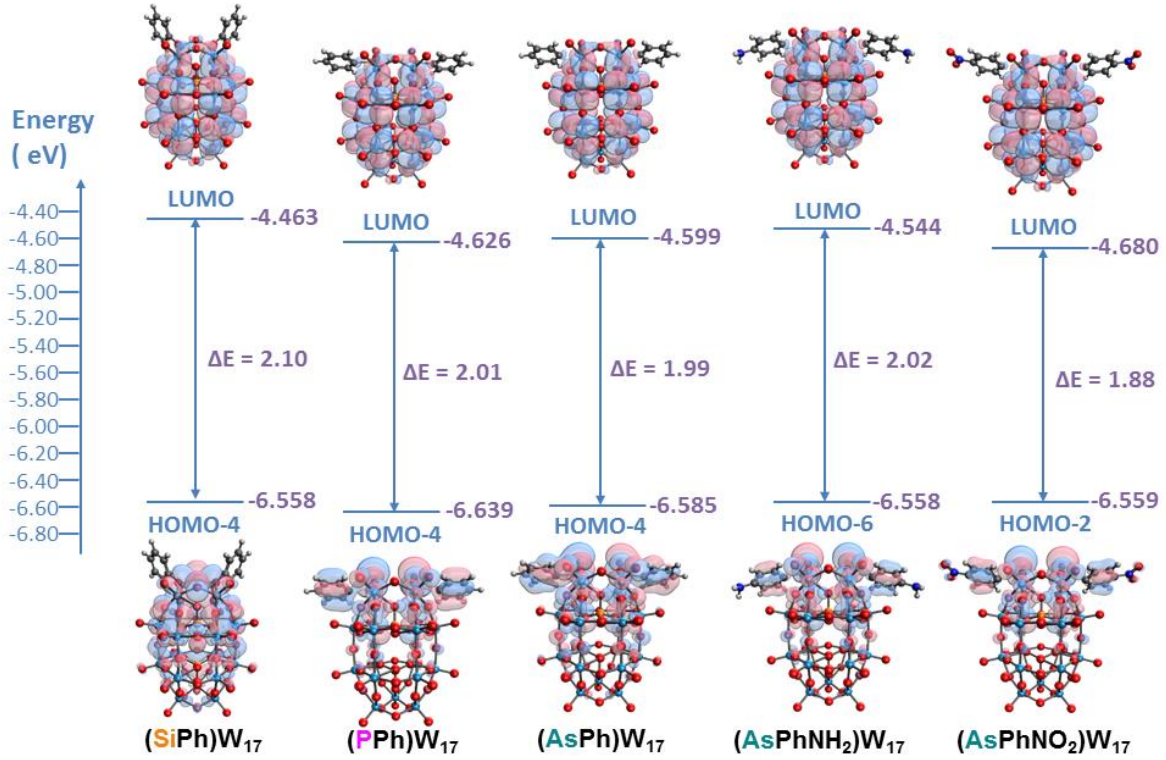


Figure 82. HOMO-LUMO orbital diagrams of [$SiPhW_{17}$], [$PPhW_{17}$], [$AsPhW_{17}$], [$AsPhNH_2W_{17}$] and [$AsPhNO_2W_{17}$] showing the calculated highest POM centred HOMO energies and LUMO energies and calculated HOMO-LUMO gaps.

Concerning the orbital values calculated from DFT, several trends are observed. Whilst the HOMO energies of the POMs could not be compared with any experimental data, the LUMO energies should correlate directly with the observed first redox potentials that we obtained from cyclic voltammetry – especially since the DFT studies were optimised with the polarisation continuum model for DMF. Excellent agreement is observed between the electrochemical and computational results for the two related series of compounds. Specifically, the series of compounds where the linker atom is modified gave first reduction potentials in the series -0.741 $V_{[PPhW17]}$ > -0.775 $V_{[AsPhW17]}$ >> -1.17 $V_{[SiPhW17]}$. The LUMO energies calculated from DFT are as follows -4.63 $eV_{[PPhW17]}$ > -4.60 $eV_{[AsPhW17]}$ >> -4.46 $eV_{[SiPhW17]}$, showing good agreement between measured and calculated results. The same accord is seen across the second series, where the nature of the aryl ring of the organoarsenic hybrid is modulated through para substitution. Here, the redox potential series, -0.723 $V_{[AsPhNO2W17]}$ > -0.775 $V_{[AsPhW17]}$ > -0.837 $V_{[AsPhNH2W17]}$, again shows a strong correlation with the calculated LUMO energies: -4.68 $eV_{[AsPhNO2W17]}$ > -4.60 $eV_{[AsPhW17]}$ > -4.54 $eV_{[AsPhNH2W17]}$. With the HOMO-X and LUMO energies for each hybrid calculated, it is theoretically possible to derive the HOMO-LUMO gap. The HOMO-LUMO gaps are calculated to fall between 1.88 and 2.10 eV for each of the hybrids. Using Equation 4 (Chapter 2), this would imply that the POMs should have absorption characteristics between 590 and 659 nm which is clearly absent within the UV-vis spectra. The POM absorption spectra suggest that the HOMO-LUMO gaps of the hybrids are > 3 eV based on the absorption edge, notwithstanding [$AsPhNH_2W_{17}$] with an absorption edge at ~1.7 eV. This demonstrates that there are some shortcomings associated with the values calculated from DFT, likely due to the difficulties of accurately predicting the HOMO energies of the POM hybrids due to the complex mixing of orbitals between the POM and the organic components.

From the above we can conclude that functionalisation has a clear and predictable influence on the LUMO energies of the hybrid POMs based on predictable rules following electron withdrawing and donating effects, however, spectroscopic studies show that the HOMO-LUMO gap remains similar across the series of hybrids, barring [$AsPhNH_2W_{17}$], implying that changes in the LUMO energy are accompanied by changes in the HOMO energy of similar magnitude. This means that, whilst functionalisation does not necessarily allow the photosensitisation of the hybrids into the visible region of the spectrum, it does allow the HOMO energy to be tuned, and hence the strength of the photooxidation catalyst can be effectively tailored. This has obvious implications in a myriad of

applications where an intimate understanding of the electronic properties of the system and the ability to controllably tune these properties is paramount, such as photonic and biomimetic catalytic systems which rely on intricate redox cascades.

3.3.4 Photoreduction studies

Encouraged by the above experimental and theoretical findings, we aimed to test the phenylarsonic hybrid POM against its phosphorus and silicon analogues for its photoreduction behaviour. Whilst [$AsPhNH_2W_{17}$] and [$AsPhNO_2W_{17}$] respectively showed promising signs of superior photoactivity through long visible tailing in the absorption spectra or small calculated HOMO-LUMO gap, these species were deemed unsuitable for solely determining the effect of the ring electronics on the system. This is due to the difficulty isolating the electronic influence of the R groups given the large difference in the molar extinction coefficients of the three species and the potential non-innocence of the amine groups of [$AsPhNH_2W_{17}$], as they can act as both hydrogen bond donors and acidic proton acceptors within a reaction pathway.

In this study, we investigated the photoreduction capabilities of the compounds using a 500 W mercury-xenon lamp (operating at 200 W) which has a broad spectral output with strong UV and visible light intensities. To determine whether the POM hybrids retained photoactivity towards visible light, parallel experiments were also performed with the use of a 395 nm cut-off filter. Following the example of Odobel et al.[27], we used DMF as the sacrificial electron donor and solvent, permitting the comparison of the reactivities of the hybrids in a simple yet informative manner. The activity of the POMs was monitored by UV-vis spectroscopy via the characteristic IVCT bands, which have different maxima for each reduced state, and thus allowed for the facile tracking of the sequential photoreduction of the POM in the presence of DMF. It was necessary to also run each photoreduction experiment in the absence of molecular oxygen, so that the rate of the photoreduction is not hampered by reoxidiation of the reduced states. Finally, the same experiments were also performed with tetra-n-butylammonium decatungstate (TBADT); which as mentioned in the introduction, is a vastly employed and well-studied POM that represents the literature standard in POM photocatalysis and will act as a benchmark for our hybrid POM species.

Firstly, the photochemistry of TBADT was probed using both UV-vis and visible irradiation. Under UV-vis irradiation (Figure 83a), the POM undergoes rapid reduction to the singly reduced state, $H[W_{10}O_{32}]^{5-}$, manifesting as a growth in an IVCT band located at 783 nm in the presence of DMF, which saturates within 30 seconds. It is uncertain here whether the hydrogen atom here originates from the solvent or the countercation as the latter is known to occur with organic cations.[32] Continuous irradiation garners the simultaneous evolution of two new IVCT bands focused at 631 nm and 962 nm which correspond to the doubly reduces species, $H_2[W_{10}O_{32}]^{6-}$. As discussed by Yamase and Usami, the growth of this peak does not actually correspond to the direct photoinduced generation of the doubly reduced state – instead $H_2[W_{10}O_{32}]^{6-}$ is generated from the disproportionation of $H[W_{10}O_{32}]^{5-}$.[33] When the 395 nm filter is employed, the photoactivity of the system is vastly depressed, within the timescale of the experiment (6900 s), the generation of the singly reduced state reaches only 47% completion based on percentage of λ_{max} as obtained from the UV experiment (Figure 83b).

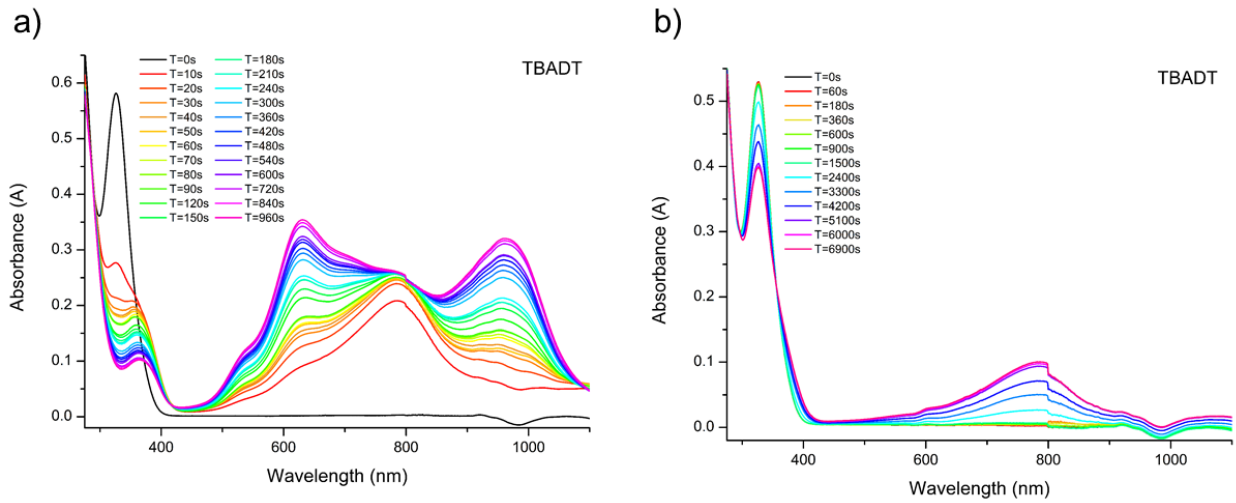


Figure 83. Photoreduction of TBADT using a) UV-vis light b) visible light showing evolution of the IVCT bands corresponding to singly and doubly reduced states.

Next, we consider the photoactivity of $[SiPhW_{17}]$ under the same conditions with both UV-vis and visible irradiation. Without the use of a filter (UV-vis regime), the hybrid undergoes the first electron reduction which is measured by an IVCT band located at 815 nm within a considerably slower timeframe of 70 s. In this instance, continued irradiation also yields the doubly reduced species with just a single band at 725 nm which saturates after 600 s. However, when the photoirradiation is continued further, the growth of a third IVCT at 692 nm occurs which corresponds to the triply reduced species and this occurs slowly over a large timeframe of 8700 s (Figure 84a). Again, switching over to the visible light only regime, a large decrease in photoactivity is observed, with similar visible light photoactivity as seen by TBADT.

That is, the singly reduced species does not saturate within the timeframe of the experiment, reaching only 27% completion after 7200 s (Figure 84b).

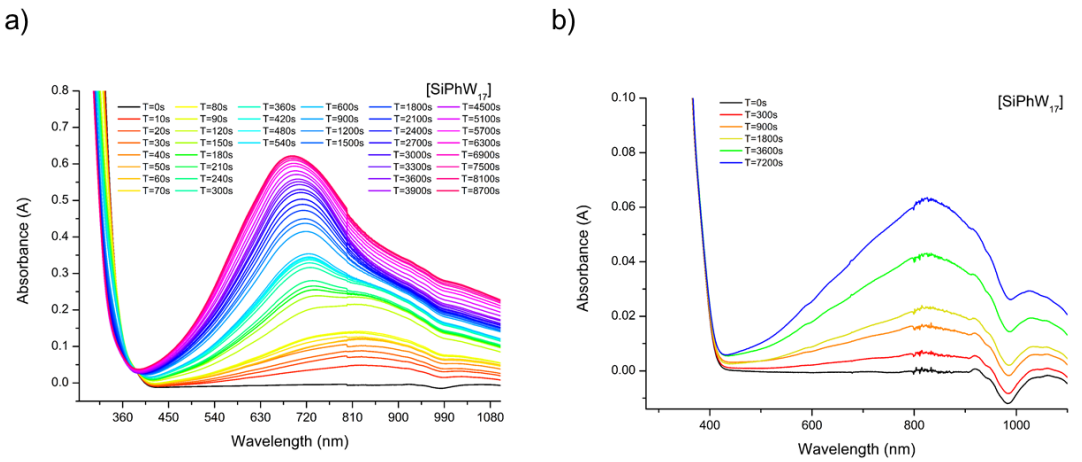


Figure 84. Photoreduction of [SiPhW$_{17}$] using a) UV-vis light b) visible light showing evolution of the IVCT bands corresponding to singly, doubly and triply reduced states.

Thirdly, [PPhW$_{17}$] is analogously photoirradiated. Under UV-vis irradiation, the rapid generation of the singly reduced state is observed with almost total saturation of the IVCT band located at 824 nm after the first 10 s time interval measurement (full saturation guaranteed after 20 s). Comparatively, [PPhW$_{17}$] then undergoes a second reduction event manifesting as an IVCT band at 672 nm at a much faster rate than both TBADT and [SiPhW$_{17}$] within 180 s. Finally, matching the behaviour of [SiPhW$_{17}$], the phenylphosphonic hybrid also undergoes a third reduction process which is monitored by the growth of an IVCT band focused at 649 nm, and this occurs at a comparatively faster rate of 5160 s vs [SiPhW$_{17}$] (cf. 8700 s), albeit still relatively slow (Figure 85a). The major difference observed with [PPhW$_{17}$] and [SiPhW$_{17}$] is when the 395 nm filter is employed - switching to the visible light regime. Under visible light irradiation, [PPhW$_{17}$] reaches saturation of its first reduced species within 2100 s, with a small shouldering peak developing at ~670 nm indicating the onset of double reduction (Figure 85b), thus [PPhW$_{17}$] is significantly more sensitised towards visible light than [SiPhW$_{17}$] as predicted by its lower energy, and hence more photooxidising, HOMO.

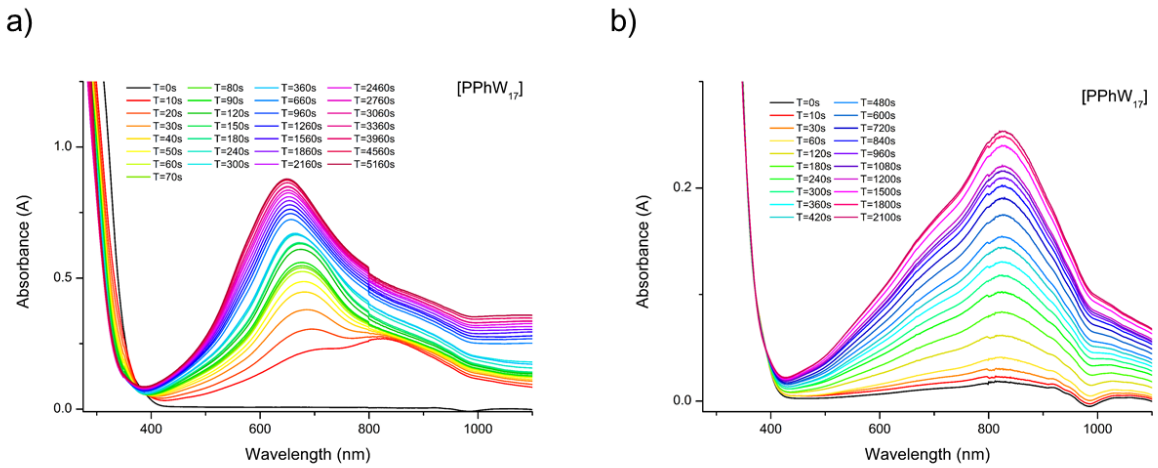


Figure 85. Photoreduction of [PPhW$_{17}$] using a) UV-vis light b) visible light showing evolution of the IVCT bands corresponding to singly, doubly and triply reduced states.

Finally, the photoreduction behaviour of [AsPhW$_{17}$] is then studied in the same manner. With UV-vis irradiation, behaviour similar to the isoelectronic [PPhW$_{17}$] is initially observed, with the rapid formation of the singly reduced species observed through the evolution of an IVCT band at 832 nm within 20 s, this is then followed by the evolution of the doubly reduced species, manifesting as an IVCT band at 703 nm, which occurs over a slightly longer timeframe than [PPhW$_{17}$] (300 s vs. 180 s) (Figure 86a). Interestingly, divergent behaviour is observed from the related phenylphosphonate and phenylsiloxane analogues upon continued irradiation. Instead of the evolution of the third reduced species, the IVCT band corresponding to the doubly reduced state starts to decay and become broader. This agrees with the behaviour observed within the electrochemical characterisation, where [SiPhW$_{17}$] and [PPhW$_{17}$] can reversibly access up to 4 reduced states, whereas for all the arylarsonic hybrids, only two reduced states are reversibly accessed. The lack of a triply reduced state coupled with the decay of the doubly reduced state supports the previous theorem that the POM undergoes degradation at highly reducing potentials. Considering the visible light photoreduction experiments, [AsPhW$_{17}$] achieves the saturation of the singly reduced state after 7200 s (Figure 86b), which is significantly slower than [PPhW$_{17}$] courtesy of a higher energy HOMO but does reach saturation within the timescale of the experiment.

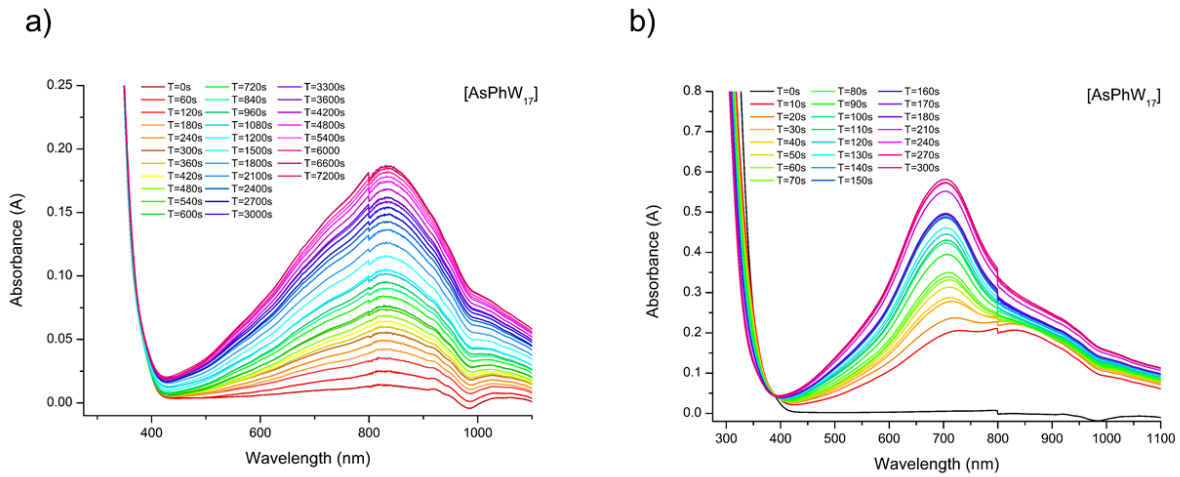


Figure 86. Photoreduction of [AsPhW$_{17}$] using a) UV-vis light b) visible light showing evolution of the IVCT bands corresponding to singly and doubly reduced states.

To directly compare the rates of photoexcitation of the different POMs under the two photoexcitation regimes, it is possible to plot the evolution of the different energy IVCT bands as time dependent percentage of their absorption maxima. Figure 87a shows the comparison of the rates of the first photoreduction under UV-vis irradiation, here it can be seen that [PPhW$_{17}$], [AsPhW$_{17}$] and TBADT undergo rapid conversion to the monoreduced species, whereby the lack of data points make it difficult to ascertain which POM is the most photoactive in this regard (although the general suggested trend is [PPhW$_{17}$] > [AsPhW$_{17}$] > TBADT). Whereas [SiPhW$_{17}$] is markedly less active, as predicted by its higher energy HOMO. More clarity is obtained from observing the rate of evolution of the doubly reduced species (Figure 87b), where a trend in activity is observed: [PPhW$_{17}$] > [AsPhW$_{17}$] > [SiPhW$_{17}$] > TBADT. It is not surprising here that decatungstate shows the slowest evolution of the doubly reduced state as it occurs via a disproportionation mechanism which will have completely different kinetics to the Dawson based species. The general trend fits the observed differences in the second reduction potentials (an estimation of the LUMO+1) of each hybrid POM determined by cyclic voltammetry, and whilst the second reduction of [AsPhW$_{17}$] occurs at slightly more positive potentials than [PPhW$_{17}$] (-1.122 V vs. -1.228 V) the rate of photoreduction seems governed by the more photooxidising lower energy HOMO of [PPhW$_{17}$]. Finally, under the UV-vis regime Figure 87c, the rate of the third reduction is compared for just [SiPhW$_{17}$] and [PPhW$_{17}$], as TBADT and [AsPhW$_{17}$] cannot access the third reduced state within reasonable conditions or without concomitant degradation respectively. As we have previously discussed, the rate of the third reduction for these two species follows the expected trends based on the energies of the systems.

The rate of photoreduction for each compound is then compared under the visible light regime (Figure 87d). It is observed that the photoabsorption rate of each species is severely slowed compared to the analogous study with UV-vis irradiation, due to the absorption maxima residing in the UV region with tailing into the visible region for all species. In general, the trend in photoactivity follows that suggested earlier for the analogous UV-vis excitation to the singly reduced species: [$PPhW_{17}$] > [$AsPhW_{17}$] > TBADT > [$SiPhW_{17}$]. This demonstrates that the POMs can still be activated by visible light but to a much lesser extent which agrees with the profiles obtain from UV-vis spectroscopy, it also shows that the energy of the HOMO still dictates the level of activity in the visible light regime. Overall, this shows that the hybrids which employ the electron withdrawing anchoring groups, including phenylarsonate, serve to activate the POM towards both visible and UV light, mainly through the energetic depression of the HOMO and LUMO energies.

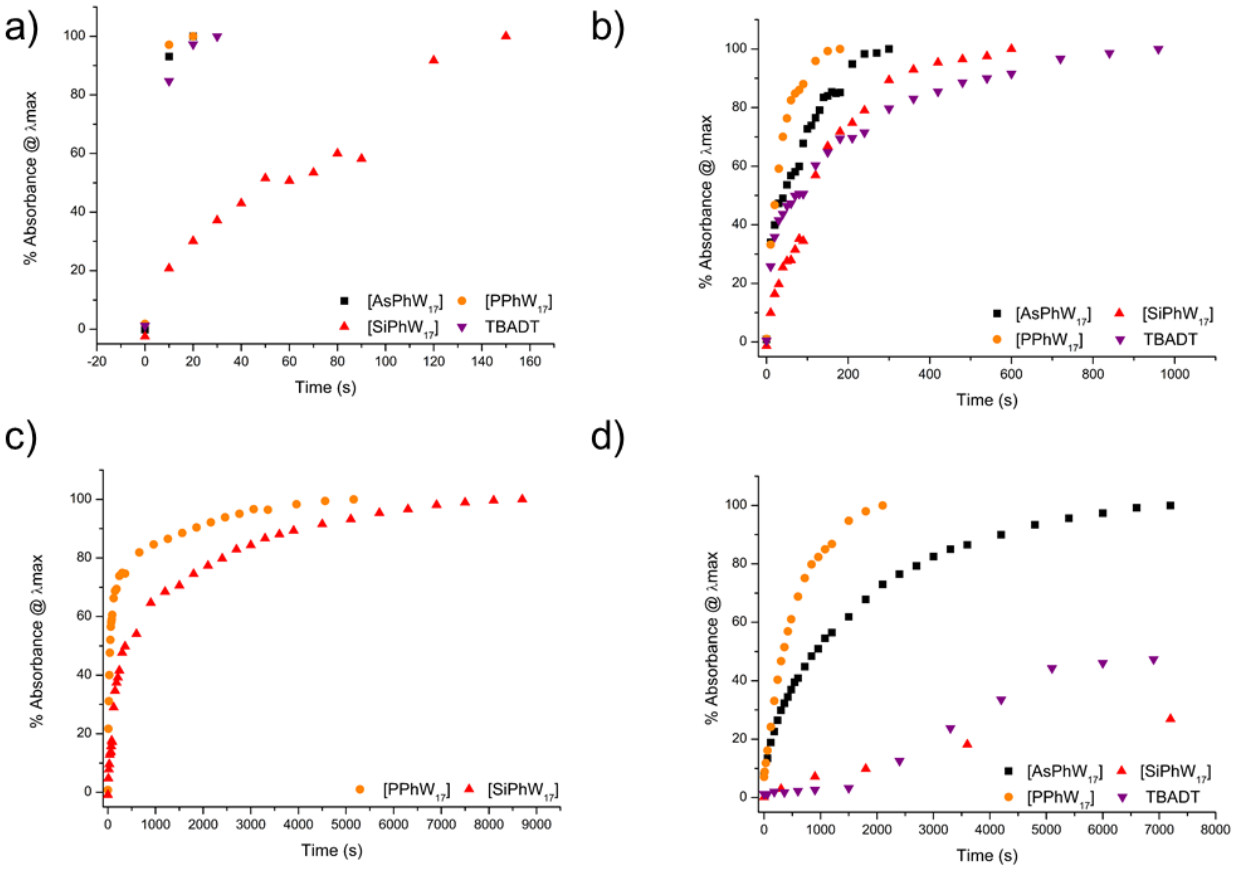


Figure 87. Rate of evolution of the IVCT bands a) singly reduced (Uv-vis), b) doubly reduced (UV-vis), c) triply reduced (UV-vis), d) singly reduced (Vis) of TBADT (purple triangles), [$SiPhW_{17}$] (red triangles), [$PPhW_{17}$] (orange circles) and [$AsPhW_{17}$] (black squares).

Considering any POM-based materials as catalytic species, whether photo-, thermo- or conventional, it is equally important to consider both the activity towards a substrate and the ability to recover the

catalyst using an appropriate oxidant. If the reduced form of the POM is not easily recovered by cheap, abundant and green oxidants such as molecular oxygen and hydrogen peroxide, the benefits of using POMs as a photocatalyst in terms of sustainability are soon outweighed through the stoichiometric use of strong oxidants. It was therefore important to verify that the reduced states of the POMs that are generated during the experiment can be recovered by a green oxidant, and to determine the relative rates of these recoveries. Due to their superior activities under both UV-vis and visible light irradiation, [$PPhW_{17}$] and [$AsPhW_{17}$] were tested as lead compounds in this experiment. Both the simplest and greenest oxidant to test was molecular oxygen, for obvious reasons, and thus we investigated the ability of the reduced POMs to be reoxidised aerobically. Experimentally, this was achieved by photoreducing the hybrid POMs in DMF as described above (i.e. under anaerobic conditions), until saturation of the desired reduced state is achieved, and then to expose the solution to air and measure any changes to the IVCT absorption bands that correspond to the population of the reduced states in the solution. For direct comparison, we investigated the rate of oxygen recovery on the doubly reduced and singly reduced species of [$PPhW_{17}$] and [$AsPhW_{17}$] which can be controllably achieved through visible light without the risk of interference from the third reduction. The recovery of the ground state from the monoreduced species show different behaviour between the two species (Figure 88). For [$PPhW_{17}$] there is initial fast recovery of the reduced species, but considerably slows after ~20% recovery of the oxidised state and decays with a linear dependence. [$AsPhW_{17}$] however shows an even faster initial recovery process until 50% recovery of the ground state, then enters a linear decay with similar rate to that of [$PPhW_{17}$]. The multi-component kinetics observed for these two reactions is indicative of an initial “true” kinetic plot for the reaction of the reduced POMs with oxygen which then becomes mass transfer limited due to the slow dissolution of oxygen from the gas phase into the solution, this is evidenced by the apparent similarities in the kinetics of this secondary linear rate, and has also been observed in other POM based aerobic catalysis systems.[34] Considering only the initial rates, this shows that the oxygen recovery of [$AsPhW_{17}$] proceeds at a faster rate than [$PPhW_{17}$] for the one electron reduced species, which is logical from a thermodynamic perspective, as the LUMO of [$AsPhW_{17}$] is higher in energy, and hence there will be a stronger driving force for transfer of the reduced state electron from the POM hybrid to the HOMO of molecular oxygen. Overall, this implies that there is a delicate balance when tuning the frontier molecular orbitals using organic modification with a view for catalytic applications, in that, whilst the POM may be more powerful photooxidisers through depression of the

HOMO, it may be counterbalanced by inferior catalyst recovery due to the accompanied depression of the LUMO.

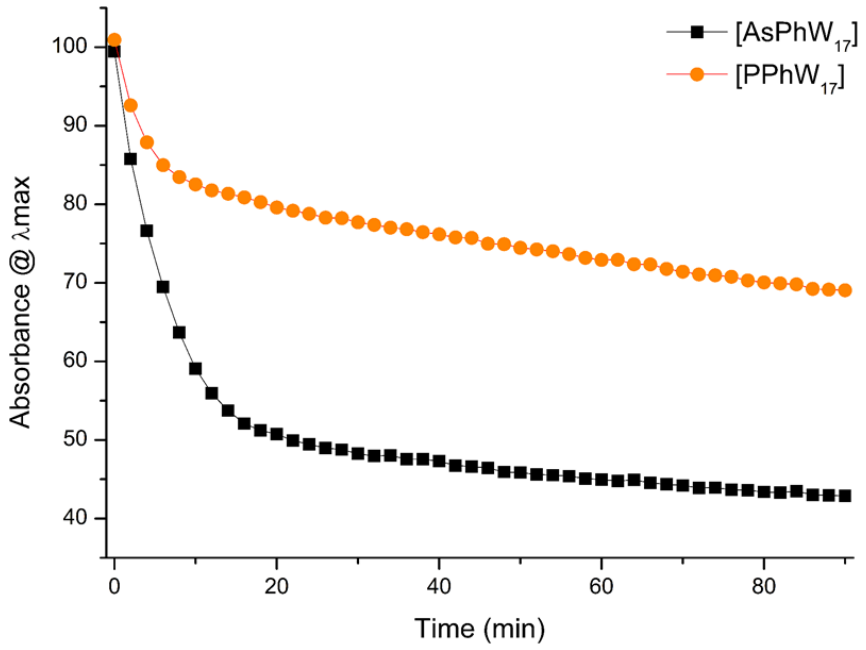


Figure 88. Rate of disappearance of the singly reduced IVCT bands for [$PPhW_{17}$] and [$AsPhW_{17}$] upon exposure of the reduced solution to air, showing that [$AsPhW_{17}$] is more easily recovered by molecular oxygen than [$PPhW_{17}$].

3.4 Conclusion

To summarise, the synthesis and characterisation of a new family of hybrids has been achieved by covalently grafting three different arylarsonic acids, to the Wells-Dawson polyoxotungstate in a 2:1 ratio, giving compounds which are isostructural to their well-characterised organophosphorus analogues. The three arylarsonic hybrids differ in the electronic nature of the appended aryl rings comprising the "neutral" phenyl group, the electron donating para-amino arene and the electron withdrawing para-nitro arene. Also synthesised were the structurally related compounds [$PPhW_{17}$] and [$SiPhW_{17}$], and isopolyoxometalate TBADT for comparative and benchmarking purposes respectively.

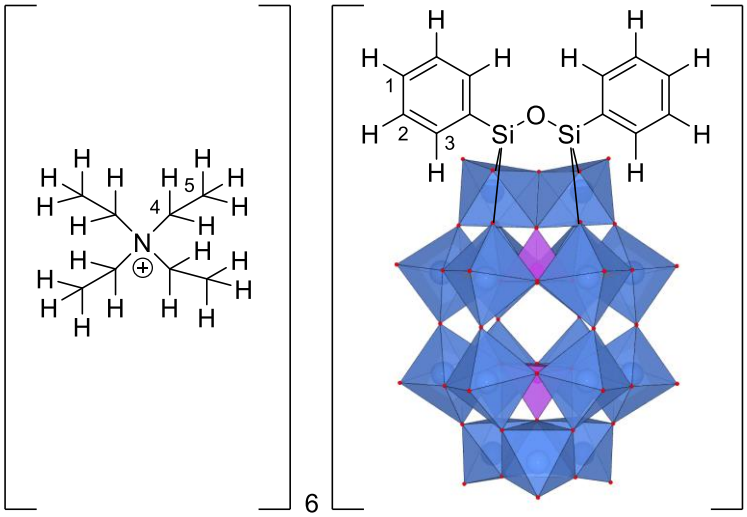
The structure of these compounds was confirmed by ^{1}H and ^{31}P NMR spectroscopy, IR spectroscopy and X-ray crystallography (in the case of [$AsPhW_{17}$]). Electronically, the compounds were characterised via cyclic voltammetry, which unequivocally demonstrated that the arylarsonic hybrids were easily reduced and the redox potentials were tuneable based on nature of the aromatic ring. UV-vis spectroscopy was also employed and showed that each hybrid possessed similar HOMO-LUMO gaps,

implying that changes to the LUMO energy were accompanied by changes to the HOMO energy of similar magnitude between all hybrid species. DFT calculations were performed for each compound and the LUMO energies correlated well with the trends in first reduction potentials, however there were difficulties in rationalising the experimentally observed HOMO-LUMO gaps likely due to problems with accurately mapping the HOMO energies. The photoreduction properties of [$AsPhW_{17}$] was compared with [$SiPhW_{17}$], [$PPhW_{17}$] and TBADT, and found to be superior to both [$SiPhW_{17}$] and TBADT under both UV-vis and visible light regimes for the first and second photoreduction events, however the performance was slightly lower than [$PPhW_{17}$] which followed the trends in the LUMO/HOMO energies. On the other hand, the reduced states of [$PPhW_{17}$] were found to be more difficult to recover with molecular oxygen than [$AsPhW_{17}$], as the LUMO is more stabilised, the thermodynamic driving force for the reduction of oxygen is lower.

Overall, the above work demonstrates that organoarsenic hybrid POMs, which have both an electron withdrawing effect on the POM and permit the redox tuning of the POM through changing the electronic nature of the aromatic ring, represents an extension to the hitherto unique influence of arylphosphonic acids on lacunary Keggin and Dawson polyoxometalates. The HOMO stabilising effect causes [$AsPhW_{17}$] to be active towards the photooxidation of DMF, although it has a higher HOMO energy than [$PPhW_{17}$] which makes it slightly more difficult to photoreduce. Nonetheless, the higher LUMO energy of [$AsPhW_{17}$] vs. [$PPhW_{17}$] facilitates its reoxidation by molecular oxygen – showing that the tuning of the frontier molecular orbital levels represents a balancing act between these two processes for attaining an efficient catalytic cycle. The development of this chemistry would clearly focus on the investigation of the para-substituted derivatives, which show interesting properties that may bolster their photoactivity such as enhanced visible tailing of the LMCT band and decreased HOMO-LUMO gaps. It would also be interesting to further probe the origin of the strong absorption properties of [$AsPhNH_2W_{17}$], as this could be indicative charge transfer processes which may alter the molecules fundamental photochemistry. Furthermore, the relatively unexplored combination with polyoxotungstates with organoarsenates in the modular approach gives an abundance of opportunities for the synthesis of new photo- and electroactive materials.

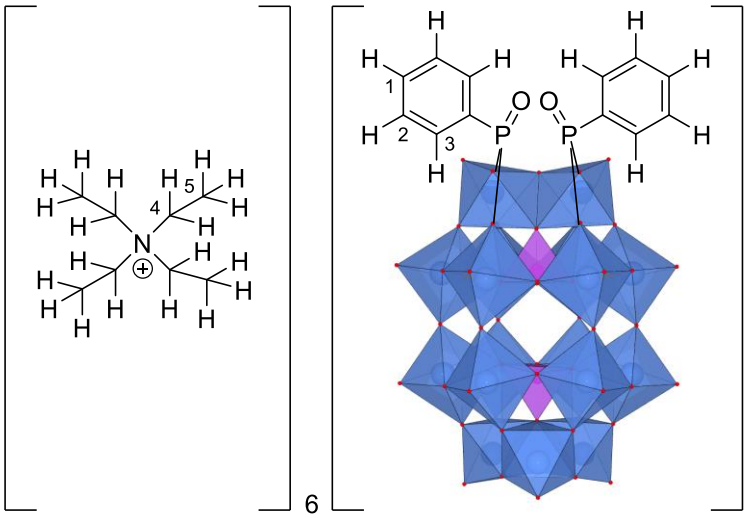
3.5 Experimental

Synthesis of $(C_8H_{20}N)_6[P_2W_{17}O_{62}(SiC_6H_5)_2]$ "[SiPhW$_{17}$]"



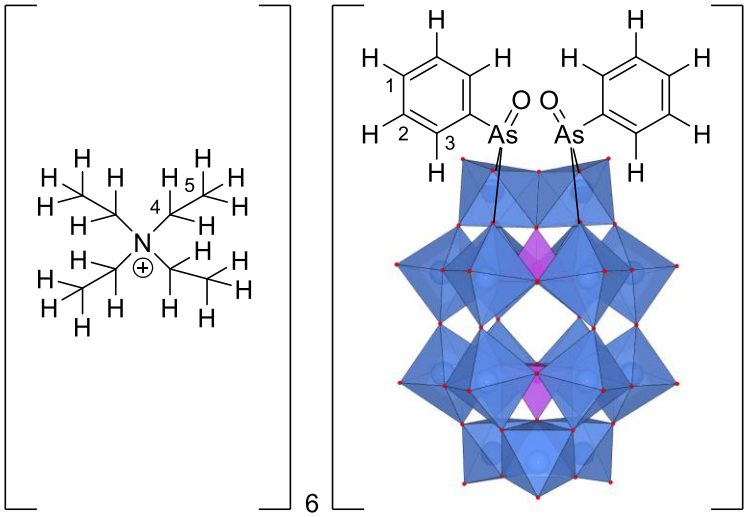
[SiPhW$_{17}$] was synthesised according to a modified literature procedure. Trimethoxysilane (37.3 µL, 0.293 mmol) was added to a mixture of methanol (15 ml) and water (5 ml). After stirring for 5 mins, $K_{10}[P_2W_{17}O_{61}]$ (0.5 g, 0.110 mmol) was added to the suspension and was stirred for a further 5 mins. The pH of the dispersion was then adjusted to 1.8 with 1 M HCL causing the dissolution of the reagents and the development of a yellow solution. The solution was stirred for 30 mins forming a white precipitate, which is removed by filtration. The filtrand is then stirred for 16 hrs and the solvent is removed *in vacuo* to give a pale-yellow powder (0.423 g). The powder was redissolved in *ca.* 10 ml water and to this was added N-tetraethylammonium bromide (0.273 g, 1.30 mmol) dissolved in 10 ml of water with stirring, causing the immediate precipitation of a pale yellow solid. The suspension was stirred for 1 hr and then filtered and washed with ethanol and diethyl ether, yielding the product as a pale-yellow powder (0.287 g, 57%). ^{1}H NMR (DMSO-d$_6$, 500MHz, ppm) δ 7.78-7.72 (C3-H, m, 4H, CH_{Ar}), 7.43-7.34 (C1/2-H, m, 6H, CH_{Ar}), 3.28 (C4-H, q, J=7.2Hz, 48H, CH_2), 1.21 (C5-H, tt, J=7.3, 1.7Hz, 72H, CH_3). ^{31}P NMR (DMSO-d$_6$, 202MHz, ppm) δ -10.76, -13.80. ATR-IR (cm^{-1}): 2980 (w,ν_{C-H}), 1482 (m,ν_{C-H}), 1391 (m,ν_{C-H}), 1128 (m, $\nu_{Si-O-Si}$), 1085 (m, ν_{P-O}), 1040 (s, ν_{Si-O-W}), 946 (s, $\nu_{W=O}$), 914 (s, ν_{P-O}), 790-741 (vs, ν_{W-O-W}), 697 (s, ν_{Si-C}).

Synthesis of $(C_8H_{20}N)_6[P_2W_{17}O_{61}(POC_6H_5)_2]$ "$[PPhW_{17}]$"



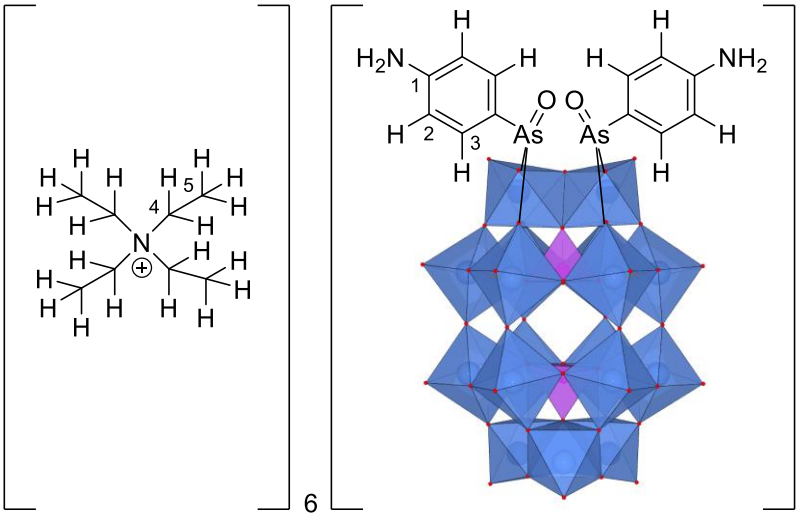
$[PPhW_{17}]$ was synthesised according to a modified literature procedure. Phenylphosphonic acid (39.5 mg, 0.250 mmol) was dissolved in DMF (15 ml) with stirring to give a colourless solution. To this was added $K_{10}[P_2W_{17}O_{61}]$ (0.5 g, 0.110 mmol) followed by 12 M HCl (49 µL, 0.588 mmol) giving a pale turbid solution. The solution was then heated at 90°C for 16 hrs after which it had become a cloudy pale-yellow suspension. This was cooled to room temperature and filtered to give a pale yellow-green solution. This was then added to a large excess of EtOAc and the suspension was centrifuged, and the supernatant was discarded leaving a sticky green solid. The sticky green solid was repeatedly sonicated in CHCl3 until it became a free-flowing powder, which was collected by centrifugation and dried *in vacuo*. The green powder was then redissolved in *ca.* 10 ml of water and to this was added N-tetraethylammonium bromide (0.273 g, 1.30 mmol) dissolved in 10 ml of water with stirring, causing the immediate precipitation of a pale blue solid. The suspension was stirred for 1 hr and then filtered and washed with ethanol and diethyl ether, yielding the product as a pale-blue powder (0.381 g, 76%). ^{1}H NMR (DMSO-d_6, 500MHz, ppm) δ 8.03-7.94 (C3-H, m, 4H, CH_{Ar}), 7.58-7.51 (C1-H, m, 2H, CH_{Ar}), 7.50-7.45 (C2-H, m, 4H, CH_{Ar}), 3.24 (C4-H, q, J=7.2Hz, 48H, CH_2), 1.19 (C5-H, tt, J=7.3, 1.8Hz, 72H, CH_3). ^{31}P NMR (DMSO-d_6, 202MHz, ppm) δ 14.93, -11.32, -12.94. ATR-IR (cm^{-1}): 2957 (w,ν_{C-H}), 1484 (m,ν_{C-H}), 1392 (m,ν_{C-H}), 1135 (m, $\nu_{P=O}$) , 1087 (m, ν_{P-O}), 953 (s, $\nu_{W=O}$), 906 (s, ν_{P-O}), 731 (vs, ν_{W-O-W}).

Synthesis of $(C_8H_{20}N)_6[P_2W_{17}O_{63}(AsC_6H_5)_2]$ "$[AsPhW_{17}]$"



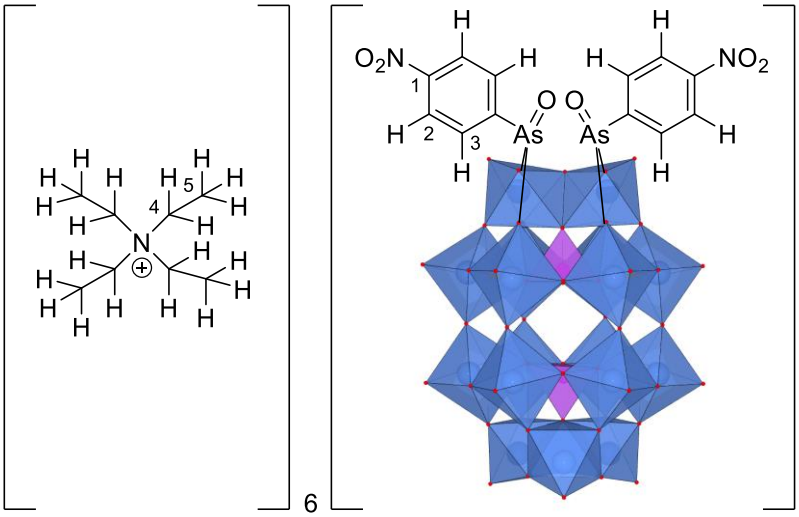
Phenylarsonic acid (50.5 mg, 0.250 mmol) was dissolved in DMF (15 ml) with stirring to give a colourless solution. To this was added $K_{10}[P_2W_{17}O_{61}]$ (0.5 g, 0.110 mmol) followed by 12 M HCl (49 µL, 0.588 mmol) giving a pale turbid solution. The solution was then heated at 90°C for 16 hrs after which it had become a cloudy off-white suspension. This was cooled to room temperature, filtered, and to this was added dry N-tetraethylammonium bromide (0.211 g, 1 mmol) and the mixture was stirred for 1 hr. The solvent was then removed *in vacuo*, giving a pale blue powder, and the solid was redissolved in the minimum amount of anhydrous DMF and precipitated by the addition of a large excess of MeCN. The suspension was then centrifuged, the supernatant discarded, and then the powder was sonicated in a large excess of MeCN. This was again centrifuged, the supernatant discarded, and the solvent was removed *in vacuo* to give the product as a pale blue powder. (0.332 g, 66%). Single crystals of $[AsPhW_{17}]$ could be grown by dissolution of 20 mg of powder in DMSO, followed by vapour diffusion of EtOAc into the solution to yield single crystals of $[AsPhW_{17}]$ after *ca.* 2 weeks (see crystallographic section for details). ^{1}H NMR (DMSO-d_6, 500MHz, ppm) δ 8.10-8.03 (C3-H, m, 4H, CH_{Ar}), 7.78-7.72 (C1-H, m, 2H, CH_{Ar}), 7.71-7.65 (C2-H, m, 4H, CH_{Ar}), 3.23 (C4-H, q, J=7.2Hz, 48H, CH_2), 1.18 (C5-H, tt, J=7.3, 1.9Hz, 72H, CH_3). ^{31}P NMR (DMSO-d_6, 202MHz, ppm) δ -11.31, -13.26. ATR-IR (cm^{-1}): 2978 (w,ν_{C-H}), 1739 (w, $\nu_{As-O\ overtone}$), 1483 (m,ν_{C-H}), 1391 (m,ν_{C-H}), 1085 (m, ν_{P-O}), 952 (s, $\nu_{W=O}$), 915(s,ν_{P-O}),773(vs,ν_{W-O-W}). Anal. *Calcd.* for $C_{60}H_{130}N_6P_2As_2O_{63}W_{17}$ (5280.74): C 13.65, H 2.48, N, 1.59. Found: C 14.23, H, 2.87, N, 1.64.

Synthesis of $(C_8H_{20}N)_6[P_2W_{17}O_{63}(AsC_6H_4NH_2)_2]$ "$[AsPhNH_2W_{17}]$"



p-Arsanilic acid (54.3 mg, 0.250 mmol) was dissolved in DMF (15 ml) with stirring to give a colourless solution. To this was added $K_{10}[P_2W_{17}O_{61}]$ (0.5 g, 0.110 mmol) followed by 12 M HCl (49 µL, 0.588 mmol) which formed a turbid orange solution. The solution was then heated at 90°C for 16 hrs after which it had become a cloudy orange-red suspension. This was cooled to room temperature, filtered and to this was added dry N-tetraethylammonium bromide (0.211 g, 1 mmol) and the mixture was stirred for 1 hr. The solvent was then removed *in vacuo*, giving an orange powder, and the solid was redissolved in the minimum amount of anhydrous DMF and precipitated by the addition of a large excess of MeCN. The suspension was then centrifuged, the supernatant discarded, and then the powder was sonicated in a large excess of MeCN. This was again centrifuged, the supernatant discarded, and the solvent was removed *in vacuo* to give the product as an orange powder. (0.354 g, 71%). ^{1}H NMR (DMSO-d_6, 202MHz, ppm) δ 7.66 (C3-H, d, J= 9.0Hz, 4H, CH_{Ar}), 6.70 (C2-H, d, J=8.9Hz, 4H, CH_{Ar}), 5.97 (N-H, s, 4H, NH_2), 3.23 (C4-H, q, J=7.2Hz, 48H, CH_2), 1.18 (C5-H, tt, J=7.5, 1.7Hz, 72H, CH_3). ^{31}P NMR (DMSO-d_6, 202MHz, ppm) δ -11.34, -13.36. ATR-IR (cm^{-1}): 3353 (w,ν_{N-H}), 2988 (w,ν_{C-H}), 1739 (w, $\nu_{As-O\ overtone}$), 1593 (w,ν_{N-H}), 1482 (m,ν_{C-H}), 1391 (m,ν_{C-H}), 1085 (m, ν_{P-O}), 953 (s, $\nu_{W=O}$), 914 (s, ν_{P-O}), 775 (vs, ν_{W-O-W}). Anal. *Calcd.* for $C_{60}H_{132}N_8P_2As_2O_{63}W_{17}$ (5310.77): C, 13.57, H 2.51, N 2.11. Found: C, 13.47, H 2.22 N, 2.72.

Synthesis of $(C_8H_{20}N)_6[P_2W_{17}O_{63}(AsC_6H_4NO_2)_2]$ "$[AsPhNO_2W_{17}]$"



p-Nitarsone (61.8 mg, 0.250 mmol) was dissolved in DMF (15 ml) with stirring to give a colourless solution. To this was added $K_{10}[P_2W_{17}O_{61}]$ (0.5 g, 0.110 mmol) followed by 12 M HCl (49 µL, 0.588 mmol) which formed a pale turbid solution. The solution was then heated at 90°C for 16 hrs after which it had become a cloudy off-white suspension. This was cooled to room temperature, filtered and to this was added dry N-tetraethylammonium bromide (0.211 g, 1 mmol) and the mixture was stirred for 1 hr. The solvent was then removed *in vacuo*, giving a blue powder, and the solid was redissolved in the minimum amount of anhydrous DMF and precipitated by the addition of a large excess of $CHCl_3$/MeCN (3:1). The suspension was then centrifuged, the supernatant discarded, and then the powder was sonicated in a large excess of MeCN. This was again centrifuged, the supernatant discarded, and the solvent was removed *in vacuo* to give the product as a blue powder. (0.224 g, 45%).^{1}H NMR (DMSO-d_6, 500MHz, ppm) δ 8.55 (C2-H, d, J= 9.0Hz, 4H, CH_{Ar}), 8.33 (C3-H, d, J=8.9Hz, 4H, CH_{Ar}), 3.23 (C4-H, q, J=7.2Hz, 48H, CH_2), 1.18 (C5-H, tt, J=7.2, 1.9Hz, 72H, CH_3). ^{31}P NMR (DMSO-d_6, 202MHz, ppm) δ -11.32, -13.15. ATR-IR (cm^{-1}): 2985 (w,ν_{C-H}), 1739 (w, $\nu_{As-O\ overtone}$), 1663 (m,ν_{N-O}), 1527 (m,ν_{N-O})1483 (m,ν_{C-H}), 1391 (m,ν_{C-H}), 1350 (m,ν_{C-N}) 1086 (m, ν_{P-O}), 955 (s, $\nu_{W=O}$), 916 (s, ν_{P-O}), 780 (vs, ν_{W-O-W}). Anal. *Calcd.* for $C_{60}H_{128}N_8P_2As_2O_{67}W_{17}$ (5370.74): C 13.42, H 2.40, N 2.09. Found: C 16.11, H 2.97, N, 2.54.

3.5 References

1. J. M. Cameron, S. Fujimoto, K. Kastner, R. J. Wei, D. Robinson, V. Sans, G. N. Newton and H. H. Oshio, *Chem. Eur. J.*, 2017, **23**, 47-50.
2. S. Fujimoto, J. M. Cameron, R.-J. Wei, K. Kastner, D. Robinson, V. Sans, G. N. Newton and H. Oshio, *Inorg. Chem.*, 2017, **56**, 12169-12177.
3. A. J. Kibler and G. N. Newton, *Polyhedron*, 2018, **154**, 1-20.
4. M. Boujtita, J. Boixel, E. Blart, C. R. Mayer and F. Odobelc, *Polyhedron*, 2008, **27**, 688-692.
5. A. Michaelis, *Ber. Dtsch. Chem. Ges.*, 1875, **8**, 1316-1317.
6. C. S. M. Hamilton, Jack F., in *Organic Reactions*, 1944, pp. 415-454.
7. D. M. Jolliffe, *J. R. Soc. Med.*, 1993, **86**, 287-289.
8. O. A. Levander, *Arsenic: Medical and Biological Effects of Environmental Pollutants*, The National Academies Press, Washington, DC, 1977.
9. J. Tanaka, T. P. Davis and P. Wilson, *Macromol. Rapid Commun.*, 2018, **39**, 1800205.
10. N. A. LaFranzo and J. A. Maurer, *Adv. Funct. Mater.*, 2013, **23**, 2415-2421.
11. J. Ahn, D.-S. Moon and J.-K. Lee, *Langmuir*, 2013, **29**, 14912-14918.
12. M. R. Antonio, L. Soderholm, G. Jennings, L. C. Francesconi, M. Dankova and J. Bartis, *J. Alloys Compd.*, 1998, **275-277**, 827-830.
13. K.-I. Sano and S. Himeno, *J. Sep. Sci.*, 2002, **25**, 438-442.
14. P. Yang, Z. Lin, B. S. Bassil, G. Alfaro-Espinoza, M. S. Ullrich, M.-X. Li, C. Silvestru and U. Kortz, *Inorg. Chem.*, 2016, **55**, 3718-3720.
15. Y. Zhang, D. Zhang, Z. Huo, P. Ma, J. Niu and J. Wang, *RSC Adv.*, 2014, **4**, 28848-28851.
16. S. Duval, S. Sobanska, P. Roussel and T. Loiseau, *Dalton Trans.*, 2015, **44**, 19772-19776.
17. M. I. Khan, Y. Chang, Q. Chen, H. Hope, S. Parking, D. P. Goshorn and J. Zubieta, *Angew. Chem. Int. Ed. Engl.*, 1992, **31**, 1197-1200.
18. J. Rabeah, A. Dimitrov, A.-E. Surkus, H. Jiao, W. Baumann, R. Stößer, J. Radnik, U. Bentrup, A. Brückner, *Organometallics*, 2014, **33**, 4905-4910.
19. W. H. Knoth, *J. Am. Chem. Soc.*, 1979, **101**, 759-760.
20. R. Villanneau, A. Ben Djamaa, L. M. Chamoreau, G. Gontard, A. Proust, *Eur. J. Inorg. Chem.*, 2013, 1815-1820.
21. X. Yi, N. V. Izarova and P. Kögerler, *Inorg. Chem.*, 2017, **56**, 13822-13828.
22. K. Kastner, A. J. Kibler, E. Karjalainen, J. A. Fernandes, V. Sans and G. N. Newton, *J. Mater. Chem. A*, 2017, **5**, 11577-11581.
23. D. S. Tawfik and R. E. Viola, *Biochemistry*, 2011, **50**, 1128-1134.
24. Z. G. Sun, Q. Liu and J. F. Liu, *Inorg. Chem. Commun.*, 2000, **3**, 328-330.
25. B. Matt, J. Fize, J. Moussa, H. Amouri, A. Pereira, V. Artero, G. Izzet and A. Proust, *Energy Environ. Sci.*, 2013, **6**, 1504-1508.
26. V. Mirkhani, M. Moghadam, S. Tangestaninejad, I. Mohammadpoor-Baltork and N. Rasouli, *Inorg. Chem. Commun.*, 2007, **10**, 1537-1540.
27. F. Odobel, M. Severac, Y. Pellegrin, E. Blart, C. Fosse, C. Cannizzo, C. R. Mayer, K. J. Eliott and A. Harriman, *Chem. Eur. J.*, 2009, **15**, 3130-3138.
28. T. Yamase, *Chem. Rev.*, 1998, **98**, 307-326.
29. B. Matt, X. Xiang, A. L. Kaledin, N. Han, J. Moussa, H. Amouri, S. Alves, C. L. Hill, T. Lian, D. G. Musaev, G. Izzet and A. Proust, *Chem. Sci.*, 2013, **4**, 1737-1745.
30. M. A. Pasek, J. M. Sampson and Z. Atlas, *Proc. Natl. Acad. Sci.*, 2014, **111**, 15468-15473.
31. I. N. Chernykh, A. P. Tomilov, A. V. Smetanin, A. V. Khudenko, *Russ. J. Electrochem.*, 2001, **37**, 942-946.
32. T. Yamase, N. Takabayashi and M. Kaji, *J. Chem. Soc. Dalton Trans.*, 1984, 793-799
33. T. Yamase and T. Usami, *J. Chem. Soc., Dalton Trans.*, 1988, 183-190.
34. M. Lechner, K. Kastner, C. J. Chan, R. Güttel and C. Streb, *Chem. Eur. J.*, 2018, **24**, 4952-4956.

4. Physical and electrochemical tuning of POM-ILs via organic functionalisation

4.1 Introduction

Revisiting the idea of Class I hybrids, we recall that through tailoring of the structure of the organic cation, extremely powerful modulation of the physical properties can be achieved. One such property that has been extensively manipulated throughout the literature is the hybrid POMs phase behaviour. When we consider conventional all-inorganic POMs, these are almost exclusively formed from metallic (alkali, transition or f-block) cations or protons. These atomic species, when paired with high symmetry polyoxometalates, obviously favour the formation of highly ordered crystalline structures. An opportunity offered by pairing polyoxometalates with organic cations is the near limitless morphologies that are synthetically accessible. Thus, the employment of organic countercations with sufficient low symmetry, steric bulk, or nano-ordering has allowed polyoxometalate chemistry to expand into the realm of soft matter. An extreme on this spectrum is that the organic cations can be so low in symmetry yet possess enough steric bulk to completely inhibit any form of ordered packing, giving rise to the field of polyoxometalate ionic liquids (POM-ILs).

Ionic liquids, liquids composed entirely of ions due to weak interactions, are of great academic interest due to their plethora of unique properties such as unprecedented solvation behaviour, large liquid range, negligible vapour pressure, electrochemical stability and the potential to alter reaction pathways. Conventionally, ionic liquids are typically formed from large asymmetric ammonium and phosphonium cations paired with smaller anionic species such as nitrate, tetrafluoroborate, triflate, hexafluorophosphate and bistriflimides (Figure 89). These anions are favoured due to their diffuse negative charge and weakly coordinating nature. Their properties are also shared with polyoxometalates, which can be viewed as their nanoscale analogues, and thus POMs too lend themselves towards the formation of ionic liquid phases with certain bulky cations. A drawback of employing polyoxometalates as the anionic component in these systems is their typical high negative charge. Although diffuse in nature, the polyanionicity of the POM causes stronger coulombic attraction forces with the cations and thus encourages ordered packing. Therefore, POM-ILs are typically formed

with POMs that have lower charge, generally corresponding to the smaller species such as Lindqvist, Keggin and smaller metal peroxo clusters.

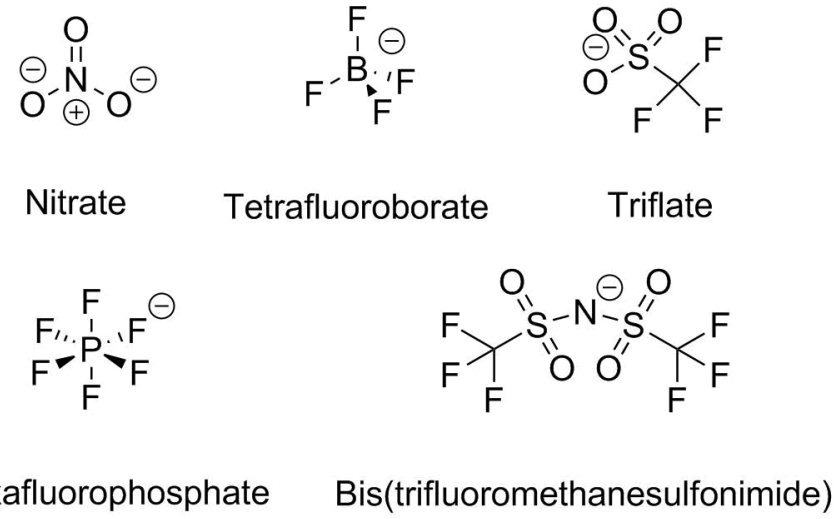


Figure 89. Commonly employed anions in ionic liquids.

Whilst the fields of POM chemistry and ionic liquids are well established, POM-ILs are a relatively young and exciting field that aims to combine the aforementioned desirable properties of both POMs and ionic liquids. The first preparation of a POM-IL was performed by Bourlinos et al. with the treatment of $H_3PW_{12}O_{40}$ with a quaternary ammonium surfactant species containing bulky polyethylene glycol chains.[1] The resulting POM-IL was a viscous, optically transparent liquid which was strongly acidic (pH~2), due to only partial exchange of the protons of the heteropolyacid, and displayed super-ionic behaviour (higher than expected conductivity from its fluidity). These properties were intriguing from both a catalytic and an electrochemical standpoint. It was not until three years later that POM-ILs were revisited by Rickert et al. through the synthesis of a trihexyl(tetradecyl)phosphonium tungsten lindqvist POM-IL.[2, 3] Within the paper, the authors candidly noted that their attempts to form new POM-ILs from the pairing of the Keggin polyoxotungstate anion with 1-alkyl-3-methylimidazolium, n-tetrabutylammonium, and tributyl(tetradecyl)phosphonium cations all yielded high melting materials (T_m > 125°C). Whereas the pairing of the Keggin anion with trihexyl(tetradecyl)phosphonium cations, or the Lindqvist hexatungstate anion with tributyl(tetradecyl)phosphonium, yielded lower melting solids (65°C and 55°C respectively). Only the title compound gave a true room temperature POM-IL material with a depressed melting point of -48°C, due to the very poor coulombic attraction between the ions (Table 16). The POM-IL was found to be thermally stable, retained its electroactivity and possessed a wide liquid range yet was highly viscous and had lower conductivity than the previously reported POM-IL.

Nonetheless it was suggested that these species could be used in high temperature (electro)chemical processes, as the viscosity was found to drop rapidly with increasing temperatures.

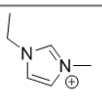
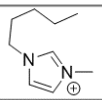
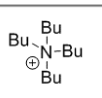
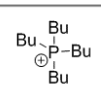
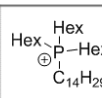
Anion	Cation					
						
$[PW_{12}O_{40}]^{3-}$	>215˚C	>215˚C	>215˚C	>215˚C	129˚C	65˚C
$[W_6O_{19}]^{2-}$	-	-	-	-	55˚C	-48˚C

Table 16. Melting points of commonly employed ionic liquid cations with [PW12O40]3- and [W6O19]2- anions, showing that more charge dense anions paired with cations with large steric bulk favoured the formation of low-melting point compounds.[3]

Following the apparent success of forming ionic liquids with lower charged POMs, Qiao et al. succeeded in synthesising a novel series of POM-ILs using the peroxotungstate dianion, $[W_2O_{11}]^{2-}$,[4] paired with either protonated or methylated n-hexyl or n-decylimidazolium cations. These highly viscous liquids were then used as catalysts for various alkene epoxidation reactions. The n-decylimidazolium derivative was unique in that it acted as a reaction induced phase separation catalyst, it exhibited the highest yields (<99%) and was extremely easy to recover as it self-separated upon completion of the reaction. The same group had further success by pairing the venturello anion $[PW_4O_{24}]^{3-}$ with a dication formed from the concomitant quaternisation and bridging of two N-alkylimidazole units with a chlorinated PEG-300 group.[5] These POM-ILs were also found to catalyse the epoxidation of olefins and exhibited the same self-separating behaviour. The PEG-2000 analogue of the cation was also paired with the Keggin phosphotungstate and this IL could be used as an efficient self-separating catalyst for the oxidative esterification of aldehydes with methanol.[5]

With the appreciation that these hybrid species could act as efficient catalysts, their scientific interest accelerated with many subsequent papers reporting other low nuclearity polyoxometalates paired with imidazolium fragments for a variety of transformations such as photocatalytic dye degradation,[6, 7] deep desulfurisation of fuels,[8, 9] substituted oxazolone synthesis,[10] alcohol oxidation,[11] biomass conversion,[12, 13] and esterifications reactions.[14, 15] However, a closer examination of the literature reveals that these species are not true room temperature (RT) POM-ILs, with melting temperatures ranging from 85 to 250°C, and so it appears that a misnomer around POM-ILs was developing due to their pairing with “ionic liquid” imidazolium cations, in fact these species were highly ordered solids often being characterised crystallographically.

RT POM-IL chemistry did not make a resurgence until the work of Streb and co-workers,[16] whereby the pairing of iron and copper substituted Keggin silicotungstates with tetraheptyl- or tetraoctylammonium cations yielded a family of POM-ILs with melting temperatures between 27 and -59°C. Here, the metal substituted clusters caused the structure to bear an overall more negative charge than the parent anion, and thus favoured the formation of an IL phase in the opposite fashion to the above pairing rules – presumably caused by having a high charge to size ratio which causes the steric overcrowding of the POM and hence disfavours packing. These species were found to be excellent acid resistant self-repairing anti-corrosion coatings for metal surfaces (Figure 90) and opened up the avenue of exploring substitution as a method of tuning the fundamental properties of the POM within POM-ILs.

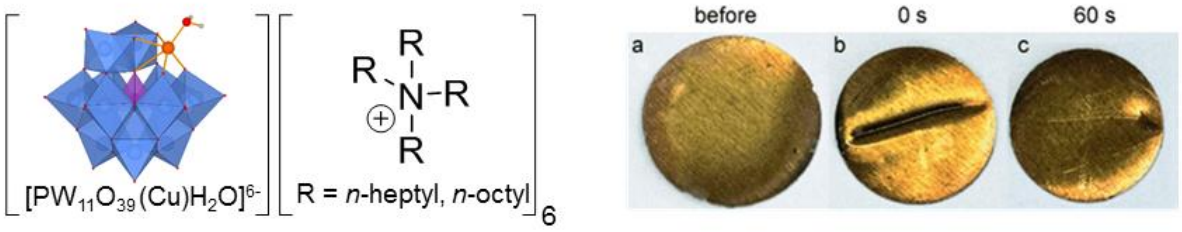


Figure 90. Self-repairing anti-corrosive coatings based on transition metal substituted POMs paired with tetraalkylammonium cations for the protection of metal surfaces. Reproduced from [16] with permission from Wiley Publishers.

Wang et al. expanded on the work of Streb by synthesising tetraheptylammonium salts of cobalt, zinc, manganese and nickel substituted Keggin silicotungstates (in addition to the iron and copper derivatives).[17] When the series was tested for the synthesis of 2-oxazolidinones via propargylic amines carboxylation, the copper derivative was found to have much superior activity to the other species and the respective components, due to its known ability to activate alkyne bonds. The ionic liquid provided a favourable environment by stabilising the carbamate intermediate and increasing its solubility and *O*-nucleophilicity. This demonstrates that the substitution of POMs within the POM-IL also allows for the introduction of specific functionality as well as controlling the clusters overall properties.

Streb and coworkers further investigated the Keggin RT-ILs by exploring the combination of quaternary ammonium ions with the lacunary derivative of silicotungstate $[SiW_{11}O_{39}]^{8-}$, again utilising a more charge dense anion for the formation of POM-ILs. Interestingly in this study, the pairing of tetrahexylammonium cations with the POM yielded a room temperature ionic liquid whereas increasing the alkyl chain lengths resulted in higher melting materials. This evidences the difficulty in predicting the phase behaviour properties of POM-ILs as melting trends do not seem to be general. The POM-IL and its solid analogues

were nonetheless found to be excellent antimicrobial agents which could be realised into antimicrobial coating and water purification devices.[18] Indeed, these properties were soon utilised in the protection of natural building stones by Streb, Mitchell and coworkers – the POM-IL films were formed from $[SiW_{11}O_{39}]^{8-}$ and tetrahepytlammonium or trihexyl(tetradecyl)ammonium cations, and combining the earlier findings, exhibited both anticorrosion and antibacterial properties (Figure 91) which gave the stones protection from both acid rain and biofilm formation (two main causes of stone deterioration).[19] The ionic liquid nature of the material assisted its application to the samples via simple brush coating and gave mechanically and chemically resistant films.

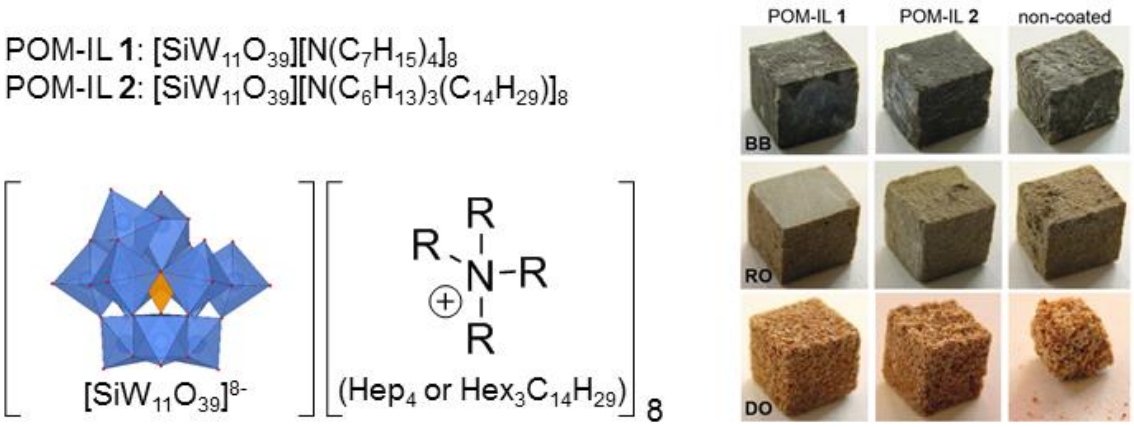


Figure 91. Anti-corrosive and anti-bacterial coatings based on lacunary Keggin POMs paired with tetraalkylammonium cations for the protection of both porous and non-porous stone. Reproduced from[19] with permission from Wiley Publishers.

Very recently, RT POM-ILs were formed from sulphate templated Keggin polyoxomolybdate and Dawson polyoxomolybdate and tungstates with tetraoctylammonium bromide or Victoria Blue B dye cations.[20] These species all exhibited low melting points which again contradicted the previously predicted trends. The POM-ILs in this case were found to be effective in the desulfurisation of fuels. In this case, whilst the all inorganic sodium salts were also found to be active under aqueous conditions, the POM-IL was the most easily separated, recovered and recycled during the reaction, thus giving it a processing advantage.

In the previous two chapters, we have separately visited and explored the concepts, advantages and disadvantages offered by Class I and Class II hybrids. As polyoxometalate chemists, the two systems are often considered dichotomous, wherein the coupling of a desired organic species with the polyoxometalate poses a choice between electrostatic or covalent binding. Given the successes highlighted above in the formation of extremely tuneable POM-ILs which incorporate transition metal

atoms within their structure (Streb/Wang), we postulated that POM-ILs that are formed from covalently functionalised POMs could yield extremely interesting materials. Inspired from the work mentioned above and the results from Chapter 3, it can be proposed that by marrying Class I and Class II hybrids, we could “have the best of both worlds” in that we can tune the physical properties via the organic cation and the electronic properties via the covalently grafted group. This approach would allow for the relatively simple design and synthesis of highly bespoke POM-IL materials which could be tailored towards a menagerie of niche applications.

4.2 Aims

The aim of this project was to synthesise and characterise the first example of POM-ILs formed from covalently functionalised polyoxometalates. From reviewing the literature above, it was decided that the Keggin phosphotungstate anion would be the most suitable POM component as it is easily functionalised, redox rich and has a strong literature precedence for forming ionic liquid with suitable cations. To demonstrate the electronic tuneability of the system, different organic groups would need to be covalently grafted to the POM. We have already highlighted in the previous chapter that two avenues exist for achieving this – either the modulation of the linker group or the use of an electron withdrawing linker with different organogroups appended. In this study the former strategy was chosen, as the use of the same organic group would give POMs of much similar morphology, allowing for the more effective decoupling of physical and electronic behaviours. The cation chosen was trihexyl(tetradecyl)phosphonium (THTP), as quaternary ammonium and phosphonium salts have shown more success than imidazolium-based cations in the formation of RT POM-ILs when paired with Keggin type-anions. The second advantage of using this phosphonium salt is that it will allow for the direct comparison of the hybrids’ properties with the plenary analogue $(THTP)_3[PW_{12}O_{40}]$, synthesised by Rickert.[3] This POM-IL was found to be a solid at room temperature but with a relatively low melt temperature of 65°C. It is also proposed that the functionalisation, which lowers the symmetry of the polyoxometalate, could result in a comparative lowering of the melt temperature through the disruption of ordered packing and hence give a secondary benefit for the use of organofunctionalisation in POM-IL materials. In summary, a family of covalently functionalised Keggin POM-ILs based on the Keggin phosphotungstate covalently modified by either phenylsiloxane or phenylphosphoryl moieties will be synthesised, characterised and compared to their plenary POM-IL analogue and their precursor salts

(target compounds given in Figure 92). Particular attention will be given to determining whether their electronic and physical properties have been effectively modulated to determine their potential as bespoke materials.

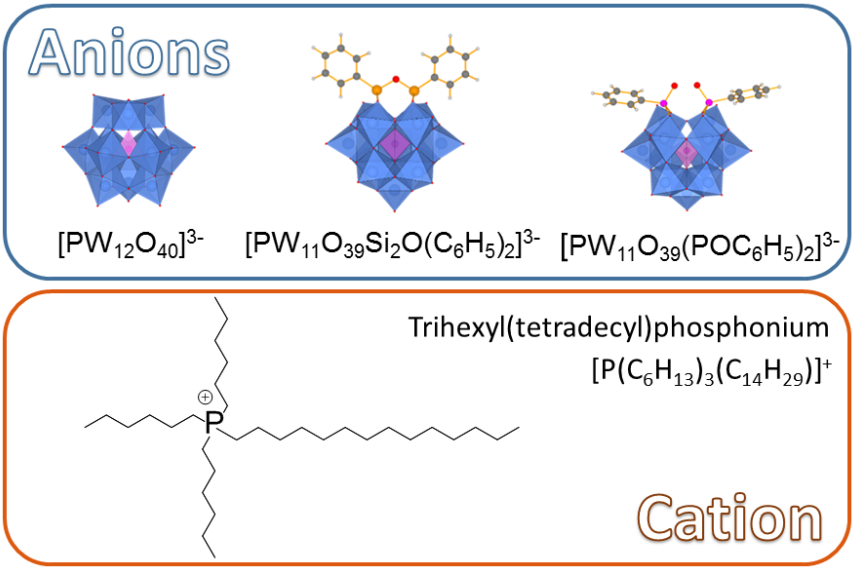
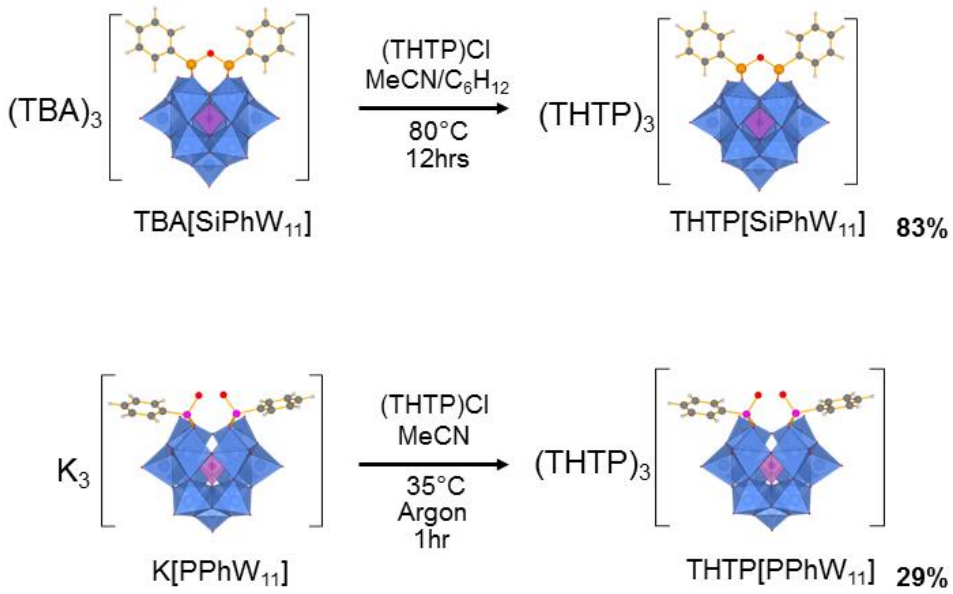


Figure 92. Composition of the target compounds; the combination of plenary and organofunctionalised phenyl Keggins with trihexyl(tetradecyl)phosphonium cations.

4.3. Results and discussion

4.3.1 Synthetic development

The synthetic pathway for the POM-ILs is given in Scheme 13. The solid precursors to the POM-ILs, $K_3[PPhW_{11}O_{39}(POPh)_2]$ and $TBA_3[PW_{11}O_{40}(SiPh)_2]$, hereon represented as $K[PPhW_{11}]$ and $TBA[SiPhW_{11}]$, as well as the parent compound $(THTP)_3[PW_{12}O_{40}]$ ($THTP[W_{12}]$) were synthesised according to modified literature procedures. The initial intention was to synthesise $K[PPhW_{11}]$ as its TBA salt, so as to have a general synthetic method for the POM-ILs applicable to both species and for direct comparison of the properties of the starting materials with each other and the POM-ILs. This compound proved challenging to make and was particularly susceptible to hydrolytic cleavage,[21] its potassium salt however seemed to be more robust and easier to isolate in higher yields (yet still showed some hydrolytic instability). The syntheses of the novel pure POM-ILs were loosely based on previous reports but required development to ensure maximum purity.[2, 16] Despite nominally being a simple ion exchange reaction, both hybrids required separate synthetic adaptations due to the difference in the precursor counteraction (K^+ vs. TBA^+) and in their relative stabilities.



Scheme 13. Synthetic route towards organofunctionalised POM-ILs; THTP[$SiPhW_{11}$] and THTP[$PPhW_{11}$].

For the starting material TBA[$SiPhW_{11}$], after some initial experiments with acetonitrile as the solvent, it was apparent that the driving force for ion exchange was minimal between the two organic cations and mixed salt products were formed. To encourage the ions to exchange, a biphasic system was proposed to force the exchange equilibrium between the POM and the cations to be driven towards the product. It was decided that a biphasic system between cyclohexane and water could drive the equilibrium toward the product, as the solvent could force the precipitation of the product whilst retaining the by-product salt, TBABr. The THTP halide salt could also act as a phase transfer catalyst for the initial solubilisation of the starting material POM into the system. After attempting the reaction at room temperature, which resulted in the formation in pure product in very low yields, it was theorised that the low conversion may be due to slow kinetics, unfavourable thermodynamics or low solubility. To combat these issues the reaction was repeated at 80°C, which after 24 hours, gave the product in high yield, spontaneously precipitating from the system once cooled. After collecting the product, it could be purified further, if necessary, by precipitation from acetonitrile with toluene.

The POM-IL synthesis from K[$PPhW_{11}$] was approached differently. On the one hand, the ion exchange between the starting material and the ionic liquid THTPBr is much more thermodynamically favourable, and the solubility of the starting materials and products are different enough for simple solvent based separation techniques. On the other hand, the starting material is much more unstable than $TBA_3[PW_{11}O_{40}(SiPh)_2]$ and so the risk of degradation during reaction is much higher. Thusly, the

reaction was performed under an inert atmosphere in the absence of light at 35°C for one hour. After this time, the by-product KBr had precipitated from the solution and could be easily filtered. Surprisingly, the THTP salt of the POM was found to possess much higher stability than the potassium salt, as it could be washed with methanol and water to remove any of the remaining starting materials without undergoing degradation (as shown by ^{1}H and ^{31}P NMR spectroscopies). It appeared that the POM-ILs $THTP_3[PW_{11}O_{40}(SiPh)_2]$ and $THTP_3[PW_{11}O_{39}(POPh)_2]$, hence referred to as ($THTP[SiPhW_{11}]$) and ($THTP[PPhW_{11}]$), were completely hydrophobic viscous liquids having high miscibility with polar organic solvents.

4.3.2 Structural characterisation

As is typical, NMR spectroscopy provided the first and most convincing line of evidence for the synthesis and purity of the target POM-ILs. In the case of $THTP[SiPhW_{11}]$, ^{31}P NMR (Figure 93) shows two well resolved phosphorus peaks at 33.58 and -13.37 ppm, which correspond the phosphorus environment of the quaternised cation centre and the template atom within the POM core respectively – confirming that no unwanted POM based transformations occurred during the ion metathesis. When compared with the precursor salt $TBA[SiPhW_{11}]$, the absence of shift in the POMs phosphorus environment indicates that the exchange to a bulkier cation has negligible effects on the electronic distribution and character of the POM. Unfortunately, ^{31}P NMR is not usually quantitative due to enhancement of the NOE (when decoupling is employed) and long longitudinal relaxation times, therefore ^{1}H NMR (Figure 94) is relied upon for the determination of the ionic ratios. Integration of the aromatic peaks of the phenyl ring against the CH_3 peaks at the terminus of the cations' alkyl chains gave the expected 10:36 ratio (1:3 POM to cation). In this instance, ^{1}H NMR is also useful for verifying that no residual TBA salts are present by the absence of the characteristic CH_2 peak at ~3.1 ppm.

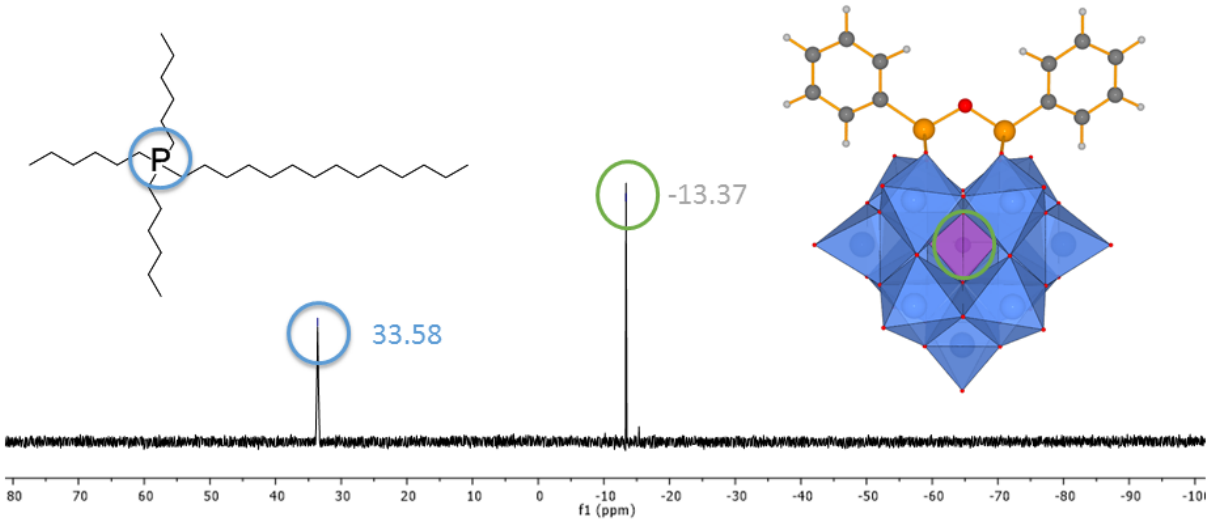


Figure 93. 31P NMR of THTP[SiPhW$_{11}$] showing the separate and well resolved phosphorus environments corresponding the phosphonium THTP cation and phosphate backbone of the POM.

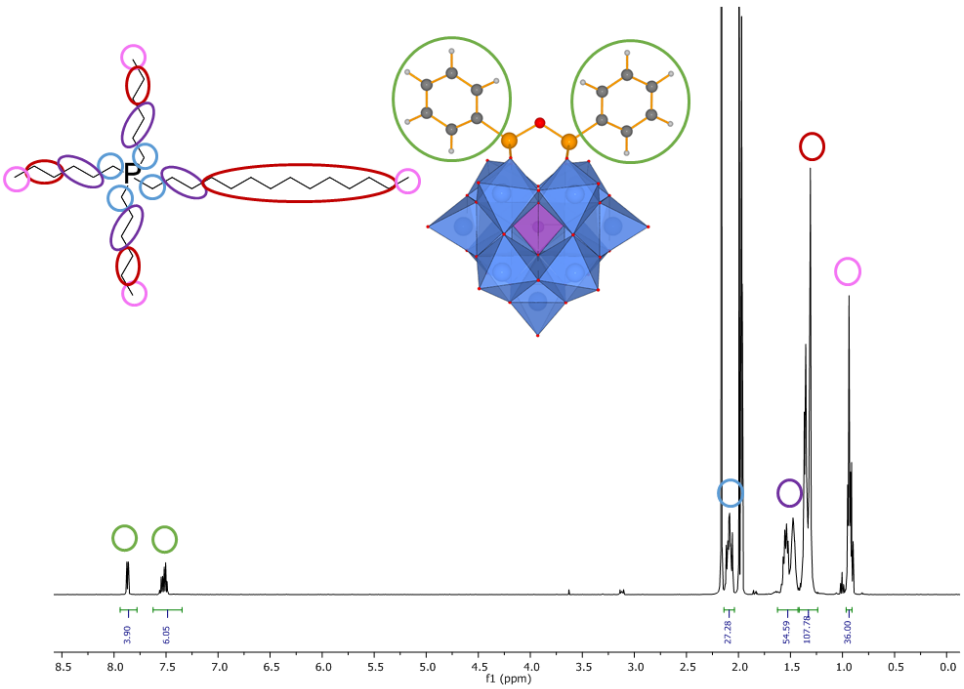


Figure 94. ^{1}H NMR of THTP[SiPhW$_{11}$] showing the aliphatic peaks contributed by the THTP cation and the aromatic peaks contributed by the aryl groups on the hybrid POM.

For THTP[PPhW$_{11}$], ^{31}P NMR shows three major peaks at 33.59, 19.43 and -13.63 ppm which are assigned as the quaternised cation centre, phenyl anchoring group and template atom within the POM respectively (Figure 95). Interestingly, the precursor POM shows a higher concentration of impurity peaks vs. the POM-IL, suggesting that the bulky organic cations stabilise the covalent hybrid POM to a greater extent. Again, there is no shift of the phosphorus signals associated with the POM meaning that the exchange of potassium to THTP cations had no effect on the electronic distribution on the POM.

The ^{1}H NMR also shows the expected 10:36 integration ratio of the aromatic peaks to the cation peaks (Figure 96). THTP[W_{12}] was also verified to be pure by NMR spectroscopies (with the use of propylene carbonate as an external standard). CHN Microanalysis (Elemental Analysis) was also employed to verify the ratio of the cations suggested by ^{1}H NMR analysis, relatively good correlation with calculated elemental mass percentages were obtained for each hybrid, confirming the ion exchange had been successful (See Section 4.5).

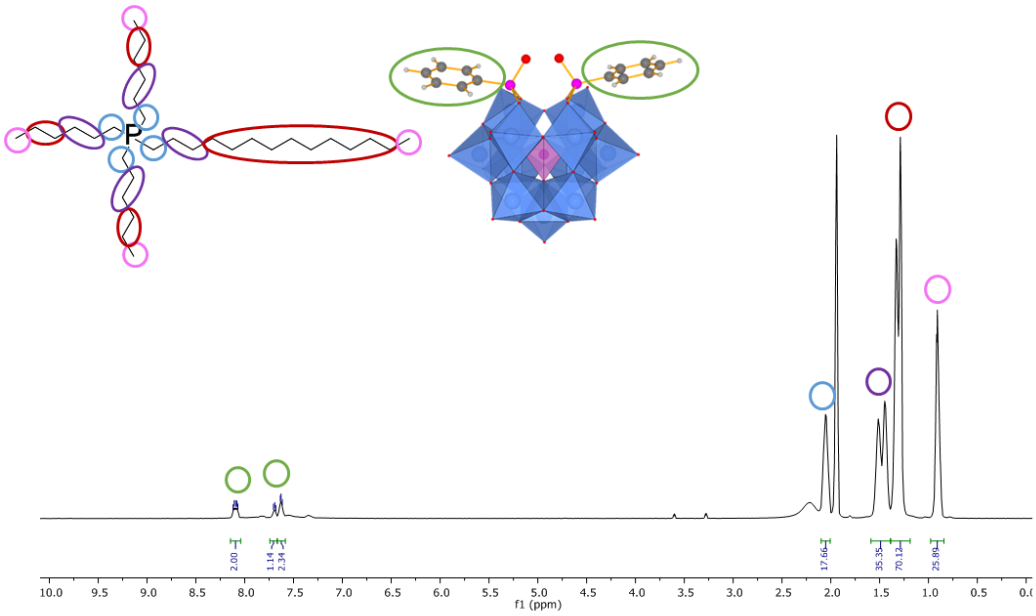


Figure 95. 31P NMR of THTP[$SiPhW_{11}$] showing the separate and well resolved phosphorus environments corresponding the phosphonium THTP cation and phosphate backbone of the POM.

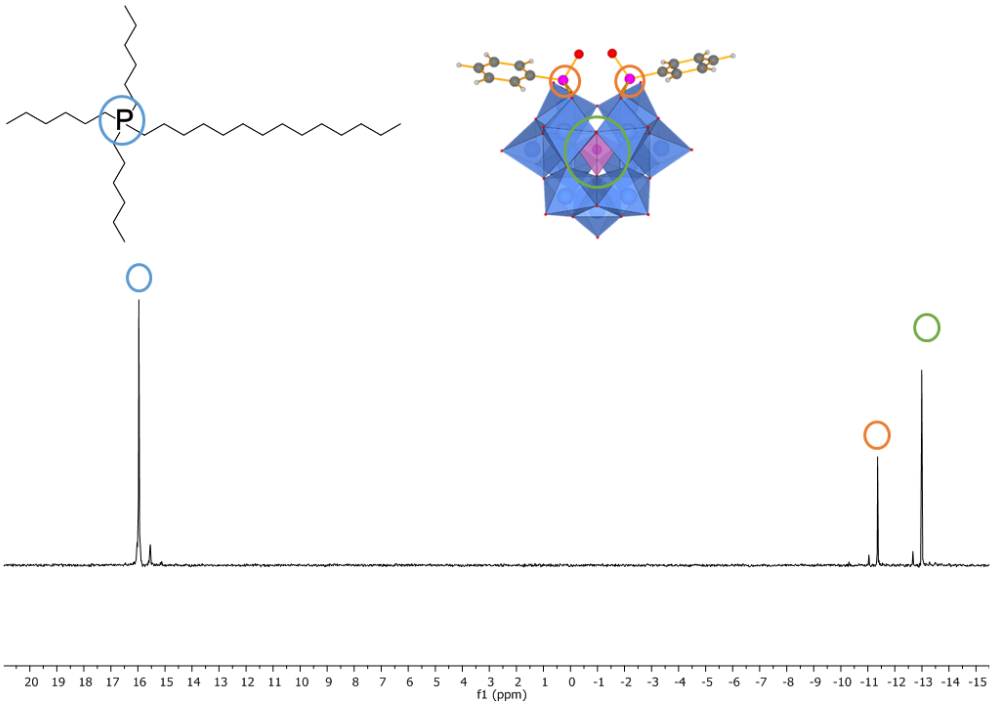


Figure 96. ^{1}H NMR of THTP[$PPhW_{11}$] showing the aliphatic peaks contributed by the THTP cation and the aromatic peaks contributed by the aryl groups on the hybrid POM (analogous to THT[$SiPhW_{11}$]).

Infra-red spectroscopy was also used to probe the change in structure upon functionalisation of the POM with organosilyl and organophosphoryl moieties. Figure 97 shows that certain features of the IR spectrum are near identical between the three species, such as the strong peaks between 3000 and 2750 cm^{-1} which correspond to the C-H stretches contributed mainly by the organic cation, and the general pattern of strong peaks below 1250 cm^{-1} which are characteristic POM-based stretches and bends. The main differences between the functionalised and plenary species are the complexity within the fingerprint region, the functionalised species shows the growth of several new weaker peaks and splitting of the larger peaks, this is logical based on the twofold effect of introducing new aryl and heteroatom based modes (with relatively low atomic abundance in relation to the total structure) and the symmetry breaking that functionalisation induces on the POM (Td to Cs).

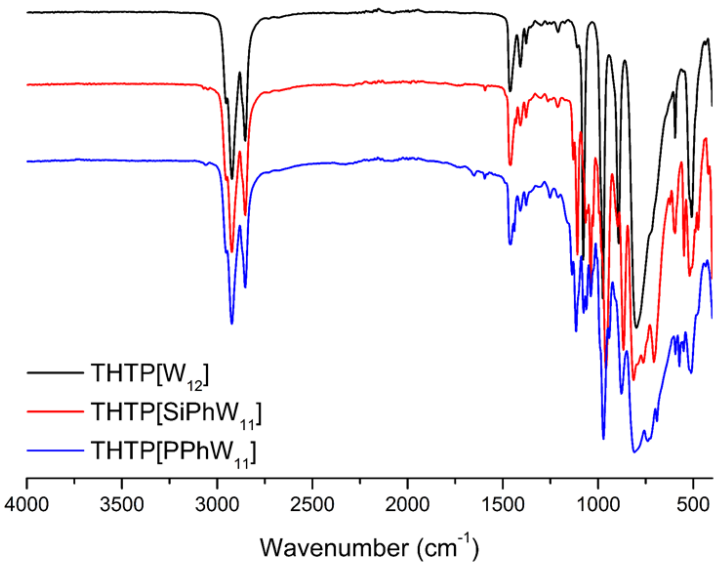


Figure 97. ATR-IR spectra of THTP[W_{12}] (black), THTP[$SiPhW_{11}$] (red) and THTP[$PPhW_{11}$] (blue) showing largely similar profiles however the hybrid species show convolution of the fingerprint region due to new aromatic absorption band and desymmetrisation of the polyoxometalate.

4.3.3 Thermophysical characterisation

As is typical for any type of ionic liquid, it is extremely important to ascertain the thermophysical properties of the system including its thermal stability and phase behaviour. For the former, thermogravimetric analysis (TGA) is a commonly employed technique that can find the thermal limit of a sample, verify the ratio between components with different decomposition temperatures and assess the relative hygroscopicity. For all samples, TGA was carried out between 30 and 1000°C with a heating

rate of 10°C per minute under an argon atmosphere. Initially, we compared the stability of THTP[W_{12}] vs. its precursor TBA[W_{12}] (Figure 98). It can clearly be seen that both materials exhibit relatively high stabilities with the onset of degradation occurring at 355°C for TBA[W_{12}] and 410°C for THTP[W_{12}]. The onset of degradation for the ionic liquid cation precursor THTPCl is reported in the literature as 350°C.[3] It therefore seems that by the POM-IL shows an enhanced thermal stability (>50°C) compared with both of its precursors. This can be rationalised by two separate phenomena. Firstly, with respect to the cation, it is well known in the literature that generally the thermal stability of phosphonium cations are superior to that of ammonium cations.[22] Secondly, with respect to the anion, there is an inverse trend between the anion nucleophilicity and the ionic liquid stability for any given cation (POMs are much weaker nucleophiles than halide anions).[3] With both the POM precursor and the POM-IL, the single weight loss event corresponds to the degradation of three cations based on percentage molecular weight calculations, confirming the structure of the species as suggested by NMR.

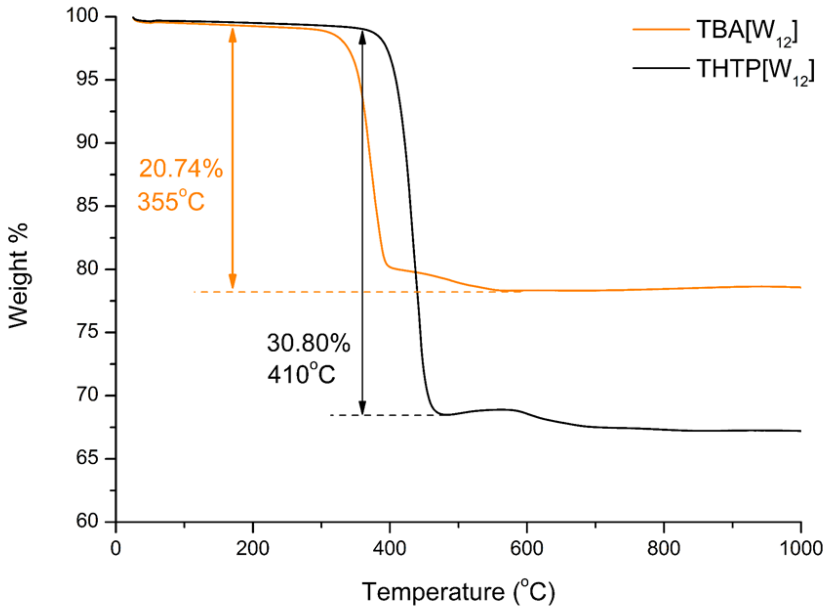


Figure 98. TGA of TBA[W_{12}] (orange) and THTP[W_{12}] (black) under argon. It is demonstrated that the POM-IL is more stable than the TBA salt by ca. 55°C.

Now regarding the phenylsilyl functionalised POM-IL THTP[$SiPhW_{11}$], the material was subject to the same thermal analysis and compared with its precursor TBA[$SiPhW_{11}$] (Figure 99). Again, it is observed that the onset of degradation for the POM-IL occurs at a higher temperature vs. the TBA precursor salt (420°C vs. 280°C). TBA[$SiPhW_{11}$] exhibits poorer thermal stability when compared to TBA[W_{12}] due to the presence of the appended organic groups on the POM, which are more prone to decomposition. It appears that the broader weight loss event experienced by TBA[$SiPhW_{11}$] encapsulates both the loss

of the appended organic groups and the organic cations based on the percentage weight loss. Comparing this to THTP[SiPhW$_{11}$], the POM-IL exhibits a single well-defined weight loss at 420°C, which corresponds to the loss of both the cation and the phenylsilyl moieties. This suggests that the stability of the system has been bolstered by 140°C.

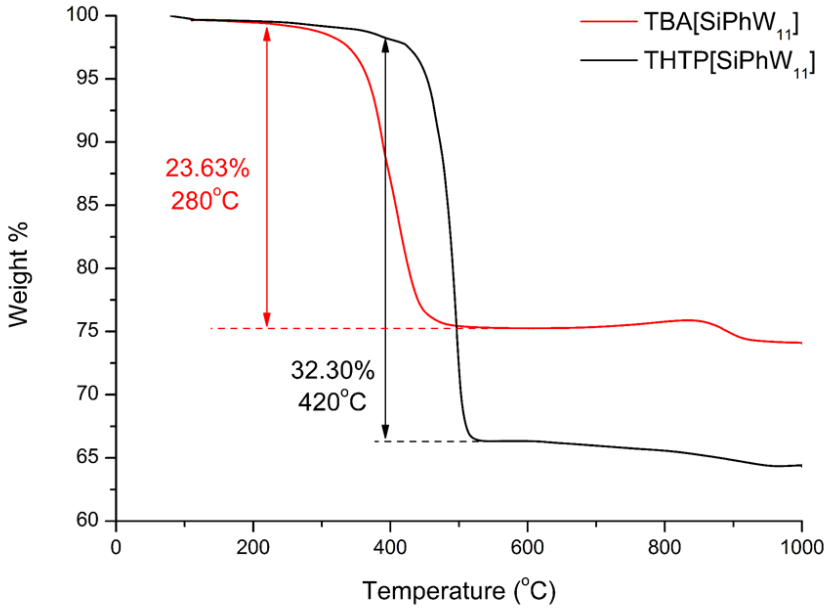


Figure 99. TGA of TBA[SiPhW$_{11}$] (red) and THTP[SiPhW$_{11}$] (black) under argon. It is demonstrated that the hybrid POM-IL is more stable than the TBA salt by ca. 140°C.

Finally, THTP[PPhW$_{11}$] is compared in the same way with its precursor K[PPhW$_{11}$] (Figure 100). Here, the precursor is evidently much less thermally stable than both the plenary Keggin and the silyl-functionalised precursors. This arises not due to the difference in cation (as the TBA salt of the POM was found to not be isolable), but due to the inherent instability of the POM hybrid, as evidenced by the extreme scarcity of phenyl functionalised Keggin phosphotungstates within the literature. Remarkably, the combination of this POM cluster with THTP cations resulted in a dramatic enhancement of the thermal stability of the system (100°C vs. 420°C). Whilst the precursor experiences the almost instantaneous decomposition of the grafted organic groups (as confirmed from percentage weight loss) in a complex multi-step decomposition starting at ~100°C, the POM-IL exhibits a single sharp decomposition event at 420°C which corresponds to both the loss of the organic cation and the phenylphosphorus moieties, as calculated from percentage weight loss. This represents a 320°C increase in the thermal stability of the POM-IL vs. its precursor POM salt.

Whilst the thermal stability of these systems appears to be high under the experimental conditions, it was also of interest to confirm that this remained true under an aerobic environment. Thus THTP[$SiPhW_{11}$] and THTP[$PPhW_{11}$] were investigated with an analogous method under an air stream (Figure 101). It was found that the thermal stability of the hybrid POM-ILs were only slightly compromised by switching from anaerobic to aerobic conditions - with degradation onsets 65°C lower (355°C) for both species. Nonetheless, the thermal stability of the hybrid POM-ILs remains remarkably high and thus could be employed in high temperature (electro)chemical applications.

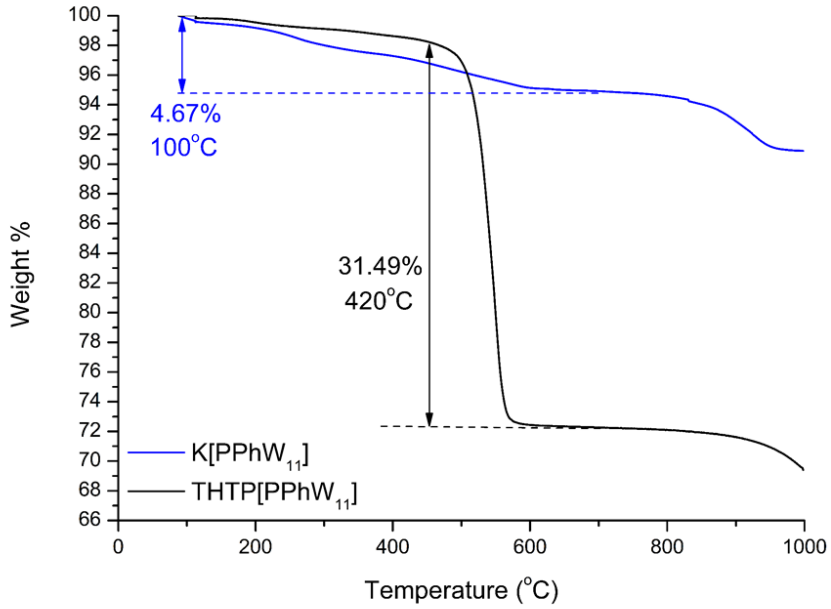


Figure 100. TGA of K[$PPhW_{11}$] (blue) and THTP[$PPhW_{11}$] (black) under argon. It is demonstrated that the hybrid POM-IL is dramatically more stable than the TBA salt by ca. 320°C.

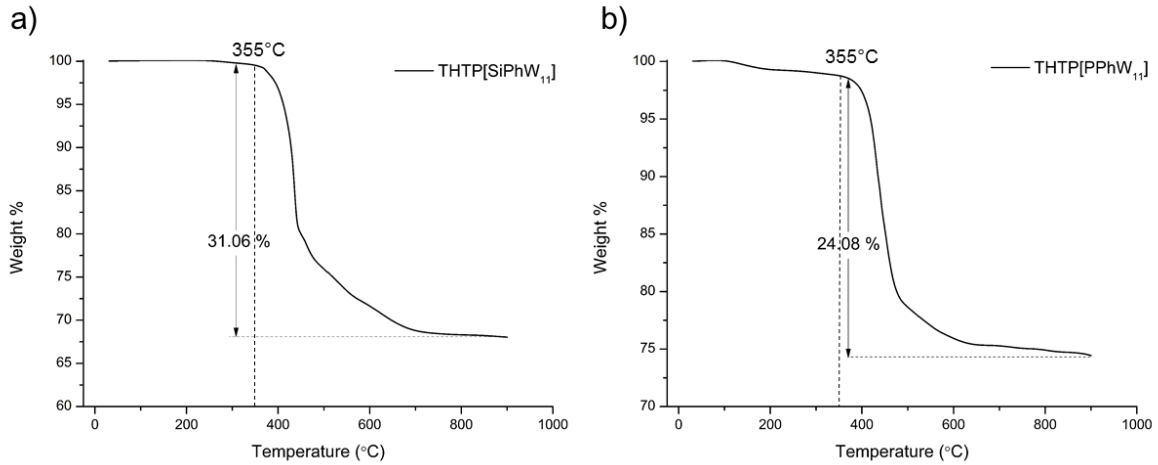


Figure 101. TGA of a) THTP[$SiPhW_{11}$] and b) THTP[$PPhW_{11}$] under air. It is demonstrated that the hybrid POM-IL is retain high thermal stability (355°C) under oxidising conditions (aerobic).

From the above we can draw several conclusions about the nature of these materials. Firstly, irrespective of the structure of the POM, the POM-IL stability is solely governed by the favourable synergic interaction of the POM and the phosphonium cation, which results in materials with exceptional thermal stability exceeding 400°C, higher than that of all the of the synthetic precursors. The fact that this relationship also holds for the unstable hybrid [$PPhW_{11}$] indicates that the cation provides a stabilising environment, this may be due to “shrink wrapping” effects which have previously been described as vital for the stabilisation of clusters that are prone to further reaction and aggregation.[23] Secondly, the complete absence of any weight loss events before their degradative behaviour above ~400°C indicates that these species are completely hydrophobic, with no discernible water content that is a feature of TGA traces of traditional hygroscopic ILs. The hydrophobic environment may also protect the hybrid derivatives from decomposition as the loss of grafted organic groups is often hydrolysis mediated.[24]

After confirming the thermal stability of these systems, it was then possible to investigate their phase behaviour by differential scanning calorimetry (DSC) analysis. Given their high thermal stability profiles, it was possible to characterise their phase behaviour within the full temperature range of the instrument (-80°C to 300°C). Each sample was ramped to 300°C, cooled to 80°C, ramped and cooled again and then ramped back to the starting temperature (25°C) at a rate of 10°C per minute, short isothermals were employed at the upper and lower limits to allow for full equilibration at those temperatures. Initially, the plenary Keggin POM-IL was investigated. Although its phase behaviour has already been reported,[3] their study only investigated the unidirectional heating of the sample from -80°C to 80°C. Figure 102 shows the DSC trace obtained from testing the POM-IL with the above temperature program. Upon the first heating ramp, a sharp endothermic peak is observed at 68.2°C (4.452 J/g), which corresponds well with the literature reported peak (65°C). This was ascribed by Rickert et al. as the melting temperature of the POM-IL – however the DSC at higher temperature also reveals a second endothermic peak at 133.6°C (1.976 J/g).[3] When the system is cooled from 300°C to -80°C, no exothermic peaks corresponding to crystallisation processes are observed, however the heat flow gradually increases up to a maximum at -80°C. The second heating cycle shows only the return of the peak at 133.6°C with no peak present at 68.2°C and again no peak is observed upon cooling. This indicates that the POM-ILs phase behaviour is more complex than initially proposed. The DSC trace could be interpreted as follows: upon the first heating cycle there is an initial transformation (68.2°C) from a crystalline phase to an

amorphous solid, which is irreversible. This then undergoes a secondary phase transition to an isotropic liquid at 133.6°C. When cooled, this liquid undergoes an ill-defined solidification process back to the amorphous phase over a very wide temperature range. This is evidenced by a return of the amorphous solid to liquid phase transition peak in the second heating sample.

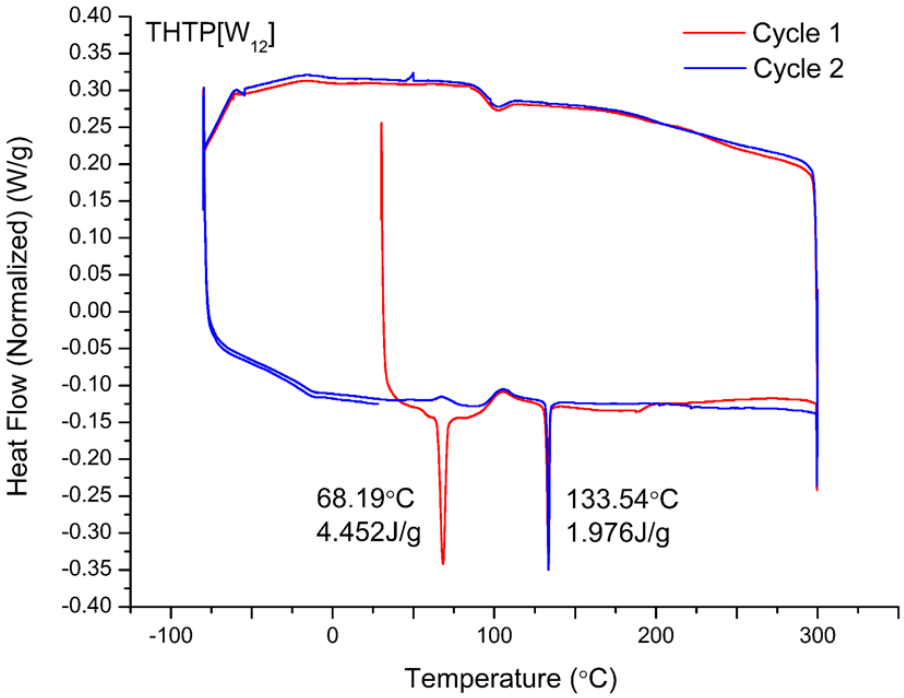


Figure 102. DSC of THTP[W_{12}], upon heating the compound undergoes an initial irreversible transition (crystalline to amorphous (68.19°C) followed by a well-defined reversible melt (133.54°C), the corresponding crystallisation is broad and occurs over a large temperature range.

When the covalently functionalised POM-ILs were subjected to the same ramping program, it was surprising to observe no exothermic or endothermic peaks within the temperature limits of the experiment for either compound (Figure 103). This indicates that the hybrid POM-ILs exhibit no phase changes over an extremely wide temperature range. Given the physical appearance of the compounds and the propensity for them to flow at higher temperatures, this phase is tentatively ascribed as a viscous liquid. The origin of this behaviour may be due to the reduction of symmetry of the POM as previously mentioned. Specifically, on functionalisation we alter both the symmetry of the polyoxometalate (T_d to C_s) and the morphology of the cluster from approximately spherical to T-shaped, without altering the formal charge on the cluster. These both hinder the ordered packing of the cations around anions and lower the crystallisation temperature (by at least 140°C determined experimentally).

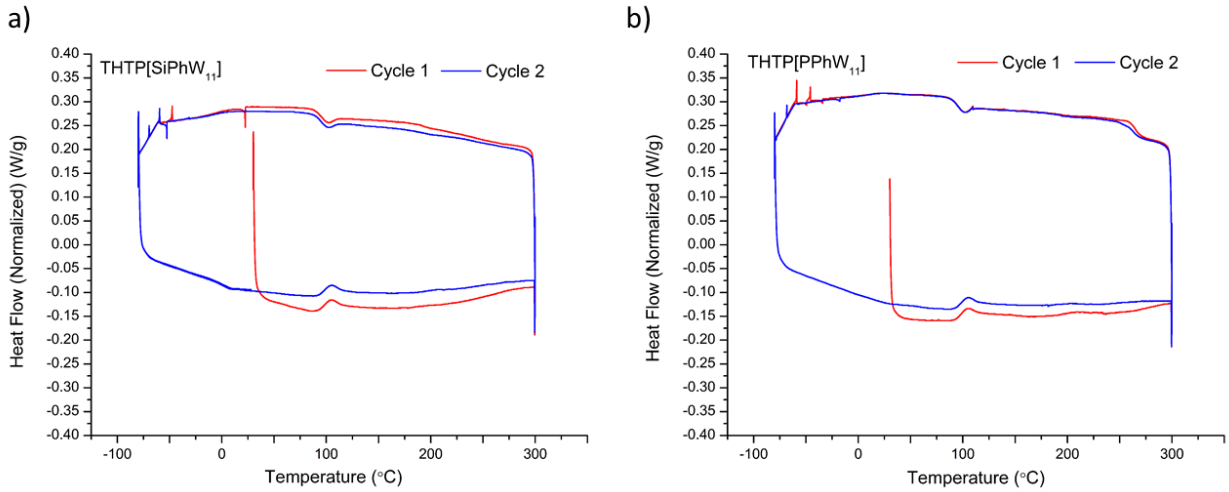


Figure 103. DSC of a) THTP[$SiPhW_{11}$] and b) THTP[$PPhW_{11}$] showing no discernible melt or phase transition processes within the experimental window.

To garner more evidence for the proposed phase behaviour from DSC, powder X-ray diffraction (PXRD) was utilised as a complementary technique. Given that single crystals of these materials would be extremely difficult or impossible to obtain, the PXRD diffractograms were used as a qualitative tool to investigate the phase behaviour and crystallinity of the samples. Figure 104a shows the pattern obtained from THTP[W_{12}] as prepared from the reaction. When compared with its TBA precursor salt (Figure 104b), it is clear that a decrease in crystallinity has occurred by the decrease in intensity of the peaks at low angle and a complete disappearance of peaks at high angle. Nonetheless, the material is clearly a solid at room temperature. Since we can irreversibly access the second phase at temperatures above 68°C, the material was heated to 80°C for 12 hours and allowed to cool to room temperature. Analysis of this phase revealed that a further decrease in crystallinity has occurred which is shown by a decreased population of peaks (Figure 105). It is also visually apparent that the consistency of the material has changed during the thermal treatment (Figure 105 inset) The presence of any peaks whatsoever confirms that this phase still contains some order and is not an isotropic liquid.

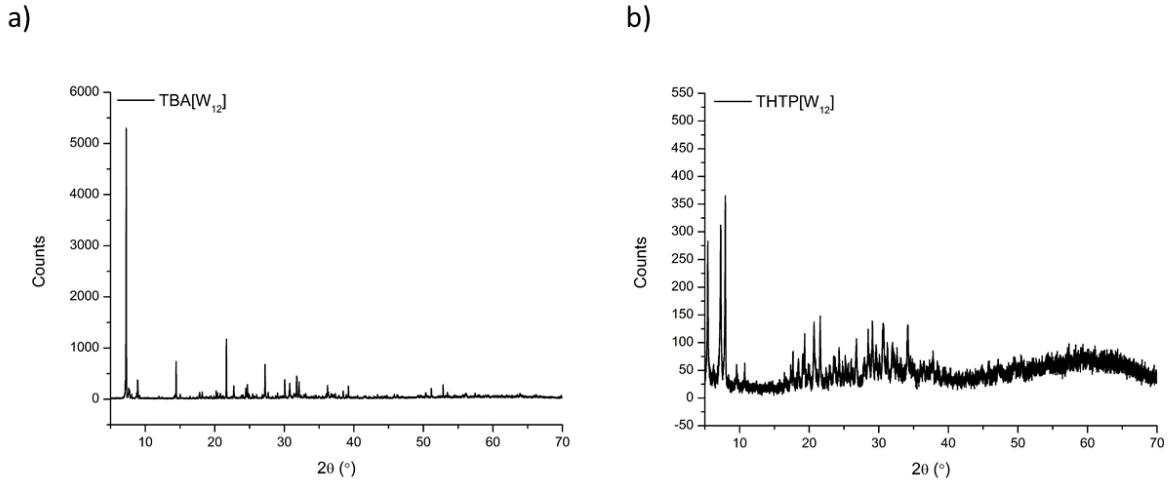


Figure 104. PXRD of a) TBA[W_{12}] and b) THTP[W_{12}], showing that the increase in cation size has decreased the population and intensity of crystalline peaks.

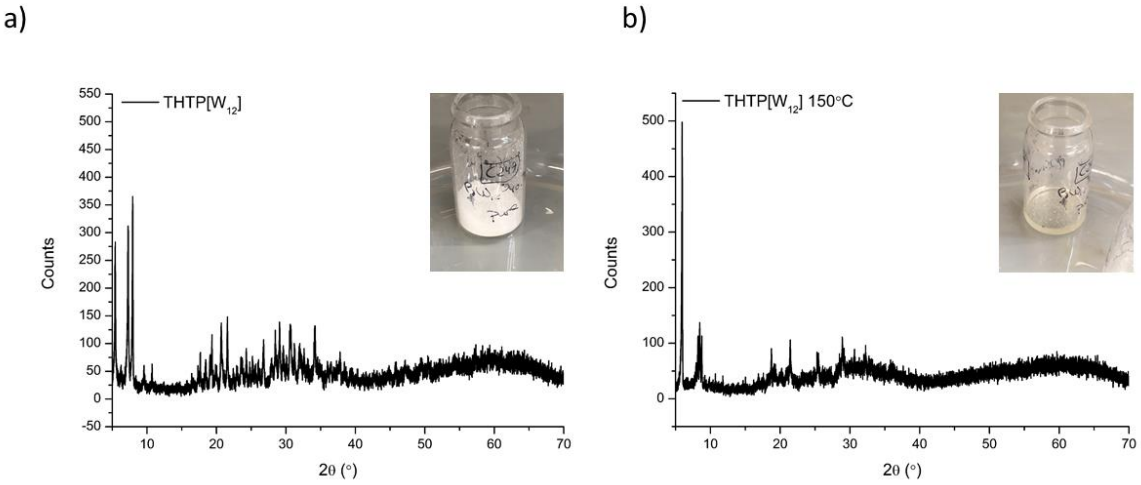


Figure 105. PXRD of a) THTP[W_{12}] as prepared and b) THTP[W_{12}] following heat treatment at 80°C for 12 hours. Inset is shown the visual appearance of the material pre- and post- thermal treatment. Heating the sample past the irreversible melting point has decreased the intensity and population of crystalline peaks.

The PXRD of the hybrid solid TBA[$SiPhW_{11}$] and POM-IL THTP[$SiPhW_{11}$] were similarly obtained. Initially, it is interesting to observe that the crystallinity of TBA[W_{12}] is superior to that of TBA[$SiPhW_{11}$] by a larger population and intensity of peaks in the former (Figure 106), this confirms that the grafting of organic groups to the POM inhibits the effective packing of the molecule even in the solid state when the same counter ion is employed. Now comparing the THTP salt to the TBA salt for the phenylsilyl hybrid (Figure 107), a complete disappearance of well-defined peaks is observed, suggestive of an isotropic liquid phase. Unfortunately, the scarcity of material for TBA[$PPhW_{11}$] precluded its analysis via this technique, however, given its structural similarity to TBA[$SiPhW_{11}$] and similar appearance and thermophysical behaviour, it can be presumed that this species too is an isotropic liquid. The above confirms the hypotheses that the large asymmetric cation and conferred asymmetry of the POM in the hybrid POM-ILs is conducive to a room temperature ionic liquid with a wide phase profile.

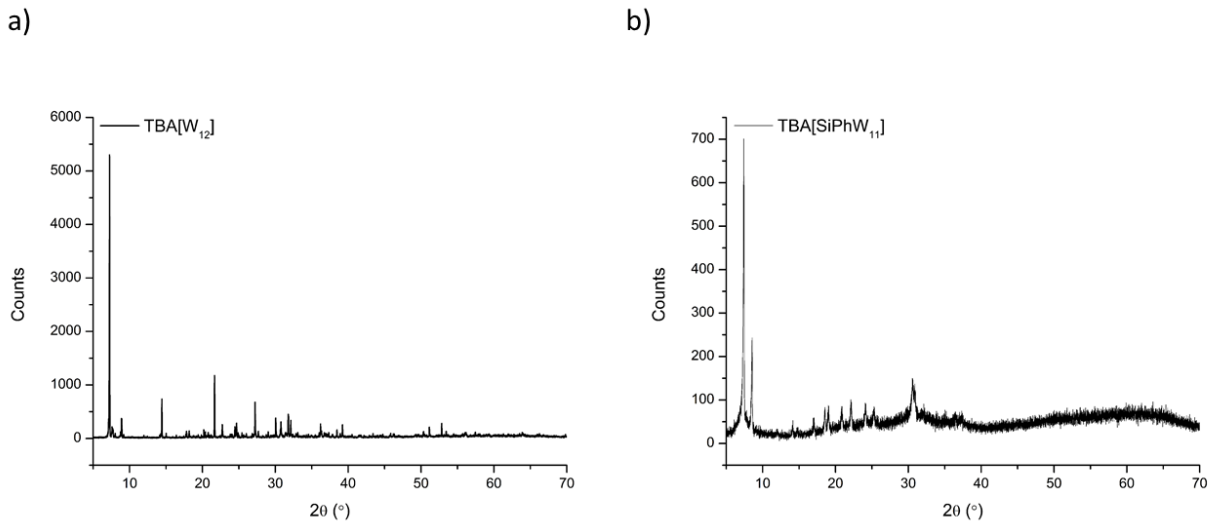


Figure 106. PXRD of a) TBA[W_{12}] and b) TBA[$SiPhW_{11}$], the introduction of aryl groups to the POM desymmetrises the cluster and causes a dramatic decrease in the number and intensity of crystalline peaks.

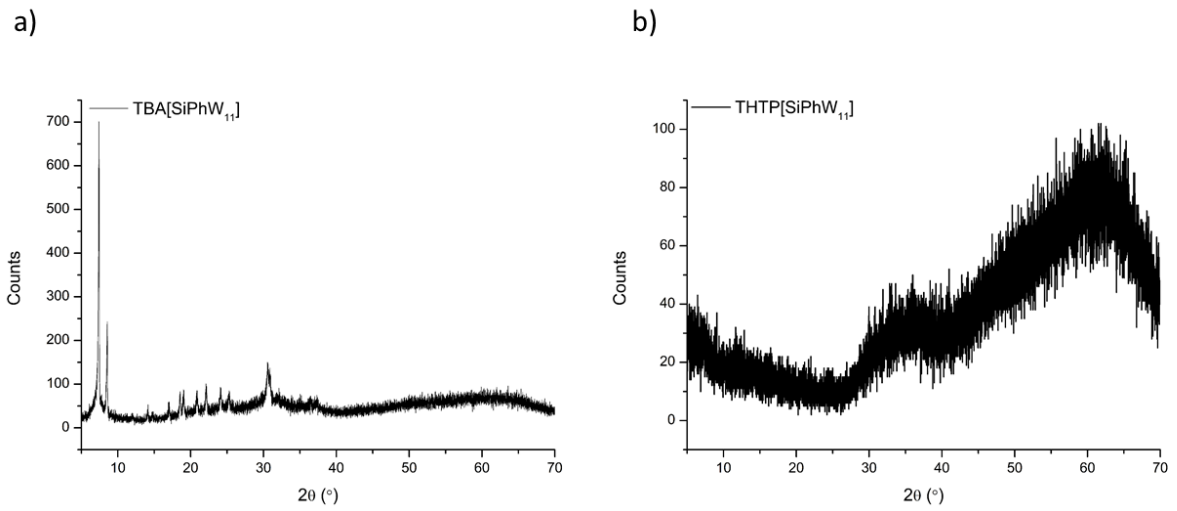


Figure 107. PXRD of a) TBA[$SiPhW_{11}$] and b) THTP[$SiPhW_{11}$], the introduction of aryl groups in combination with the bulky THTP cations completely prohibits ordered packing and results in a completely amorphous phase (no crystalline peaks).

4.3.4 Electronic characterisation

Having ascertained that the use of THTP allows the modulation of the physical properties of the molecule by increasing their thermal stability and encouraging the formation of an ionic liquid phase, it was pertinent to then explore the electronic character of the systems. As described in Section 4.2, the motivation for forming two POM-ILs with nominally similar ligands (and hence similar morphologies), but linked to the structure by different anchoring groups was to demonstrate that the electronic properties of the system can be independently tuned by mechanisms that have been well described in Chapter 3. As expected, based on similar behaviour of the functionalised Dawson analogues analysed in the previous chapter, the UV-vis spectra of the POM-IL materials and their precursor salts were

largely uninformative for the electronic nature of the compounds. It appears that neither salt exchange nor functionalisation of the cluster by different groups caused any meaningful shifts in the electronic spectra for each of the species (Figure 108). It was at least gratifying to observe and analyse the low lying LMCT band in each of these species as these salts were soluble in MeCN which has a lower cut-off window than both DMF and DMSO. The LMCT band in each species exhibited maxima at either 265 or 266 nm, with molar extinction coefficients of 12754, 53546 and 57308 $dm^3mol^{-1}cm^{-1}$ for $THTP[PPhW_{11}]$, $THTP[SiPhW_{11}]$ and $THTP[W_{12}]$.

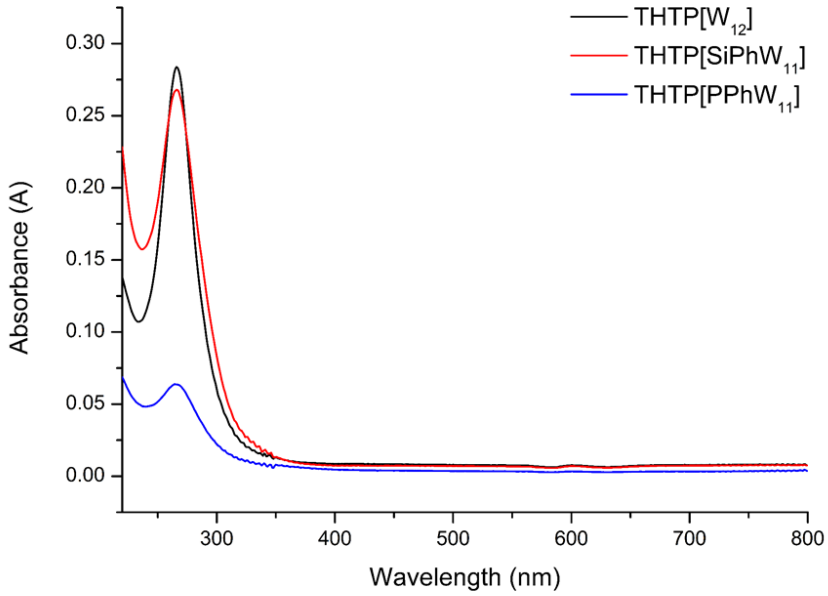


Figure 108. UV-vis spectra of $THTP[W_{12}]$ (black), $THTP[SiPhW_{11}]$ (red) and $THTP[PPhW_{11}]$ (blue) in acetonitrile (5×10^{-6} M), allowing the visualisation of the POM LMCT bands occurring at similar wavelengths, but with contrasting extinction coefficients.

As before, electrochemical methods were much more informative in determining the electronic nature of the polyoxometalate centres within the POM-IL materials. Each POM-IL was analysed using a similar set-up as employed previously. Briefly, the POM-ILs (0.25 mM) were dissolved in anhydrous MeCN with 0.1 M $TBAPF_6$ as electrolyte, at 100 mV scan rate under a positive argon pressure. A three-electrode set-up was employed with a glassy carbon working electrode, (d = 1.6 mm), Pt wire counter-electrode and a Ag-wire pseudo-reference electrode, with Fc^+/Fc redox couple as an external reference. Interestingly, despite the reports on the effect of linker atom on the electrochemistry of the Dawson polyoxotungstate,[25] the results below represent, to the best of our knowledge, the first example of the analogous study of the effect of linker atom on the electrochemistry of the phosphotungstate Keggin chemistry with phosphorus and silicon. Figure 109 shows the electrochemical behaviour of $THTP[W_{12}]$,

$THTP[SiPhW_{11}]$ and $THTP[PPhW_{11}]$ within the potential window permitted by the solvent (+0.2 V to -3.0 V vs. Fc^{+}/Fc). Each species clearly indicates 4 chemically reversible 1-electron reductions (based on previous reports of polyoxotungstate Keggin electrochemistry), with $THTP[PPhW_{11}]$ also exhibiting a small additional redox process centred at approximately $E_{1/2}$ = -1.25 V which corresponds to the presence of the lacunary POM $[PW_{11}O_{39}]^{7-}$, the hydrolysed decomposition product of the organophosphorus hybrid - this was determined by comparison of the voltammogram with $TBA_4H_3[PW_{11}O_{39}]$ under the same conditions. For the main peaks, the ratio of the anodic to cathodic peak currents, $i_{p,a}/i_{p,c}$, was about 1 in each case, as expected for freely-diffusing species undergoing a mass-transport controlled faradaic reaction. The peak-to-peak separation for each couple was in the region of 70 to 100 mV, which is slightly higher than that expected for a fully electrochemically-reversible redox couple, however the ferrocene redox couple had a peak to peak seperation of 86 mV (59/*n*, where *n* is the number of electrons transferred during the redox reaction), indicating that sluggish electron transfer influenced the voltammetric responses. Comparison of the three CVs shows that the peak currents increased in the order $THTP[SiPhW_{11}] < THTP[PPhW_{11}] < THTP[W_{12}]$. This difference is due to the increased steric bulk of $THTP[SiPhW_{11}]$ and $THTP[PPhW_{11}]$, relative to that of $THTP[W_{12}]$, which decreases the rate of mass transport of the hybrids to the electrode surface.

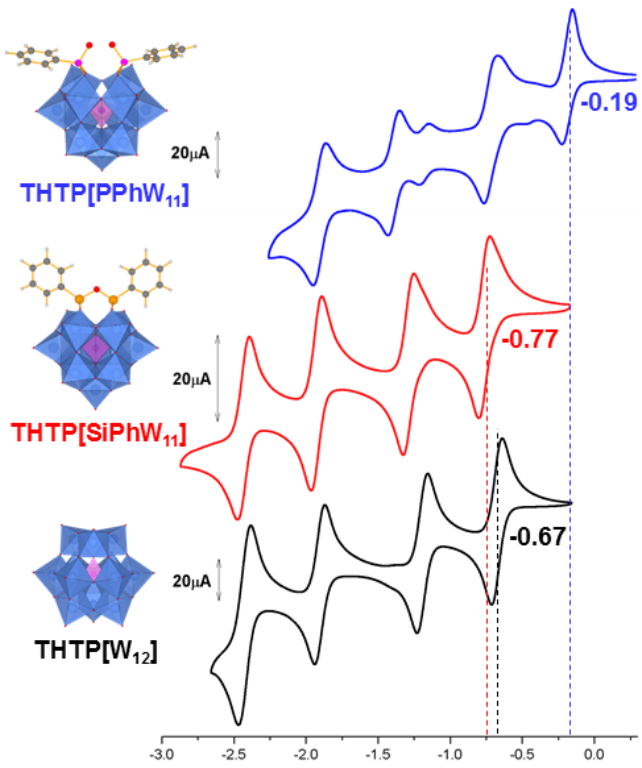


Figure 109. Cyclic voltammograms for THTP[W_{12}] (black), THTP[$SiPhW_{11}$] (red) and THTP[$PPhW_{11}$] (blue) in acetonitrile reported vs. Fc/Fc+ as an external reference. It is clearly demonstrated that the linker atoms have strong electronic effects on the POM core by the shifts in the first redox potentials as reported in Section 3.3.3.

Regarding the observed half wave potentials between the three species, shown in Table 17 with values obtained for starting materials, a clear difference is observed. Following the general trends observed by Boujtita et. al. and seen in Chapter 3 for the analogous Wells-Dawson species, the strong electron withdrawing phenylphosphonate groups dramatically decrease the electron density on the POM which decreases its LUMO energy and facilitates its reduction. The weak electron donating effects of the phenylsilyl groups cause the opposite effect compared to the plenary structure, by increasing the electron density on the POM core and thus slightly impedes its reduction. This results in first reduction potentials of the POMs following the predicted trend THTP[$PPhW_{11}$] ($E_{1/2}$ = -0.19 V) >> THTP[W_{12}] ($E_{1/2}$ = -0.67 V) > THTP[$SiPhW_{11}$] ($E_{1/2}$ = -0.77 V). The peak potentials for all compound including the electroactive POM precursors are given in Table 17. Furthermore, the positive redox shift reported here for the phenylphosphorus Keggin anion (+0.48 V for $PPhW_{11}$ vs.W_{12}) is much more dramatic than those reported for the analogous Dawson anion (+0.30 V for$PPhW_{17}$ vs. W_{18}),[25] which suggests that the

electron withdrawing influence of the phenylphosphorus moiety is more pronounced over smaller POM systems where the effect is not shared over as many orbitals.

	E_1/V (ΔE_1)	E_2/V (ΔE_2)	E_3/V (ΔE_3)	E_4/V (ΔE_4)
TBA[W_{12}]	-0.66 (0.07)	-1.19 (0.07)	-1.89 (0.06)	-2.42 (0.09)
THTP[W_{12}]	-0.67 (0.08)	-1.16 (0.07)	-1.90 (0.07)	-2.42 (0.07)
TBA[SiPhW_{11}]	-0.75 (0.09)	-1.28 (0.08)	-1.92 (0.08)	-2.43 (0.07)
THTP[SiPhW_{11}]	-0.77 (0.10)	-1.29 (0.08)	-1.93 (0.08)	-2.35 (0.09)
K[PPhW_{11}]	-0.21 (0.04)	-0.73 (0.08)	-1.22 (0.23)	---
THTP[PPhW_{11}]	-0.19 (0.07)	-0.73 (0.09)	-1.40 (0.08)	-1.92 (0.09)

Table 17. Reduction potentials of the POM-ILs and their POM precursor salts. Potentials are given as the half-wave potentials in volts (E_x/V) referenced vs. Fc/Fc^+ and peak separation in brackets (ΔE_x).

The profile of the CV of each species is similar to that of the precursor POMs confirming that the redox behaviour of the materials was dominated by the POM redox centre and confirming that the hybrid POMs remained intact after ion exchange. It is also important to note that exchanging the cation only has a negligible effect on the redox potentials of the POM (maximum shift of 0.02 V for THTP[$PPhW_{11}$] vs. K[$PPhW_{11}$]), meaning that the observed shifts between the POM-ILs are exclusively an effect of the different hybridisation strategies. It is possible that this lack of shift or behavioural differences is originating from ion exchange of each POM with the electrolyte, $TBAPF_6$. To eliminate this possibility, the electrochemistry of the [$SiPhW_{11}$] anion was investigated with different combinations of electrolyte and paired cation. Figure 110 shows that when TBA[$SiPhW_{11}$] is paired with $TBAPF_6$ as electrolyte, THTP[$SiPhW_{11}$] is paired with $TBAPF_6$ as electrolyte or THTP[$SiPhW_{11}$] is paired with $THTPPF_6$ as electrolyte – there is virtually no differences observed in the redox behaviour and potentials of the POM, verifying that the POM redox couples are truly independent on the nature of the cation.

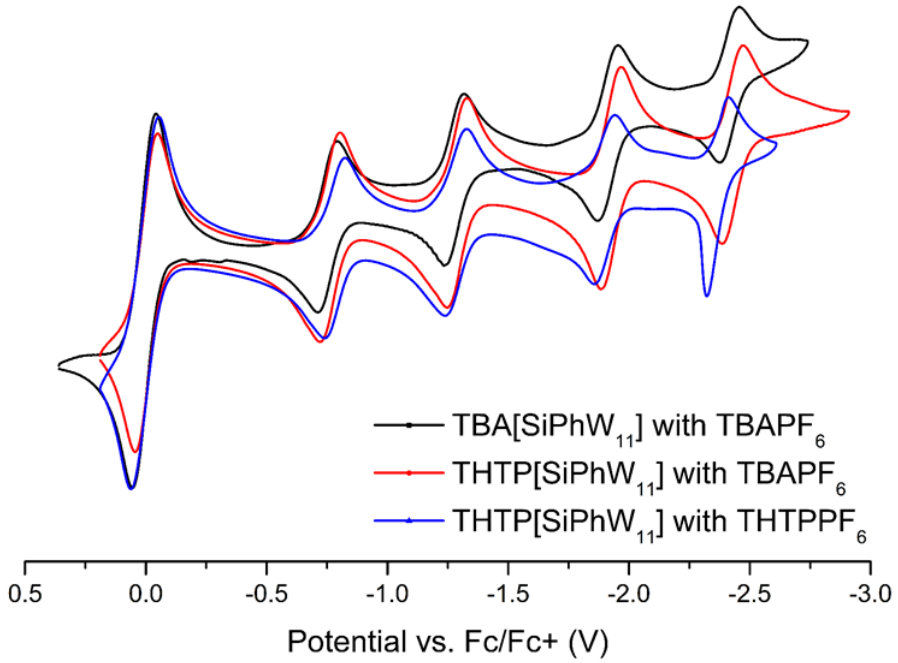


Figure 110. Cyclic voltammograms of TBA[SiPhW$_{11}$] with TBAPF$_6$ electrolyte (black), THTP[SiPhW$_{11}$] with TBAPF$_6$ electrolyte (red) and THTP[SiPhW$_{11}$] with THTPPF$_6$ electrolyte (blue) demonstrating that the effects of cations on the reversibility and reduction potentials within the system are negligible.

The one exception to the above behaviour is the voltammogram of THTP[PPhW$_{11}$] when compared with K[PPhW$_{11}$]. Figure 111 shows the voltammograms of K[PPhW$_{11}$] and THTP[PPhW$_{11}$] recorded under the exact same conditions. It is immediately clear that for K[PPhW$_{11}$], the electrochemical reversibility of the system becomes progressively worse at more reducing potentials, suggesting a lack of chemical stability of the analyte under more reducing conditions. Comparing this to THTP[PPhW$_{11}$], the peaks are well resolved and much closer to ideal Nernstian behaviour. Indicating that the THTP ions may form strong ion pairs with the POM (and its reduced states) and protect it through the aforementioned “shrink-wrapping” phenomenon. Irrespective of the exact mechanism, THTP cations clearly have a pronounced stabilisation effect on the electrochemical properties of the POM.

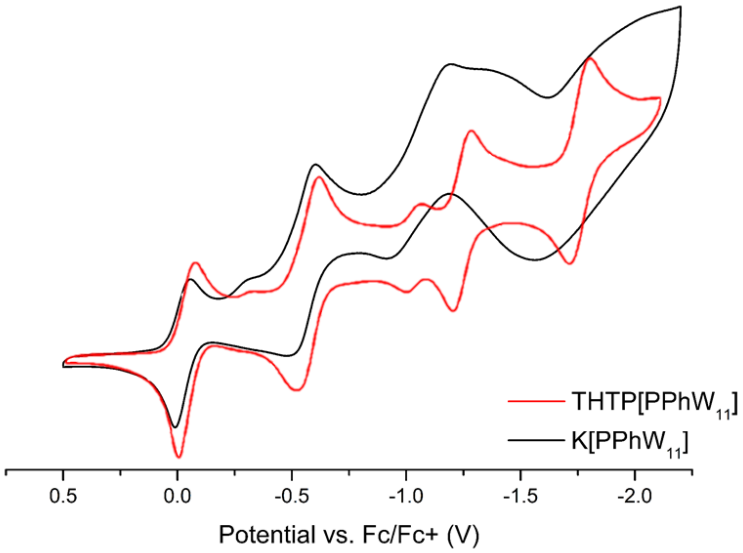


Figure 111. Cyclic voltammograms of $K[PPhW_{11}]$ (black) and $THTP[PPhW_{11}]$ (red) in dry acetonitrile referenced vs. Fc^{+}/Fc. The use of THTP as a cation results in an increase in the electrochemical stability of the system at more reducing potentials vs. K^{+} due to "shrink wrapping" effects.

4.4 Conclusion

In summary, the synthesis and characterisation of the first examples of POM-ILs featuring covalently functionalised polyoxometalates as the anionic component has been achieved. The covalent hybrid POM-ILs were formed from the combination of potassium or TBA hybrid precursors with THTPCl, which yielded room temperature POM-ILs. Two different covalent hybrid POM-ILs were synthesised ($THTP[SiPhW_{11}]$ and $THTP[PPhW_{11}]$) with the same phenyl organic group but the linker between the POM and the phenyl ring differed between the electron withdrawing phosphoryl group or the electron donating silyl group. The same cation was also combined with the plenary Keggin phosphotungstate ($THTP[W_{12}]$), and this literature reported molecule was used as a comparative aid and benchmark.

Confirmation of the structure and purity of the samples were verified by ^{1}H and ^{31}P NMR spectroscopy, IR spectroscopy and CHN microanalysis. The thermal stability and phase behaviour were also probed using TGA, DSC and PXRD respectively. It was found that all POM-ILs exhibited superior thermal stability compared to their synthetic precursors and were similarly high across all of the samples (>400°C), suggesting that the nature of the cation dominates this property. The phase behaviour of $THTP[W_{12}]$ was determined to be more complex than previously reported, with a crystalline phase that transforms to an amorphous phase at 68.2°C which then undergoes reversible melting at 133.6°C to a liquid phase, the assignment of the first two phases were assisted by PXRD measurements. The phase

behaviour of THTP[$SiPhW_{11}$] and THTP[$PPhW_{11}$] were simpler, exhibiting just one measurable liquid phase across the entire measurable temperature range (supported by PXRD measurements). It was found that the inclusion of organic groups into the POM core, combined with a highly asymmetric and bulky cation, favoured the formation of an IL phase with a wide temperature range though desymmetrisation and inhibition of ordered packing. The electronic nature of the POM-ILs were investigated using voltammetry, it was found that the POM was the only contributor to the electroactivity of the POM-ILs. The redox chemistry of the POMs were stable over the entire measurement window, with four 1-electron peaks which showed near-Nernstian reversibility. The redox potentials, and hence the LUMO energies, were found to be tunable based on the linker used to append the organic groups to the POM, with no cation dependence. The THTP cation was found to be an excellent thermal (over fourfold increase in the onset of decomposition) and electrochemical stabiliser for the more labile and reactive [$PPhW_{11}$] anion.

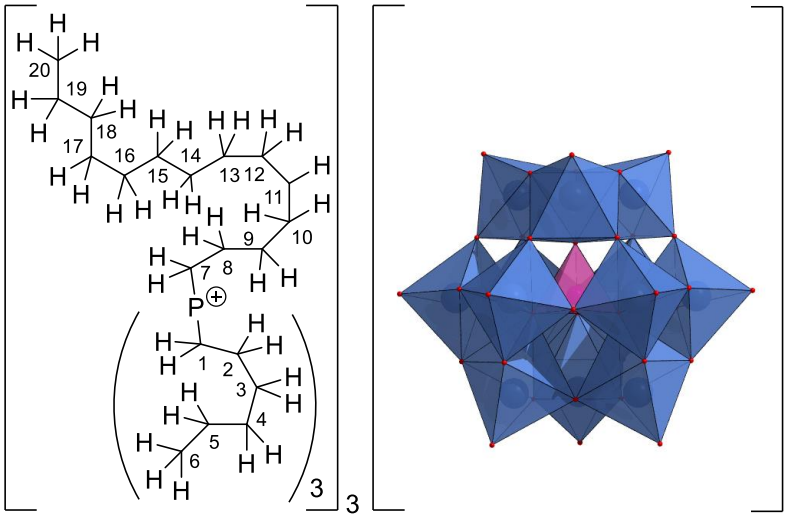
Chiefly, the work described here demonstrates that POM-ILs formed from covalently functionalised polyoxometalates are a new family of materials that possess several benefits over their non-functionalized derivatives. The first being that the functionalisation results in desymmetrisation and morphological changes to the POM anion, which encourages the formation of a POM-IL phase by discouraging packing. The second, and perhaps most important benefit, is the ability to tune the electrochemical behaviour of the POM without affecting the physical properties of the material, through the modulation of the electronics of the grafted organic group. This total independent control of physical and electronic properties of electroactive ionic liquids represents a new paragon in the “designer solvent” aspect of ionic liquid chemistry. Another opportunity offered by this chemistry is the thermal and electrochemical protection of reactive POM species or isolation of reactive POM intermediates.

When considering the development of this area, there are an abundance of applications that spring to mind based on the findings above. Again returning to the idea of “designer solvents”, these materials with their unique phase behaviour and tuneable electrochemistry would be particularly well suited for energy storage applications, either as dual electrolyte-solvent systems (if high viscosity issues could be averted through molecular design or operating high temperature) in batteries and supercapacitors, as electroactive films on the surface of electrodes or as electroactive layers between components in such devices. Whilst here we showcase only the electronic tuning of the system, equally the physical

properties of the system could be tailored to achieve specific properties such as introducing polyether linkages to aid viscosity or perfluoro groups to access new solubility – the ability to us this near limitless design concept embodied within the ethos of organic chemistry either on the cation or on the site of functionalisation gives an unprecedented degree of tuneability. A final opportunity is offered by the so called “shrink-wrapping” protective effect of these bulky ionic liquid cations. The purposeful formation of an IL phase could be used as a tool for stabilising certain reactive species, perhaps with interesting fluorescent or magnetic properties that are sensitive to environment and bimolecular interactions. Or even as an isolating tool during the complex formation of larger POM species, i.e. to tackle problems of speciation and reactive intermediates during POM self-assembly processes which are often black box in nature.

4.5 Experimental

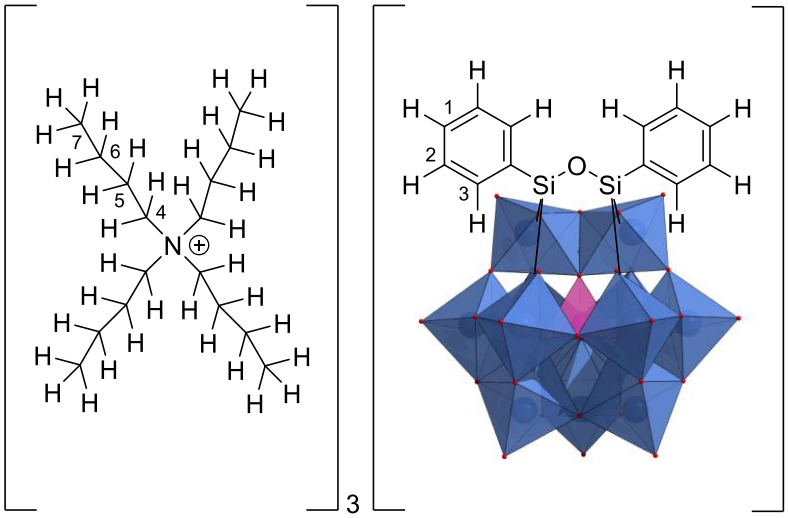
Synthesis of $(C_{32}H_{68}P)_3[PW_{12}O_{40}]$ “THTP[W_{12}]”



The synthesis of $(THTP)_3PW_{12}O_{40}$ was carried out according to a modified literature procedure.[3] To a solution of $Na_3PW_{12}O_{40}$ (6.0 g, 2.0 mmol, 1 equiv.) in acetonitrile (30 mL) was added a solution of trihexyl(tetradecyl)phosphonium bromide (4.6 g, 8.1 mmol, 4 equiv.) in DMF (5 mL). The mixture was stirred at r.t for 1 h. A white and sticky solid was obtained after removal of the solvent *in vacuo* (rotary evaporator). The product was purified by washing with water and methanol. The solid was then dissolved in acetonitrile and precipitated by addition of methanol giving the final product as an off-white powder (4.8 g, 55%). ^{1}H NMR ($CDCl_3$, 500 MHz. ppm): δ = 2.29-2.17 (C1/7-H, m, 24H, CH_2), 1.66-1.22

(C2-6/8-19-H, m, 144H, CH_2), 0.97-0.85 (C6/20-H, m, 36H, CH_3); ^{31}P NMR ($CDCl_3$, 202MHz. ppm): δ = 33.2, -15.3. ATR-IR (cm^{-1}): 2923 (m,ν_{C-H}), 2853 (m,ν_{C-H}), 1462 (w,ν_{C-H}), 1408 (vw,,ν_{C-H}), 1077 (s,ν_{P-O}), 984 (s,$\nu_{W=O}$), 893 (s,ν_{W-O-W}), 798 (vs,ν_{W-O-W}). λ_{max} (MeCN): 266 nm (ε = 57308 $dm^3mol^{-1}cm^{-1}$). Anal. *Calcd.* for $C_{96}H_{204}O_{40}P_4W_{12}$ (4328.59): C 26.64, H 4.75, N 0.0. Found: C 26.63, H 4.73, N 0.0.

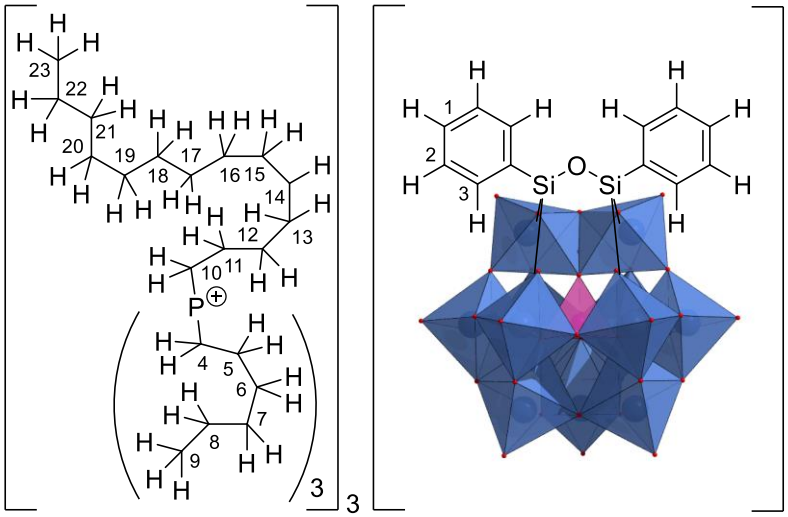
Synthesis of $(C_{16}H_{36}N)_3[PW_{11}O_{40}(SiC_6H_5)_2]$ "TBA[SiPhW$_{11}$]"



The synthesis of "TBA[SiPhW$_{11}$]" was carried out a;ccording to a modified literature procedure.[26] $(TBA)_4H_3PW_{11}O_{39}$ (5.0 g, 1.4 mmol) was dissolved in 60 ml of acetonitrile under an inert atmosphere. To this was added trichlorophenylsilane (0.44 ml, 2.7 mmol) dropwise which caused the solution to turn from cloudy white to pale yellow. The mixture was then allowed to stir at room temperature for 15 hours in the absence of light. After reaction completion, the solvent was evaporated to give the crude product. The crude product was then dissolved in the minimum amount of acetonitrile, at this point if the POM was reduced (solid is blue), bromine was added to reoxidise it, and precipitated with the addition of water. The suspension is then filtered and washed with water and diethyl ether to give the final product as a pale-yellow powder (2.9 g, 57%). ^1H NMR (CD_3CN, 500MHz, ppm): δ = 7.87 (C3-H, m, 4H, CH_{Ar}), 7.52 (C1/2-H, m, 6H, CH_{Ar}), 3.13 (C4-H, m, 24H, CH_2), 1.64 (C5-H, tt, J=8.1, 6.1Hz, 24H, CH_2), 1.40 (C6-H, m, 24H, CH_2), 1.01 (C7-H, t, J=7.3Hz, 3H, CH_3). ^{31}P NMR (CD_3CN, 202MHz, CD_3CN, ppm): δ = -13.36. ATR-IR (cm^{-1}): 2961 (w,ν_{C-H}), 2873 (w,ν_{C-H}), 1463 (w,ν_{C-H}), 1379 (vw,ν_{C-H}), 1109 (m,$\nu_{Si-O-Si}$),

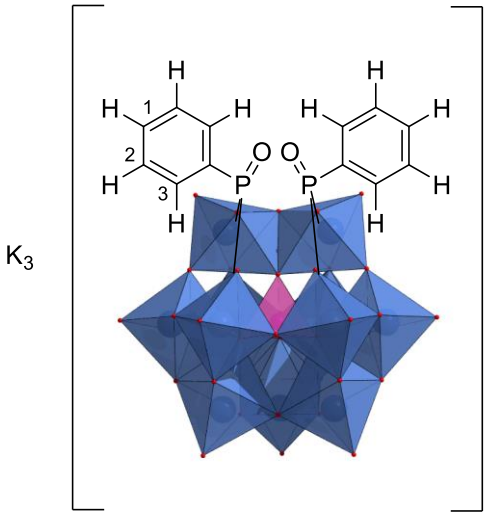
958 (s,$\nu_{W=O}$), 865 (m,ν_{W-O-W}), 818-705 (vs,ν_{W-O-W}). λ_{max} (MeCN): 266 nm (ε = 53835 $dm^3mol^{-1}cm^{-1}$). Anal. *Calcd.* for $C_{60}H_{118}N_3O_{40}Si_2PW_{11}$ (3630.96): C 19.85, H 3.28, N 1.16. Found: C 20.58, H 3.47, N1.10

Synthesis of $(C_{32}H_{68}P)_3[PW_{11}O_{40}(SiC_6H_5)_2]$ "THTP[SiPhW$_{11}$]"



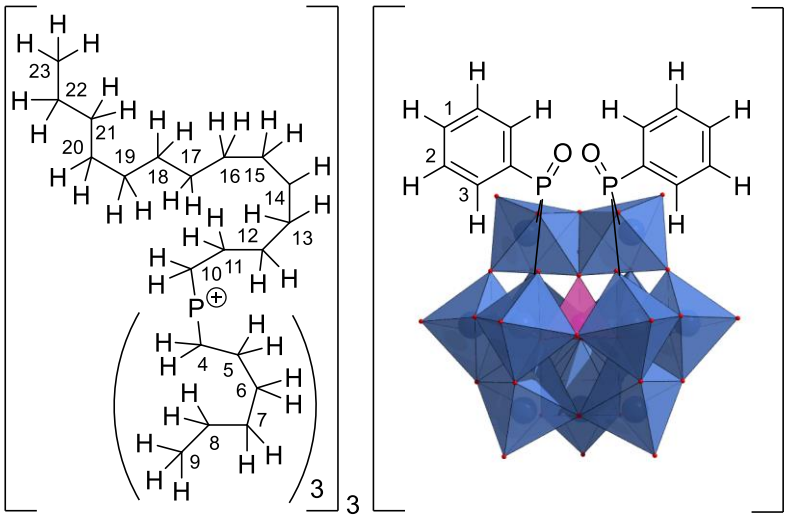
TBA[SiPhW$_{11}$] (1.0 g, 0.30 mmol) was suspended in 30 ml of water. To this was added a solution of trihexyltetradecylphosphonium chloride (0.50 g, 0.80 mmol) in cyclohexane (20 ml) dropwise under vigorous stirring. The suspension was then heated overnight at 80°C with vigorous stirring and in the absence of light. The solution was then allowed to cool causing the precipitation of a clear amorphous sticky solid, the solution was carefully decanted from the reaction flask and the solid was dissolved in the minimum amount of acetonitrile. This solution was then poured into a large excess of toluene (ca. 300 ml) and the volume was reduced to 15 ml (rotary evaporator) causing the precipitation of the solid. The toluene solution was carefully decanted and the solid was sonicated in toluene and decanted twice more. The final product was then dried on the Schlenk line yielding the final product as a glassy colourless solid (1.0 g, 83%). ^{1}H NMR (CD_3CN, 500MHz, ppm): δ = 7.87 (C3-H, m, 4H, CH_{Ar}), 7.52 (C1/2-H, m, 6H, CH_{Ar}), 2.09 (C4/10-H, m, 24H, CH_2), 1.30-1.60 (C5-8/11-22-H, m, 144H, CH_2), 0.93 (C9/23-H, m, 36H, CH_3). ^{31}P NMR (CD_3CN, 202MHz, ppm): δ = 33.7, -13.4. ATR-IR (cm^{-1}): 2923 (m,ν_{C-H}), 2853 (m,ν_{C-H}), 1459 (w,ν_{C-H}), 1407 (vw,ν_{C-H}), 1109 (m,$\nu_{Si-O-Si}$), 1038 (m,ν_{P-O}) 958 (vs,$\nu_{W=O}$), 867 (vs,ν_{W-O-W}) 813-706 (vs,ν_{W-O-W}). λ_{max} (MeCN): 266 nm (ε = 53546 $dm^3mol^{-1}cm^{-1}$). Anal. *Calcd.* for $C_{108}H_{214}O_{40}Si_2P_4W_{11}$ (4355.13): calcd. C 29.78, H 4.95, N 0.0. Found: C 29.50, H 4.82, N 0.0.

Synthesis of $K_3[PW_{11}O_{39}(POC_6H_5)_2]$ "K[PPhW$_{11}$]"



The synthesis of K[PPhW$_{11}$] was carried out according to a modified literature procedure.[27] $K_7PW_{11}O_{39}$ (1.5 g, 0.50 mmol, 1 equiv.) was dissolved in 60 ml of dry acetonitrile under an inert atmosphere. Phenyphosphoryl dichloride (135 µl, 1.0 mmol, 2 equiv.) was then added dropwise to the solution. The mixture was then allowed to stir at 35ºC for 2 days in the absence of light. After reaction completion, the solid was filtered and discarded. The filtrate was evaporated (rotary evaporator) to give a yellow solid. Then, K[PPhW$_{11}$] was dissolved in acetonitrile and precipitated by addition of diethyl ether to give the final product as a pale-yellow powder (0.6 g, 41%). ^{1}H NMR (CD_3CN, 500MHz, ppm): δ = 8.13-8.06 (C3-H, m, 4H, CH_{Ar}), 7.73-7.68 (C1-H, m, 2H, CH_{Ar}), 7.66-7.60 (C2-H, m, 4H, CH_{Ar}); ^{31}P NMR (CD_3CN, 202MHz, ppm): δ = 19.5, -13.7. ATR-IR (cm^{-1}): 1613 (vw,$\nu_{C=C}$), 1439 (w,ν_{C-H}), 1112 (m,$\nu_{P=O}$), 1061 (m,ν_{P-O-W}), 1038(m,ν_{P-O}), 967 (s,$\nu_{W=O}$), 875 (s,ν_{W-O-W}), 725 (vs,ν_{W-O-W}). λ_{max} (MeCN): 265 nm (ε = 43415 dm^{3}mol^{-1}cm^{-1}). Anal. *Calcd.* for $C_{10}H_{12}K_3PSi_2W_{11}O_{40}$ (3020.86): C 4.77, H 0.33, N 0.00. Found: C 5.97, H 0.74, N 0.36.

Synthesis of $(C_{32}H_{68}P)_3[PW_{11}O_{39}(POC_6H_5)_2]$ "THTP[PPhW$_{11}$]



0.50 g K[PPhW$_{11}$] (160 µmol, 1 equiv.) and 0.30 g of trihexyltetradecylphosphonium bromide (0.50 mmol, 3.1 equiv.) were suspended in 50 ml of dry acetonitrile. The suspension was then heated at 35°C with vigorous stirring in the absence of light. After 1 h the solid was filtered and discarded. The solvent was evaporated (rotary evaporator) to give a sticky solid. Then, the hybrid material was purified by washing with water and methanol. Finally, the product was dissolved in acetonitrile and precipitated by addition of diethyl ether to give a sticky pale yellow solid (0.2 g, 29%). ^{1}H NMR (CD_3CN, 500MHz, ppm): δ = 8.12-8.07 (C3-H, m, 4H, CH_{Ar}), 7.73-7.68 (C1-H, m, 2H, CH_{Ar}), 7.67-7.59 (C2-H, m, 4H, CH_{Ar}), 2.19-2.09 (C4/10-H, m, 24H, CH_2), 1.59-1.21 (C5-8/11-22-H, m, 144H, CH_2), 0.96-0.83 (C9/23-H, m, 36H, CH_3);^{31}P NMR (CD_3CN, 202 MHz, ppm): δ = 33.6, 19.4, -13.7. ATR-IR (cm^{-1}): 2923 (m,ν_{C-H}), 2853 (m,ν_{C-H}), 1458 (w,ν_{C-H}), 1408 (vw,ν_{C-H}), 1116 (m,ν_{P-H}), 1076 (m,ν_{P-O-W}), 1038 (m,ν_{P-O}), 971 (vs,$\nu_{W=O}$), 877 (s,ν_{W-O-W}), 809 (vs,ν_{W-O-W}). λ_{max} (MeCN): 266 nm (ε = 12754 dm^{3}mol^{-1}cm^{-1}). Anal. *Calcd.* for $C_{108}H_{214}O_{41}P_6W_{11}$ (4355.13): C 29.64, H 4.93, N 0.0. Found: C 25.56, H 4.29, N 0.0.

4.6 References

1. A. B. Bourlinos, K. Raman, R. Herrera, Q. Zhang, L. A. Archer and E. P. Giannelis, *J. Am. Chem. Soc.*, 2004, **126**, 15358-15359.
2. P. G. Rickert, M. R. Antonio, M. A. Firestone, K.-A. Kubatko, T. Szreder, J. F. Wishart and M. L. Dietz, *Dalton Trans.*, 2007, 529-531.
3. P. G. Rickert, M. R. Antonio, M. A. Firestone, K.-A. Kubatko, T. Szreder, J. F. Wishart and M. L. Dietz, *J. Phys. Chem. B*, 2007, **111**, 4685-4692.

4. Y. Qiao, Z. Hou, H. Li, Y. Hu, B. Feng, X. Wang, L. Hua and Q. Huang, *Green Chem.*, 2009, **11**, 1955-1960.
5. H. Li, Y. Qiao, L. Hua, Z. Hou, B. Feng, Z. Pan, Y. Hu, X. Wang, X. Zhao and Y. Yu, *Chemcatchem*, 2010, **2**, 1165-1170.
6. P. Sun, S. Zhang, J. Pang, Y. Tan, D. Sun, C. Xia, X. Cheng and X. Xin, *J. Mol. Liq.*, 2018, **272**, 180-187.
7. S. Liang, Y.-M. Nie, S.-H. Li, J.-L. Zhou and J. Yan, *Molecules*, 2019, **24**, 806.
8. W. Zhu, W. Huang, H. Li, M. Zhang, W. Jiang, G. Chen and C. Han, *Fuel Process. Technol.*, 2011, **92**, 1842-1848.
9. P. Zhao, M. Zhang, Y. Wu and J. Wang, *Ind. Eng.*, 2012, **51**, 6641-6647.
10. M. Rostami, A. R. Khosropour, V. Mirkhani, I. Mohammadpoor-Baltork, M. Moghadam and S. Tangestaninejad, *C. R. Chimie*, 2011, **14**, 869-877.
11. Z.-g. Wang, Y. Yang, X.-h. Cao and M. Lu, *J. Iran. Chem. Soc.*, 2015, **12**, 1765-1770.
12. J. A. Abia and R. Ozer, *Bioresources*, 2013, **8**, 2924-2933.
13. X. Chen, B. Souvanhthong, H. Wang, H. Zheng, X. Wang and M. Huo, *Appl. Catal. B*, 2013, **138**, 161-166.
14. X.-X. Han, Y.-F. He, C.-T. Hung, L.-L. Liu, S.-J. Huang and S.-B. Liu, *Chem. Eng. Sci.*, 2013, **104**, 64-72.
15. X. Duan, G. Sun, Z. Sun, J. Li, S. Wang, X. Wang, S. Li and Z. Jiang, *Catal. Commun.*, 2013, **42**, 125-128.
16. S. Herrmann, M. Kostrzewa, A. Wierschem and C. Streb, *Angew. Chem. Int. Ed.*, 2014, **53**, 13596-13599.
17. M.-Y. Wang, Q.-W. Song, R. Ma, J.-N. Xie and L.-N. He, *Green Chem.*, 2016, **18**, 282-287.
18. A.-L. Kubo, L. Kremer, S. Herrmann, S. G. Mitchell, O. M. Bondarenko, A. Kahru and C. Streb, *ChemPlusChem*, 2017, **82**, 867-871.
19. A. Misra, I. Franco Castillo, D. P. Müller, C. González, S. Eyssautier-Chuine, A. Ziegler, J. M. de la Fuente, S. G. Mitchell and C. Streb, *Angew. Chem. Int. Ed.*, 2018, **57**, 14926-14931.
20. C. Li, B. Zha, Z. Yao and Z. Jiang, *Polyhedron*, 2019, **159**, 176-181.
21. G. S. Kim, K. S. Hagen and C. L. Hill, *Inorg. Chem.*, 1992, **31**, 5316-5324.
22. C. Maton, N. De Vos and C. V. Stevens, *Chem. Soc. Rev.*, 2013, **42**, 5963-5977.
23. C. P. Pradeep, D.-L. Long and L. Cronin, *Dalton Trans.*, 2010, **39**, 9443-9457.
24. S. Fujimoto, J. M. Cameron, R.-J. Wei, K. Kastner, D. Robinson, V. Sans, G. N. Newton and H. Oshio, *Inorg. Chem.*, 2017, **56**, 12169-12177.
25. M. Boujtita, J. Boixel, E. Blart, C. R. Mayer and F. Odobelc, *Polyhedron*, 2008, **27**, 688-692.
26. D. Agustin, J. Dallery, C. Coelho, A. Proust and R. Thouvenot, *J. Organomet. Chem.*, 2007, **692**, 746-754.
27. Z. G. Sun, L. C. Zhang, Z. M. Liu, L. Y. Cui, C. H. Tian, H. D. Liang, Z. M. Zhu and W. S. You, *J. Coord. Chem.*, 2006, **59**, 1557-1564.

5. Conclusions and Outlook

As each results chapter separately offers a comprehensive conclusion of the work detailed within, including specific future developments that could be made for each project, it seems fitting that this final chapter should be dedicated to the broad conclusions of the research as a whole. The overarching goal of this project was to investigate the influence that different organofunctionalisation strategies had on the fundamental properties of the polyoxometalate. This has certainly been achieved throughout this work, with several methods adopted based on the two established routes of organofunctionalisation; Class I via electrostatic interactions and Class II through covalent grafting of organic groups to the POM.

With regards to the two strategies (Class I vs. Class II), it can be surmised that whilst both offer distinct advantages, Class I approaches were extremely effective for modulating the physical properties of the hybrids due to ionic interactions, where it was demonstrated that those that are capable of forming robust hydrogen bonding networks had no true melting temperature (only decomposition temperature) and very low solubility, whereas those that form no direct interactions with the POM and hinder structured packing through large asymmetric morphology formed POM-ILs with wide solubility windows. The electronic properties of Class II hybrids were more easily modulated through rational design of the organic component and judicious choice of covalent linker, in all cases, trends observed could be rationalised through considering the electronics of the entire system.

Novel concepts that have been explored within this work have opened up new avenues of exploration, particularly, the coupling of two photoactive acceptor molecules for proposed “double photoexcitation induced electron transfer” (i.e. polyoxometalates and BTD cations as in Figure 60 – Chapter 2) could pose an interesting concept, not only in polyoxometalate based catalysis, but other systems where the entrapment of high energy electrons is desirable for photoreduction of inert substrates. Another intriguing concept is the HOMO-LUMO orbital engineering of POMs in the optimisation of catalysis through consideration of all steps required to close a catalytic cycle, often too much emphasis is placed on compressing the HOMO-LUMO gap with little regard for the final energies of the HOMO and LUMO respectively. Exploring novel organic modification approaches contributes to the understanding of how to manipulate the frontier orbitals of POMs to design molecules and materials with optimal electronic properties. The last body of work describes the independent physical and electronic modulation of POM properties through the tandem approach of both Class I and Class II hybridisation methods. This

approach exemplifies that the consideration of all the components of the system is vital for applications-based research. Conceptually, one could design a host of compounds that combine physical (ionic liquids, films, liquid crystals) and electronic (redox activity, magnetism, optical properties) attributes for the design of bespoke materials with well-defined properties.

To conclude, we have demonstrated the versatility offered by different organofunctionalisation approaches to generate inorganic-organic POM hybrids with distinct properties. These studies are highly instructive towards the understanding of how functionalisation approaches affect the intrinsically remarkable properties of POMs and can act as a guide and inspiration toward the intelligent design of “designer” organic-inorganic hybrid POMs for targeted applications.

6. Methods, Materials and Instrumentation

All commercially available solvents and reagents were purchased from *Thermo Fisher Scientific*, *Sigma Aldrich Corporation*, *Alfa Aesar*, *Honeywell Fluka* or *Tokyo Chemical Industries UK Ltd.* and used without further purification.

Nulcear Magnetic Resonance (NMR) spectroscopy experiments was performed on a Bruker AV400 or Bruker AV(III)500 spectrometer at 298 K. Chemical shifts (δ) are recorded in parts per million (ppm), coupling constants (J) are given in Hertz (Hz), and the residual solvent shift is used as an internal standard. Peak multiplicity is denoted by the following abbreviations: singlet (s), doublet (d), triplet (t), quartet (q), multiplet (m) and triplet of triplets (tt).

Electrospray Ionisation Mass Spectrometry (ESI-MS) was recorded either using a Bruker micro-TOF II or Bruker Impact II mass spectrometer with adapted instrument parameters for the detection of high molecular weight polyoxometalate anions. For [$AsPhW_{17}$], [$AsPhNH_2W_{17}$] and [$AsPhNO_2W_{17}$], the samples were delivered to the ionisation source by a pure acetonitrile stream to avoid sample hydrolysis either prior to or during ionisation.

Attenuated Total Reflection Fourier-transform Infra-red spectroscopy (ATR-FTIR) was recorded on a Bruker Tensor 27 spectrometer equipped with a Pike GladiATR module with a diamond crystal.

UV-vis spectroscopy (UV-vis) was performed on an Agilent Cary 5000 UV-Vis-NIR Absorption spectrometer. Solution phase measurements were performed using the standard double cuvette holder module in absorption mode. Solid state diffuse reflectance absorption measurements were performed using a DRA-900 InGaAs integrating sphere.

Fluorescence measurements were recorded on an Edinburgh Instruments FLS980 Photoluminescence spectrometer equipped with a powder sample holder with excitation wavelength of 305 nm using a 260 nm filter.

CHN Elemental Microanalysis was performed by the University of Nottingham School of Chemistry elemental microanalysis services on a Exeter analytical CE-440 Elemental Analyser.

Single crystal X-ray diffraction measurements were performed using the following procedure: a single crystal was selected and mounted using Fomblin® (YR-1800 perfluoropolyether oil) on a polymer-tipped MiTeGen MicroMountTM and cooled rapidly to 120 K in a stream of cold N_2 using an Oxford Cryosystems open flow cryostat.[1] Single crystal X-ray diffraction data were collected on a SuperNova Duo diffractometer (Atlas CCD area detector, mirror-monochromated Mo-Kα radiation source; λ = 0.71073 Å; ω scans) or an XtaLAB PRO MM007 (PILATUS3 R 200K Hybrid Pixel Array detector, mirror-monochromated Cu-Kα radiation source; λ = 1.54184 Å, ω scans). Cell parameters were refined from the observed positions of all strong reflections and absorption corrections were applied using a Gaussian numerical method with beam profile correction (CrysAlisPro). The structure was solved within Olex²[2] by dual space iterative methods (SHELXT)[3] and all non-hydrogen atoms refined by full-matrix least-squares on all unique F2 values with anisotropic displacement parameters (SHELXL)[4]. Hydrogen atoms were refined geometries and riding thermal parameters. Crystal structures containing voids with disordered solvent and counterions had their electronic contribution to the structure factor ascertained using the PLATON SQUEEZE procedure.[5] Structures were checked with checkCIF.

Powder X-ray Diffraction (PXRD) measurements were performed using a PANalytical X'Pert PRO diffractometer with a Copper line focus X0ray tube (40 kV, 40 mA), with monochromator tuned to K-alpha1 (Kα1 = 1.540598) and a PIXcel detector (length 3°). The diffractometer had Bragg-Brentano geometry and was operated in reflection transmission mode with samples mounted on brass powder sample holders on a spinning stage. An incident beam Soller slit of 0.04 rad, 1° fixed anti scatter slit, incident beam mask of 10 mm and programmable automated divergence slit giving a constant illuminated path length of 5.0 mm were used.

Thermogravimetric Analysis (TGA) were performed either using a TA-Q500 (TA Instruments) or a TGA Discovery Instrument using a high temperature platinum pan within a temperature range of 25°C to 1000°C either under argon, nitrogen or air flow streams.

Differential Scanning Calorimetry (DSC) was performed on a TA-Q2000 (TA instruments) or TGA Discovery Instrument which were calibrated with an indium standard under nitrogen flow, samples were cycled at 10°C/min in a sealed aluminium pan.

Electrochemical methods, cyclic voltammetry (CV) and square wave voltammetry (SWV), were perfomed either on a CHI600E workstation for solution state measurements or an Autolab PGSTAT302N potentiostat for solid state measurements. A standard three electrode set-up was employed with a glassy carbon working electrode (d = 1.6 mm or 3 mm), Pt wire counter electrode and either a Ag wire pseudo reference with the addition of ferrocene as an external reference (solution state) or a Ag/AgCl non-aqueous reference electrode (solid state).

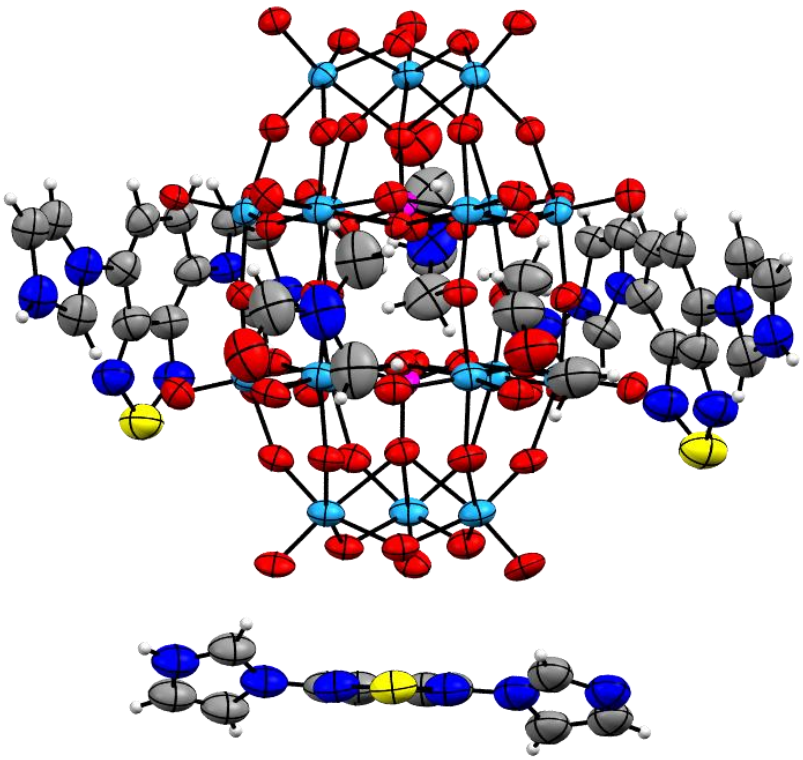
DFT calculations were performed using the BP86 functional[6] with the CRENBL basis set[7] and effective core potential used to model the core electrons. Solvation effects were accounted for using the polarisable continuum model (PCM). Calculations were performed with the Q-Chem software.[8]

Photocatalytic measurements (CO_2 reduction) were conducted by placing 50 mg of catalyst into a quartz reactor (20 ml), this was then purged with CO_2 three times and charged to a pressure of 1 bar, The reactor was then charged with 3 bar of H_2 giving a total pressure of 4 bar. The system was then irradiated with a Xe 300 W Cermax lamp (operating at 200 W) which was equipped with a UV cut-off filter. The photocatalytic activity was monitored by GC equipped with a specialist column for the separation of small molecules operating an FID/TCD detector.

Photooxidation measurements were conducted by preparing 4×10^{-5} M solutions of the analyte in DMF, 2.5ml of sample is transferred to a sealable cuvette and degassed for 30 minutes in an inert atmosphere followed by sealing of the system. The solution was then irradiated with a Xe 300 W Cermax lamp (operating at 200 W) either with or without a UV cut-off filter with no stirring, with measurements of the sample at specific time intervals by transferral to the UV-vis spectrometer in the absence of light. Catalyst recovery measurements were performed by opening the sealed system to the air and taking UV-vis measurements at defined time intervals on cycle mode.

7. Appendix

7.1. Crystal data and structure refinement for BTDImH[W_{18}]



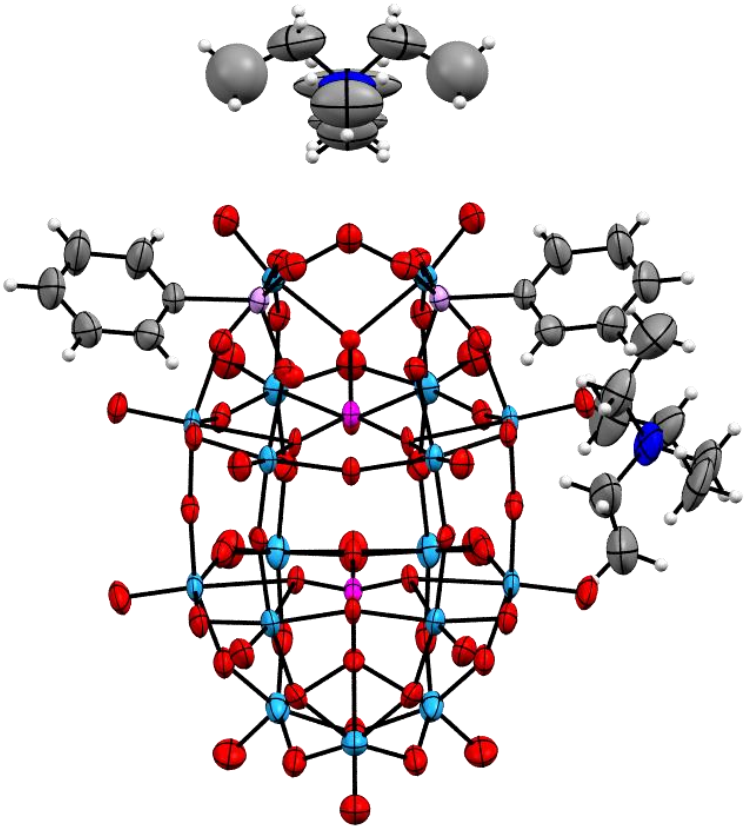
Compound	BTDImH[W_{18}]
Empirical formula	$C_{69}H_{107}N_{29}O_{73}P_2S_3W_{18}$
Formula weight	5978.25
Temperature/K	120.00(10)
Crystal system	triclinic
Space group	P-1
a/Å	14.0842(6)
b/Å	20.2347(9)
c/Å	21.3071(7)
α/°	91.830(3)
β/°	105.314(4)
γ/°	91.440(4)
Volume/Å^3	5850.2(4)
Z	2
ρ_{calc}g/cm^3	3.394
μ/mm^{-1}	33.488
F(000)	5436.0
Crystal size/mm^3	0.1 × 0.024 × 0.011
Radiation	CuKα (λ = 1.54184)
2Θ range for data collection/°	7.718 to 133.202
Index ranges	-16 ≤ h ≤ 8, -24 ≤ k ≤ 23, -25 ≤ l ≤ 25
Reflections collected	71800
Independent reflections	20405 [R_{int} = 0.1309, R_{sigma} = 0.1040]
Data/restraints/parameters	20405/2934/1392
Goodness-of-fit on F^2	1.062
Final R indexes [I>=2σ (I)]	R_1 = 0.0961, wR_2 = 0.2766
Final R indexes [all data]	R_1 = 0.1363, wR_2 = 0.3108
Largest diff. peak/hole / e Å^{-3}	5.03/-6.08

Hydrogen Bond List for BTDImH[W_{18}]

D	H	A	d(D-H)/Å
N(12)	H(12)	O(11S)[1]	0.8
N(17)	H(17)	O(6S)[2]	0.8
C(11)	H(11)	O(2)	0.9
C(11)	H(11)	N(2)	0.9
C(16)	H(16)	N(9)	0.9
C(18)	H(18)	O(8)[3]	0.9
N(32)	H(32)	O(12)[4]	0.8
C(25)	H(25)	O(10)	0.9
C(25)	H(25)	O(47)[5]	0.9
C(26)	H(26)	O(46)[5]	0.9
C(31)	H(31)	N(22)	0.9
C(36)	H(36)	O(5)	0.9
C(36)	H(36)	N(29)	0.9
C(38)	H(38)	O(1S)[5]	0.9
C(39)	H(39)	O(10)[5]	0.9
C(39)	H(39)	O(46)[5]	0.9
N(57)	H(57)	O(13)[4]	0.8
C(45)	H(45)	O(44)	0.9
C(46)	H(46)	O(44)	0.9
C(46)	H(46)	O(50)[6]	0.9
C(51)	H(51)	N(42)	0.9
C(54)	H(54)	O(14)	0.9
C(56)	H(56)	O(13)[4]	0.9
C(56)	H(56)	N(49)	0.9
C(59)	H(59)	O(14)[6]	0.9
C(2S)	H(2S)	O(15)	0.9
C(5S)	H(5SA)	O(53)[4]	0.9
C(9S)	H(9SA)	O(7)	0.9
C(10S)	H(10B)	O(13)	0.9
C(15S)	H(15A)	O(11S)	0.9
C(15S)	H(15B)	O(1)[7]	0.9

[1]1-X,1-Y,2-Z; [2]1-X,-Y,2-Z; [3]-X,-Y,2-Z;
[4]-1+X,+Y,+Z; [5]-X,1-Y,1-Z; [6]-X,-Y,1-Z;
[7]1+X,+Y,+Z

7.2. Crystal data and structure refinement for [AsPhW$_{17}$]



Compound	[AsPhW$_{17}$]
Empirical formula	$C_{82.2}H_{184.5}As_{1.69}N_6O_{74.85}P_2S_4W_{17.15}$
Formula weight	5925.40
Temperature/K	120(2)
Crystal system	orthorhombic
Space group	Pnma
a/Å	35.3840(3)
b/Å	25.6967(3)
c/Å	15.3245(2)
α/°	90
β/°	90
γ/°	90
Volume/Å^3	13933.8(3)
Z	4
ρ_{calc}g/cm^3	2.825
μ/mm^{-1}	27.406
F(000)	10951.0
Crystal size/mm^3	0.361 × 0.18 × 0.05
Radiation	CuKα (λ = 1.54184)
2Θ range for data collection/°	6.066 to 149.286
Index ranges	-44 ≤ h ≤ 44, -29 ≤ k ≤ 31, -19 ≤ l ≤ 19
Reflections collected	167022
Independent reflections	14493 [R_{int} = 0.0669, R_{sigma} = 0.0268]
Data/restraints/parameters	14493/211/598
Goodness-of-fit on F^2	1.069
Final R indexes [I>=2σ (I)]	R_1 = 0.0694, wR_2 = 0.1698
Final R indexes [all data]	R_1 = 0.0712, wR_2 = 0.1708
Largest diff. peak/hole / e Å^{-3}	3.95/-3.14

[1] J. Cosier and A. M. Glazer, Journal of Applied Crystallography 1986, 19, 105-107.

[2] O. V. Dolomanov, L. J. Bourhis, R. J. Gildea, J. A. K. Howard and H. Puschmann, Journal of Applied Crystallography 2009, 42, 339-341.

[3] G. M. Sheldrick, Acta Crystallographica a-Foundation and Advances 2015, 71, 3-8.

[4] G. M. Sheldrick, Acta Crystallographica Section C-Structural Chemistry 2015, 71, 3-8.

[5] P. Vandersluis and A. L. Spek, Acta Crystallographica Section A 1990, 46, 194-201.

[6] A. D. Becke, Density Matrices and Density Functionals (Dordrecht) 1987, pp. 443-455.

[7] W. C. Ermler, R. B. Ross and P. A. Christiansen, International Journal of Quantum Chemistry 1991, 40, 829-846.

[8] Y. Shao, Z. Gan, E. Epifanovsky, A. T. B. Gilbert, M. Wormit, J. Kussmann, A. W. Lange, A. Behn, J. Deng, X. Feng, D. Ghosh, M. Goldey, P. R. Horn, L. D. Jacobson, I. Kaliman, R. Z. Khaliullin, T. Kuś, A. Landau, J. Liu, E. I. Proynov, Y. M. Rhee, R. M. Richard, M. A. Rohrdanz, R. P. Steele, E. J. Sundstrom, H. L. Woodcock, P. M. Zimmerman, D. Zuev, B. Albrecht, E. Alguire, B. Austin, G. J. O. Beran, Y. A. Bernard, E. Berquist, K. Brandhorst, K. B. Bravaya, S. T. Brown, D. Casanova, C.-M. Chang, Y. Chen, S. H. Chien, K. D. Closser, D. L. Crittenden, M. Diedenhofen, R. A. DiStasio, H. Do, A. D. Dutoi, R. G. Edgar, S. Fatehi, L. Fusti-Molnar, A. Ghysels, A. Golubeva-Zadorozhnaya, J. Gomes, M. W. D. Hanson-Heine, P. H. P. Harbach, A. W. Hauser, E. G. Hohenstein, Z. C. Holden, T.-C. Jagau, H. Ji, B. Kaduk, K. Khistyaev, J. Kim, J. Kim, R. A. King, P. Klunzinger, D. Kosenkov, T. Kowalczyk, C. M. Krauter, K. U. Lao, A. D. Laurent, K. V. Lawler, S. V. Levchenko, C. Y. Lin, F. Liu, E. Livshits, R. C. Lochan, A. Luenser, P. Manohar, S. F. Manzer, S.-P. Mao, N. Mardirossian, A. V. Marenich, S. A. Maurer, N. J. Mayhall, E. Neuscamman, C. M. Oana, R. Olivares-Amaya, D. P. O'Neill, J. A. Parkhill, T. M. Perrine, R. Peverati, A. Prociuk, D. R. Rehn, E. Rosta, N. J. Russ, S. M. Sharada, S. Sharma, D. W. Small, A. Sodt, T. Stein, D. Stück, Y.-C. Su, A. J. W. Thom, T. Tsuchimochi, V. Vanovschi, L. Vogt, O. Vydrov, T. Wang, M. A. Watson, J. Wenzel, A. White, C. F. Williams, J. Yang, S. Yeganeh, S. R. Yost, Z.-Q. You, I. Y. Zhang, X. Zhang, Y. Zhao, B. R. Brooks, G. K. L. Chan, D. M. Chipman, C. J. Cramer, W. A. Goddard, M. S. Gordon, W. J. Hehre, A. Klamt, H. F. Schaefer, M. W. Schmidt, C. D. Sherrill, D. G. Truhlar, A. Warshel, X. Xu, A. Aspuru-Guzik, R. Baer, A. T. Bell, N. A. Besley, J.-D. Chai, A. Dreuw, B. D. Dunietz, T. R. Furlani, S. R. Gwaltney, C.-P. Hsu, Y. Jung, J. Kong, D. S. Lambrecht, W. Liang, C. Ochsenfeld, V. A. Rassolov, L. V. Slipchenko, J. E. Subotnik, T. Van Voorhis, J. M. Herbert, A. I. Krylov, P. M. W. Gill and M. Head-Gordon, Molecular Physics 2015, 113, 184-215.